

# Pattern Formation in Rotating Fluid Systems under the Influence of Magnetic Fields

Von der Universität Bayreuth  
zur Erlangung des Grades eines  
Doktors der Naturwissenschaften (Dr. rer. nat.)  
genehmigte Abhandlung

vorgelegt von

Erol Kurt

geboren am 19. Dezember 1975 in Ünye, Türkei

1. Gutachter: Prof. Dr. W. Pesch  
2. Gutachter: Prof. Dr. F.H. Busse

Tag der Einreichung: 04. 06. 2004  
Tag des Kolloquiums: 20. 07. 2004



# Contents

<b>Zusammenfassung</b>	<b>iii</b>
<b>Introduction</b>	<b>1</b>
<b>1 Mathematical Description of Pattern Forming Instabilities</b>	<b>3</b>
1.1 Linear analysis . . . . .	4
1.2 Galerkin analysis . . . . .	6
1.2.1 Representation of periodic patterns . . . . .	6
1.2.2 Stability of the rolls . . . . .	6
1.3 Order parameter equations . . . . .	7
1.3.1 General calculational scheme . . . . .	8
1.3.2 Landau Equation . . . . .	9
1.3.3 Coupled amplitude equations near a codimension-2 point . . . . .	11
1.4 Patterns with resonant- modes interaction . . . . .	12
1.5 Numerical simulations . . . . .	14
<b>2 Convection in a Rotating Annulus with an Azimuthal Magnetic Field</b>	<b>17</b>
Introduction . . . . .	17
2.1 Mathematical Formulation of the Problem and Numerical Methods . . . . .	18
2.2 Linear Analysis for the Onset of Convection . . . . .	22
2.3 Nonlinear Analysis of Roll Solutions . . . . .	29
2.3.1 Nusselt number . . . . .	29
2.3.2 Stability diagrams of rolls at large $P$ . . . . .	32
2.3.3 Stability diagrams of rolls at low $P$ . . . . .	36
2.4 Subharmonic Varicose ( $SHV$ ) and Knot Patterns . . . . .	40
2.4.1 General shortwave destabilizations . . . . .	41
2.4.2 Subharmonic varicose patterns . . . . .	42
2.4.3 Knot instability . . . . .	49
2.5 Direct Simulations . . . . .	54
2.5.1 Simulations at large $P$ . . . . .	55
2.5.2 Simulations at low $P$ . . . . .	59
2.6 Concluding Remarks . . . . .	67

---

<b>3</b>	<b>Pattern Formation in Magnetic Ekman-Couette Layer</b>	<b>71</b>
	Introduction . . . . .	71
3.1	Mathematical Formulation of the Problem and Numerical Methods . .	73
	3.1.1 The Ekman spiral . . . . .	73
	3.1.2 Basic equations and geometry . . . . .	74
3.2	Linear Analysis . . . . .	82
	3.2.1 Stationary bifurcation at small $\tau$ . . . . .	83
	3.2.2 The oscillatory instabilities for high Coriolis number . . . . .	89
3.3	Nonlinear Analysis of Roll Solutions . . . . .	98
	3.3.1 Nusselt number . . . . .	98
	3.3.2 Stability diagrams of stationary rolls at low $\tau$ . . . . .	101
	3.3.3 Weakly nonlinear analysis near the codimension-2 point . . . . .	104
3.4	Numerical Simulation of the Ekman-Couette Patterns . . . . .	105
	3.4.1 Simulations at low $\tau$ . . . . .	105
	3.4.2 Simulations in the traveling wave regime . . . . .	107
3.5	Solitary Vortex Solutions . . . . .	111
	3.5.1 The directional Nusselt numbers . . . . .	113
	3.5.2 The onset of the solitary vortex solutions . . . . .	116
	3.5.3 Stability analysis of the solitary vortex solutions . . . . .	117
3.6	Concluding Remarks . . . . .	119
<b>4</b>	<b>General Conclusion</b>	<b>121</b>
<b>A</b>	<b>Coupled Amplitude Equations for the <i>SHV</i> and Knot instabilities</b>	<b>123</b>
	A.1 Subharmonic varicose instability . . . . .	123
	A.2 Coupled amplitude equations for knots . . . . .	128
<b>B</b>	<b>Numerical Details of the Simulation Process</b>	<b>131</b>
	B.1 The Galerkin modes . . . . .	131
	B.2 The Adams-Bashforth time integration scheme . . . . .	132
	B.3 Construction of the fields . . . . .	133
	<b>Bibliography</b>	<b>135</b>

# Zusammenfassung

In dieser Arbeit werden Musterbildungsphänomene in zwei unterschiedlichen, rotierenden, elektrisch leitenden Flüssigkeitssystemen unter dem Einfluß eines Magnetfeldes untersucht. Es handelt sich einmal um den sog. rotierenden Annulus, der z.B. Konvektionsstrukturen im äquatorialen Bereich von rotierenden Himmelskörpern modelliert. In dem zweiten Beispiel geht es um Scherströmungsinstabilitäten, wenn einer Fluidschicht von außen ein Geschwindigkeitsgradient aufgeprägt wird. Neben vielen technischen Anwendungen (Turbinen) wird diese Situation auch über den Wind, der an der Wasseroberfläche der Ozeane angreift, realisiert. Die Konkurrenz zwischen Corioliskräften, Auftriebs- bzw. Scherkräften und besonders den magnetischen Kräften, die bisher in der Literatur für diese beiden Systeme praktisch nicht betrachtet wurden, führt zu reizvollen komplexen Musterbildungsphänomenen.

Beide Systeme werden durch gekoppelte, nichtlineare partielle Differentialgleichungen beschrieben. Die mathematischen Standardmethoden zur ihrer Analyse werden in **Kapitel 1** besprochen. Der Einsatz der musterbildenden Instabilitäten als Funktion der verschiedenen äußeren Kontrollparameter ist im Rahmen einer linearen Stabilitätsanalyse zu charakterisieren. Im schwach-nichtlinearen Bereich werden die resultierenden Muster mit Hilfe von sog. Ordnungsparametergleichungen, deren Herleitung leicht verallgemeinert wurde, beschrieben. Im voll nichtlinearen Bereich sind dann die Grundgleichungen numerisch exakt zu lösen, wobei wir verschiedene Galerkinmethoden verwenden.

Unter dem “rotierenden Annulus” (**Kapitel 2**) verstehen wir eine von innen gekühlte Fluidschicht im Mantelbereich eines rotierenden Zylinders unter dem Einfluß eines azimuthalen Magnetfeldes. Neben der Rayleighzahl  $R$  als Maß für den angelegten Temperaturgradienten und der Prandtlzahl  $P$  (das Verhältnis von Dissipation durch Strömung und durch Wärmeleitung), spielen die Rotationsfrequenz (parametrisiert durch die dimensionslose Corioliszahl  $\tau$ ) und die Stärke des angelegten Magnetfeldes (beschrieben durch die dimensionslose magnetische Feldenergie  $Q$ ) eine wichtige Rolle. Das Verhältnis von  $Q$  und  $\tau^2$  bestimmt z.B. die Orientierung der Konvektionsrollen bezüglich der Rotationsachse. Ausgehend von einer ausführlichen Analyse des linearen Bereichs wird der nichtlineare Bereich untersucht, in den man experimentell z.B. durch Vergrößerung  $R$  vorstößt. Von besonderem Interesse waren die sog. Knoten- und Hexaroll Muster, bei denen sich entlang der Rollenachse kurzweilige Modulationen ausbilden. Im Falle großer Prandtlzahlen  $P$  konnte Multistabilität der Muster nachgewiesen werden, d.h. verschiedenartige Rollenmuster stehen in Konkurrenz. Neben räumlich periodischen Mustern können sich bei gleichen äußeren Parametern solche mit

---

komplexer raum-zeitlicher Dynamik ausbilden, die sogar oft einen größeren Einzugsbereich haben. Der Fall kleiner  $P$  erwies sich als noch komplizierter, da viele Bifurkationen subkritisch waren.

Im **Kapitel 3** wurde das magnetische Ekman-Couette Problem untersucht. Eine Fluidschicht befindet sich zwischen zwei Platten, die in entgegengesetzter Richtung mit konstanter Geschwindigkeit (parametrisiert durch die dimensionslose Reynoldszahl  $Re$ ) bewegt werden. Die Anordnung wird um eine Achse senkrecht zu den Platten rotiert, das Magnetfeld zeigt in die gleiche Richtung. Es bildet sich im Grundzustand ein Geschwindigkeitsgradient senkrecht zu den Platten aus. Ohne Rotation der gesamten Anordnung ergibt sich so eine einfache Couetteströmung. Sie ist linear stabil für beliebige  $Re$ . Bei endlichem  $\tau$  bilden sich jedoch eine Grenzschicht an den Platten aus, in der sich der Geschwindigkeitsgradient konzentriert ("Ekman Layer"); er liegt dann in einer Ebene, die nicht parallel zur Zugrichtung der Platten ist. Die Grenzschichten werden linear instabil gegen Rollenstrukturen, die stationär sein können aber auch wie eine ebenen Welle laufen können. Es werden wieder die im Kapitel 1 beschriebenen Methoden angewendet, wobei die Existenz einer Strömung schon im Grundzustand die Rechnungen deutlich komplizierter macht. Abgesehen von der Berücksichtigung des endlichen Magnetfeldes ( $Q \neq 0$ ) wurden schon bekannte lineare und nichtlineare Analysen für  $Q = 0$  deutlich erweitert durch Verbesserung der numerischen Techniken. Besonderes Augenmerk wurde auf die zwei unterschiedlichen Typen (I/II) von laufenden Wellen gelegt, die sich sowohl in ihrer Ausbreitungsrichtung als auch ihre Frequenz unterscheiden. Spektakuläre Auswirkungen eines endlichen Magnetfeldes wurden allerdings nicht entdeckt. Es wirkt generell stabilisierend und führt eher zu quantitativen Verschiebung von Stabilitätsgrenzen.

Es besteht einige Hoffnung, daß in der nächster Zeit Experimente in Angriff genommen werden, mit denen sich unsere Ergebnisse direkt vergleichen lassen. Mit den in dieser Arbeit entwickelten Codes stehen alle theoretischen Hilfsmittel zu ihrer Analyse bereit.

# Introduction

*As waves upon my head the circling curl,  
So in the sacred dance weave ye and whirl.  
Dance then, O heart, a whirling circle be.  
Burn in this flame - is not the candle He?*  
Mevlana -The Masnavi (1250 AD)

Patterns are observed in many different systems in nature. They are seen in the cloud streets, in sand ripples, in the morphology of plants and animals, on weather maps, in chemical reactions [1]. In all these cases one deals with open, continuous dissipative systems which are driven out of equilibrium by an external stress. If this stress is larger than a certain threshold value, the symmetry of the temporally and spatially homogeneous ground state is spontaneously broken [1]. The resulting patterns show then periodicity in space and/or in time.

One of the best studied examples is the convection instability when a fluid layer is subjected to a temperature gradient. For instance, in a horizontal fluid layer heated from below and cooled from above a striped patterns of convection rolls develop. This scenario describes the famous Rayleigh- Bénard convection (*RBC*), as a standard paradigm of pattern formation [2, 3, 4, 5]. Many concepts and mathematical tools to analyze the patterns have been developed and tested for this case [1, 2, 6, 7].

This thesis deals with two different pattern forming systems, namely a particular example of a convection instability and the case of a shear flow driven instability. In the first part of the thesis, a variation of the standard *RBC* is investigated. We consider the problem of convection induced by radial buoyancy in an electrically conducting fluid contained in a rotating (*angular frequency*,  $\Omega$ ) cylindrical annulus which is cooled at the inner surface and heated from outside. In addition, an azimuthal *magnetic field* ( $B$ ) is applied for instance by an electrical current through the cylinder axis. The motivation of this study has come originally from the geophysical context. This setup is hoped to capture some important features of convection patterns in rotating stars and planets near the equatorial regions [8, 9, 10, 11]. The problem is also of considerable interest from a more general point of view in that it is concerned with formations of patterns in the presence of two competing directional effects, in this case rotation and the magnetic field.

The second part of the thesis is devoted to the the pattern formation by a shear flow between two rotating and infinitely electrically conducting plates with a magnetic field perpendicular to the plates. This geometry is called the magnetic Ekman-Couette layer and has been a basic model for magnetic activities at the boundary of the Earth's

liquid core or at the tachocline in the Sun below the convection zone for a few decades [12, 13, 14, 15, 16].

To analyze the forementioned problems, various codes and computational tools had to be developed, for instance, we were able to describe complex spatio-temporal patterns by the direct simulations of the underlying hydrodynamic equations for our problems.

The discussion of the physical details of the systems are postponed to the introductory sections of the corresponding parts of the thesis. In Chapter 1, a general formulation of the linear and nonlinear analysis, methods, which are applicable to both pattern forming systems in this work will be presented. The investigation of thermal convection in a plane layer which is a geometry equivalent to the cylindrical annulus will be discussed in Chapter 2. The next chapter (Chapter 3) covers both the linear and nonlinear analyses in the case of magnetic Ekman-Couette layer problem. Finally, in Chapter 4, we will present the general conclusions on both of the systems.

# Chapter 1

## Mathematical Description of Pattern Forming Instabilities

In this chapter, we describe common theoretical methods to analyze pattern forming non-equilibrium systems under an external stress, where we follow closely previous presentations [2, 1, 17, 18]. Particular emphasis is laid on the universal features shared by patterns in different systems.

We exclusively study large aspect-ratio fluid systems, where the horizontal extension of a fluid layer in the  $x-y$  plane is much larger than its vertical extension ( $z$ -direction). Thus lateral boundaries are assumed to play no crucial role and as usual periodic boundary conditions are adopted, which lead to a convenient description of our patterns by Fourier modes in a 2D-wave vector ( $\mathbf{q}$ ) space. This characterization applies to the Ekman-Couette problem where the fluid layer is between two large plates with small distance and also to the rotating cylindrical annulus when the gap is small compared to the height and the radius of the cylinder. The external stress, which drives the system out of equilibrium, is associated with a control parameter  $R$ . At low values of  $R$ , the system is spatially homogenous in the two horizontal directions. Above a certain threshold value,  $R = R_c$ , this basic state becomes unstable and a regular periodic pattern in the  $x-y$  plane develops. Thus, the translational symmetry in the plane is broken. The periodicity of the pattern is described in Fourier space by the number of non-vanishing Fourier components. In most cases one observes the nucleation of stripes (*rolls*) at  $R_c$  with one Fourier mode at a critical wave vector  $\mathbf{q}_c$ , while squares require two and hexagons three modes for their description. Note that in counting modes we do not distinguish between  $\mathbf{q}$  and  $-\mathbf{q}$  because the pair contributes equally to the pattern in real space. With increasing  $R$  the patterns encounter sequences of secondary bifurcations which lead to increasingly complex scenarios with diminishing degree of symmetry.

The derivation of the basic equations is a separate problem. One rests on a hydrodynamic description with the use of Navier-Stokes equations for the velocity field supplemented, for instance, by the heat-diffusion equation in the annulus problem. Thus, from a mathematical perspective, we have to analyze the solution manifolds of coupled nonlinear partial differential equations combined with bifurcation analyses to

assess the stability of the solutions. For simplicity we use a symbolic vector notation  $\mathbf{V}$  for the collection of the field variables relevant in the specific problem (temperature, velocity, etc.) and introduce the following condensed notation for the full set of the (hydrodynamic) equations:

$$\mathcal{D} \frac{\partial \mathbf{V}}{\partial t} = \mathcal{L}(R)\mathbf{V} + \mathbf{N}(\mathbf{V}, \mathbf{V}). \quad (1.1)$$

We assume the fields to be normalized in such a way, that  $\mathbf{V} = 0$  corresponds to the basic (primary) unstructured state. The symbols  $\mathcal{L}$  and  $\mathcal{D}$  represent linear matrix differential operators;  $\mathbf{N}$  denotes the quadratic nonlinear couplings of the fields in our systems. The solutions of Eq. (1.1) have to fulfill certain boundary conditions in the vertical direction at the confining plates of the fluid layer, e.g. the velocity field has to vanish there.

In the following sections we will first discuss the linear stability of basic state, which determines the threshold  $R_c$  and the critical wave vector  $\mathbf{q}_c$  of the patterns. Then we discuss the construction of 2D-periodic solutions of Eq. (1.1) in the nonlinear regime and their stability. Slightly above threshold, the calculations can be simplified in terms of the weakly nonlinear analysis which leads to order parameter equations. Finally, we discuss briefly the direct simulations of the equations.

## 1.1 Linear analysis

In the present thesis we consider axially anisotropic systems. For definiteness, the preferred axis (e.g. the rotation axis in the annulus problem) is assumed to be parallel to the  $y$ -axis of a Cartesian coordinate system. The pattern forming instability is obtained from a standard linear stability analysis of the basic (primary) state  $\mathbf{V} = 0$ . An ansatz  $\mathbf{V}(\mathbf{x}, t) = e^{\lambda t} e^{i\mathbf{q}\cdot\mathbf{r}} \mathbf{U}(\mathbf{q}, z)$  with  $\mathbf{x} = (x, y, z) = (\mathbf{r}, z)$  and  $\mathbf{q} = (q_x, q_y)$  diagonalizes the problem. From (1.1) one arrives at the linear eigenvalue problem:

$$\lambda \mathcal{D}(\partial_{\mathbf{r}} \rightarrow i\mathbf{q}, \partial_z) \mathbf{U}(\mathbf{q}, z) = \mathcal{L}(\partial_{\mathbf{r}} \rightarrow i\mathbf{q}, \partial_z, R) \mathbf{U}(\mathbf{q}, z). \quad (1.2)$$

The eigenvalues  $\lambda$  depend on  $\mathbf{q}$  and the control parameter  $R$ . We concentrate on the eigenvalues  $\lambda = \sigma(\mathbf{q}, R) + i\omega(\mathbf{q}, R)$  with the largest real part, determining the growth rate  $\sigma$  and the frequency  $\omega$  (possibly zero) of planforms near onset. In our systems with a preferred direction (axial anisotropy)  $\lambda$  depends separately on the two variables  $q_x^2$  and  $q_y^2$  (in an isotropic systems only the rotationally invariant combination  $q^2 = q_x^2 + q_y^2$  appears). Furthermore complex eigenvalues appear in pairs  $\lambda_{1,2} = \sigma \pm i\omega$ .

The condition  $\sigma(\mathbf{q}, R) = 0$  defines the *neutral surface*  $R = R_0(\mathbf{q})$  in the  $R, \mathbf{q}$ -space that separates the exponentially growing ( $R > R_0(\mathbf{q})$ ) from the decaying linear modes ( $R < R_0(\mathbf{q})$ ). The threshold  $R_c$  is obtained by minimizing  $R_0$  with respect to  $\mathbf{q}$  (equivalently by maximizing  $\sigma$ ). This gives the critical wave vector  $\mathbf{q}_c$  and the critical frequency  $\omega_c = \omega_0(\mathbf{q}_c, R_c)$ . Note that in isotropic systems  $\mathbf{q}_c$  is continuously degenerate on a circle. If  $\omega_c = 0$ , which is the simpler and more common case, one has a stationary bifurcation leading to a stationary pattern. Otherwise one has a Hopf (or

oscillatory) bifurcation. Then we have two degenerate linear modes corresponding to waves traveling in opposite directions.

In the isotropic case one cannot extract more information from the linear analysis, except in special situations, e.g. where two minima of  $R_0(\mathbf{q})$  coincide *accidentally* or nearly coincide. Then one deals with a codimension-2 bifurcation scenario that calls for special treatment.

In an axially anisotropic system one can further distinguish two cases. If the direction of  $\mathbf{q}_c = (q_c, p_c)$  is perpendicular to the preferred axis one speaks of *transverse* rolls ( $p_c = 0$ ), in contrast to *longitudinal* rolls when  $q_c = 0$ . On the other hand, if  $\mathbf{q}_c$  is at an oblique angle to the preferred axis, one speaks of *oblique* rolls. Then one has an additional spontaneously broken symmetry (chirality) and two symmetry-degenerate directions with  $\pm\mathbf{q}_c$  (*zig* and *zag*).

Let us finally add some technical remarks. Eq. (1.2) can be solved by Galerkin methods, where one expands  $\mathbf{U}(\mathbf{q}, z)$  with respect to a finite number of test functions, which satisfy the boundary conditions in the transverse ( $z$ ) direction. The operators  $\mathcal{D}$ ,  $\mathcal{L}$  are thus mapped on matrices, which act on the "vector" of the expansion coefficients. For the resulting algebraic eigenvalue problem fast effective computer routines are available. Thus the linear properties can be obtained easily by fully automated iterative procedures. The neutral curve  $R_0(\mathbf{q})$  as the smallest zero of  $\sigma(\mathbf{q}, R) = 0$  for a given  $\mathbf{q}$  is easily constructed by standard root-finding algorithm [19]. Also for the minimization of  $R_0(\mathbf{q})$  to determine  $\mathbf{q}_c$ ,  $R_c$  robust and powerful methods are available [20].

In the case of stationary bifurcations, the calculation of the neutral surface becomes even more simple. It is then useful to rewrite the linear operator in the following form  $\mathcal{L}(\mathbf{q}) = \mathcal{A}(\mathbf{q}) + R\mathcal{B}(\mathbf{q})$ . Since  $\lambda \equiv 0$  in Eq. (1.2) the neutral curve can alternatively be obtained as the smallest positive eigenvalue  $R = R_0(\mathbf{q})$  of the linear eigenvalue problem :

$$(\mathcal{A}(\mathbf{q}) + R\mathcal{B}(\mathbf{q})) \mathbf{V} = 0. \quad (1.3)$$

It is interesting, that one may obtain already quite reliable analytical expressions (*one mode approximation*) for the growthrate  $\sigma(\mathbf{q})$  and the neutral surface  $R_0(\mathbf{q})$ , by restricting to one trial function for each component of  $\mathbf{U}(\mathbf{q})$ .

Note that Galerkin methods are much faster, more robust and easier to implement than the often applied shooting methods. For instance, we found the effort for systematic parameter studies of the linear Ekman problem to be reduced at least by a factor of  $10^2$ . In addition there is a continuous connection to the nonlinear regime, where in general Galerkin methods are almost exclusively applied.

## 1.2 Galerkin analysis

### 1.2.1 Representation of periodic patterns

To describe the spatially periodic nonlinear solutions  $\mathbf{V}_{nl}$  of the problem posed by (1.1) subject to the boundary conditions we use the Galerkin method as well. As a representative example from the annulus problem, we give the expression for temperature field  $\Theta(x, y, z, t)$ , in the fluid layer of thickness  $d$  confined by plates at  $z = \pm \frac{d}{2}$ , (the other fields are represented in a similar form):

$$\Theta(x, y, z, t) = \sum_{n=1}^N \sum_{l, m=-M}^M \Theta_{lm;n}(t) \exp [i (l q_x x + m q_y y)] \sin \frac{n\pi}{d} (z + \frac{d}{2}). \quad (1.4)$$

It is clear that  $\Theta(x, y, z, t)$  vanishes for all  $x, y, t$  at  $z = \pm \frac{d}{2}$ . Rolls correspond to certain restrictions of the the expansion parameters: Transverse rolls are realized if  $\Theta_{lm;n} \equiv 0$ , for  $m \neq 0$ , longitudinal rolls if  $\Theta_{lm;n} \equiv 0$ , for  $l \neq 0$ , while  $\Theta_{lm;n} \equiv 0$ , for  $l \neq m \neq 0$  describes an oblique roll pattern. Besides rolls we will also analyze genuine three-dimensional patterns in this thesis ( e.g. *knots* and *hexarolls*), where the indices  $l, m$  vary independently from each other. Injecting ansatz (1.4) and the corresponding ones for the other fields into Eq. (1.1), one arrives at a system of nonlinear *ODE*'s in time for the expansion coefficients like  $\Theta_{lm;n}$ . In the stationary case, the *ODE* become nonlinear coupled algebraic equations for the expansion coefficients, which are iteratively solved by the Newton-Raphson method. The iteration starts from weakly nonlinear solutions (see Sec. (1.3)) and not from some *educated guess* to allows automotation to a large extent. Note that Eq. (1.4) involves truncations  $(N, M)$  whose accuracy we check by varying  $N, M$ .

### 1.2.2 Stability of the rolls

To examine the linear stability of the nonlinear solutions  $\mathbf{V}_{nl}$  constructed in the previous section, we use the ansatz  $\mathbf{V} = \mathbf{V}_{nl} + \delta\mathbf{V}$  in Eq. (1.1) and arrive at the following equation linear in the perturbation  $\delta\mathbf{V}$ :

$$\frac{\partial}{\partial t} \delta\mathbf{V}(t) = \mathcal{L} \delta\mathbf{V} + \hat{\mathbf{N}}(\mathbf{V}_{nl}, \delta\mathbf{V}) \quad (1.5)$$

Here we have introduced the *symmetrized* nonlinearity

$$\begin{aligned} \hat{\mathbf{N}}(\mathbf{V}_1, \mathbf{V}_2) &= \mathbf{N}(\mathbf{V}_1, \mathbf{V}_2) + \mathbf{N}(\mathbf{V}_2, \mathbf{V}_1), \quad \text{if } \mathbf{V}_1 \neq \mathbf{V}_2; \\ \hat{\mathbf{N}}(\mathbf{V}_1, \mathbf{V}_2) &= \mathbf{N}(\mathbf{V}_1, \mathbf{V}_2), \quad \text{if } \mathbf{V}_1 = \mathbf{V}_2. \end{aligned} \quad (1.6)$$

Eq. (1.5) is solved by the ansatz  $\delta\mathbf{V} = \exp[\lambda_{nl} t] \delta\mathbf{U}$ . Consequently Eq. (1.5) transforms into

$$\lambda_{nl} \delta\mathbf{U} = \mathcal{L} \delta\mathbf{U} + \hat{\mathbf{N}}(\mathbf{V}_{nl}, \delta\mathbf{U}). \quad (1.7)$$

Explicitly,  $\delta\mathbf{U}$  is represented again by a Galerkin ansatz. However, when examining the stability of periodic solution  $\mathbf{V}_{nl}$ , we have to allow for the possibility of new periodicities, i.e. the nucleation of Fourier modes with a wave vector  $\mathbf{s}$  not commensurate

to  $\mathbf{q}$ . Thus, in close analogy to Eq. (1.4) the most general (Floquet) ansatz for the temperature part of  $\delta\mathbf{U}$  reads as follows:

$$\delta\Theta(\mathbf{x}, z) = \exp[i\mathbf{s} \cdot \mathbf{r}] \sum_{n=1}^N \sum_{m=-M}^M \delta\Theta_{nm}(\mathbf{q}, \mathbf{s}) \exp[m i (\mathbf{q} \cdot \mathbf{r})] \sin \frac{n\pi}{d} \left(z + \frac{d}{2}\right). \quad (1.8)$$

As in the linear problem we concentrate on the leading eigenvalue  $\lambda_{nl} = \sigma_{nl} + i\omega_{nl}$  with the largest real part  $\sigma_{nl}$ . At fixed  $\mathbf{q}, R$  we have to determine the maximum  $\bar{\sigma}_{nl}$  of  $\sigma_{nl}(\mathbf{q}, R, \mathbf{s})$  with respect to  $\mathbf{s}$ , which is obtained at  $\mathbf{s} = \bar{\mathbf{s}}$ . The solution  $\mathbf{V}_{nl}$  for given  $R, \mathbf{q}$  is unstable if  $\bar{\sigma}_{nl}(R, \mathbf{q}, \bar{\mathbf{s}}) > 0$ . The regimes of stable and unstable patterns in the  $\mathbf{q}, R$  space above the neutral surface  $R_0(\mathbf{q})$ , which are separated by the surfaces where  $\bar{\sigma}_{nl}(R, \mathbf{q}, \bar{\mathbf{s}})$  passes zero, is often called the *Busse balloon* after Prof. Busse, who was the first to investigate systematically such stability diagrams in *RBC*. The Floquet vector  $\bar{\mathbf{s}}$  is characterized by its magnitude  $|\bar{\mathbf{s}}|$  and its orientation angle  $\Psi$  with respect to the orientation of the wave vector of the rolls:

$$\bar{\mathbf{s}} = |\bar{\mathbf{s}}|(\cos \Psi, \sin \Psi). \quad (1.9)$$

Let us first remind, that translational invariance involves the existence of neutral modes, for which at least one of the eigenvalues of Eq. (1.7),  $\lambda_0(\mathbf{s})$ , vanishes in the limit  $|\mathbf{s}| \rightarrow 0$ . The corresponding linear eigenvectors (one for rolls and two for patterns periodic in two directions) denote infinitesimal uniform shifts of the pattern in the *periodicity directions* (e.g. perpendicular to the roll axes). Because of reflection symmetry  $\Re(\lambda_0)$  grows quadratically at finite  $\mathbf{s}$  from zero in the form  $\Re(\lambda_0) = as^2 + \mathcal{O}(s^4)$ . A *longwave instability* corresponds to the case that  $\lambda_0$  coincides with the leading eigenvalue  $\lambda_{nl}$  and if  $a = \frac{\sigma_{nl}}{s^2}|_{s \rightarrow 0} > 0$ . The factor  $a$  depends on  $\Psi$ . We speak of the Eckhaus instability (modulation of the roll distance) if  $a > 0$  is maximal for  $\Psi = 0$ , of a zig-zag instability (undulations along the roll axis) if  $a$  is maximal for  $\Psi = \frac{\pi}{2}$  and of a skewed varicose instability for arbitrary angles  $\Psi$ .

*Short wavelength* instabilities  $|\bar{\mathbf{s}}| \approx |\mathbf{q}|$  do not correspond to modulated shifts of the patterns. Since the modes depend on  $|\bar{\mathbf{s}}|$  and  $\Psi$  a simple universal classification scheme as in the long wavelength case does not exist and we will discuss these instabilities separately for our two systems.

### 1.3 Order parameter equations

The purely numerical Galerkin construction of periodic solution and their stability easily hide the physical mechanism. In fact, in the regime slightly above threshold weakly nonlinear perturbation methods have been developed, which serve also as a unifying concept to extract the universal features of physically different pattern forming systems. In our case particular emphasis is laid on three-dimensional periodic patterns, which develop from secondary bifurcations of rolls. The basic calculational scheme has been proposed at first for hexagonal patterns in *RBC* in the non-Boussinesq case [21]. However, in our case strong resonant couplings between modes of different  $\mathbf{q}$  turn out

to be crucial. Thus we have adapted a calculational scheme, that has been introduced before in the context of electro-hydrodynamic convection in nematics [22] to our case.

In the following section (Sec. 1.3.1), we will at first sketch the basic concepts behind the order parameter approach. In Sec. 1.3.2 we will describe in more detail the order parameter equation for rolls. Sec. 1.3.3 is devoted to coupled order parameter equations near a codimension-2 point. Finally we present in Sec. 1.4 as a sketch the resonantly coupled amplitude equations relevant in this work.

### 1.3.1 General calculational scheme

To present the procedure in a most transparent manner, (see [22]) we suppress the spatial variables and start again from Eq. (1.1). At first we solve the right- and left linear eigenvalue problems:

$$\lambda_i \mathcal{D} \mathbf{U}_i \rangle = \mathcal{L} \mathbf{U}_i \rangle, \quad (1.10a)$$

$$\lambda_i \langle \mathbf{U}_i | \mathcal{D} = \langle \mathbf{U}_i | \mathcal{L}. \quad (1.10b)$$

The eigenvalues are assumed to be ordered in decreasing order with respect to their real parts  $\Re(\lambda_i) \equiv \sigma_i$ :  $\sigma_1 \geq \sigma_2 \geq \sigma_3 \dots$ . Note that the growth rate  $\sigma_1(R)$  passes zero at  $R = R_c$ . The eigenvectors are orthogonal and can obviously be normalized in such a way that the following relations hold:

$$\langle \mathbf{U}_i | \mathcal{D} \mathbf{U}_j \rangle = \delta_{i,j}, \quad \langle \mathbf{U}_i | \mathcal{L} \mathbf{U}_j \rangle = \lambda_i \delta_{i,j}, \quad (1.11)$$

where the appropriate scalar product will be defined later in detail. We assume that the linear operator  $\mathcal{L}$  is normal, so that the  $\mathbf{U}_i \rangle$  span the state space.

The solution of of Eq. (1.1) is now expanded in terms of the eigenvectors of the linear problem Eq. (1.11) :

$$\mathbf{V} = \sum_{i=1}^N A_i \mathbf{U}_i \rangle \quad (1.12)$$

where we confine ourselves in practice to a finite number ( $N$ ) of terms. Thus Eq. (1.1) is transformed into a set of  $N$  coupled *ODE*'s for the expansion coefficients  $A_i$  :

$$\partial_t A_i(t) = \lambda_i A_i(t) - \langle \mathbf{U}_i | \mathbf{N}(\mathbf{V}, \mathbf{V}) \rangle, \quad i = 1, 2 \dots N, \quad (1.13)$$

where the nonlinear part becomes a quadratic form in the coefficients  $A_i$ . It is obvious, that Eqs. (1.13) for  $N \rightarrow \infty$  are equivalent to Eq. (1.1). Thus Galerkin solutions can be expressed in terms of the  $A_i$  and vice versa.

The first step in deriving amplitude equations is to single out  $M$  *active* modes among the  $\mathbf{U}_i \rangle$  in contrast to the remaining *passive* modes with  $N \geq i > M$ . In selecting the active modes we are guided by physical reasoning and also from the results of the Galerkin analysis. In any case the modes with small growthrates  $\sigma_i$  are considered to be active; in addition modes responsible for resonances (see below) come into play. The time derivatives for the passive modes with  $i > M$  in Eq. (1.13) are adiabatically

neglected such that their expansion coefficients are given as  $A_i = \langle \mathbf{U}_i | \mathbf{N}(\mathbf{V}, \mathbf{V}) \rangle / \lambda_i$ . In other words, the dynamics is carried by the  $M$  active modes to which the remaining ones are slaved.

The splitting of the configuration space  $\mathbf{V}$  into the space  $\mathbf{V}_a = \sum_{i=1}^M A_i \mathbf{U}_i$  spanned by the active modes and its orthogonal complement  $\mathbf{V}_\perp$  can be formulated in terms of a suitable projection operator  $\mathcal{P}$  as follows:

$$\mathbf{V} = \mathbf{V}_a + \mathbf{V}_\perp \equiv \mathcal{P}\mathbf{V} + (1 - \mathcal{P})\mathbf{V}; \quad (1.14a)$$

$$\mathcal{P} = \sum_{k=1}^M \mathcal{D} \mathbf{U}_k \langle \mathbf{U}_k \quad (1.14b)$$

The projection operator fulfills obviously  $\mathcal{P}\mathcal{L} = \mathcal{L}\mathcal{P}$ . Thus Eq. 1.1 can be split as:

$$\begin{aligned} \partial_t \mathcal{D}\mathbf{V}_a &= \mathcal{L}\mathbf{V}_a - \mathcal{P}\mathbf{N}(\mathbf{V}, \mathbf{V}); \\ 0 &= \mathcal{L}\mathbf{V}_\perp - (1 - \mathcal{P})\mathbf{N}(\mathbf{V}, \mathbf{V}). \end{aligned} \quad (1.15a)$$

Projecting Eqs. (1.15a) on the  $\mathbf{U}_i$  we recover the coupled Eqs. (1.13) for the expansion coefficients  $A_i$  with zero time derivative for the passive modes ( $i > M$ ). The standard amplitude equations are obtained by expanding systematically up to cubic order in the amplitudes  $A_i$ ,  $i = 1, \dots, M$ .

In the case of periodic boundary conditions the eigenvector space falls into disjoint classes, which are characterized by the different  $\mathbf{q}$ -vectors. Thus the indices  $i$  have to be understood as a kind of super index: For each  $\mathbf{q}$  there exists a discrete spectrum  $\lambda_i(\mathbf{q})$  again with  $\sigma_1(\mathbf{q}) \geq \sigma_2(\mathbf{q}) \dots$  together with the corresponding left and right eigenvectors  $\langle \mathbf{U}_i(\mathbf{q})$  and  $\mathbf{U}_i(\mathbf{q})$ , respectively. Eigenvectors belonging to different  $\mathbf{q}$  are automatically orthogonal.

### 1.3.2 Landau Equation

In order to present the calculational scheme in a less abstract manner, we focus here on a roll pattern characterized by a wave vector  $\mathbf{q}_0$ . We use the following ansatz for the nonlinear solution  $\mathbf{V}$  in Eq. (1.1)

$$\mathbf{V}(\mathbf{r}, z, t) = A(\mathbf{q}_0, t) e^{i\mathbf{q}_0 \cdot \mathbf{r}} \mathbf{U}(\mathbf{q}_0, z) + c.c., \quad (1.16)$$

where  $\mathbf{U} \equiv \mathbf{U}_1(\mathbf{q})$  is the leading linear eigenvector (see Eqs. (1.2, 1.10a)). Besides  $\mathbf{U}$  we will also need the solution  $\mathbf{U}^\dagger$  of the adjoint eigenvalue problem for  $\lambda = \lambda_1(\mathbf{q}_1)$  (cf. Eq. (1.10b)).

$$\lambda^* \mathcal{D}^\dagger(\partial_{\mathbf{r}}, \partial_z) \mathbf{U}^\dagger(\mathbf{r}, z) = \mathcal{L}^\dagger(\partial_{\mathbf{r}}, \partial_z) \mathbf{U}^\dagger(\mathbf{r}, z) \quad (1.17)$$

where  $\mathcal{L}^\dagger$  and  $\mathcal{D}^\dagger$  denote the adjoint operators to  $\mathcal{L}$  and  $\mathcal{D}$ , respectively. For arbitrary vectors  $\mathbf{U}$  and  $\mathbf{V}$ , the operator  $O^\dagger$  adjoint to  $O$  is defined as usual by the relation

$$\langle \mathbf{U} | O\mathbf{V} \rangle = \langle O^\dagger \mathbf{U} | \mathbf{V} \rangle \quad (1.18)$$

where the appropriate scalar product is defined as:

$$\langle \mathbf{U} | \mathbf{V} \rangle = \int \mathbf{U}^\dagger \mathbf{V} d^3x \quad (1.19)$$

The integration is performed over an appropriate periodicity (*Wigner-Seitz cell*) in the  $x - y$  plane and across the height of the fluid layer in the  $z$ -direction.

The amplitude  $A$  will be determined by a systematic expansion of the solutions of Eq. (1.13) up to cubic order in  $A$ . In an intermediate step, we need the passive-modes contribution  $\mathbf{V}_\perp$  to order  $A^2$  which is perpendicular to  $\mathbf{V}$ .  $\mathbf{V}_\perp$  fulfills the equations (see Eq. (1.15a))

$$0 = \mathcal{L}\mathbf{V}_\perp - \mathbf{N}(\mathbf{V}, \mathbf{V}). \quad (1.20)$$

In Fourier space  $\mathbf{V}$  contains two contributions ( $\mathbf{V}_\perp \equiv \mathbf{V}_1 + \mathbf{V}_2$ ), at  $\mathbf{q} = 2\mathbf{q}_0$  and  $\mathbf{q} = 0$ , respectively which read:

$$\mathbf{V}_\perp^1(\mathbf{q}_0, \mathbf{q}_0) = \mathcal{L}^{-1}(2\mathbf{q}_0) |A(\mathbf{q}_0)|^2 \hat{\mathbf{N}}(\mathbf{U}(\mathbf{q}_0), \mathbf{U}(\mathbf{q}_0)). \quad (1.21)$$

and

$$\mathbf{V}_\perp^2(\mathbf{q}_0, -\mathbf{q}_0) = \mathcal{L}^{-1}(0) |A(\mathbf{q}_0)|^2 \hat{\mathbf{N}}(\mathbf{U}(\mathbf{q}_0), \mathbf{U}(-\mathbf{q}_0)). \quad (1.22)$$

In this section no projections were required since  $\mathbf{V}_\perp$  and  $\mathbf{U}$  have different wave vectors and are thus orthogonal. Inserting Eqs. (1.16, 1.21, 1.22) into Eq. (1.20) and expanding up to  $\mathcal{O}(A^3)$  results in the order parameter equation for  $A$  in  $\mathbf{q}$ -space

$$\langle \mathbf{U}(\mathbf{q}_0), \mathcal{D}\mathbf{U}(\mathbf{q}_0) \rangle \partial_t A(\mathbf{q}_0) = \langle \mathbf{U}(\mathbf{q}_0), \mathcal{L}\mathbf{U}(\mathbf{q}_0) \rangle A(\mathbf{q}_0) + \langle \mathbf{U}(\mathbf{q}_0) | \hat{\mathbf{N}}(\mathbf{V}, \mathbf{V}_\perp) \rangle \quad (1.23)$$

With the use of the definitions

$$\begin{aligned} a_1(\mathbf{q}) &= \langle \mathbf{U}(\mathbf{q}) | \mathcal{D}(\mathbf{q}) \mathbf{U}(\mathbf{q}) \rangle = 1, \\ a_2(\mathbf{q}) &= \langle \mathbf{U}(\mathbf{q}) | \mathcal{L}(\mathbf{q}) \mathbf{U}(\mathbf{q}) \rangle, \\ a_3(\mathbf{q}) &= \langle \mathbf{U}(\mathbf{q}) | \hat{\mathbf{N}}(\mathbf{V}_\perp(\mathbf{q}, -\mathbf{q}), \mathbf{U}(\mathbf{q})) \rangle + \langle \mathbf{U}(\mathbf{q}) | \hat{\mathbf{N}}(\mathbf{V}_\perp(\mathbf{q}, \mathbf{q}), \mathbf{U}(-\mathbf{q})) \rangle. \end{aligned} \quad (1.24)$$

Eq. (1.23) reads finally:

$$\partial_t A = \lambda A - a |A|^2 A. \quad (1.25)$$

The coefficients  $\lambda \equiv a_2(\mathbf{q}_0)$ ,  $a \equiv a_3(\mathbf{q})$  are often called *Landau coefficients* after Landau [23], who has originally introduced Eq. (1.25) to describe second- order equilibrium phase transitions.

The coefficients  $\lambda \equiv \sigma(\mathbf{q}, R) + i\omega(\mathbf{q}, R)$  and  $a \equiv a_r + ia_i$  can be complex. Near onset  $\sigma$  is usually approximated as (i.e. for  $\mathbf{q} \approx \mathbf{q}_c$  and  $R \approx R_c$ )

$$\sigma = \tau_0^{-1} \left[ \varepsilon - \xi_{xx}^2 (q_x - q_{cx})^2 - \xi_{yy}^2 (q_y - q_{cy})^2 - 2 \xi_{xy}^2 (q_x - q_{cx})(q_y - q_{cy}) \right] \quad (1.26)$$

with the relaxation time  $\tau_0$  and  $\varepsilon = \frac{R-R_c}{R_c}$  the reduced control parameter. The  $\xi$ 's denote the coherence lengths. They describe the ellipsoidal contour lines of  $R_0(\mathbf{q})$  near onset, which become circles in isotropic systems ( $\xi_{xx}^2 = \xi_{yy}^2 = \xi^2$ ;  $\xi_{xy}^2 = 0$ ). Note

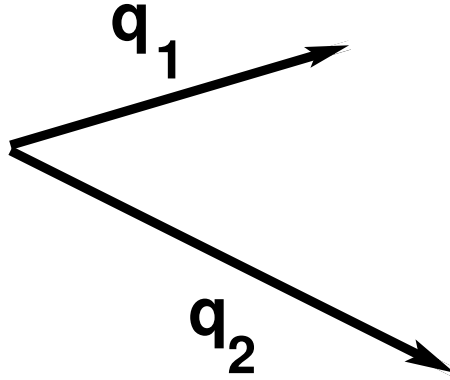


Figure 1.1: The vectors  $\mathbf{q}_j$  near a codimension-2 point.

that Eq. (1.25) can be derived by a rigorous asymptotic expansion about the threshold  $\varepsilon = 0$ .

The simplest solution of Eq. (1.25) is given as  $A = \exp(i\Omega t) |A|$ . From Eq. (1.25) we obtain easily :

$$\partial_t |A| = \sigma |A| - a_r |A|^3, \quad \Omega = \omega - a_i |A|^2. \quad (1.27)$$

The bifurcation is called stationary for  $\omega, a_i = 0$  and oscillatory otherwise. For a supercritical (forward) bifurcation the condition  $a_r > 0$  is necessary and we obtain  $|A|^2 = \frac{\sigma}{a_r}$ . For  $a_r < 0$  the bifurcation is subcritical, since  $|A| > 0$  for  $\varepsilon < 0$ . In this case, fifth- order terms in the expansion of Eq. (1.23) had to be included. Since the calculation of the necessary coefficients is tedious and not very illuminating, we have preferred to calculate directly the fully nonlinear Galerkin solution.

### 1.3.3 Coupled amplitude equations near a codimension-2 point

In the Ekman- Couette problem we will meet a codimension-2 bifurcation where the growthrates  $\sigma(\mathbf{q}_1, R), \sigma(\mathbf{q}_2, R)$  for two different wave vectors  $\mathbf{q}_1, \mathbf{q}_2$  fulfill the condition  $\sigma(\mathbf{q}_1^c, R_c) = \sigma(\mathbf{q}_2^c, R_c) = 0$ . Thus for any set  $R, \mathbf{q}_1, \mathbf{q}_2$  near the critical values  $R_c, \mathbf{q}_1^c, \mathbf{q}_2^c$  the growthrates remain near zero. For simplicity we introduce the following shorthand notation for the amplitudes and the eigenvalues of the active modes:

$$\begin{aligned} A &:= A_1(\mathbf{q}_1), \quad B := A_1(\mathbf{q}_2); \\ \lambda_A &= \lambda_1(\mathbf{q}_1) =: \sigma_A(\mathbf{q}_1) + i\omega_A, \quad \lambda_B = \lambda_1(\mathbf{q}_2) =: \sigma_B(\mathbf{q}_2) + i\omega_B. \end{aligned} \quad (1.28)$$

The ansatz for  $\mathbf{V}$  contains two terms of the form shown in Eq. (1.16), the first for  $\mathbf{q}_1$  ( $A$ ) and the second one for  $\mathbf{q}_2$  ( $B$ ). According to our general scheme we arrive at the following coupled amplitude equations:

$$\partial_t A(t) = \lambda_A A(t) - A[a_{11}|A|^2 - a_{12}|B|^2], \quad (1.29a)$$

$$\partial_t B(t) = \lambda_B B(t) - B[a_{21}|A|^2 - a_{22}|B|^2]. \quad (1.29b)$$

Let us assume  $\sigma_A > 0$ ,  $\sigma_B \approx 0$ ,  $\Re(a_{11}) > 0$  (forward bifurcation). Thus the solution  $|A|^2 = \frac{\sigma_A}{\Re(a_{11})}$ ;  $B = 0$ , i.e. a pure roll pattern, exists. It is easy to see that the  $B$  mode can be excited as well if the condition  $\sigma_B - \sigma_A \left( \frac{\Re(a_{21})}{\Re(a_{11})} \right) > 0$  is fulfilled.

The calculation of the coefficients in Eqs. (1.29) follows our general scheme. We find for instance:

$$\begin{aligned} a_{11} &= \langle \mathbf{U}(\mathbf{q}_1) | \left[ \hat{\mathbf{N}}(\mathbf{V}_\perp(\mathbf{q}_1, -\mathbf{q}_1), \mathbf{U}(\mathbf{q}_1)) + \hat{\mathbf{N}}(\mathbf{V}_\perp(\mathbf{q}_1, \mathbf{q}_1), \mathbf{U}(-\mathbf{q}_1)) \right] \rangle, \\ a_{12} &= \langle \mathbf{U}(\mathbf{q}_1) | \left[ \hat{\mathbf{N}}(\mathbf{V}_\perp(\mathbf{q}_1, -\mathbf{q}_2), \mathbf{U}(\mathbf{q}_2)) + \hat{\mathbf{N}}(\mathbf{V}_\perp(\mathbf{q}_2, -\mathbf{q}_2), \mathbf{U}(\mathbf{q}_1)) \right] \rangle. \end{aligned} \quad (1.30a)$$

where  $\mathbf{U}(\mathbf{q}_1) \equiv \mathbf{U}_1(\mathbf{q}_1)$  etc.

As in Eq. (1.21) the solutions  $\mathbf{V}_\perp$  in second- order are indexed by the two wave vectors  $\mathbf{q}_i, \mathbf{q}_j$ , which belong to the two modes in the nonlinearity  $\hat{\mathbf{N}}(\mathbf{U}(\mathbf{q}_i), \mathbf{U}(\mathbf{q}_j))$  when solving Eq. (1.20). In the present case projections in the second order (see Eq. (1.15a)) are not required, since  $\mathbf{V}_\perp$  is automatically orthogonal to  $\mathbf{U}(\mathbf{q}_1), \mathbf{U}(\mathbf{q}_2)$ . In the following examples, this property does not always exist and the calculations become much more tedious.

## 1.4 Patterns with resonant- modes interaction

In this section, we describe coupled amplitude equations for patterns which display more than two basic Fourier- spots in  $\mathbf{q}$  space. Translational invariance implies, that the phases of two of the complex amplitudes needed to describe the pattern can be chosen to be zero. The phases of the remaining amplitudes adjust themselves in an 'optimal' way, for instance to drive instabilities. This mechanism is addressed as (geometrical) *resonance* in this thesis.

In the case of the rotating annulus we will meet different types of resonances, which are well known from the work of Prof. Busse and his co-workers [24, 25]. To give a general impression we have combined all types in Fig. 1.2. The basic roll system (wave vector  $\mathbf{q}_1$ ) can become unstable at a secondary bifurcation by the excitation of short wavelength perturbations with wave vectors  $\mathbf{q}_{2,4,6}$

$$\mathbf{q}_6 = \mathbf{s}, \quad \mathbf{q}_4 = \mathbf{q}_1 + \mathbf{s}, \quad \mathbf{q}_2 = -\mathbf{q}_1 + \mathbf{s}. \quad (1.31)$$

with a short wave modulation  $\mathbf{s} = (s_x, s_y)$ , i.e.  $s \sim \mathcal{O}(q_1)$ . The other modes shown in Fig. 1.2 are mirror symmetric with respect to the  $\mathbf{q}_1$  line. Obviously the following resonances are fulfilled:

$$\mathbf{q}_1 = \mathbf{q}_6 - \mathbf{q}_2, \quad \mathbf{q}_1 = \mathbf{q}_4 - \mathbf{q}_6, \quad \mathbf{q}_1 = \mathbf{q}_7 - \mathbf{q}_3, \quad \mathbf{q}_1 = \mathbf{q}_5 - \mathbf{q}_7 \quad (1.32)$$

$$\mathbf{q}_3 - \mathbf{q}_2 = \mathbf{q}_5 - \mathbf{q}_4 = \mathbf{q}_7 - \mathbf{q}_6, \quad \mathbf{q}_4 - \mathbf{q}_2 = 2\mathbf{q}_1, \quad \mathbf{q}_5 - \mathbf{q}_3 = 2\mathbf{q}_1. \quad (1.33)$$

With the use of the general approach explained in Sec. 1.3.1, it is straightforward to write down the seven coupled amplitude equations for the modes  $A_1(\mathbf{q}_j)$ ,  $j = 1, 2, \dots, 7$ .

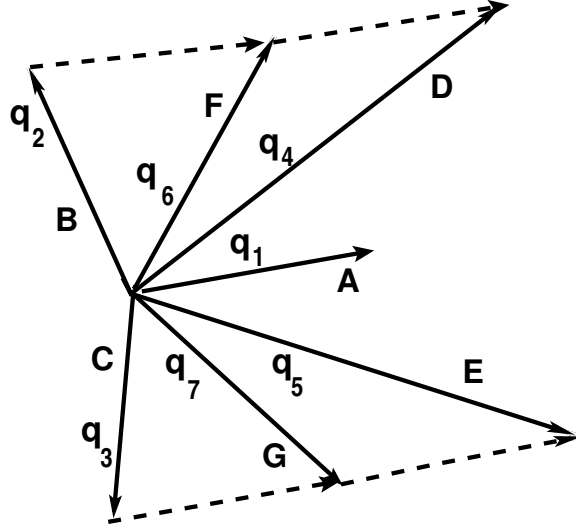


Figure 1.2: The vectors  $\mathbf{q}_j, j = 1, 2, \dots, 7$  responsible for double resonance (see text). The letters denote the corresponding amplitudes (see Eq. (1.33) below)

For each  $\mathbf{q}_j$  we have to determine leading eigenvalues  $\lambda_1(\mathbf{q}_j)$  and the corresponding left and right eigenvectors  $\langle \mathbf{U}_1(\mathbf{q}_j)$  and  $\mathbf{U}_1(\mathbf{q}_j) \rangle$ . In our case the leading eigenvalues  $\lambda_1(\mathbf{q}_j)$  are real, i.e  $\lambda(\mathbf{q}_i) \equiv \sigma(\mathbf{q}_i)$ . The following definitions are used in the thesis:

$$\begin{aligned}
 A &:= A_1(\mathbf{q}_1), \quad B := A_1(\mathbf{q}_2), \quad C := A_1(\mathbf{q}_3), \\
 D &:= A_1(\mathbf{q}_4), \quad E := A_1(\mathbf{q}_5), \quad F := A_1(\mathbf{q}_6), \quad G := A_1(\mathbf{q}_7); \\
 \sigma_A &= \sigma_1(\mathbf{q}_1), \quad \sigma_B = \sigma_1(\mathbf{q}_2), \quad \sigma_C = \sigma_1(\mathbf{q}_3), \\
 \sigma_D &= \sigma_1(\mathbf{q}_4), \quad \sigma_E = \sigma_1(\mathbf{q}_5), \quad \sigma_F = \sigma_1(\mathbf{q}_6), \quad \sigma_G = \sigma_1(\mathbf{q}_7).
 \end{aligned} \tag{1.34}$$

To give a demonstration for the resonances let us consider the shortwave instabilities of a roll system with wave vector  $\mathbf{q}_1$ , which is determined by the following coupled amplitude equations linear in the amplitudes  $B, D, F$ :

$$\partial_t B = \sigma_B B - a_{21} B |A_0|^2 - \eta_{21} A_0^* F - \rho_{21} A_0^* A_0^* D, \tag{1.35a}$$

$$\partial_t D = \sigma_D D - a_{41} D |A_0|^2 - \eta_{41} A_0 F - \rho_{42} A_0 A_0 B \tag{1.35b}$$

$$\partial_t F = \sigma_F F - a_{61} F |A_0|^2 - \eta_{61} A_0 B - \eta_{62} A_0^* D. \tag{1.35c}$$

$A_0$  is an undisturbed roll amplitude. The amplitudes  $C, E, G$  fulfill analogous equations.

In fact, the most general interaction of seven modes shown in Fig. 1.2, which leads to Eqs. (1.35) has not been observed in the rotating annulus system in the case of axial rolls where  $\mathbf{q}_1 = (q, 0)$ . It turns out that it is sufficient to restrict ourselves to two special cases, the subharmonic varicose (*SHV*) and the knot instabilities. They involve certain subsets of the modes  $A, B, \dots$  which are shown in Fig. 1.3.

The detailed analysis of the corresponding amplitude equations will be presented in App. A.

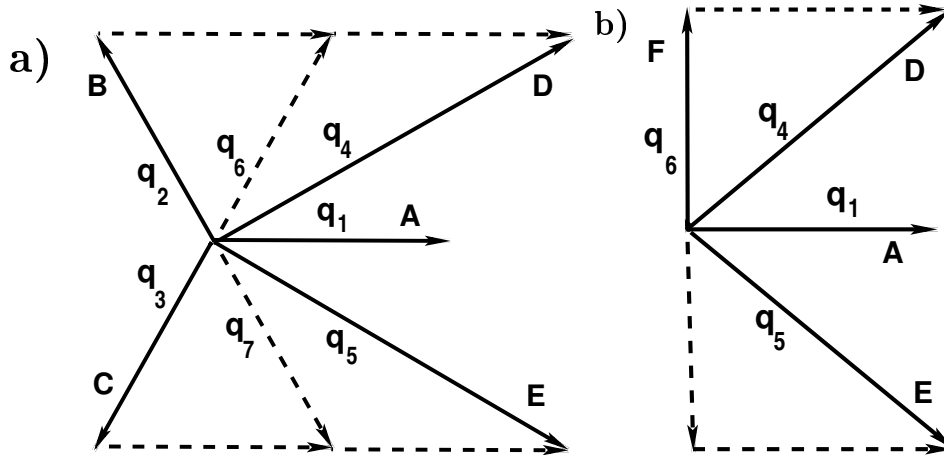


Figure 1.3: The vectors  $\mathbf{q}_j, j = 1, 2, \dots, 5$  responsible for *SHV* (left panel, present section) and for knot instability (right panel, see following section). The letters denote the corresponding amplitudes.

## 1.5 Numerical simulations

Besides regular, spatially periodic solutions, our systems show also spatio-temporal complex patterns. They appear in some cases as competing attractors to the periodic patterns or they show up as transients, when the systems are approaching a new state after having passed a secondary bifurcation. The complex patterns are often characterized by topological defects (dislocations), which present spatial variations on a length scale considerably smaller than the basic wavelength  $\lambda_c = 2\pi/q_c$ . On the other hand, it is sometimes important to describe large- aspect ratio systems with a lateral extension  $L \gg \lambda_c$  to capture properly modulational instabilities of rolls. Furthermore, in particular at moderate Prandtl numbers, *meanflow* effects come into play, which are slowly decaying in space. They are for instance responsible for spiral defect chaos in *RBC* [5, 26].

One option is to solve the hydrodynamic equations directly by discretization in space. The codes run then on supercomputers and  $L < 30 \lambda_c$  is the practical limit. Alternatively one can switch to  $\mathbf{q}$ -space where the horizontal derivatives become multiplications with the components of  $\mathbf{q}$ . Not too far from onset the vertical variations are not too strong, such that they can be resolved by few Galerkin modes. However, a wide range of  $\mathbf{q}$ -vectors in the Galerkin ansatz is required to cover the different length scales in complex pattern. The calculations are done on a grid  $\mathbf{q}$ -space on discrete interpolation points  $\mathbf{q}_{m,n} = \Delta \mathbf{q} (m, n)$  with  $-\frac{N}{2} \leq m, n \leq \frac{N}{2}$ . We chose typically  $\Delta \mathbf{q} = q_c/k$ , which corresponds to  $L = k \lambda_c$ . Furthermore  $k \leq N/6$  is required to include at least the higher harmonics with wave vector  $3 q_c$ . A reasonable choice is  $N = 128, k = 12$  but  $N = 256$  can easily be handled as well. It is obvious that the direct solution of the *ODE*'s for the Galerkin expansion coefficients is only possible for small  $N$  ( $\leq 10$ ), which is not sufficient to describe reliably complex patterns. However,

---

the system of *ODE*'s in Eq. (1.13) ( $N \times N \times 3M$  coupled equations) has turned to be very useful to generate numerical solutions of the hydrodynamic equations for large systems. In contrast to standard discretization schemes it allows to concentrate on the most important active modes ( $\Re(\lambda)$  not too small) which carry the dynamics of the system, whereas the passive modes can be adiabatically eliminated. It is crucial that the most time consuming manipulations can be based on the fast Fourier transformations (*FFT*). With respect to time, the linear operator is diagonal and can be treated fully implicit whereas the nonlinear part is treated with an explicit slightly modified Adams- Bashforth scheme (for further details, see App. B) The scheme is very robust and allows large time steps. Due to a one- to- one correspondence to the Galerkin scheme the solutions can be tested by comparison. In this way, for the first time typical modern convection experiments could be reproduced in numerical simulations. It has been even demonstrated that to some extent two- dimensional experimental snapshots of patterns (temperature field at the upper plane) can be used to construct reliably the full three dimensional convection structure (see [18, 5]).



# Chapter 2

## Convection in a Rotating Annulus with an Azimuthal Magnetic Field

### Introduction

Convection driven by thermal buoyancy in rotating fluid layers heated from below in the presence of a magnetic field is a typical problem encountered in planetary and stellar fluid dynamics. The most commonly treated version of this problem corresponds to the case when both, the axis of rotation and the direction of the imposed homogenous magnetic field, are parallel to the gravity vector. The onset of convection in this case was considered by Chandrasekhar [27]. He found the surprising result that Lorentz force and Coriolis force may counteract each other such that the critical Rayleigh number for onset of convection is lower than in cases when either the magnetic field or the rotation rate vanishes.

For planetary and stellar application the configuration of rotation axis and magnetic field direction perpendicular to each other and perpendicular to the gravity vector could be more important. It corresponds to the case of convection in the equatorial regions of rotating spherical fluid shells when an azimuthal magnetic field is imposed. Toroidal magnetic fields in the electrically conducting cores of planets or in the solar atmosphere are believed to be often much stronger than the poloidal components which can be measured from the outside. It is thus of interest to study the properties of convection in this situation which can also be realized in laboratory experiments through the use of the rotating annulus configuration (see Fig. 2.1a). In this case the centrifugal force is used as an effective gravity. Although the motivation for studying the rotating magnetic annulus convection has originally arisen in the geophysical context, the problem is also of interest from a more general point of view since it is a good example for pattern formation in the presence of two competing directional effects. In fact, as will be demonstrated in this thesis a large variety of convection patterns is found already at small values of the rotation and magnetic field parameters for moderate values of the Rayleigh number. In this respect the present study can be regarded as an extension of the paper by Auer et al. [24] to the case when a homogeneous magnetic field is added. A rotating annulus experiment corresponding to the paper of Auer et al. [24] has been

performed by Jaletzky and Busse [28].

In Sec. (2.1) the mathematical formulation of the problem is discussed. In the small gap approximation, the problem reduces to the case of a horizontal fluid layer heated from below with magnetic field, axis of rotation, and the vertical direction corresponding to the  $x$ -,  $y$ - and  $z$ - axis of a Cartesian system of coordinates. A sketch of the geometrical configuration to be considered in this thesis is shown in Fig. 2.1b.

The results of the linear theory for the onset of convection which has first been considered by Eltayeb [8] more than 30 years ago are discussed in Sec. (2.2). In order to obtain simple expressions, Eltayeb has used idealized boundary conditions, namely stress-free conditions for the velocity field and electrically infinitely conducting boundaries for the magnetic field. In the present study the more realistic case of rigid, electrically insulating boundaries is considered. The weakly nonlinear analysis and a stability analysis of convection rolls is described in Sec. (2.3). Some of the instabilities of convection rolls can be understood on the basis of analytical results obtained in earlier work on the related problem of convection in the absence of a magnetic field [24, 25]. But new mechanisms of instability are introduced by the Lorentz force. Future research and potential application are discussed in the concluding section. Some results of this chapter have been already accepted for publication [29].

## 2.1 Mathematical Formulation of the Problem and Numerical Methods

In the following, we refer to the situation shown in Fig. 2.1b. We use a Cartesian system of coordinates with the unit vectors  $\mathbf{i}$ ,  $\mathbf{j}$ ,  $\mathbf{k}$  in the direction of the  $x$ ,  $y$ ,  $z$ - axes. The effective gravity is provided by the centrifugal force,  $g = \frac{\Omega^2(R_1+R_2)}{2}$ , its direction is given by the unit vector  $\mathbf{k}$ . The upper and lower boundaries are kept at the constant temperatures  $T_1$  and  $T_2$ ,  $T_2 > T_1$ , respectively. We assume the rotation rate  $\Omega$  to be so large that effects of ordinary gravity ( $-\mathbf{k}$ ) can be neglected [24, 25, 28]. They lead in principle to a base flow with cubic profile along  $\mathbf{k}$ , but not to a distortion of the applied linear temperature profile

$$T_0(z) = \frac{T_1 + T_2}{2} - (T_2 - T_1)\frac{z}{d}. \quad (2.1)$$

The hydrodynamic equations suitably nondimensionalized will depend on Rayleigh number  $R$ , the Prandtl number  $P$ , the Coriolis parameter  $\tau$  and the Chandrasekhar number  $Q$ , which are defined as:

$$R = \frac{\alpha(T_2 - T_1)gd^3}{\nu\kappa}, \quad P = \frac{\nu}{\kappa}, \quad \tau = \frac{\Omega d^2}{\nu}, \quad Q = \frac{B_0^2 d^2}{\rho\mu\lambda\nu}, \quad (2.2)$$

where  $\alpha$ ,  $\nu$ ,  $\kappa$ ,  $\mu$ ,  $\rho$  and  $\lambda$  are the coefficients of thermal expansion, kinematic viscosity, thermal diffusivity, magnetic permeability, density and magnetic diffusivity of the fluid,

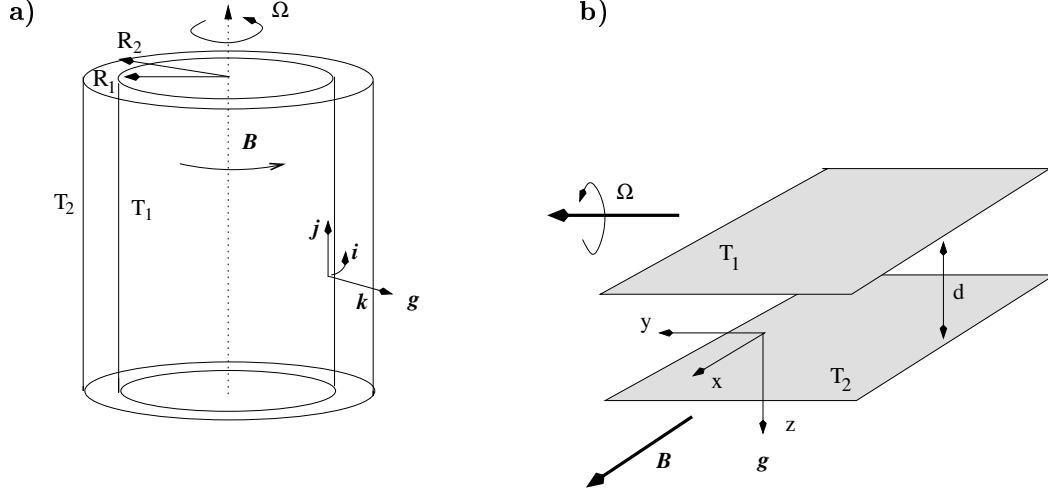


Figure 2.1: (a) Schematic representation of the rotating annulus. (b) The analogy to the planar convection ( $d \equiv R_2 - R_1$ ).

respectively. We have used the thickness  $d$  of the layer as length scale, the vertical diffusion time,  $\frac{d^2}{\kappa} = t_v$ , as time scale,  $\frac{(T_2 - T_1)}{R}$  as temperature scale, and the magnetic imposed flux density  $B_0$  as scale of the magnetic field. Then the basic equations of motion for the velocity field  $\mathbf{u}$ , the heat equation for the deviation  $\Theta$  of the temperature from the basic profile  $T_0(z)$  and the equation of magnetic induction in dimensionless form read as follows:

$$P^{-1} \left( \frac{\partial}{\partial t} + \mathbf{u} \cdot \nabla \right) \mathbf{u} + 2\tau \mathbf{j} \times \mathbf{u} = -\nabla \Pi - \mathbf{k} \Theta + \nabla^2 \mathbf{u} + Q \left( \mathbf{i} + \frac{\kappa}{\lambda} \mathbf{b} \right) \cdot \nabla \mathbf{b}, \quad (2.3a)$$

$$\nabla \cdot \mathbf{u} = 0, \quad (2.3b)$$

$$\left( \frac{\partial}{\partial t} + \mathbf{u} \cdot \nabla \right) \Theta = -R \mathbf{k} \cdot \mathbf{u} + \nabla^2 \Theta, \quad (2.3c)$$

$$\frac{\kappa}{\lambda} \left( \frac{\partial}{\partial t} \mathbf{b} + \mathbf{u} \cdot \nabla \mathbf{b} - \mathbf{b} \cdot \nabla \mathbf{u} \right) = \mathbf{i} \cdot \nabla \mathbf{u} + \nabla^2 \mathbf{b}, \quad (2.3d)$$

$$\nabla \cdot \mathbf{b} = 0, \quad (2.3e)$$

where all gradient terms in (2.3a) have been combined into the pressure term  $\nabla \Pi$ . The magnetic field has been represented in the form  $\mathbf{B} = B_0 \left( \mathbf{i} + \frac{\kappa}{\lambda} \mathbf{b} \right)$  where  $\mathbf{i}$  is the unit vector in the  $x$ -direction. In the following we shall focus the attention on the case of liquid metals where  $\frac{\kappa}{\lambda}$  is of the order  $10^{-4}$  to  $10^{-5}$ . Hence we shall adopt in this thesis the limit  $\kappa \ll \lambda$  and drop the terms on the left hand side of (2.3d) and the term multiplied by  $\frac{\kappa}{\lambda}$  in equation (2.3a).

We use no-slip boundary conditions for the velocity field and assume that the plates are perfectly heat conducting. Furthermore the plates are electrically insulating, i.e. the normal component of the electric current density  $\mathbf{j} = \nabla \times \mathbf{b} / \mu_0$  has to vanish there.

Thus the following boundary conditions have to be fulfilled:

$$\mathbf{u} = 0, \quad \Theta = 0, \quad \nabla \times \mathbf{b} \cdot \mathbf{k} = 0 \quad \text{at } z = \pm \frac{1}{2}. \quad (2.4)$$

The continuity of the magnetic field  $\mathbf{b}$  across the boundaries does not have to be taken into account explicitly in the limit  $\kappa \ll \lambda$  as will be pointed out below. Following earlier papers [24, 25] we assume the idealization of an infinitely extended fluid layer in the horizontal plane, thus we use periodic boundary conditions and i.e the  $x, y$ -dependence is captured by a  $2D$  Fourier series. The agreement between the results of those papers and the experimental observations of Jaletzky and Busse [28] indicates that the periodic boundary conditions as well as the small gap approximation are appropriate for the rotating annulus experiment at the moderate values of  $\tau$  to be considered in this study. In order to eliminate the pressure term in (2.3a) we introduce the general representations for the solenoidal vector fields  $\mathbf{u}$  and  $\mathbf{b}$ , (see (2.3b) and (2.3e)):

$$\mathbf{u} = \bar{\mathbf{u}} + \nabla \times (\nabla \times \mathbf{k}v) + \nabla \times \mathbf{k}w =: \bar{\mathbf{u}} + \boldsymbol{\delta}v + \boldsymbol{\varepsilon}w, \quad (2.5a)$$

$$\mathbf{b} = \bar{\mathbf{b}} + \nabla \times (\nabla \times \mathbf{k}h) + \nabla \times \mathbf{k}g =: \bar{\mathbf{b}} + \boldsymbol{\delta}h + \boldsymbol{\varepsilon}g, \quad (2.5b)$$

where overbars in  $\bar{\mathbf{u}}$  and  $\bar{\mathbf{b}}$  denote the average over the  $x, y$ - plane of  $\mathbf{u}$  and  $\mathbf{b}$ . The functions  $v, h$  and  $w, g$  describing the poloidal and toroidal components of the velocity and the magnetic field, respectively, are uniquely defined if the conditions  $\bar{v} = \bar{h} = \bar{w} = \bar{g} = 0$  are imposed. After the application of the differential operators  $\boldsymbol{\delta}$  and  $\boldsymbol{\varepsilon}$  on the velocity equation (2.3a) we arrive at the following equations for  $v$  and  $w$

$$P^{-1} \left[ \frac{\partial}{\partial t} \nabla^2 \Delta_2 v + \boldsymbol{\delta} \cdot (\mathbf{u} \cdot \nabla) \mathbf{u} \right] = \nabla^4 \Delta_2 v - 2\tau \frac{\partial}{\partial y} \Delta_2 w + \Delta_2 \theta + Q \mathbf{i} \cdot \nabla \nabla^2 \Delta_2 h, \quad (2.6a)$$

$$P^{-1} \left[ \frac{\partial}{\partial t} \Delta_2 w + \boldsymbol{\varepsilon} \cdot (\mathbf{u} \cdot \nabla) \mathbf{u} \right] = \nabla^2 \Delta_2 w + 2\tau \frac{\partial}{\partial y} \Delta_2 v + Q \mathbf{i} \cdot \nabla \Delta_2 g. \quad (2.6b)$$

In addition, an equation for the mean flow  $\bar{\mathbf{u}}$  is obtained by averaging the velocity equation (2.3a) over the  $x - y$  plane.

$$P^{-1} \left( \frac{\partial}{\partial t} \bar{\mathbf{u}} - \frac{\partial}{\partial z} \overline{\Delta_2 v \left( \nabla_2 \frac{\partial}{\partial z} v + \boldsymbol{\varepsilon} w \right)} \right) + 2\tau \mathbf{j} \times \bar{\mathbf{u}} = \frac{\partial^2}{\partial z^2} \bar{\mathbf{u}}. \quad (2.7)$$

The heat equation (2.3c) can now be written in the form

$$\frac{\partial}{\partial t} \Theta + (\boldsymbol{\delta}v + \boldsymbol{\varepsilon}w + \bar{\mathbf{u}}) \cdot \nabla \Theta = \nabla^2 \Theta + R \Delta_2 v. \quad (2.8)$$

Analogously, when applying  $\boldsymbol{\delta}$  and  $\boldsymbol{\varepsilon}$  on the right hand side of the magnetic equation (2.3d), we obtain in the limit  $\frac{\kappa}{\lambda} \rightarrow 0$

$$\nabla^2 \Delta_2 h = -\mathbf{i} \cdot \nabla \Delta_2 v, \quad (2.9a)$$

$$\nabla^2 \Delta_2 g = -\mathbf{i} \cdot \nabla \Delta_2 w. \quad (2.9b)$$

The mean distortion  $\bar{\mathbf{b}}$  of the magnetic field does not enter the problem since it vanishes in the limit  $\kappa \ll \lambda$ . In writing down Eqs. (2.6) and (2.8) we have introduced the horizontal gradient,  $\nabla_2 \equiv \nabla - \mathbf{k}(\mathbf{k} \cdot \nabla)$ , and the horizontal Laplacian,  $\Delta_2 \equiv \nabla_2 \cdot \nabla_2$ . In line with (2.4, 2.5) the basic Eqs. (2.6) - (2.8) must be solved subject to the boundary conditions

$$v = \frac{\partial}{\partial z}v = w = \Theta = g = 0 \quad \text{at} \quad z = \pm \frac{1}{2}. \quad (2.10)$$

The equation (2.9a) for  $h$  and the corresponding boundary condition can be dropped, since  $h$  can be immediately eliminated from the problem by replacing  $\nabla^2 \Delta_2 h$  in (2.6a) with  $\mathbf{i} \cdot \nabla \Delta_2 v$  in accordance with (2.9a). With  $g(z = \pm 1/2) = 0$  the condition  $\mathbf{k} \nabla \times \mathbf{b} = -\Delta_2 g = 0$  (Eq. 2.4) is fulfilled automatically.

Following Eq. (1.1), Eqs. (2.6) - (2.8) are written as

$$\mathcal{D} \frac{d}{dt} \mathbf{V}(\mathbf{x}, t) = \mathcal{L} \mathbf{V}(\mathbf{x}, t) + \mathbf{N}(\mathbf{V}(\mathbf{x}, t), \mathbf{V}(\mathbf{x}, t)), \quad \mathcal{L} = \mathcal{A} + R \mathcal{B}, \quad (2.11)$$

where the symbolic vector  $\mathbf{V}(\mathbf{x}, t) = (v, w, g, \Theta, \bar{\mathbf{u}})$  represents all fields in equations (2.6-2.8).  $\mathbf{V}(\mathbf{x}, t) \equiv 0$  corresponds to the ground state. The linear operator  $\mathcal{A}$  can be read off from the right-hand side of Eqs. (2.6), (2.7), (2.8). The operator  $\mathcal{B}$  associated with  $R$  appears only in the temperature equation (2.8). The linear operators  $\mathcal{D}$  appears in the left-hand side of Eqs. (2.6), (2.7), (2.8). The advection of the velocity (2.6) and of the temperature  $\Theta$  (2.8) yield the quadratic nonlinearity  $\mathbf{N}$ .

The  $2D$ - periodic solutions of Eq. (2.11), which fulfill the required boundary conditions at  $z = \pm \frac{1}{2}$ , are represented in the framework of the Galerkin method (see Sec. (1.2)) as follows:

$$v(x, y, z, t) = \sum_{n=1}^N \sum_{l, m=-M}^M v_{lmn}(t) \exp[i(lq_x x + mq_y y)] f_n(z), \quad (2.12a)$$

$$w(x, y, z, t) = \sum_{n=1}^N \sum_{l, m=-M}^M w_{lmn}(t) \exp[i(lq_x x + mq_y y)] S_n(z), \quad (2.12b)$$

$$g(x, y, z, t) = \sum_{n=1}^N \sum_{l, m=-M}^M g_{lmn}(t) \exp[i(lq_x x + mq_y y)] S_n(z), \quad (2.12c)$$

$$\Theta(x, y, z, t) = \sum_{n=1}^N \sum_{l, m=-M}^M \Theta_{lmn}(t) \exp[i(lq_x x + mq_y y)] S_n(z), \quad (2.12d)$$

$$\bar{\mathbf{u}}(z, t) = \sum_{n=1}^N \mathbf{u}_n(t) S_n(z). \quad (2.12e)$$

Here,  $f_n(z)$  denote the Chandrasekhar functions [27] with the properties  $f_n(\pm \frac{1}{2}) = \frac{\partial}{\partial z} f_n(\pm \frac{1}{2}) = 0$  (see App. B).

The summations in the velocity expressions (2.12a - 2.12c) run through all positive integers  $n$  and through all integers  $l$  and  $m$  with the exception of the case  $l = m = 0$ . In

the sum (2.12d) the term  $l = m = 0$  must be included since it describes the distortion of the mean temperature profile. Reality of all fields requires  $v_{l,m,n} = v_{-l,-m,n}^*$ , etc., where the star indicates the complex conjugate.

The expressions (2.12) are inserted into Eqs. (2.6), (2.9), (2.8) and projected onto the various expansion functions appearing in (2.12). Thus, one obtains a set of ordinary nonlinear differential equations for the coefficients  $v_{lmn}(t)$ ,  $w_{lmn}(t)$ ,  $g_{lmn}(t)$  and  $\mathbf{u}_n(t)$ . Since the coefficients  $g_{lmn}(t)$  are slaved to the  $w_{lmn}(t)$  according to equation (2.9b) as:

$$g_{lmn}(t) = \frac{i l q_x w_{lmn}(t)}{l^2 q_x^2 + m^2 q_y^2 + n^2 \pi^2}, \quad (2.13)$$

they can be eliminated from the beginning.

We are interested in solutions for moderate Rayleigh number  $R$  and find that typically truncation parameters  $M = 4$  and  $N = 4$  have been sufficient to achieve already an accuracy of about 1% in the Galerkin approach for periodic solutions. To check the accuracy of these solutions the truncation parameters have been increased to larger values in some cases.

## 2.2 Linear Analysis for the Onset of Convection

In Sec. (1.1), we have sketched the linear analysis of the basic state  $\mathbf{V} = 0$ , which yields the neutral curve  $R_0(\mathbf{q})$ , the critical Rayleigh number  $R_c$  and the critical wave vector  $\mathbf{q}_c$  at the onset of convection. The ensuing Galerkin scheme is based on the expansions shown in Eqs. (2.12). In the linear regime only the Fourier modes with  $|l|, |m| \leq 1$  come into play. We will use the notations *axial* for the longitudinal rolls ( $|l| = 1, m = 0$ ), *zonal* for the transverse rolls ( $l = 0, |m| = 1$ ) and *oblique* for the general case  $|l| = |m| = 1$ . We have found that the onset of convection is always stationary, in accordance with the findings of Eltayeb [9] with stress-free boundary conditions and in the limit  $\kappa \ll \lambda$  as well. Thus the neutral curve  $R_0(\mathbf{q})$  is obtained from a modified eigenvalue problem (see Eq. (1.3)).

Inspection of linearized equations (2.6) - (2.8) shows at first that the Prandtl number  $P$  drops out from the linear problem. Furthermore they are invariant against the reflection ( $z \rightarrow -z$ ) at the midplane  $z = 0$ . Thus the linear eigenvectors have to be even or odd functions of  $z$ . The even case (i.e. standard rolls) is realized at onset as in most convection problems.

Additional symmetries of the linearized Eqs. (2.6) - (2.8) lead to a further classification of the linear solutions and are also used to check the numerical analysis. Invariance against a reflection at the rotation axis ( $x \rightarrow -x$ ) is immediately obvious. Furthermore under reflections with respect to the  $x$  axis ( $y \rightarrow -y$ ) the equations are invariant if the fields are in parallel transformed as follows :

$$\begin{aligned} \Theta(x, y, z) &\rightarrow \Theta(x, -y, z), & v(x, y, z) &\rightarrow v(x, -y, z), \\ w(x, y, z) &\rightarrow -w(x, -y, z), & g(x, y, z) &\rightarrow -g(x, -y, z). \end{aligned} \quad (2.14)$$

Furthermore, there exists invariance against the combined transformation  $\tau \rightarrow -\tau$  and  $y \rightarrow -y$ . The symmetries described before hold also in Fourier space when  $\mathbf{r} = (x, y)$  is replaced by  $\mathbf{q} = (q_x, q_y)$ . With the use of the reality condition  $\mathbf{V}(\mathbf{q}) = \mathbf{V}^*(-\mathbf{q})$ , one sees easily that the Fourier components  $\Theta(\mathbf{q})$  and  $v(\mathbf{q})$  have to be real in  $\mathbf{q}$ -space, i.e.  $\Theta(\mathbf{r}, z)$  and  $v(\mathbf{r}, z)$  are proportional to  $\cos(\mathbf{q} \cdot \mathbf{r})$ , whereas  $w$  and  $g$  are purely imaginary, i.e. they are proportional to  $\sin(\mathbf{q} \cdot \mathbf{r})$  in position space. The symmetries imply that the neutral curve can only depend on  $q_x^2, q_y^2$  whereas a mixed term  $\propto q_x q_y$  is not allowed. Note also that the toroidal velocity potential  $w$  has to vanish for axial rolls.

Already the one- mode approximation yields a very useful analytical expression for  $R_0(\mathbf{q})$  which reflects the symmetries discussed before and which allows to study quickly the parameter dependencies:

$$R_0(\mathbf{q}) = R^{RB}(q^2) + \frac{4\tau^2(q^2 + \pi^2)^2 \sin^2 \chi}{(q^2 + \pi^2)^2 + Qq^2 \cos^2 \chi} + c_1 Q(q^2 + \pi^2) \cos^2 \chi, \quad (2.15a)$$

$$R^{RB}(q^2) = \frac{(q^4 + 2\pi^2 c_2 q^2 + \pi^4 c_3)(q^2 + \pi^2) c_1}{q^2}. \quad (2.15b)$$

Here,  $q = \sqrt{q_x^2 + q_y^2}$  is the modulus of  $\mathbf{q}$  and the obliqueness angle  $\chi = \arctan(\frac{q_y}{q_x})$  denotes the angle between the rolls and the rotation axis. The numerical constants  $c_1, c_2, c_3$  are combinations of certain overlap integrals of trigonometric and Chandrasekhar functions and assume the values  $c_1 = 1.0281, c_2 = 1.2465$  and  $c_3 = 5.1388$ . The minimum of  $R^{RB}(q^2)$  yields an approximate Rayleigh-Bénard ( $RB$ ) threshold ( $\tau = Q = 0$ ) with  $q_c = 3.0963, R^{RB} = 1728.38$ . The well- known rigorous values  $q_c = 3.116$  and  $R^{RB} = 1707.76$  differ by less than 1.2% from the approximate ones. Note that Eq. (2.15) is exact for the unrealistic free boundary conditions where  $c_i = 1$  for  $i = 1, 2, 3$  holds. However, the threshold values ( $q_c = \frac{\pi}{\sqrt{2}}, R_c = 657$  in the  $RB$  case) deviate substantially from the rigorous ones. So we see no reason to study stress free boundary conditions at all, which have even more deficiencies in the nonlinear regime, since the damping of the vorticity field  $w$  is largely underestimated.

From (2.15) it is obvious that in the case  $\tau \gg Q$  the minimum of  $R_c = R_0(\mathbf{q}_c)$  is obtained for  $\chi_c = 0^\circ$  (*axial rolls*). It is interesting that the relation

$$R_c(\mathbf{q}) = R^{RB}(q^2) + 4\tau^2 \sin^2 \chi \quad (2.16)$$

which derives from (2.15) for  $Q = 0$  is mathematically rigorous if the exact neutral curve  $R^{RB}(q^2)$  for Rayleigh-Bénard convection is chosen. In the opposite limit,  $Q \gg \tau$ , the minimum of  $R_0(\mathbf{q})$  is found at  $\chi_c = 90^\circ$  (*zonal rolls*). In the intermediate regime  $Q \sim \tau$  we have oblique rolls at onset ( $0^\circ < \chi_c < 90^\circ$ ), for instance,  $\chi_c = 55^\circ$  for  $Q = 14$  and  $\tau = 8$ .

The general numerical results for  $R_c$  and  $q_c$  as function of  $\tau$  and  $Q$  are shown in Figs. (2.2 - 2.5). The critical Rayleigh number,  $R_c(\tau, Q)$  in Fig. 2.2 is always larger than  $R^{RB}(\mathbf{q}_c)$ . It increases linearly at small  $Q$  and quadratically at small  $\tau$ , in perfect agreement with the analytical approximation (2.15). The modulus  $q_c = |\mathbf{q}_c|$  of the critical wave vector shown in Fig. 2.3 decreases monotonously from the  $RB$  value

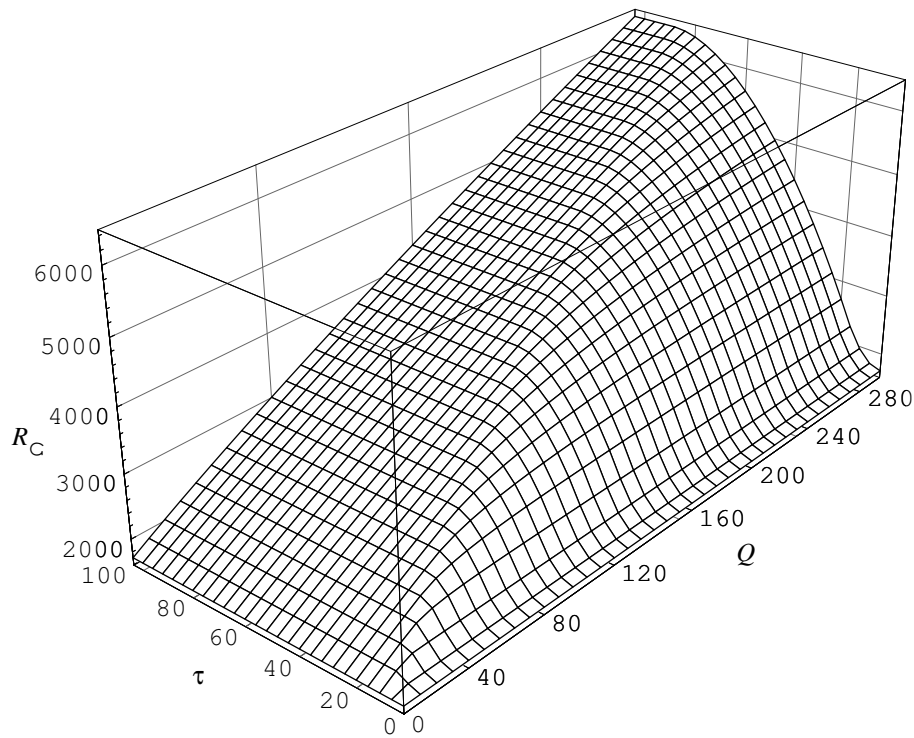


Figure 2.2: Critical Rayleigh number,  $R_c$ , as a function of  $\tau$  and  $Q$ .

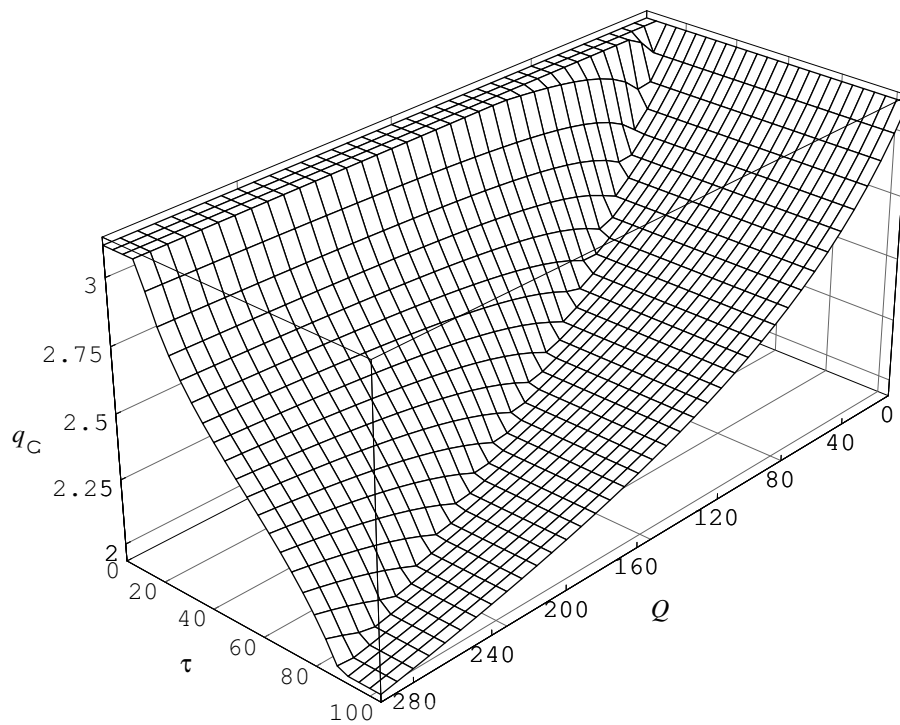


Figure 2.3: Critical wave number,  $q_c$ , as a function of  $\tau$  and  $Q$ .

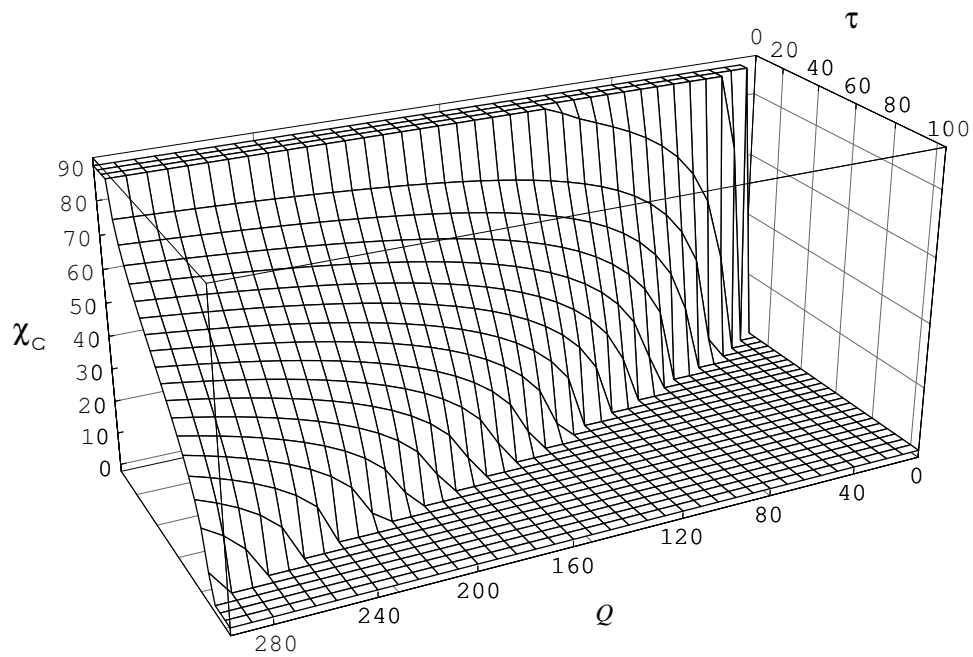


Figure 2.4: The critical obliqueness angles,  $\chi_c$ , (see text) as a function of  $\tau$  and  $Q$ .

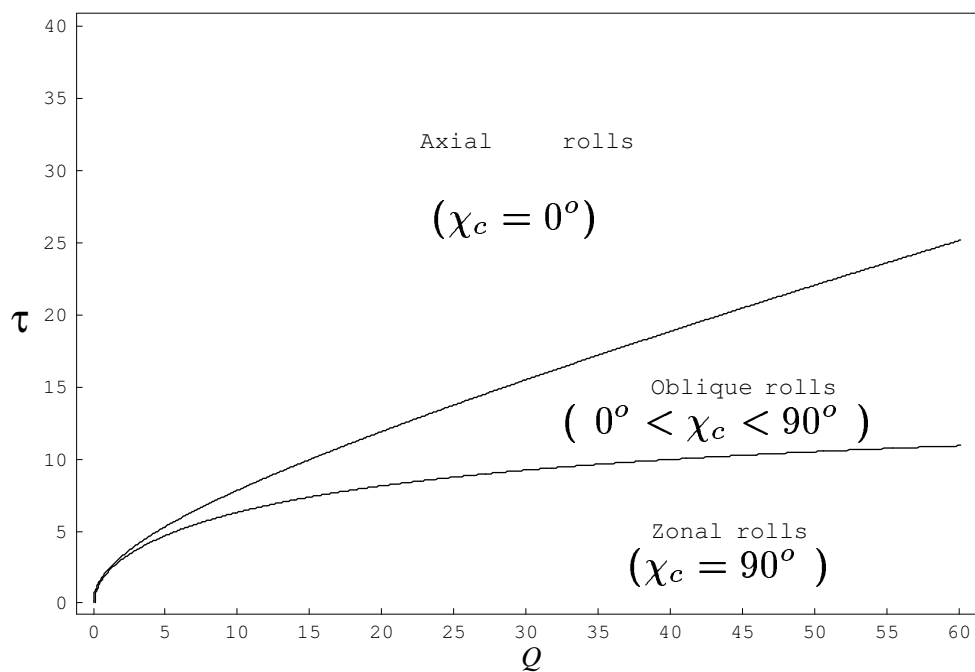


Figure 2.5: The transition lines between zonal rolls and oblique rolls,  $\tau_L(Q)$ , and between oblique rolls and axial rolls,  $\tau_U(Q)$ , in the  $Q - \tau$  plane (see text).

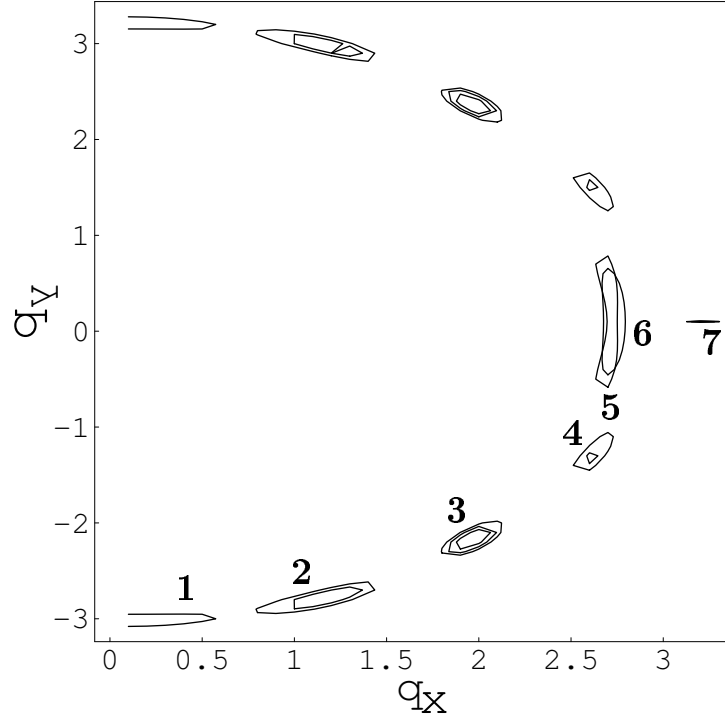


Figure 2.6: The variation of the critical Rayleigh number,  $R_c$  in the wave vector space  $\mathbf{q} = (q_x, q_y)$  for various values of  $\tau$  and  $Q$ . The numbers in the figure correspond to the following parameters: (1)  $\tau = 0$ ,  $Q = 14$ ,  $R_c = 1707.8$ ,  $q_c = 3.11$ ,  $\chi_c = 90^\circ$ ; (2)  $\tau = 10$ ,  $Q = 30$ ,  $R_c = 2103.4$ ,  $q_c = 3.07$ ,  $\chi_c = 70^\circ$ ; (3)  $\tau = 14$ ,  $Q = 42$ ,  $R_c = 2364.7$ ,  $q_c = 2.93$ ,  $\chi_c = 50^\circ$ ; (4)  $\tau = 14$ ,  $Q = 30$ ,  $R_c = 2265.2$ ,  $q_c = 2.87$ ,  $\chi_c = 30^\circ$ ; (5)  $\tau = 24$ ,  $Q = 58$ ,  $R_c = 2769.1$ ,  $q_c = 2.64$ ,  $\chi_c = 10^\circ$ ; (6)  $\tau = 30$ ,  $Q = 56$ ,  $R_c = 2735.0$ ,  $q_c = 2.63$ ,  $\chi_c = 0^\circ$ ; (7)  $\tau = 34$ ,  $Q = 0$ ,  $R_c = 1707.8$ ,  $q_c = 3.11$ ,  $\chi_c = 0^\circ$ .

( $q_c = 3.116$ ) to smaller values for increasing  $\tau$  and  $Q$ . The critical obliqueness angle  $\chi_c$  as function of  $\tau$  and  $Q$  is given in Fig. 2.4. With increasing  $\tau$  at fixed  $Q$  one observes a transition from zonal rolls ( $\chi_c = 90^\circ$ ) to oblique rolls at a lower Lifshitz point  $\tau_L$ , which go over to axial rolls ( $\chi_c = 0^\circ$ ) at an upper Lifshitz point  $\tau_U$ . The transition lines between zonal rolls, oblique rolls and axial rolls in the  $Q - \tau$  plane are shown in Fig. 2.5. (see also the upper and lower faces of the parallelepiped in Fig. 2.4). Apparently, the oblique roll region is confined by an almost linear upper curve and an approximately parabolic lower curve as indicated in Fig. 2.5, i.e.  $\tau^2 \sim c_1 \pi^2 Q$ , see Eq. (2.15a). In general the approximate values for  $q_c$ ,  $\chi_c$  and  $R_c$  obtained from (2.15) deviate by less than 1% from the exact (numerical) ones (Figs. 2.2, 2.3). For instance,  $\tau = 84$  and  $Q = 300$ , we find  $R_c = 6417.048$ ,  $q_c = 1.9927$  and an oblique angle,  $\chi_c = 10.97^\circ$ , which compares well with the corresponding approximate values  $R_c = 6459.938$ ,  $q_c = 2.0022$  and  $\chi_c = 13.34$  from Eq. (2.15).

In the following we exemplify the neutral curve in the vicinity of  $\mathbf{q}_c = (q_{xc}, q_{yc})$ ,  $R_c$  in detail. In Fig. 2.6 we have roughly sketched contour lines of the neutral curve  $R_0(\mathbf{q})$

for several combinations of  $Q, \tau$ . The corresponding values  $\mathbf{q}_c$  are at the midpoint of the *ellipses*. When the magnetic field strength is increased, we approach the zonal-roll case, i.e.  $q_{xc} = 0$  (see case (1)) with increasing  $\tau$  the rolls become increasingly oblique (finite  $q_{xc}, q_{yc}$ ). For  $Q = 0$  we have axial rolls ( $q_{yc} = 0$ , case (7)). Fig. 2.6 has been generated by an automated procedure, where the whole  $q_x, q_y$  regime shown was scanned. It is obvious that the symmetries discussed above are perfectly reproduced, e.g. the reflection symmetry  $q_y \rightarrow -q_y$ . The neutral surface  $R_0(\mathbf{q})$  does not depend on the Prandtl number  $P$ , in contrast to the linear eigenvalue spectra as function of  $\mathbf{q}, R$  since the time derivatives  $\propto P^{-1}$  come into play.

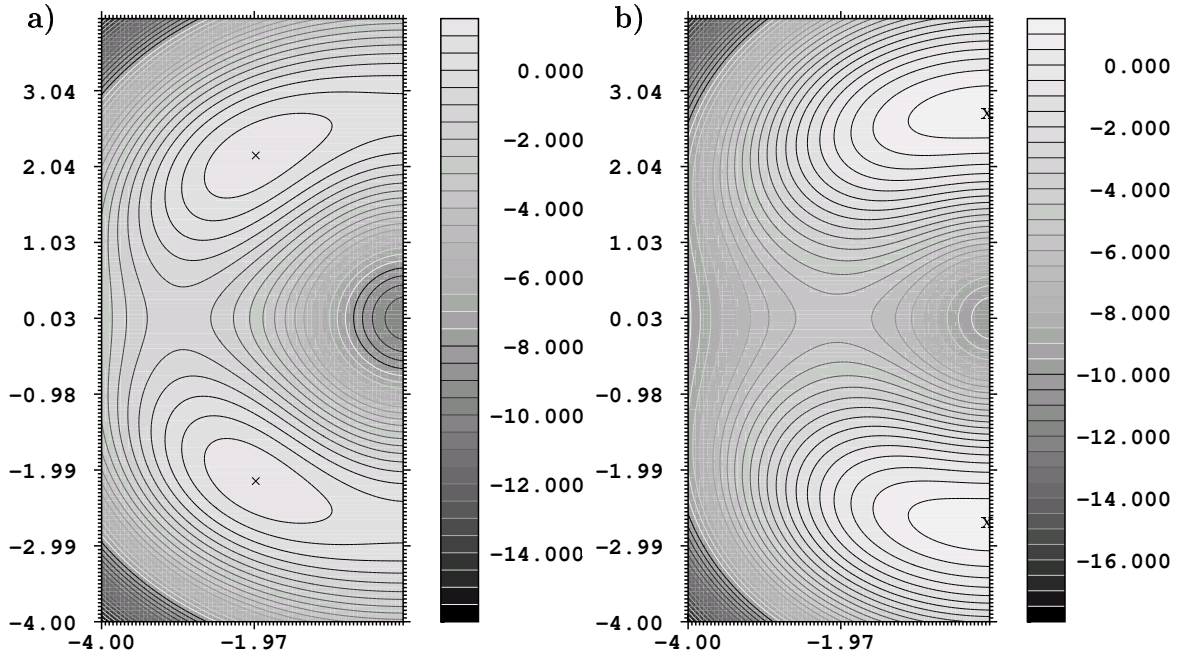


Figure 2.7: Contour plots of the growthrates  $\sigma(\mathbf{q} = (q_x, q_y), R)$  for  $P = 10$  at  $R = 1.08R_c$  for  $\tau = 18, Q = 54$  (left panel) and  $\tau = 26, Q = 54$  (right panel).  $q_x$  varies along the vertical axis ( $-4 \leq q_x \leq 4$ ) and  $q_y$  along the horizontal axis ( $-4 \leq q_y \leq 0$ ).

In Fig. 2.7 we have concentrated on two particular parameter combinations of  $Q, \tau$  and show the growthrates for large  $P$  in the  $\mathbf{q}$  plane slightly above onset ( $\varepsilon = 0.08$ ) where  $\sigma(\mathbf{q}) \approx -R_0(\mathbf{q})$ . In the left panel we have addressed an oblique roll bifurcation: The absolute maxima at  $\mathbf{q}_c$  are indicated by the two crosses. There exists also a local minimum for  $\mathbf{q} = 0$  with a strongly negative growthrate. An axial roll case for relatively large  $\tau$  is shown on the right panel of Fig. 2.7. The absolute maxima are located at  $\pm q_{xc}$  with  $q_{yc} = 0$  (see crosses).

In Fig. 2.8 we show examples of the eigenvalue spectra for small  $P = 0.1$ . On the upper panels, the magnetically dominated case with critical zonal rolls ( $q_{xc} = q_{yc} \neq 0$ ) is addressed. Whereas for large  $P$  the leading eigenvalues are always real we find a small crescent region where  $\Im(\lambda(\mathbf{q})) \neq 0$ . The two lower panels (Fig. 2.8c,d) are more

interesting because the effect of low Prandtl number  $P = 0.1$  is seen more clearly if we compare to the growthrates for  $Pr = 10$  in Fig. 2.7b. In both cases the absolute maxima are at  $q = \pm q_c$  (axial rolls with  $\mathbf{q}_c = (q_{xc}, 0)$ ). However, for  $P = 0.1$  a new local maximum has appeared in the growthrate (Fig. 2.8c) at  $q_x = 0$  (zonal)

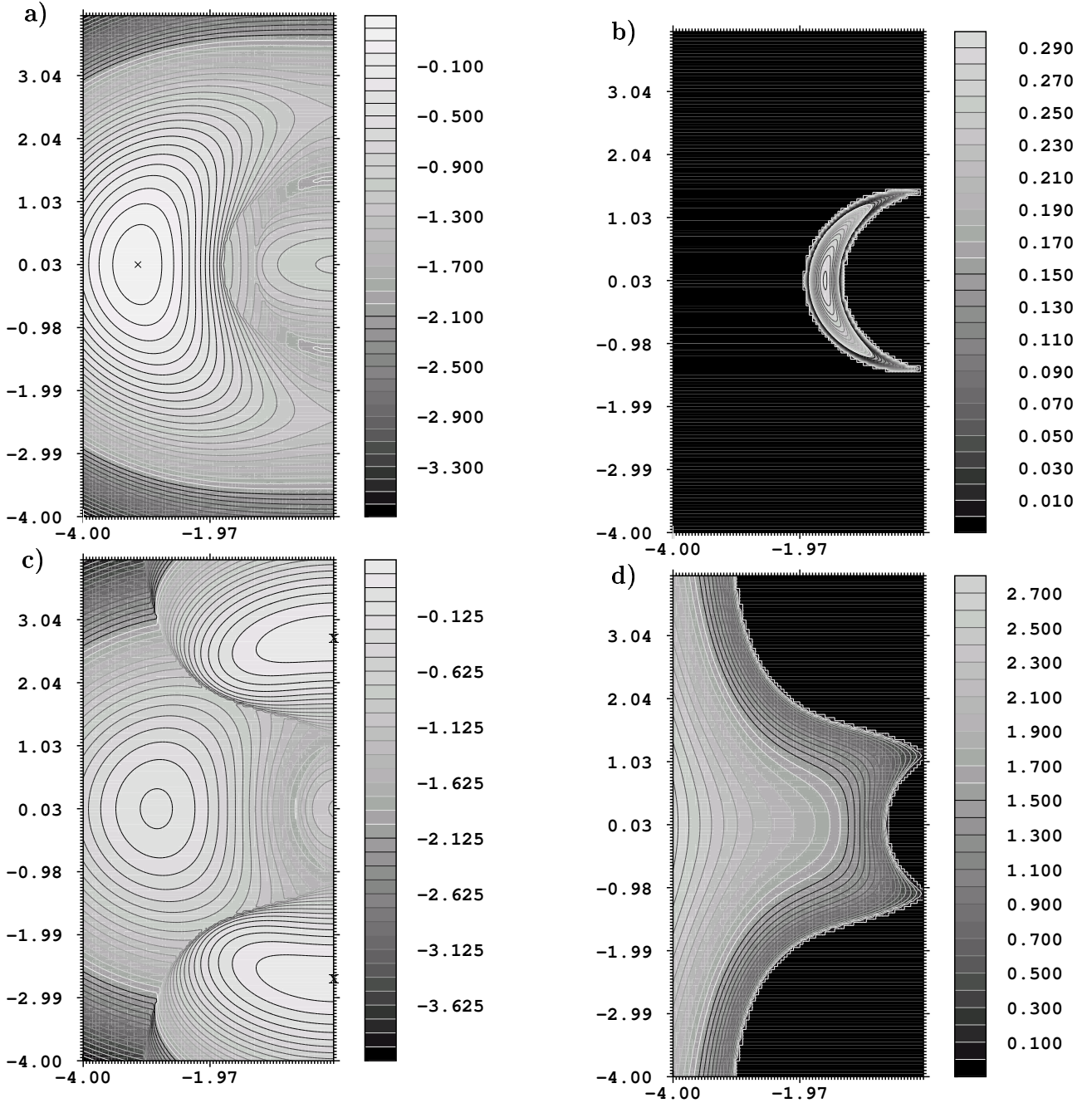


Figure 2.8: Real (left panel) and imaginary (right panel) parts of the leading eigenvalues as function of  $\mathbf{q}$  at  $R = 1.01R_c$  and  $P = 0.1$  for  $\tau = 4, Q = 54$  (a,b) and  $\tau = 26, Q = 54$  (c,d).

which is accompanied with a non-vanishing  $\Im(\lambda(\mathbf{q}))$ . We expect that such substantial modifications of the eigenvalue spectra will play an important role for higher  $\varepsilon$  values, where the growth rates of modes, which are slightly negative at  $R_c$  and  $\mathbf{q} \neq \mathbf{q}_c$ , become positive and dynamically active.

## 2.3 Nonlinear Analysis of Roll Solutions

In this section we present results for the nonlinear properties of rolls on the basis of the weakly nonlinear analysis and Galerkin calculations. We concentrate mainly on the region near onset with small  $\varepsilon := (R - R_c)/R_c$ . Even there the analysis is far from complete in view of the large parameter space of  $\tau$ ,  $Q$  and  $P$ , that has to be scanned. In Sec. 2.3.1 we study the horizontal average of convective heat transport (the Nusselt number). This global quantity is typically recorded when visualization of the patterns is not possible, by which for instance secondary bifurcations become immediately evident. In Sec. 2.3.2, we discuss the secondary bifurcations of rolls at large Prandtl number  $P$ . The small-  $P$  case is addressed in Sec. 2.3.3.

### 2.3.1 Nusselt number

The total heat current  $J_{tot} = -\kappa \frac{d}{dz} \bar{T}(z)$  is determined by the horizontally averaged temperature gradient. Since  $J_{tot}$  is a conserved quantity it can be evaluated for instance at the lower plate ( $z = -\frac{1}{2}$ ). The total heat current is the sum of the conductive heat current  $J_{cond} = -\kappa \frac{T_2 - T_1}{d}$ , which derives from the basic profile  $T_0(z)$  (see Eq. (2.1)) and the convective part  $J_{conv} = -\kappa \frac{\Delta T}{Rd} \frac{d}{dz} \bar{\Theta}(\mathbf{r}, z = -\frac{1}{2})$ .

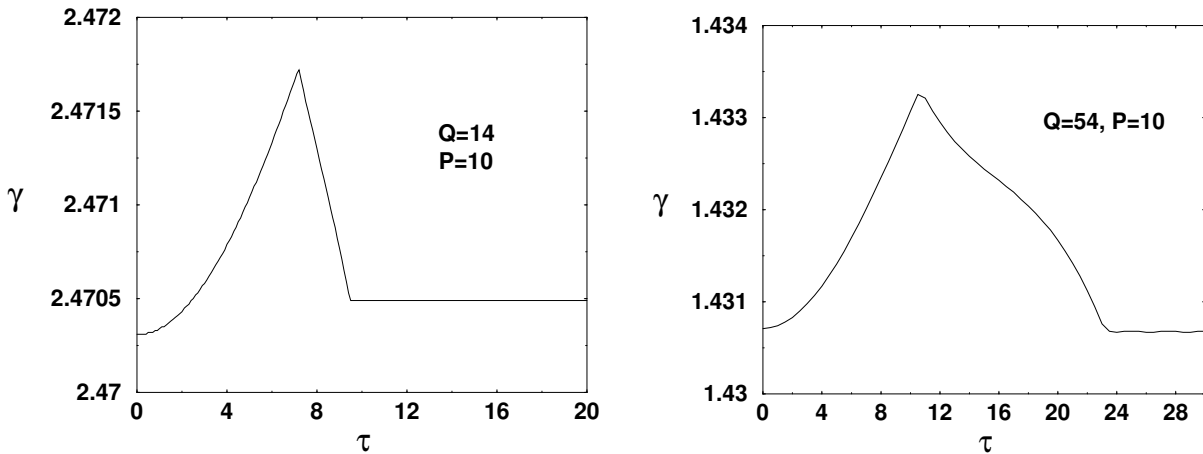


Figure 2.9: The slope  $\gamma$  of the Nusselt number (see Eq. (2.18)) at  $\varepsilon = 0$  for  $P = 10$  as function of  $\tau$  for two different  $Q$  at  $\mathbf{q}_c$ : Left panel  $Q = 14$ , right panel  $Q = 54$ .

The horizontal average corresponds to the  $\mathbf{q} = 0$  component of  $\Theta$  in Fourier space.

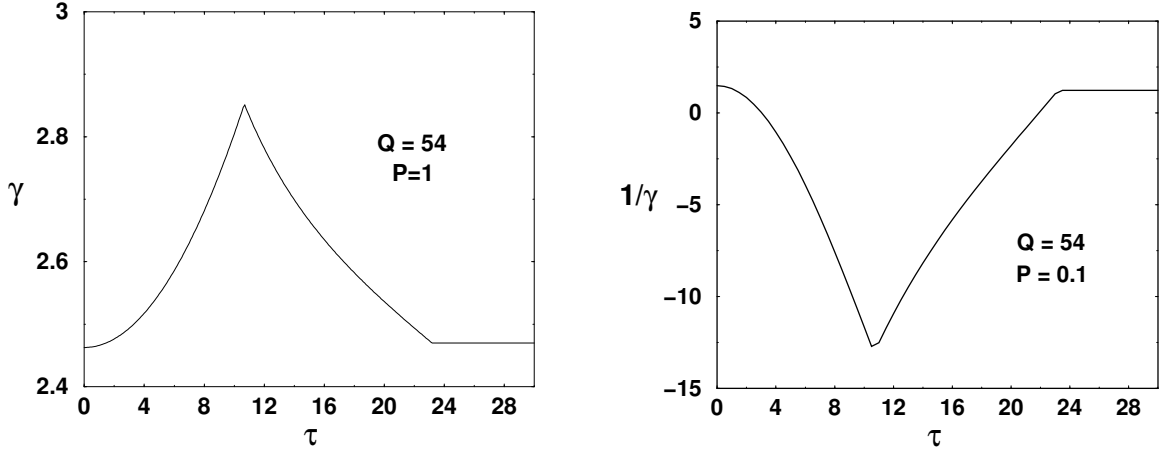


Figure 2.10: The slope  $\gamma$  of  $Nu$  as function of  $\tau$  at  $\mathbf{q}_c$  for  $P = 0.1$  (left), and  $P = 1$  (right) at  $Q = 54$ .

The Nusselt number  $Nu$ , the non-dimensional measure of  $J_{tot}$ , is defined as:

$$Nu = \frac{J_{tot}}{J_{cond}} = 1 - \frac{1}{R} \frac{d}{dz} \Theta(\mathbf{q} = 0, z = -\frac{1}{2}). \quad (2.17)$$

Near onset  $Nu$  can be calculated via the weakly nonlinear analysis, according to  $\bar{\Theta} \propto A^2 \propto \varepsilon$ . Thus we have:

$$Nu = 1 + \gamma\varepsilon \quad \text{for} \quad \varepsilon = (R - R_c)/R_c \rightarrow 0 \quad (2.18)$$

In the following we first give some characteristic examples of the slope  $\gamma$  of  $Nu$  at  $\varepsilon = 0$  for various  $\tau, Q$  and  $P$ . In most cases we observe a supercritical bifurcation ( $\gamma > 0$ ) but at small  $P$  subcritical bifurcations ( $\gamma < 0$ ) are identified as well.

In Fig. 2.9 at small  $\tau$  we have zonal rolls where  $\gamma$  grows at first continuously with  $\tau$ . At the lower Lifshitz point,  $\tau_L$ , an oblique roll bifurcation takes place and the slope of  $\gamma$  vs  $\tau$  changes abruptly. In the oblique roll regime  $\gamma$  decreases then monotonously until at the upper Lifshitz point,  $\tau_U$ , axial rolls are reached. In the axial roll regime  $\gamma$  is  $\tau$ -independent. As can be seen from the Fig. 2.9, variations of  $Q$  would modify only the onset and the width of the oblique roll regime. In Fig. 2.10 we show the slope  $\gamma$  for smaller  $P$ . At  $P = 1$  (Fig. 2.10a) the curve looks similar to the one in Fig. 2.9, however,  $\gamma$  varies over a much wider range. In contrast, at small  $P = 0.1$  a subcritical bifurcation has appeared, since with increasing  $\tau$  the cubic coefficient  $a \propto 1/\gamma$  of the Landau equation (Eq. (1.25)) decreases, passes to zero and becomes positive again (see Fig. 2.10b).

The calculation of  $Nu$  for arbitrary  $\varepsilon$  requires the fully nonlinear Galerkin solutions. In Fig. 2.11, the Nusselt number  $Nu$  is shown as function of  $\varepsilon$  for different  $q = |\mathbf{q}|$ . The basic state becomes linearly unstable for  $R \geq R_0(\mathbf{q}) \geq R_c$ . Thus for  $\mathbf{q} \neq \mathbf{q}_c$  the onset of convection is shifted towards larger  $\varepsilon$ . In Figs. 2.12a,b, we concentrate on the the Prandtl number dependence of  $Nu$ . The curves start at the same value  $R = R_0(\mathbf{q})$ ,

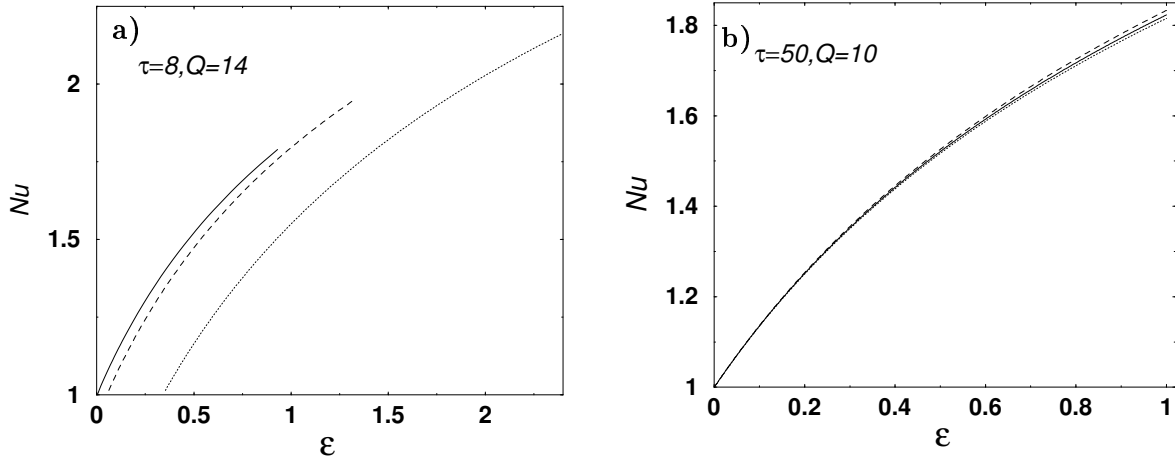


Figure 2.11: The Nusselt number  $Nu$  as function of the  $\varepsilon$  for different  $|\mathbf{q}|$  at (a)  $\tau = 8$ ,  $Q = 14$  and (b)  $\tau = 50$  and  $Q = 10$ , where the  $|\mathbf{q}|$  dependence is almost invisible, at fixed  $P = 10$ . The wave numbers are  $|\mathbf{q}| = \mathbf{q}_c = 3.0$  (solid),  $|\mathbf{q}| = 3.11$  (dashed) and  $|\mathbf{q}| = 2.7$  (dotted). Note that  $\chi = 0$  is used in the case of  $|\mathbf{q}| = 3.11$  and  $|\mathbf{q}| = 2.7$  in (a) and (b)

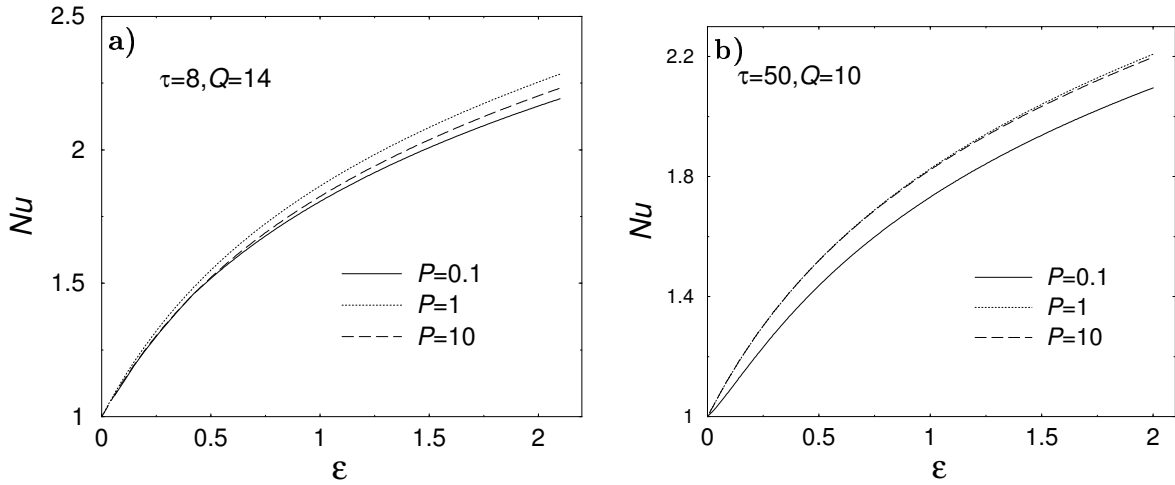


Figure 2.12: The Nusselt number  $Nu$  as function of  $\varepsilon_0$  at  $\tau = 8$ ,  $Q = 14$ ,  $|\mathbf{q}_c| = 3.05$  (left) and  $\tau = 50$ ,  $Q = 10$ ,  $|\mathbf{q}_c| = 3.0$  (right) in the case  $P = 0.1$ ,  $P = 1$  and  $P = 10$ .

since  $R_0(\mathbf{q})$  does not depend on  $P$ . With increasing  $R$ , we observe a slight splitting of the curves consistent with the slopes in Figs. 2.9, 2.10a.

For the parameters  $\tau = 12$ ,  $Q = 54$  and  $P = 0.1$ , the bifurcation is subcritical (see Fig. 2.10b). The corresponding Nusselt numbers in this case for different values of  $q$  are presented in Fig. 2.13a. As already discussed  $Nu$  increases linearly ( $\gamma \sim \varepsilon$ ) at  $\varepsilon = 0$ . With decreasing  $\varepsilon$  the saddle point is reached and the  $Nu$  bends back and increases further with increasing  $\varepsilon$ . This subcritical character will be explored in

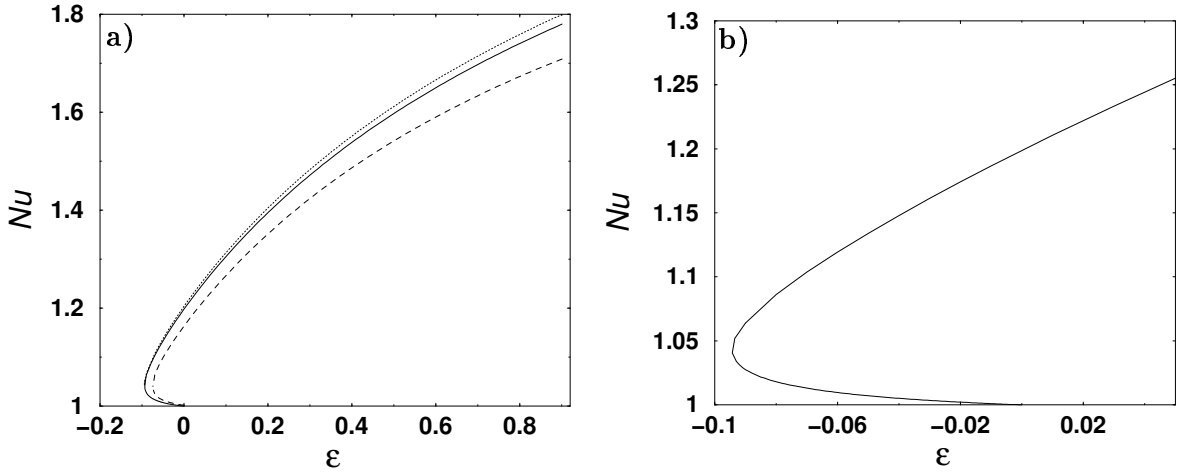


Figure 2.13: (a) The Nusselt number  $Nu$  in the subcritical region as function of  $\varepsilon$  for different  $|\mathbf{q}|$  at  $\tau = 12$ ,  $Q = 54$  at  $P = 0.1$ . The wave numbers are  $|\mathbf{q}| = 3.2$  (dotted),  $|\mathbf{q}| = \mathbf{q}_c = 3.05$  (solid) and  $|\mathbf{q}| = 2.7$  (dashed). (b) The Nusselt number  $Nu$  as function of  $\varepsilon$  near  $\varepsilon = 0$  for  $|\mathbf{q}| = \mathbf{q}_c = 3.05$  at  $\tau = 12$ ,  $Q = 54$  and  $P = 0.1$ . In both plots,  $\chi = \chi_c = 71.6^\circ$

following chapters in more detail also on the basis of numerical simulations.

### 2.3.2 Stability diagrams of rolls at large $P$

In the following section we discuss roll solutions and their stability for large  $P$  not too far from onset on the basis of weakly nonlinear and Galerkin solutions.

In Fig. 2.14 we start with the stability diagram of rolls in the  $\tau - \varepsilon$  plane. Note that we use instead of  $\varepsilon$  also  $\varepsilon_o := (R - R_c^{RB})/R^{RB}$  with respect to the standard Rayleigh-Bénard threshold  $R_c^{RB} (= 1708)$  at  $\tau = 0$  to describe the distance from onset. Convection exists above the neutral curve  $R_0(\mathbf{q}_c)$ . As discussed in the previous section we find zonal rolls at low  $\tau$ . With increasing  $\tau$  we enter at the lower Lifshitz point  $\tau_L$  the oblique roll regime. The critical obliqueness angle  $\chi_c$  decreases continuously from  $\chi_c = 90^\circ$  to  $\chi_c = 0^\circ$  at the upper Lifshitz point  $\tau_U$ , then the axial roll regime begins. The threshold increases at first continuously for  $\tau \leq \tau_U$ , then it settles down to a constant value. The stability diagrams in Fig. 2.14 for two different magnetic field strengths ( $Q = 14, 54$ ) are qualitatively similar. For  $Q = 54$  the oblique roll regime is wider, i.e.  $\tau_L = 10.7$ ,  $\tau_U = 23.1$  compared to  $\tau_L = 7.2$ ,  $\tau_U = 9.5$  for  $Q = 14$ . Since the axial-roll threshold increases roughly linear with  $Q$ , the variation of  $\varepsilon_o$  with  $\tau$  is more pronounced for  $Q = 54$ . In order to indicate the reduction of the threshold by rotating the roll axis, the zonal threshold extends into the large- $\tau$  regime. Rolls with the critical wave vector  $\mathbf{q}_c$  are always stable against longwave perturbations with a Floquet vector ( $|\mathbf{s}| \ll |\mathbf{q}_c|$ ) up to fairly large  $R$ . Zonal rolls at small  $\tau$  and also rolls with relatively large  $\chi_c \approx 90^\circ$  slightly above  $\tau_L$  are stable against shortwave ( $|\mathbf{s}| \approx |\mathbf{q}_c|$ ) instabilities as well. However, when  $\tau$  increases the stability regime becomes limited from above by a short wavelength instability line ( $SW$ ), which rises steeply with decreasing  $\tau$  (see

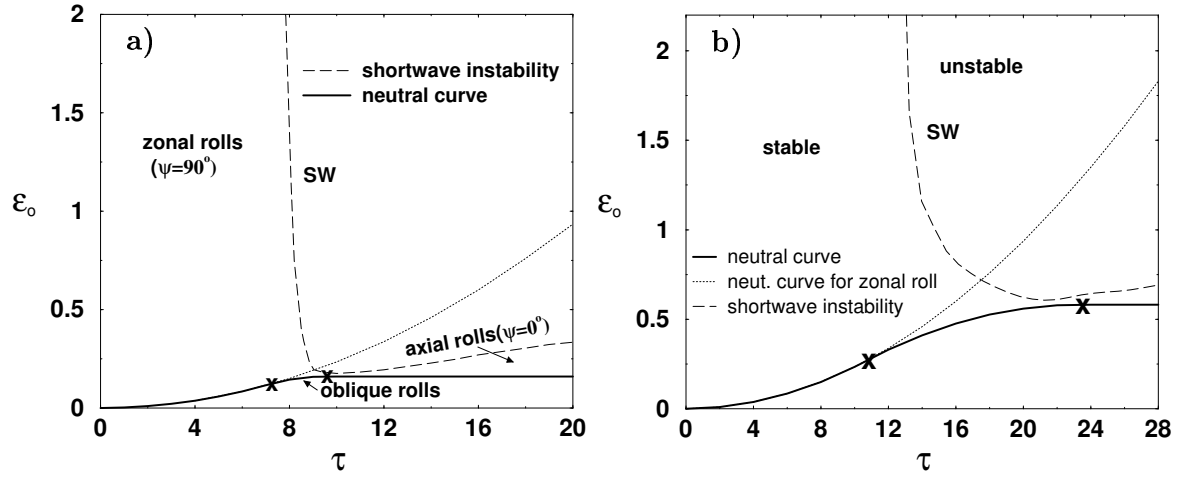


Figure 2.14: Stability diagram for rolls with the critical wave vector  $\mathbf{q}_c$  in the  $\varepsilon_o - \tau$  plane with  $\varepsilon_o = (R - R_c^{RB})/R_c^{RB}$  at (a)  $Q = 14, P = 10$  and (b)  $Q = 54, P = 10$ . The solid curve denote the neutral curve and the dotted curve the threshold for zonal rolls. The crosses indicate the two Lifshitz points  $\tau_L$  and  $\tau_U$ . The long-dashed curve presents a secondary short wavelength instability of rolls (SW).

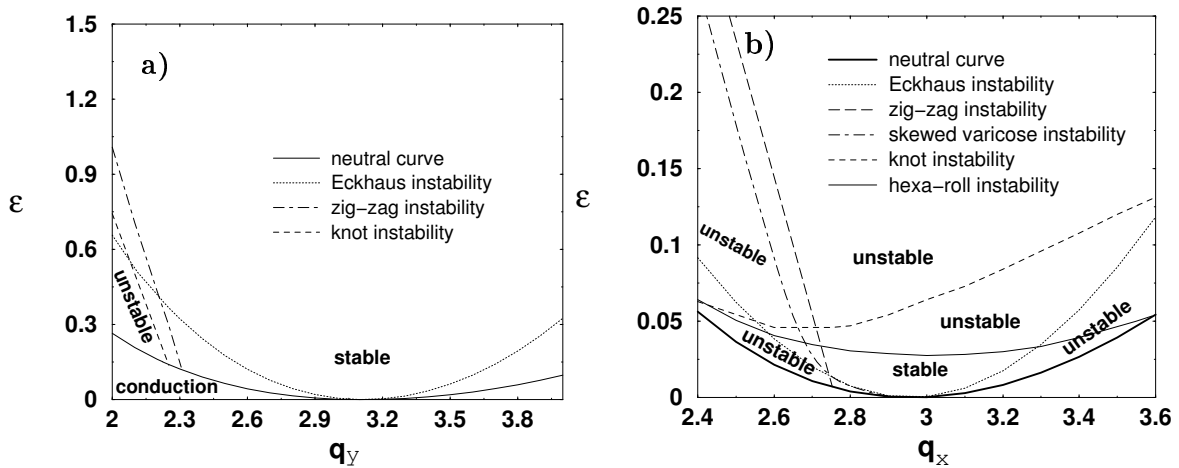


Figure 2.15: Stability diagram for zonal and axial rolls at  $\tau = 4, Q = 54$  (left), and  $\tau = 12, Q = 14$  (right), respectively, with  $P = 10$  in the  $\varepsilon - \tau$  plane.

Fig. 2.14).

For  $\tau < \tau_U$  the Floquet vector  $\mathbf{s}$  of the most destabilizing mode is essentially perpendicular to  $\mathbf{q}_c$  with a modulus  $|\mathbf{s}| \approx \frac{2}{3}|\mathbf{q}_c|$ . For  $Q = 14$ , the stability line joins smoothly the *SHV* bifurcation line at  $\tau = \tau_U$  (see also similar results for  $Q = 0$  in [24, 25], where  $|\mathbf{s}| \cong |\mathbf{q}|$  and the angle between  $\mathbf{s}$  and  $\mathbf{q}_c$  approaches  $60^\circ$ ). At even larger  $\tau$  a knot roll bifurcation prevails where  $\angle(\mathbf{s}, \mathbf{q}_c) = 90^\circ$  and  $|\mathbf{s}| \sim \frac{2}{3}q_c$ . For  $Q = 54$  the knot roll instability is dominant for all  $\tau > \tau_U$ . The instability mechanism and the bifurcating three-dimensional (3D) patterns will be discussed later in detail.

In Fig. 2.14 we have only addressed rolls with  $\mathbf{q} = \mathbf{q}_c$ . However, with increasing

$\varepsilon_o$  stable rolls with wave vector  $\mathbf{q} \neq \mathbf{q}_c$  must exist, which differ both in  $|\mathbf{q}|$  and  $\chi$  from the critical values. In Fig. 2.15a, longwave and shortwave instability lines near onset are given in the case of high magnetic field ( $Q = 54$ ) for zonal rolls ( $\tau = 4$ ), along the line  $\mathbf{q} = (0, q_y)$  in the  $\mathbf{q}$ -plane. Convection exists above the neutral curve  $R_0(\mathbf{q}) \approx \zeta^2(q_y - q_c)^2$  with its minimum at  $R_c = R_0(\mathbf{q}_c)$  i.e. at  $\varepsilon = \frac{R-R_c}{R_c} = 0$ . For  $q_y \neq q_c$  rolls are Eckhaus unstable for  $R_0(q_y) \leq R \leq 3R_0(q_y)$ . For  $q_y < q_c$  the rolls are in addition unstable below the long wavelength  $ZZ$  (zig-zag) instability line for sufficiently small  $q_y$ . In addition we find a short wavelength transverse instability line with  $|\mathbf{s}| \perp \mathbf{q}$ . Thus if one would fix  $q_y$  externally (e.g. by a temperature grid) the primary bifurcation would lead to oblique rolls. In Fig. 2.15b we show the stability diagram for axial rolls (large  $\tau$ ) along the line  $\mathbf{q} = (q_x, 0)$ . When exchanging  $q_y$  vs.  $q_x$  the discussion of Fig. 2.15a applies in principle. However, the stability diagram is in addition limited from above by SHV and knot - instability lines. At the small-  $q_x$  side mainly the  $ZZ$ - instability line restricts again the stability regime (note that in an axially anisotropic systems the  $ZZ$ -line does not start at  $q_x = q_c$ ).

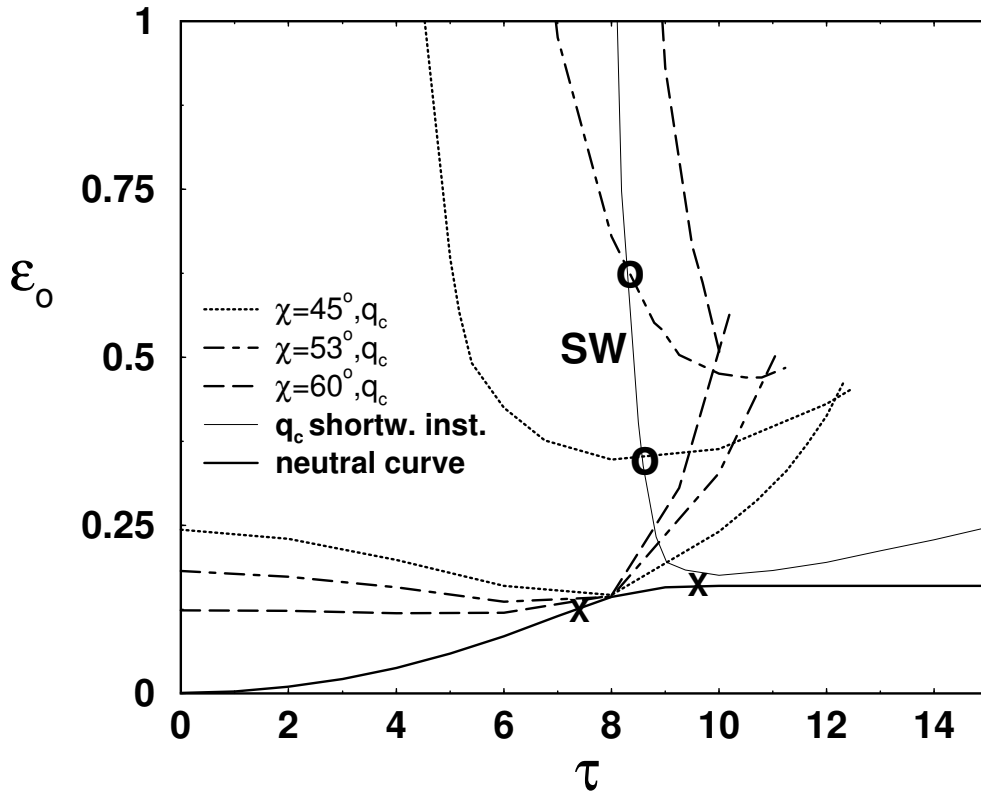


Figure 2.16: Stability regions of rolls with  $|\mathbf{q}| = |\mathbf{q}_c(\tau)|$  and different  $\chi$  at  $Q = 14$  and  $P = 10$ . The crosses denote the lower and upper Lifshitz points,  $\tau_L$ ,  $\tau_U$ , respectively. The circles mark crossing points of a shortwave instability line with the the SW line (see Fig. 2.14) at  $\tau = \bar{\tau}(\chi)$  for  $\chi = 45^\circ$ ,  $53^\circ$ , respectively (see text).

It is almost impossible to study the possible nonlinear stable patterns exhaustively

in the  $\mathbf{q} - \varepsilon$  space. In addition most of them will not be observed in standard experiments, where one would increase  $R$  slowly at fixed  $Q$ ,  $\tau$  or alternatively quench to a  $R > R_c$ . We will rather discuss some features, which are reflected in our simulations, when starting for instance from random initial conditions.

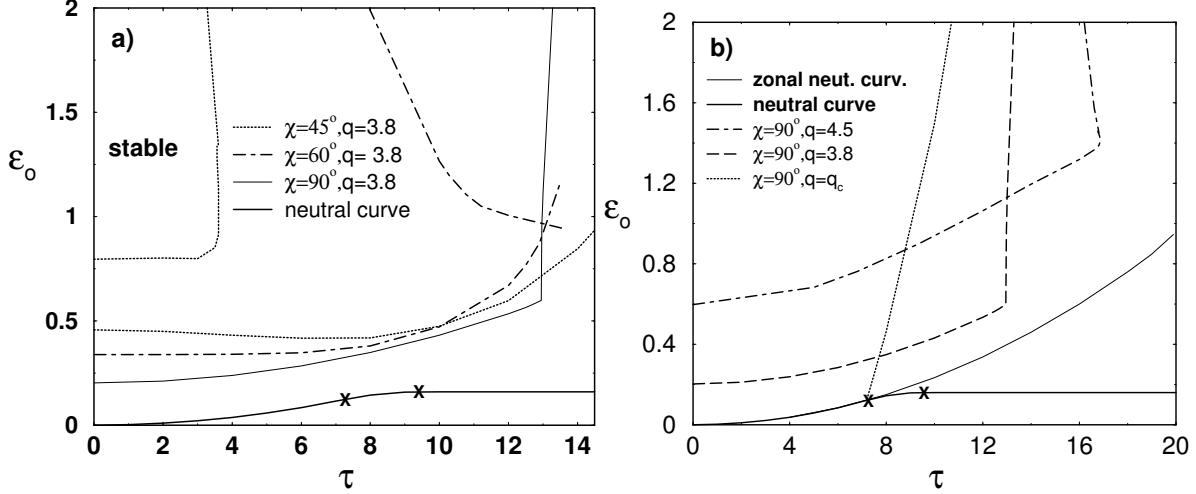


Figure 2.17: (a) The stability regions for various roll angles  $\chi$  as function of  $\tau$  at  $Q = 14$ ,  $P = 10$  and fixed  $q = 3.8$ . (b) The stability regions for zonal rolls  $\chi = 90^\circ$  for various values of  $q$  at  $Q = 14$ ,  $P = 10$ .

In Fig. 2.16 we show the stability regime of rolls for different roll angle  $\chi$  where  $|\mathbf{q}|$  was taken for simplicity as  $|\mathbf{q}_c(\tau)|$ . Let us at first focus on  $\chi_o = 45^\circ$ . The neutral curve (not shown) starts above  $\varepsilon_o = 0$  at  $\tau = 0$  and approaches from above the neutral curve in the oblique roll regime at a particular  $\bar{\tau}(\chi_o)$ , where the function  $\bar{\tau}(\chi)$  is defined by  $\chi_c(\bar{\tau}(\chi_c)) \equiv \chi_c$ . Stable  $45^\circ$ -rolls exist above a long wavelength instability line of the  $ZZ$ -type, which meets the neutral curve at  $\bar{\tau}(\chi_o)$  as well. This trend is obvious, since for instance any deviation from  $\chi = 90^\circ$  (zonal rolls) leads for small  $\varepsilon_o$  and  $\tau$  to long wavelength instabilities as discussed before. At larger  $\varepsilon_o$  the regime of stable  $45^\circ$  rolls is limited from above by a short wavelength instability line (dotted) with  $\angle(\mathbf{q}, \mathbf{s}) \approx 90^\circ$  and  $|\mathbf{s}| \approx \frac{2}{3}q_c$ . This line goes continuously down with increasing  $\tau$  and meets obviously the short wavelength instability line SW (see Fig. 2.14a) at  $\bar{\tau}(\chi_o)$ . Proceeding to larger  $\tau$  the lower  $ZZ$ -line is crossed as well at a certain  $\tau = \tau_{SZ}(45^\circ) \approx 11$  in Fig. 2.16. Thus  $45^\circ$ -rolls are stable in the beak-like regime between the two stability curves (dotted lines). Analogous stability diagrams can be constructed for any  $\chi$ . The upper short wavelength line moves to larger  $\varepsilon_o$  with increasing  $\chi$ , since  $\bar{\tau}(\chi)$  decreases with  $\chi$  and the crossings with the short wavelength SW line at  $\bar{\tau}(\chi)$  are shifted towards larger  $\varepsilon_o$ . In parallel the lower  $ZZ$ -line moves down, since one approaches the critical zonal rolls. Consequently the crossing of the two stability lines happens at smaller  $\tau = \bar{\tau}_{SZ}(\chi)$  and the wedge-like stability regime grows. Note that for  $\chi \geq 55^\circ$ , the  $\varepsilon_o$  crossing points of the upper shortwave instability line with the SW curve at  $\bar{\tau}(\chi)$  lie outside the graph.

Besides the angle  $\chi$  one can also vary the modulus of  $\mathbf{q}$ . We found that increasing  $|\mathbf{q}|$  would also enlarge the stability regime. This is shown in Fig. 2.17a. For  $|\mathbf{q}| = 3.8$  the  $45^\circ$ -rolls are long wavelength stable above the dotted line but unstable against shortwave instabilities except in the rectangular region at small  $\tau$ . The main result of these considerations is, that stable oblique rolls can be found in a large  $\tau$  interval in a certain  $\varepsilon_o$  range, irrespective of the critical  $\mathbf{q}_c(\tau)$ . In particular zonal rolls are good candidates to be present in a large  $\tau$  interval. In Fig. 2.17b we show that their stability region can be extended considerably towards larger  $\tau$  if  $|\mathbf{q}|$  is taken large enough. In fact for  $\chi = 60^\circ$ , and  $\chi = 90^\circ$  we obtain stable oblique rolls in  $\tau, \varepsilon_o$  regions considerably larger than those in Fig. 2.17a.

### 2.3.3 Stability diagrams of rolls at low $P$

In this section, it will be shown that the stability diagrams change qualitatively in the case of small  $P$ , though the neutral curve and thus the oblique roll regime do not depend on the Prandtl number  $P$  as already mentioned in Sec. 2.2.

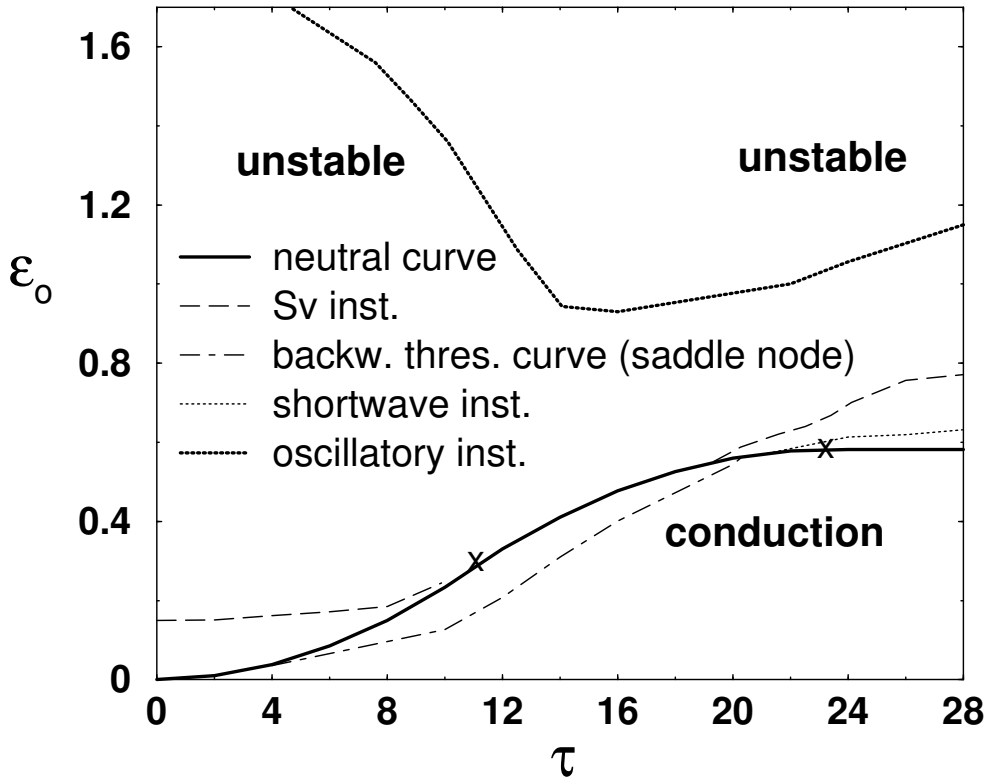


Figure 2.18: Stability diagram for rolls with critical wave vector  $\mathbf{q}_c$  as function of the Coriolis number  $\tau$  for increasing  $\varepsilon_o$  in the case  $Q = 54, P = 0.1$  (for the various stability lines see text).

A typical example is presented in Fig. 2.18 for  $P = 0.1$ . At first, the bifurcation becomes subcritical in a fairly large  $\tau$  interval ( $4 \leq \tau \leq 21$ ).

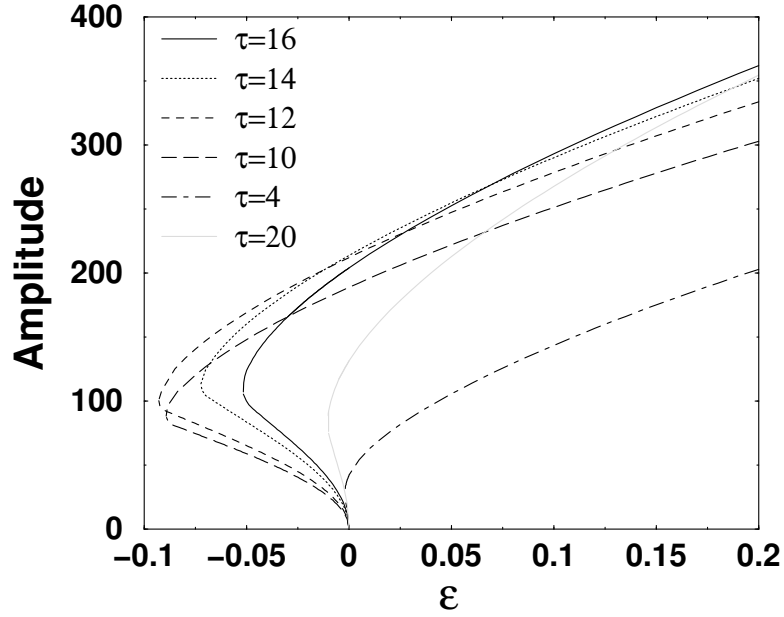


Figure 2.19: Saddle-node points of the subcritical bifurcation for  $P = 0.1$  for various  $\tau$  at  $Q = 54$  and  $\mathbf{q} = \mathbf{q}_c$ .

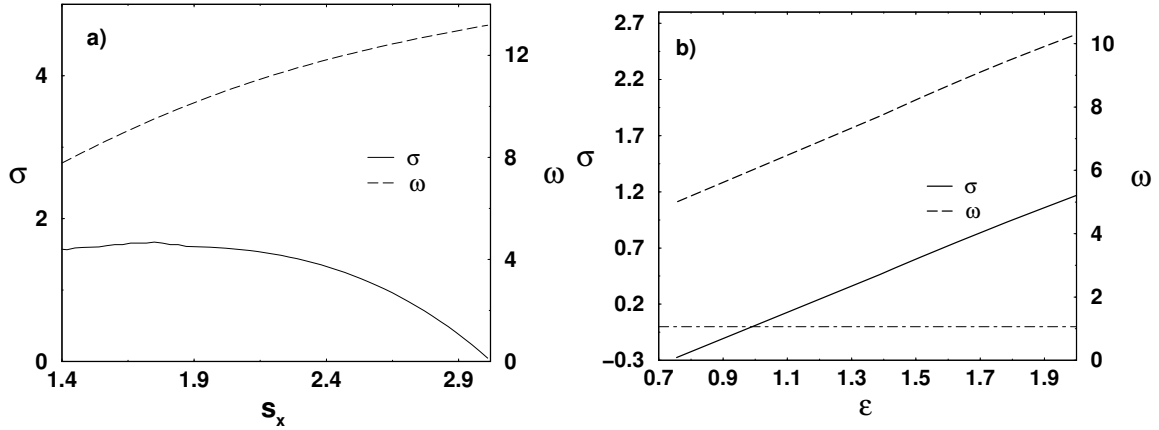


Figure 2.20: (a) Hopf bifurcation as function of the modulation wave number  $s_x$  (see text), at  $\varepsilon = 1.8$ ,  $q_c = 3.11$ ,  $\tau = 4$ ,  $Q = 54$  and  $P = 0.1$ . (b) Growth rates as function of  $\varepsilon$  for  $\tau = 26$ ,  $Q = 54$  and  $P = 0.1$ .

We have plotted a characteristic amplitude defined as the Fourier component  $\Theta(\mathbf{q}_c, z = \frac{1}{2})$  of the temperature field as function of  $\varepsilon$  for different  $\tau$  values in Fig. 2.19. According to Fig. 2.19, the smallest saddle-node point is found around  $\varepsilon \sim -0.098$  for  $\tau_{max} = 12$  where also the distance of the neutral curve and the saddle-node curve (dashed-dotted)

in Fig. 2.18 is maximal. The saddle-node and the neutral curve approach each other for increasing  $|\tau - \tau_{max}|$  and cross at a lower tricritical point ( $\tau \simeq 4$ ) and an upper tricritical point ( $\tau \simeq 21$ ).

The secondary bifurcations differ also qualitatively from the large  $P$  case, (Fig. 2.14). Near onset, the zonal rolls are mainly unstable against the skewed-varicose ( $Sv$ ) instability for  $\tau < 11$ , whereas the knot instability dominates at relatively high rotation rates  $\tau$ .

For sufficiently large  $\tau$  and  $\varepsilon_o$ , an oscillatory instability is important (see the thick-dotted line in Fig. 2.18). In Fig. 2.20 the growthrate  $\sigma$  and the corresponding Hopf frequency  $\omega$  are shown for two cases. The Floquet vector  $\mathbf{s}$  is perpendicular to  $\mathbf{q}$  and of the order  $\frac{2}{3}q_c$ . In Fig. 2.20a,  $\sigma$  and  $\omega$  are plotted as function of  $\mathbf{s}$  ( $= (s_x, 0)$ ).  $\sigma$  has a very shallow maximum for  $s_x \equiv 1.8$ . The growthrate as function of  $\varepsilon$  for the specific parameter set,  $\tau = 26$ ,  $Q = 54$  at the maximal Floquet vector is seen in Fig. 2.20b. The values of  $\sigma$  increase linearly as function of  $\varepsilon$  and change sign around  $\varepsilon = 1$  consistent with Fig. 2.18. Comparing Figs. 2.20b and 2.20a, we conclude that  $\Im(\sigma) = \omega$  is of the order of 10 even for relatively high rotation rates  $\tau$ . The exploration of the stability region in the  $\tau - \varepsilon$  plane for arbitrary  $\mathbf{q}$ ,  $\chi$  is even more tedious than in the large  $P$ - case, because of the backward bifurcation. So, we have limited ourselves to some examples.

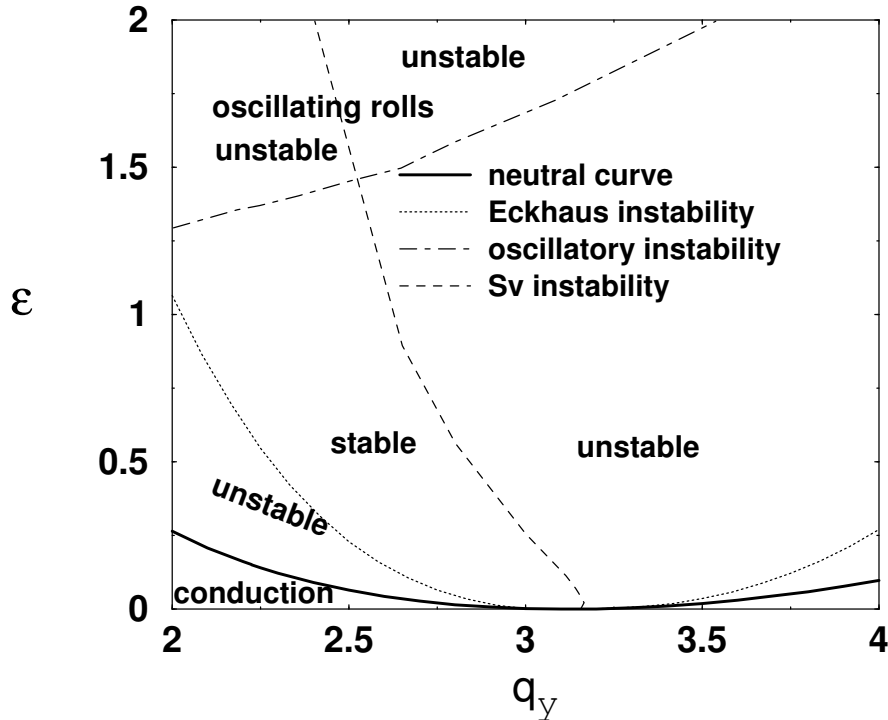


Figure 2.21: Stability diagram for zonal rolls for  $q_y$  near onset at  $\tau = 4$ ,  $Q = 54$  and  $P = 0.1$ .

In Fig. 2.21, longwave and shortwave instability lines are given for zonal rolls at

$P = 0.1$  in the  $q - \varepsilon$  plane. In contrast to the high Prandtl number case, the  $Sv$  instability plays an important role by restricting the stable region from above for fairly small  $\varepsilon_o$  at  $q_y < q_c$ . The Eckhaus instability characterizes the lower boundary of the stable region similar to the earlier stability diagrams in Fig. 2.14 and prevails for  $q_y > q_c$  as in standard  $RBC$ . For  $q_y < q_c$  the rolls are unstable below the  $ZZ$  (zig-zag) instability line as in the axial roll regime for high  $q_y$  (see in Fig. 2.15). In contrast to the axial roll case, zonal rolls are found to be stable against the  $SHV$  instability, but one meets the knot instability for smaller  $q_y$  values.

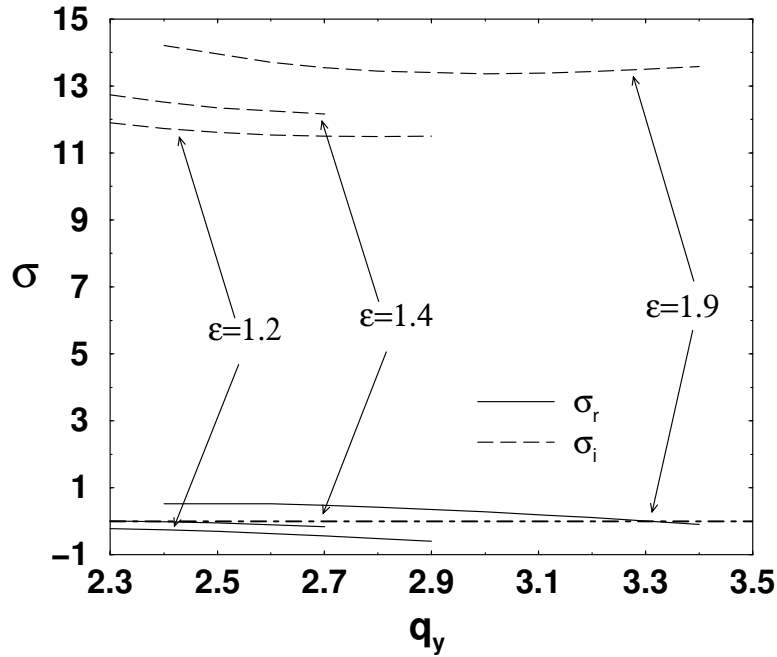


Figure 2.22: Oscillatory instability as function of zonal rolls  $\mathbf{q} = (0, q_y)$  for various  $\varepsilon$  values. Same parameters with Fig. 2.21. (Dashed-dotted line corresponds to  $\sigma = 0$ )

In Fig. 2.22, the leading eigenvalue  $\lambda = \sigma + i\omega$  of the oscillatory instability, which is already described in Fig. 2.21 for large  $\tau$ , is plotted as function of  $q_y$  for several  $\varepsilon$  values. According to Fig. 2.22, the growthrate  $\sigma$  and the Hopf frequency  $\omega$  for all  $q_y$  depend on the wave number quadratically at small  $q_y$ . For  $\varepsilon = 1.2$ , the zonal rolls are stable since  $\sigma < 0$ . With increasing  $\varepsilon$ , the oscillatory instability occurs for  $q_y < q_c$  at  $\varepsilon = 1.4$ . This behavior can also be seen in Fig. 2.21 for  $\varepsilon = 1.4$ . At  $\varepsilon = 1.9$ , the growthrates  $\sigma$  are already positive up to the wave number  $q_y = 3.4$ . Note also that the Hopf frequencies  $\omega$  increase with  $\varepsilon$ .

In the following parts of thesis, the results on the instabilities will be addressed in detail by direct simulations. In Sec. 2.5, the study of the stability of rolls by the Galerkin method has been complemented by the direct simulation method. In Sec. 2.4, we will present the simulation results of the subharmonic varicose ( $SHV$ ) and knot instabilities.

## 2.4 Subharmonic Varicose (*SHV*) and Knot Patterns

In this chapter, we present a rather detailed analysis of the characteristic secondary shortwave instabilities of axial and oblique rolls at larger  $\tau$ , which have been for instance marked as *SW* in Fig. 2.14. It will turn out that the instabilities are driven through particular resonant interactions among several modes, which have been explained already in Sec. 1.4. Particular emphasis will be laid on two special cases, namely the *SHV* and the knot destabilizations. The corresponding modes have been indicated in Fig. 1.3. The detailed discussions can be found in App. A. In Fig. 2.23 the *SW* line for  $\tau > \tau_U$  in Fig. 2.14 is plotted on a larger scale. In fact the nature of the instability changes with increasing  $\tau$ . At first *SHV* instability line prevails, which starts around  $\varepsilon = 0.0108$  at  $\tau = 10$  to increase almost linearly with  $\tau$ . At  $\tau = 18.5$  the knot instability line is crossed, which determines the *SW* instability for larger  $\tau$ . The solid line results from a rigorous Galerkin stability analysis of the axial rolls. The circles have been calculated with the help of the weakly nonlinear analysis according to Eq. (A.26) and Eq. (A.37), respectively. Whereas the *SHV* line is reproduced with high accuracy even at larger  $\varepsilon$ , the weakly nonlinear analysis of the knot bifurcation becomes less satisfactory when  $\tau$  increases.

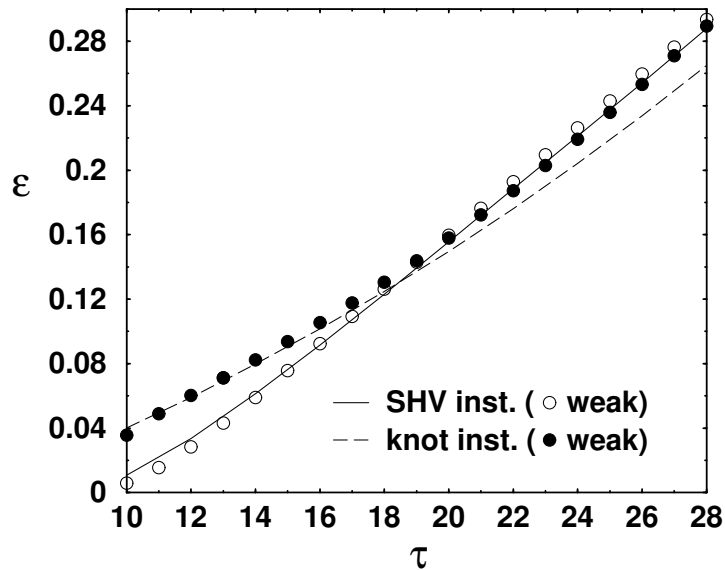


Figure 2.23: The onset of *SHV* and knot instabilities as function of  $\tau$  in the case  $Q = 14$ ,  $P = 10$ ,  $\mathbf{q} = \mathbf{q}_{xc} = 2.958$ .

In the following sections we will discuss the *SHV* and knot destabilizations and the resulting patterns in more detail. Though the methodology is the same as for rolls, the ensuing book-keeping problems seem to have discouraged other researchers in the past. The Galerkin analysis is backed up and extended by the direct numerical solutions of

the full hydrodynamic equations, which allow to cover also complex spatio- temporal patterns, which result from higher bifurcations.

### 2.4.1 General shortwave destabilizations

In Sec. 1.4 we have addressed various resonant shortwave destabilization mechanisms of rolls. In the oblique roll regime, the most general situation shown in Fig. 1.2 becomes important, where  $\mathbf{q}_1$  is given as  $\mathbf{q}_c = q_c (\cos(\chi_c), \sin(\chi_c)) = (q_x, q_y)$ . In the following we revisit as a representative example the case  $P = 10, Q = 54$  (see the general stability diagram in Fig. 2.14b). With increasing  $\tau$  we move along the neutral curve from zonal via oblique to axial rolls, where  $q_c, \chi_c$  as function of  $\tau$  are plotted in Fig. 2.24. The Lifshitz points ( $\tau_L = 10.6, \tau_U = 23.2$ ) are seen clearly. Along the oblique region,  $q_c$  and  $\chi_c$  decrease with  $\tau$ .

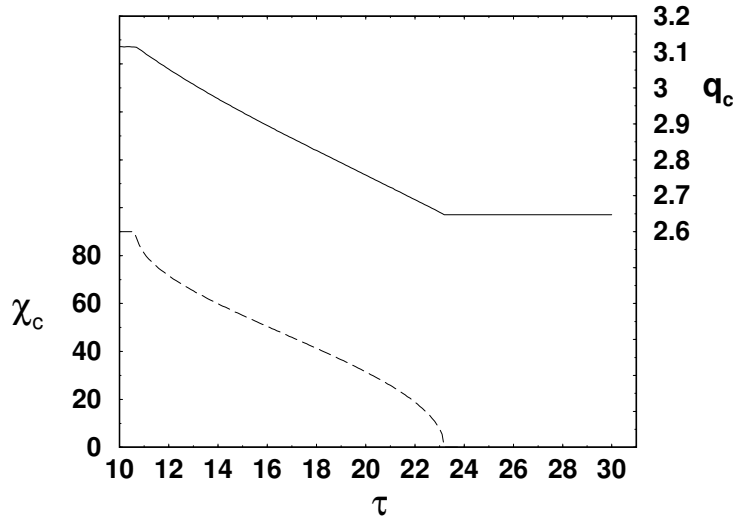


Figure 2.24: Critical roll angle  $\chi_c$  and  $|\mathbf{q}_c|$  as function of  $\tau$  for  $Q = 54, Pr = 10$ .

According to Fig. 2.25a the knot instability prevails for  $\tau > \tau_U$  where the shortwave modulation  $\mathbf{s}$  includes an angle  $\psi = 90^\circ$  with  $\mathbf{q}_c$ . The *SHV* line ( $\psi = \angle(\mathbf{s}, \mathbf{q}) \approx 60^\circ$ ) and  $|\mathbf{s}| = |\mathbf{q}|$  lies above. Below  $\tau = \tau_U$  the two lines bend upwards. However, the stability regime is limited from above by the *SW* line below associated in general with angles  $\psi \neq 60^\circ, 90^\circ$ . According to Fig. 2.25b the angle  $\psi$  decreases with decreasing  $\tau$  until  $\psi = 60^\circ$ , where we observe a sudden jump to  $\psi = 120^\circ$  (equivalent to  $\psi = -60^\circ$ ). At this point we have  $\chi_c = 23.3^\circ$ . This situation corresponds to a (generalized) hexaroll destabilization with  $|\mathbf{s}| = q_c/2$ . Since  $\mathbf{q}$  is at an finite angle with respect to the preferred  $\tau$  axis, the angles  $\pm\psi$  are no more equivalent (which implies for the corresponding amplitudes  $|B| \neq |C|$ ). The case  $\psi = 60^\circ$  is obviously realized where the continuation of the *SHV* from larger  $\tau$  and the *SW* line meet at  $\tau = 21.3$  in Fig. 2.25a. With decreasing  $\tau$ , the  $\psi(\tau)$  curve decreases monotonously, too. When  $\psi = 90^\circ$  is reached at about  $\tau = 17$  we have a generalized knot instability, which is also reflected in the

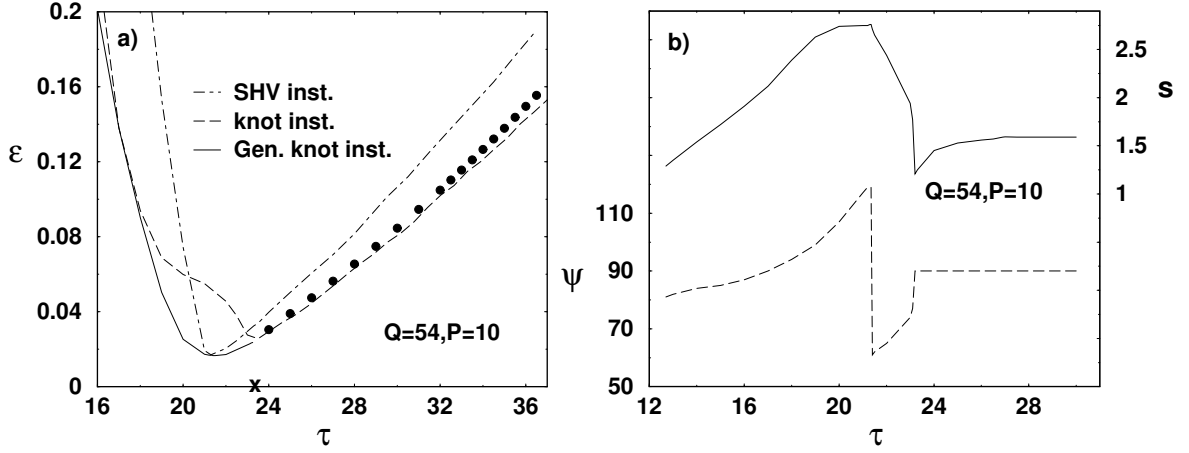


Figure 2.25: (a) *SW* stability of rolls for  $\mathbf{q} = \mathbf{q}_c$  (oblique for  $\tau \leq \tau_U = 23.2$ , axial for  $\tau \geq \tau_U$ ) with  $\mathbf{q} = \mathbf{q}_c$  for  $Q = 54$  in the  $\tau, \varepsilon$  plane. For comparison the lines for fixed angles  $\psi = 90^\circ, 60^\circ$ , respectively, are shown with  $\psi = \angle(\mathbf{q}_c, \mathbf{s})$ . Notes denote the result of weakly nonlinear analysis in the case of knot instability. (b) The modulus of  $\mathbf{s}$  and the angle  $\psi$  along the *SW* line (for details see text).

touching of the *SW* and the knot line in Fig. 2.25a. At this point the roll angle is given as  $\chi_c = 45.9^\circ$ .

It is obvious that the knot and the *SHV* patterns are strictly periodic in the plane, since their Fourier module (for details see [30, 31]) consists of integer combinations of two basis vectors. In the *SHV* case, a period doubling along the  $\mathbf{q}$  direction is involved. The more general resonant patterns as presented in Fig. 1.2 in Fourier space are quasiperiodic, since their Fourier module contains in general three incommensurate basis vectors (e.g.  $\mathbf{q}_1, \mathbf{q}_6$  and  $\mathbf{q}_4$ ). In the following we will focus on the short wavelength destabilizations of axial rolls for high Coriolis numbers  $\tau$  above the upper Lifshitz point  $\tau_U$ .

## 2.4.2 Subharmonic varicose patterns

In this section, we discuss the *SHV* patterns in the axial roll regime, the mode-structure (see Fig. 1.3) is discussed in App. A. Consistent with the Galerkin solutions and direct numerical simulations, two dimensional (*2D*) *SHV* patterns  $f(x, y)$  which describe for instance the temperature field at the midplane of the fluid layer can be reconstructed from the amplitudes  $A, B, D$  in the following manner:

$$\begin{aligned}
 f(x, y) = & \Re \left( A \exp [iq_x x] + B (\exp [-i\frac{q_x}{2}x + iq_y y] - i \exp [-i\frac{q_x}{2}x - iq_y y]) \right. \\
 & \left. + D (\exp [i\frac{3q_x}{2}x + iq_y y] - i \exp [i\frac{3q_x}{2}x - iq_y y]) \right) \quad (2.19)
 \end{aligned}$$

or

$$\begin{aligned}
 f(x, y) = & A \cos(q_x x) - 2 \left( B \cos\left(\frac{q_x}{2}x + \frac{\pi}{4}\right) \right. \\
 & \left. + D \cos\left(\frac{3q_x}{2}x + \frac{\pi}{4}\right) \right) \sin(q_y y - \frac{\pi}{4})
 \end{aligned}
 \tag{2.20}$$

Note that we have included the phases of the amplitudes according to Eq. (A.19).

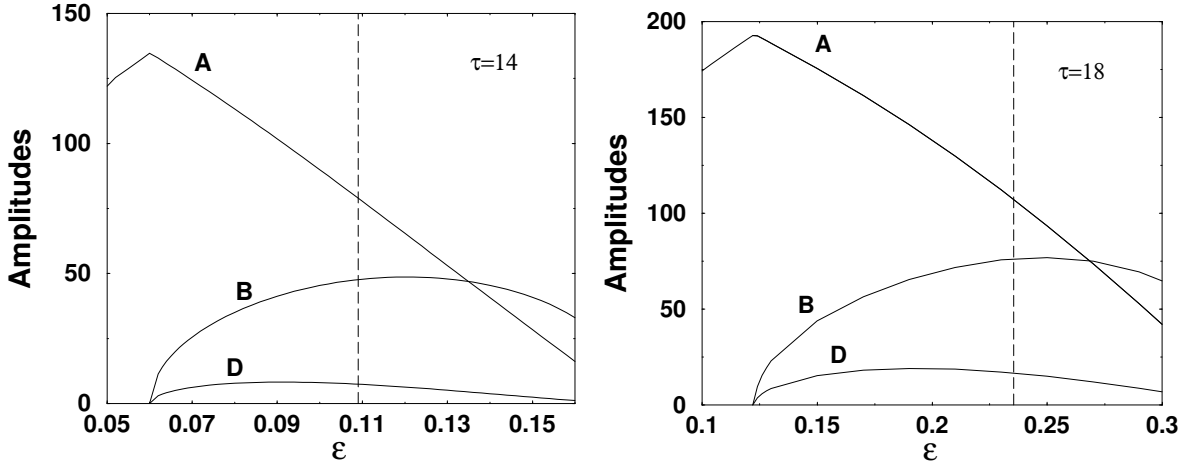


Figure 2.26: Amplitudes  $A$ ,  $B$ ,  $D$  for *SHV* patterns (Eq. 2.20) as function of  $\epsilon$  for  $\tau = 14$  (left panel),  $\tau = 18$  (right panel) in the case  $Q = 14$ ,  $P = 10$ . The dashed lines denote the oscillatory instability of the *SHV* patterns.

Historically, the *SHV* destabilization mechanism has been detected at first in the rotating annulus problem for  $Q = 0$  [25] and analyzed in a nice and clever way by concentrating on the modes  $A$ ,  $B$ . In the limit  $\tau \rightarrow 0$  the mode  $D$  is not important. For finite  $Q$ , the *SHV* instability is shifted to finite  $\tau$  values. The weakly nonlinear analysis can be considerably refined by the explicit inclusion of  $D$ . In addition, as explained in App. A.1 appropriate projection techniques have to be used when calculating the coefficients  $A$ ,  $B$ ,  $D$  in Eq. (2.19) by the amplitude equations in App. A.1.

We will concentrate here on typical examples for the parameters  $Q = 14$ ,  $P = 10$ , where the *SHV* and knot instabilities have been already shown in Fig. 2.23. In Fig. 2.26, we have plotted the amplitudes  $A$ ,  $B$ ,  $D$  for different  $\tau$  values below the crossover to the knot instability ( $\tau = 18.5$ ) and in Fig. 2.27 for  $\tau$  values above the crossover. The modes  $B$ ,  $D$  bifurcate at  $\epsilon = \epsilon_{SV}$ , where  $\epsilon_{SV}$  increases with  $\tau$  in line with Fig. 2.23. Figs. 2.26, 2.27 confirm the general expectation that the amplitude  $A$  of the axial rolls decreases above the *SHV* destabilization while the amplitudes  $B$ ,  $D$  grow supercritically like  $\sim \sqrt{(\epsilon - \epsilon_{SV})}$  in agreement with our general analysis (see App. A.1). It is also evident, that the relative importance of the mode  $D$  grows with increasing  $\tau$ . In addition, the  $\mathbf{q}$ -vector of the mode  $B$ , which we will parameterize as  $\mathbf{q} = \frac{q_x}{2}(1, p_{SV})$  deviates more and more from the ideal hexaroll case ( $p_{SV} = p_{hex} = \sqrt{3}$ ) which is for

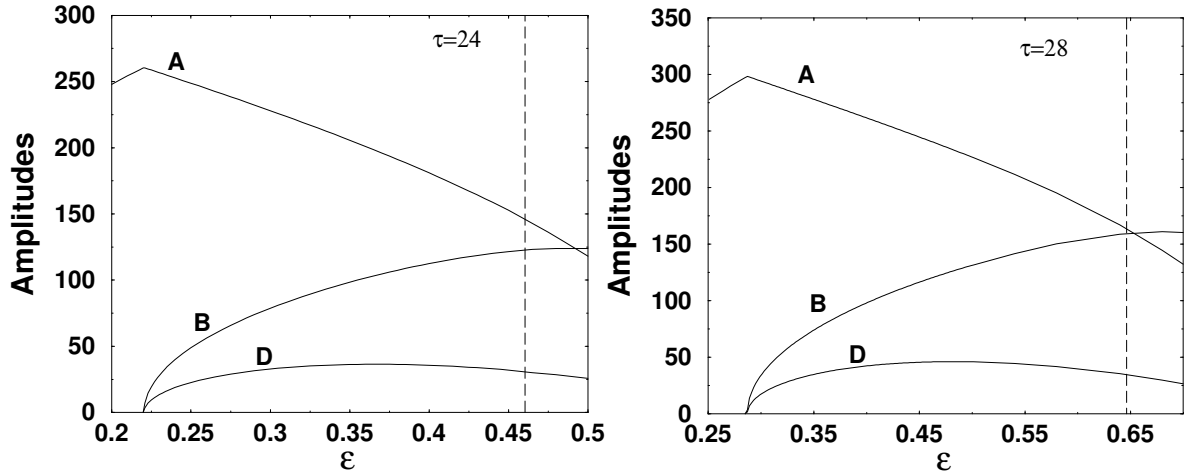


Figure 2.27: Amplitudes  $A$ ,  $B$ ,  $D$  for  $SHV$  patterns (Eq. 2.19) as function of  $\varepsilon$  for  $\tau = 24$  (left panel),  $\tau = 28$  (right panel) in the case  $Q = 14$ ,  $P = 10$ . The dashed lines denote the oscillatory destabilization of the  $SHV$  patterns (from Galerkin analysis).

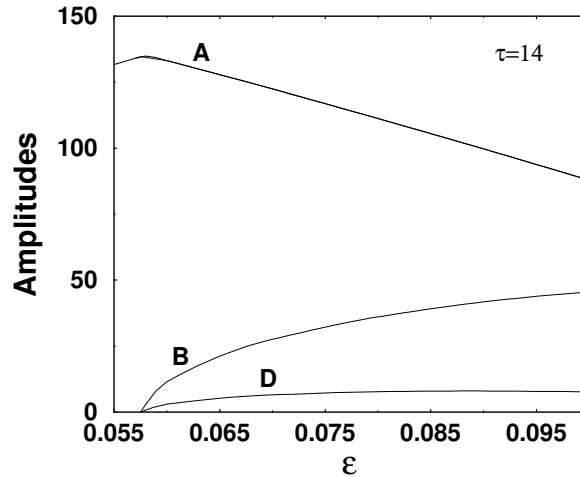


Figure 2.28: Amplitudes  $A$ ,  $B$ ,  $D$  of  $SHV$  patterns from direct simulation as function of  $\varepsilon$  for  $Q = 14$ ,  $\tau = 14$ ,  $P = 10$ .

instance realized for  $Q = 0$  and small  $\tau$ . We found the values  $p_{SV} = a p_{hex}$  with  $a = 0.96, 0.9, 0.81, 0.76$  for  $\tau = 14, 18, 24, 28$ , respectively. Note that in all discussions of amplitudes, we consider only the natural case  $q_x = q_c = 2.95$  and  $q_y = p_{SV}$  in Eq. (2.19).

According to our Galerkin stability analysis the resulting  $SHV$  patterns are stable against long wavelength modulations in the whole  $\varepsilon$  range covered in the Figs. 2.26, 2.27. However we found oscillatory amplitude instabilities at  $\varepsilon = \varepsilon_{osc}$  which have been marked by the vertical dashed lines in these figures. For  $\tau = 14, 18, 24, 28$ , we

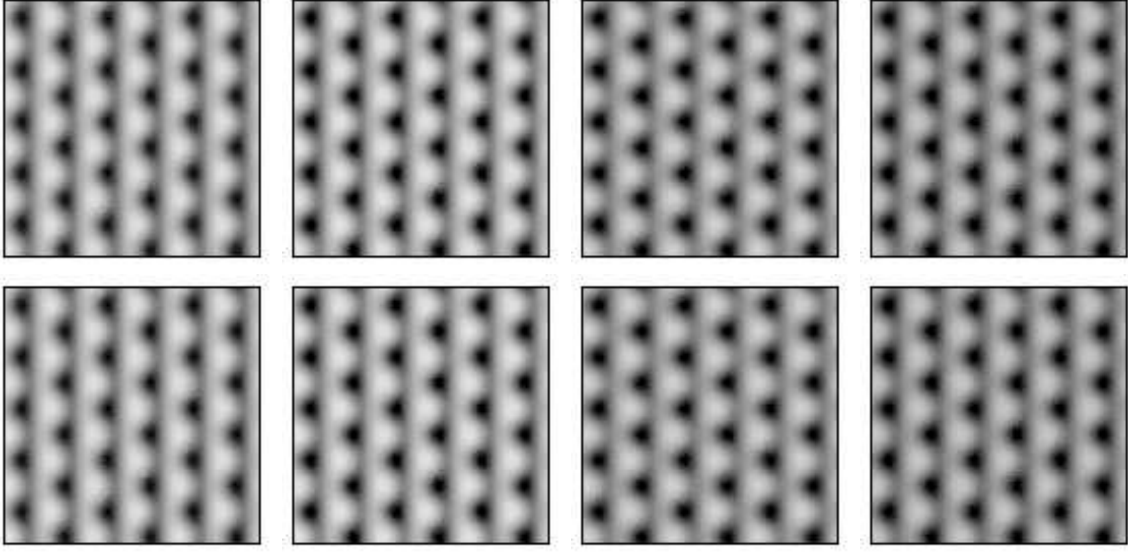


Figure 2.29: Oscillatory *SHV* patterns at  $\tau = 14$ ,  $Q = 14$ ,  $\varepsilon = 0.1095$ . The teeth in patterns oscillate in horizontal direction with small amplitude. The plots from left to right correspond to times  $t = 10, 11, 12, 13, 14, 15, 16, 17$ . The aspect ratio is  $\Gamma = 12$ .

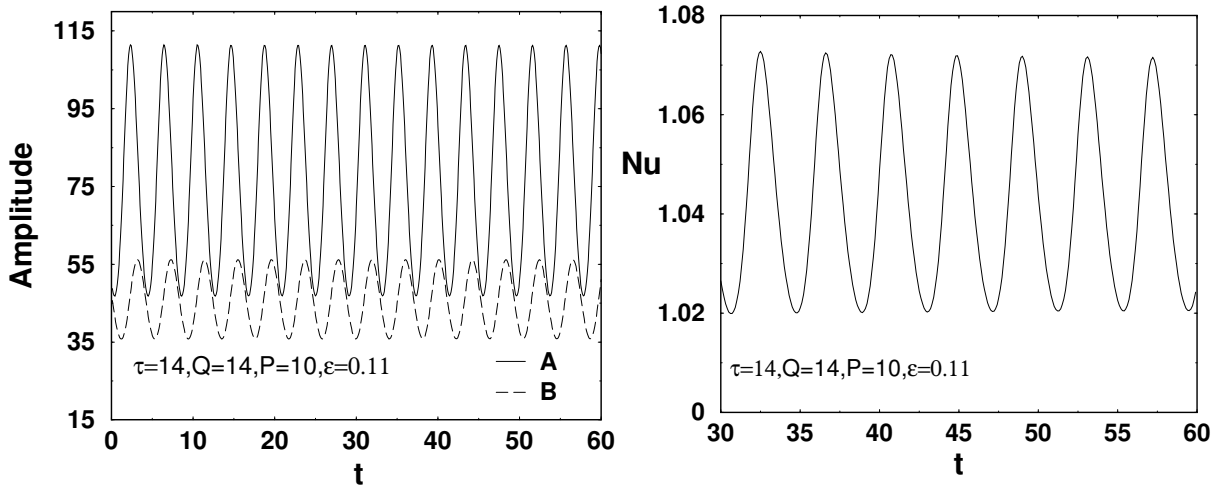


Figure 2.30: The *SHV* amplitudes  $A, B$  (see Eq. 2.20) mode for  $\varepsilon > \varepsilon_{osc}$  as function of time (in  $t_v$ ) from a simulation at  $\varepsilon = 0.11$ ,  $Q = 14$ ,  $\tau = 14$  and  $P = 10$  (left panel) and the corresponding Nusselt number (right panel).

have obtained the following Hopf frequencies  $\omega_{SV} = 1.6, 2.4, 4, 6$ , respectively. The oscillatory instability will lead to time dependent patterns, where in the simplest case the amplitudes  $A, B, D$  oscillate about some constant values.

We will not discuss these instabilities in detail, for instance by following the previous interesting analysis based on amplitude equations for small  $\tau$  at  $Q = 0$  [25]. Instead we

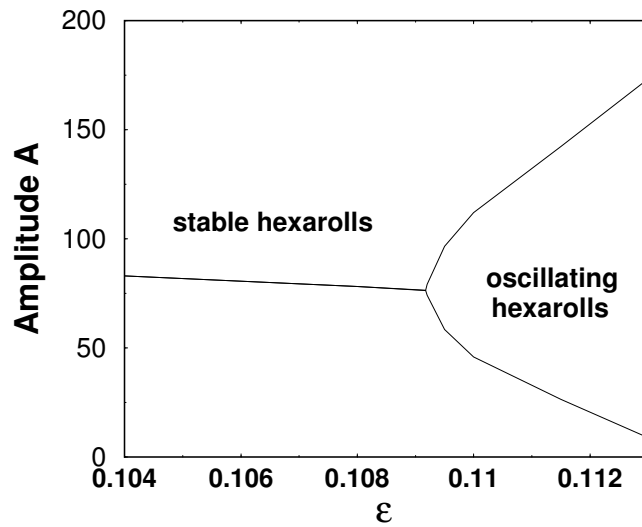


Figure 2.31: Maxima and minima of the oscillating *SHV* amplitude  $A$  as function of  $\varepsilon$  at  $\tau = 14$ ,  $Q = 14$ ,  $P = 10$ .

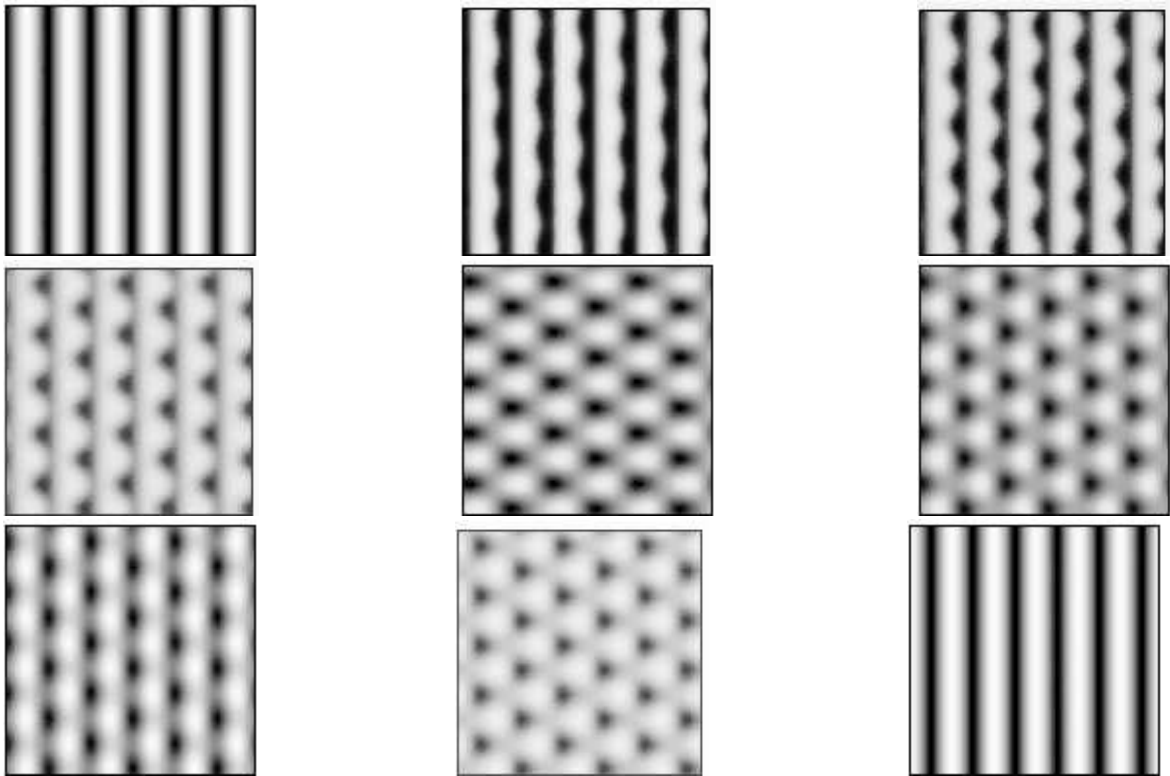


Figure 2.32: Heteroclinic cycle for the axial regime.  $\tau = 14$ ,  $Q = 14$ ,  $\varepsilon = 0.114$  and  $P = 10$ . The plots from left to right correspond to times  $t = 33, 36.2, 36.5, 36.9, 37.2, 37.4, 37.6, 38$  and  $40.5$ . The aspect ratio is  $\Gamma = 12$ .

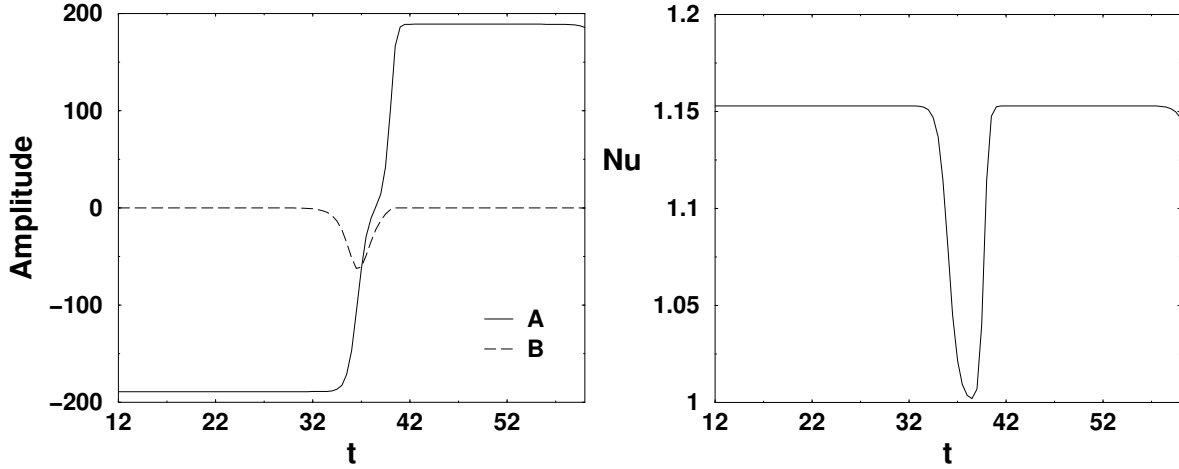


Figure 2.33: Amplitudes (left) and  $Nu$  (right) in the case of the heteroclinic cycle at the same simulation as in Fig. 2.32 ( $\varepsilon = 0.114$ ).

present typical results of full simulations, which have been consistent in all cases with the Galerkin analysis. Typically we start from random initial conditions in the *SHV* unstable regime. For instance, the amplitudes extracted from a simulation at small  $\varepsilon < \varepsilon_{osc}$  which have been plotted in Fig. 2.28 fit perfectly the previous Galerkin result (Fig. 2.26) for the same parameter set (i.e for  $\tau = 14$ ,  $Q = 14$ ,  $P = 10$ ).

Slightly above the oscillatory instability of the *SHV* pattern at  $\varepsilon = 0.1092$  (see Fig. 2.26) we observe, in fact, periodic *SHV* states in a small  $\varepsilon$  range ( $\varepsilon \leq 0.113$ ). In Fig. 2.29, we show a corresponding time sequence of the patterns. However the time dependence of the patterns is not strongly expressed. In any case the subharmonic contribution of the mode  $B$  is easily visible, since the *teeth* attached to the axial rolls repeat every second line. Better insight to the pattern is obtained from the time periodic amplitudes  $A, B, D$  which are constructed according to Eq. (2.19) and plotted in Fig. 2.30. The period agrees perfectly with the Hopf frequency at  $\varepsilon = \varepsilon_{osc}$ .

In Fig. 2.30, we have followed the amplitude  $A$  for  $\varepsilon$  in the vicinity of  $\varepsilon_{osc}$  (see also the vertical line in Fig. 2.26). For  $\varepsilon \leq \varepsilon_{osc}$  the amplitude is constant (already shown in Fig. 2.26). For  $\varepsilon > \varepsilon_{osc}$ ,  $A$  oscillates between a maximal and a minimal value (see Fig. 2.30). These extrema are plotted in Fig. 2.31 to visualize the pitchfork bifurcation at  $\varepsilon = \varepsilon_{osc}$ .

However, for even slightly increasing  $\varepsilon$ , the destabilization of the oscillatory *SHV* pattern is revealed. In Fig. 2.32 we show typical snapshots from our simulations. At first, we see an axial roll pattern (left upper corner), with increasing time (from left to right) contributions of the amplitude  $B$  are activated, which grows at the expense of  $A$  until  $B$  dominates the dynamics. At later times  $A$  starts growing again and one returns to the axial roll state (lower right corner), which is shifted by half a wavelength perpendicular to the roll axis. The time dependence involves abrupt changes in the amplitude which are evident in Fig. 2.33, where the amplitudes  $A$  and  $B$  are shown

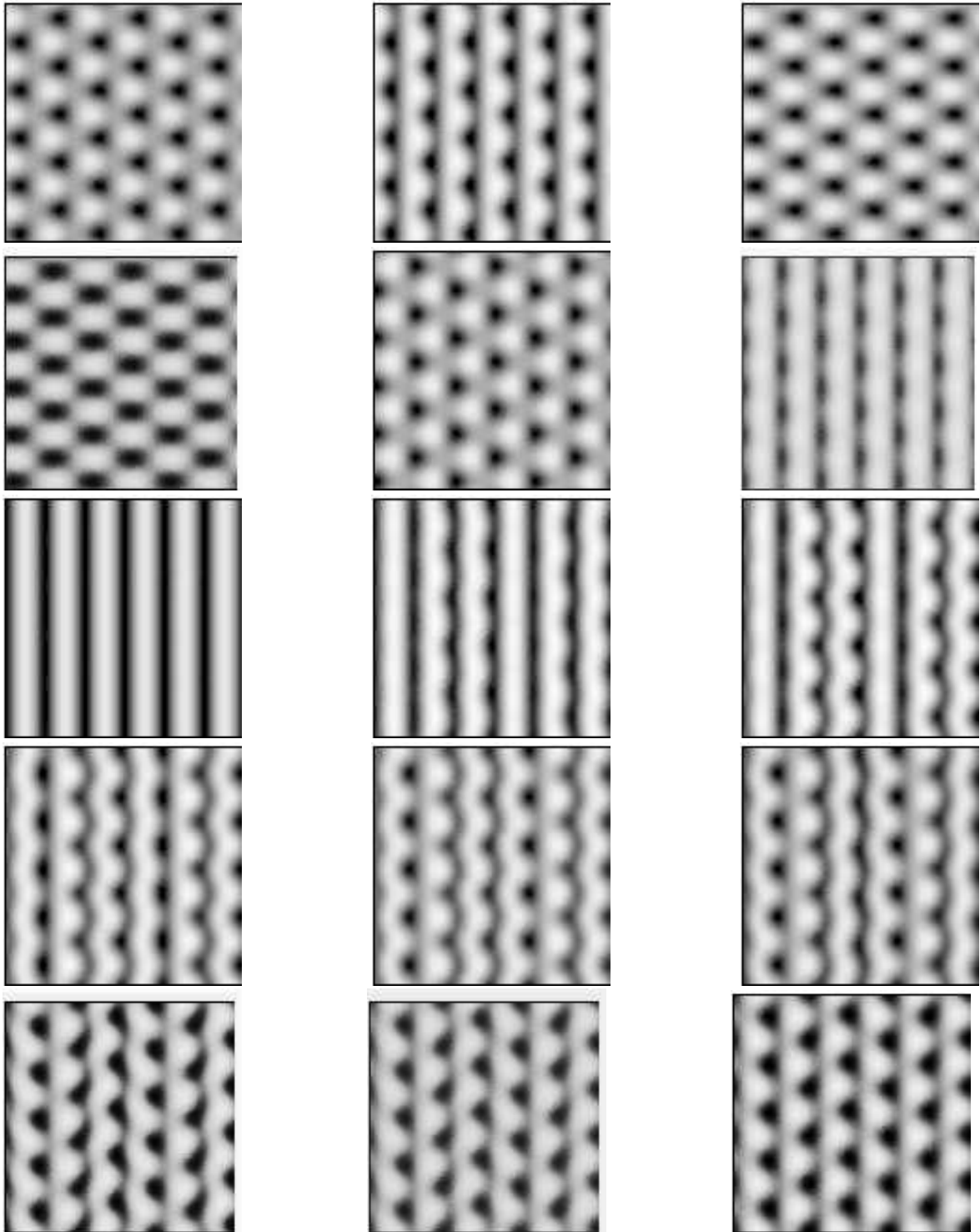


Figure 2.34: Heteroclinic cycle in the co-existence region of  $SHV$  and knot instabilities at  $\tau = 14$ ,  $Q = 14$ ,  $\varepsilon = 0.115$  and  $P = 10$ . The plots from left to right correspond to times  $t = 111, 111.5, 111.9, 112, 112.1, 112.2, 112.4, 113.7, 114, 115.7, 116, 118, 118.5, 119, 119.7$ . The aspect ratio is  $\Gamma = 12$ .

together with the Nusselt number. The  $\pi$  phase shift between the pure roll patterns ( $B = 0$ ) (see also the first and last panel in Fig. 2.32) is obvious. During a relatively short time interval (about  $t \approx 37$ ) the  $B$  mode dominates (see the fourth and fifth panel in Fig. 2.32). Such a scenario is typical for a *heteroclinic* orbit, which describes in general a situation where different attractors ( $A, B$  in our case) are regularly visited by a system. Heteroclinic cycles have been studied in earlier studies of Busse and co-workers for the non-magnetic case [25, 32].

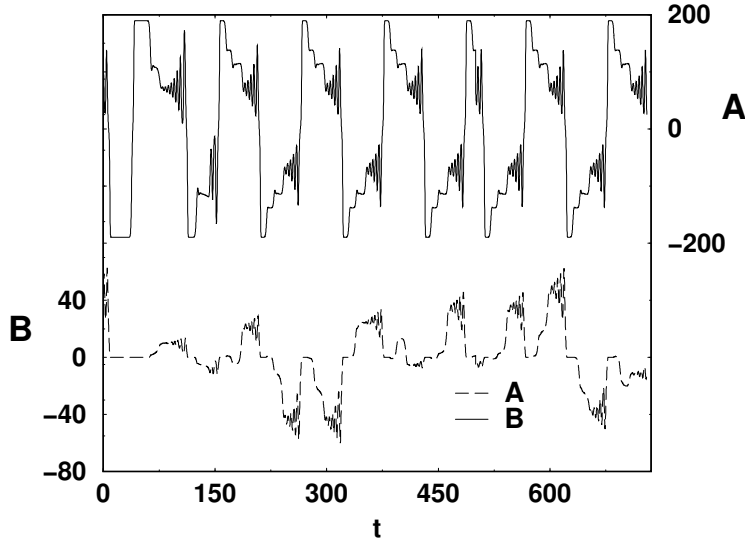


Figure 2.35: Leading two amplitudes as function of time for *SHV* for the same parameters as in Fig. 2.34.

The time evolution of the patterns depends sensitively on  $\varepsilon$ , which becomes obvious when we compare Fig. 2.34 for  $\varepsilon = 0.115$  with Fig. 2.32 for  $\varepsilon = 0.114$ . We have observed a kind of mixture of rolls, *SHV* and knot patterns (see third and fourth row in Fig. 2.34). In the knot pattern (see the following section) the *teeth* of neighboring rolls match in contrast to *SHV* patterns. It is not surprising that knot patterns come into play, since the knot instability of axial rolls is at  $\varepsilon = 0.0798$  for  $\tau = 14$  and  $Q = 14$ . In Fig. 2.35, we have plotted the amplitudes  $A, B$  of Fig. 2.34. In particular the curve for  $A$  reveals an approximate time periodicity.

### 2.4.3 Knot instability

In this section, we will present an analysis of knot patterns, which bifurcate at  $\varepsilon = \varepsilon_{kn}$  from axial rolls. The analysis is based on Galerkin methods and full simulations. In Fig. 2.23 we see that the knot destabilization line  $\varepsilon_{kn}(\tau)$  is near the *SHV* line for  $Q = 14, P = 10$  in the whole interval  $10 < \tau < 28$ .

According to Fig. 1.3 and Eq. (A.31), 2D knot patterns have the following repre-

sensation (for details we refer to App. A.2):

$$f(x, y) = \Re \left( A \exp [iq_x x] + D (\exp [iq_x x + iq_y y] - \exp [iq_x x - iq_y y]) - i F \exp [iq_y y] \right), \quad (2.21)$$

or

$$f(x, y) = A \cos (q_x x) - 2D \sin (q_x x) \sin (q_y y) + F \sin (q_y y). \quad (2.22)$$

In our system we find  $D > F$ . The case  $F = 0$  describes the wavy instability, which corresponds for small  $D$  to a phase modulation of the axial rolls. This is evident from the following Taylor expansion

$$\begin{aligned} f(x, y) &= A \cos (q_x x) + \frac{2D}{A} \sin (q_y y) \\ &= A \cos (q_x x) - 2D \sin (q_x x) \sin (q_y y) + O\left((D/A)^2\right). \end{aligned} \quad (2.23)$$

The opposite case  $D = 0$ ,  $F \neq 0$  corresponds to a standard knot instability ( $q_x \neq q_y$ ). For  $Q = 0$  and in the limit  $\tau = 0$ , one finds the special case of the cross-roll *CR* instability ( $q_x = q_y$ ) [24, 25]. For historical reasons we keep the notion *knot* instability in our situation for  $D \neq 0$ ,  $F \neq 0$ . Note that our description in terms of three coupled amplitude equations allows to fix the phases involved in the representation Eq. (2.21), which is not possible when the wavy mode ( $D$ ) is neglected. In Fig. 2.36, we show typical knot patterns obtained from simulations for  $\varepsilon > \varepsilon_{kn}$ , from which we can extract the dominant amplitudes  $A$ ,  $D$ ,  $F$  according to Eq. (2.21) for  $\varepsilon > \varepsilon_{kn}$ . We started from random initial conditions. As to be expected the patterns have selected in Eq. (2.21) the critical wavenumber  $q_x = q_c = 2.95$  of the axial rolls and the critical transverse wavenumbers  $q_y = p_{kn}$  at  $\varepsilon = \varepsilon_{kn}$ . For instance, parameterizing the transverse wave number as  $p_{kn} = a q_c$  ( $a = 1$  corresponds to the *CR* instability), we found the values  $a = 0.78, 0.705, 0.64, 0.605$  for  $\tau = 14, 18, 24, 28$ , respectively. Thus,  $p_{kn}$  decreases considerably with increasing  $\tau$ . Perfect agreement with the Galerkin results has been achieved as in the *SHV* case before.

Representative examples of the amplitudes are shown in Fig. 2.37 in the case  $\tau = 14$  (left panel) where the *SHV* instability precedes. To avoid the competition with the *SHV* modes we have in the following focused on  $\tau = 24$  where the knot patterns bifurcate directly from the axial rolls (Fig. 2.37b). The amplitudes extracted from simulations shown in Fig. 2.37b agree with the Galerkin results in Fig. 2.37c. Our Galerkin analysis shows that the knot patterns are at first stable slightly above  $\varepsilon_{kn}$  ( $\varepsilon_{kn} = 0.209$  in Fig. 2.37c). This is confirmed in Fig. 2.38 where the amplitudes and the Nusselt number for a simulation at  $\varepsilon = 0.22$  have settled down to a stationary pattern. It is obvious that the knot bifurcation is supercritical, since the  $D$ ,  $F$  grow like  $\sim \sqrt{\varepsilon - \varepsilon_{kn}}$ .

At  $\varepsilon = 0.38$  the Galerkin analysis has revealed an oscillatory instability with a Floquet modulation vector  $\mathbf{s} = 0.2(0, p_{kn})$  (corresponding to mode  $F$ ). This instability leads to complex pattern dynamics. One is inclined to interpret the time sequence

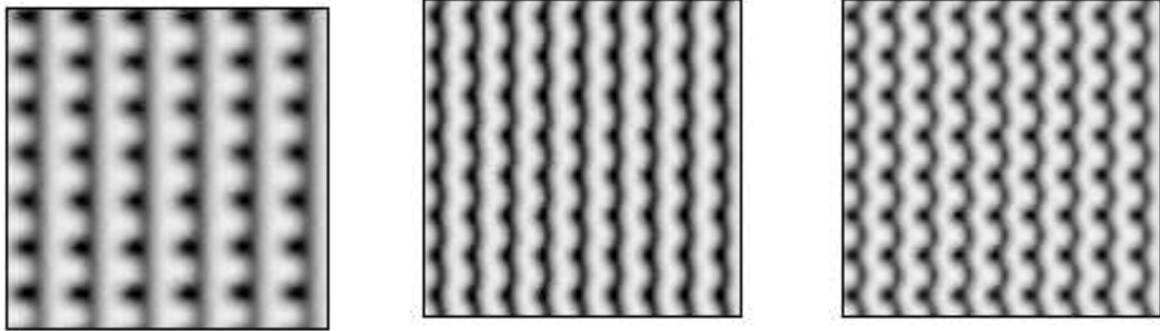


Figure 2.36: Stable knot convection patterns for  $\tau = 14$ ,  $\varepsilon = 0.08$  (left plot),  $\tau = 18$ ,  $\varepsilon = 0.13$  (middle plot) and  $\tau = 18$ ,  $\varepsilon = 0.15$  (right plot). The aspect ratios are  $\Gamma = 12$  (left panel) and  $\Gamma = 18$  (middle and right panels).

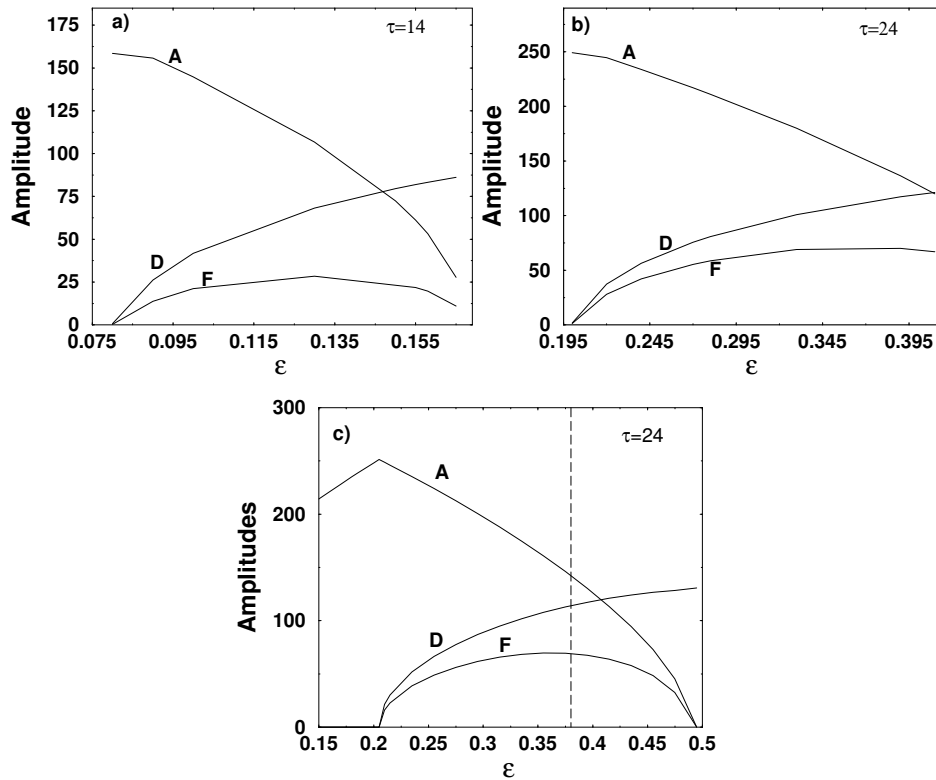


Figure 2.37: Leading three amplitudes for knot solution as function of  $\varepsilon$  at (a)  $\tau = 14$ , (b)  $\tau = 24$  from simulations and (c)  $\tau = 24$  from weakly nonlinear analysis in the case  $Q = 14$ ,  $P = 10$  (see text). The dashed lines denote the oscillating instabilities of knots.

shown in Fig. 2.39 as part of a periodic cycle. However, in a different time intervals as shown in Fig. 2.40 we have also observed traveling knots in the case  $\tau = 24$  and

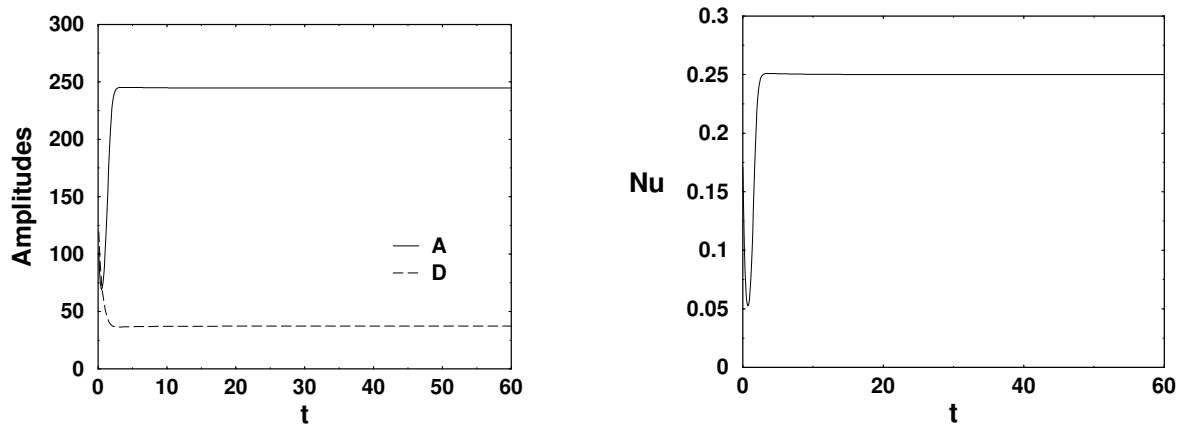


Figure 2.38: Amplitudes  $A$  and  $D$  (left) and the Nusselt number  $Nu$  as function of time for knot solution at  $\tau = 24$ ,  $\varepsilon = 0.22$ ,  $Q = 14$ ,  $P = 10$ .

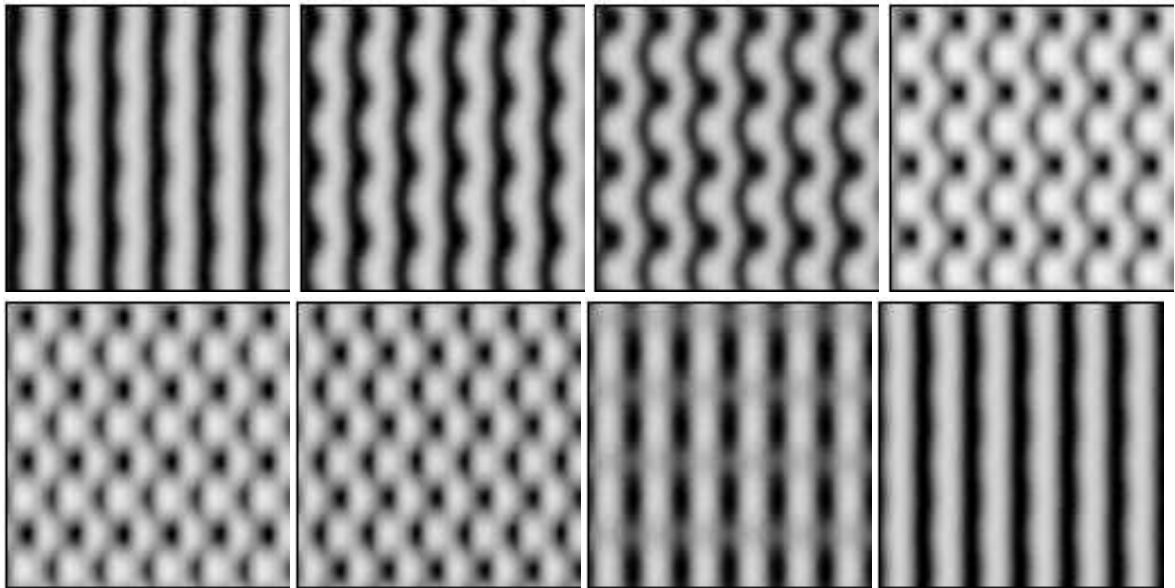


Figure 2.39: Evolution of knots at  $\varepsilon = 0.43$ ,  $\tau = 24$ ,  $Q = 14$ ,  $P = 10$ . Plots from left to right correspond to times  $t = 13.3, 13.4, 13.5, 13.6, 13.65, 13.75, 14.3$  and  $14.4$ . The aspect ratio is  $\Gamma = 12$ .

$\varepsilon = 0.43$  during a relatively short time interval.

Considering the entire simulation period in the case  $\varepsilon = 0.43$ ,  $\tau = 24$ ,  $Q = 14$  and  $P = 10$ , a rather chaotic time dependence of the amplitudes and the Nusselt number is seen in Fig. 2.41. Nevertheless one can identify globally a certain oscillation frequency in this graph, which agrees very well with the Hopf frequency at the onset of the oscillatory instability in Fig. 2.37c.

We have expected, that the *chaotic* time dependences would become stronger at

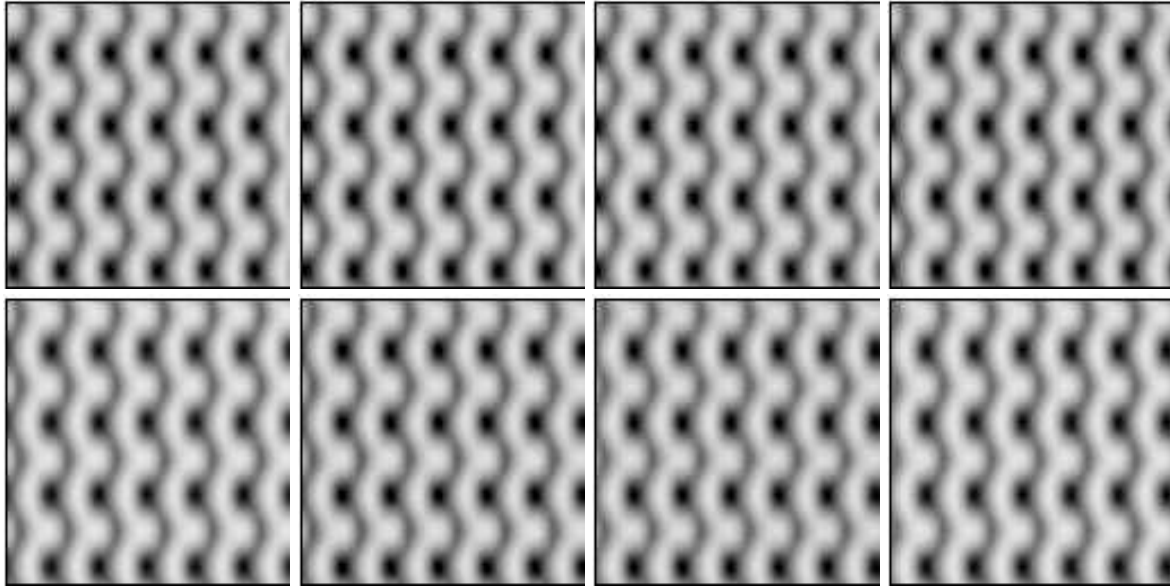


Figure 2.40: Knots traveling to left at  $\varepsilon = 0.43$ ,  $\tau = 24$ ,  $Q = 14$ ,  $P = 10$ . Plots from left to right correspond to times  $t = 22, 22.4, 22.8, 23.2, 23.6, 24, 24.4$  and  $24.8$ . The aspect ratio is  $\Gamma = 12$ .

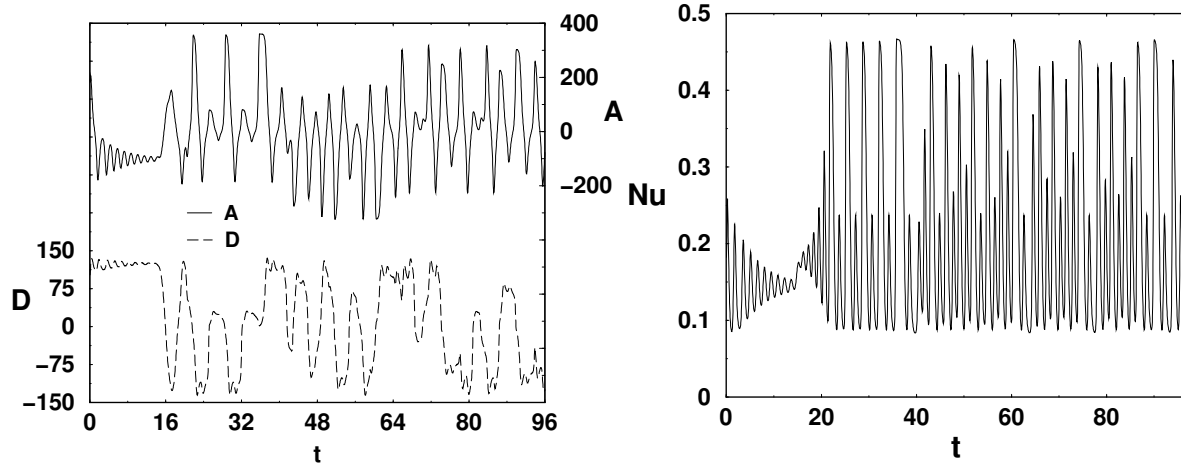


Figure 2.41: Amplitudes  $A$ ,  $D$  (left) and  $Nu$  (right) of the knot instability with respect to time at  $\varepsilon = 0.43$ ,  $\tau = 24$ ,  $Q = 14$  and  $P = 10$ .

larger  $\varepsilon$ , but in fact it has become in some sense more periodic as demonstrated by the amplitudes and the Nusselt number in Fig. 2.42. A typical time sequence of the corresponding patterns is shown in Fig. 2.43. We have observed slightly perturbed rolls (i.e.  $A$  dominant) (first panel, first row), patterns dominated by  $D$  (first panel, second row) as well as knot patterns ( $A$ ,  $D$  and  $F$  finite, last panel, second row). Note that in

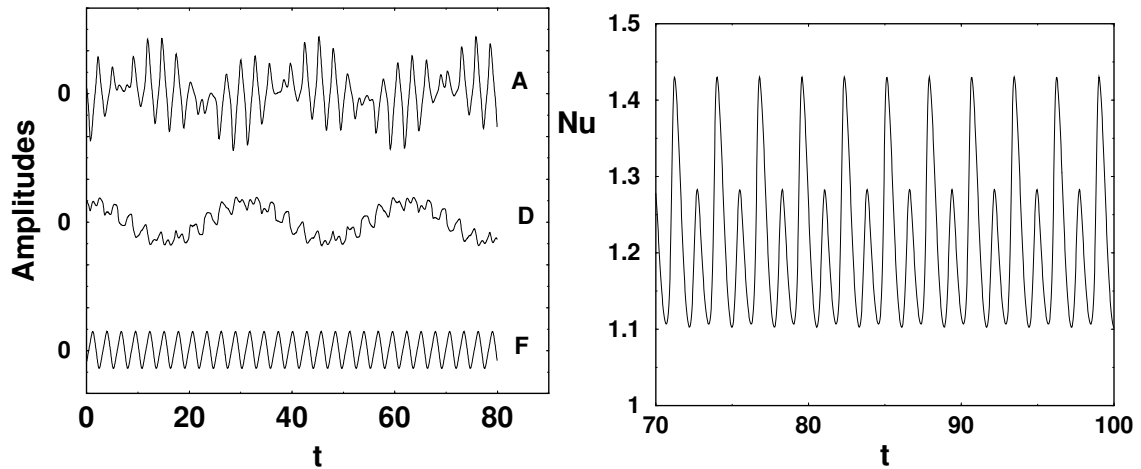


Figure 2.42: Amplitudes  $A$ ,  $D$ ,  $F$  (left) and  $Nu$  (right) for knot patterns as function of time at  $\varepsilon = 0.45$ ,  $\tau = 24$ ,  $Q = 14$  and  $P = 10$ .

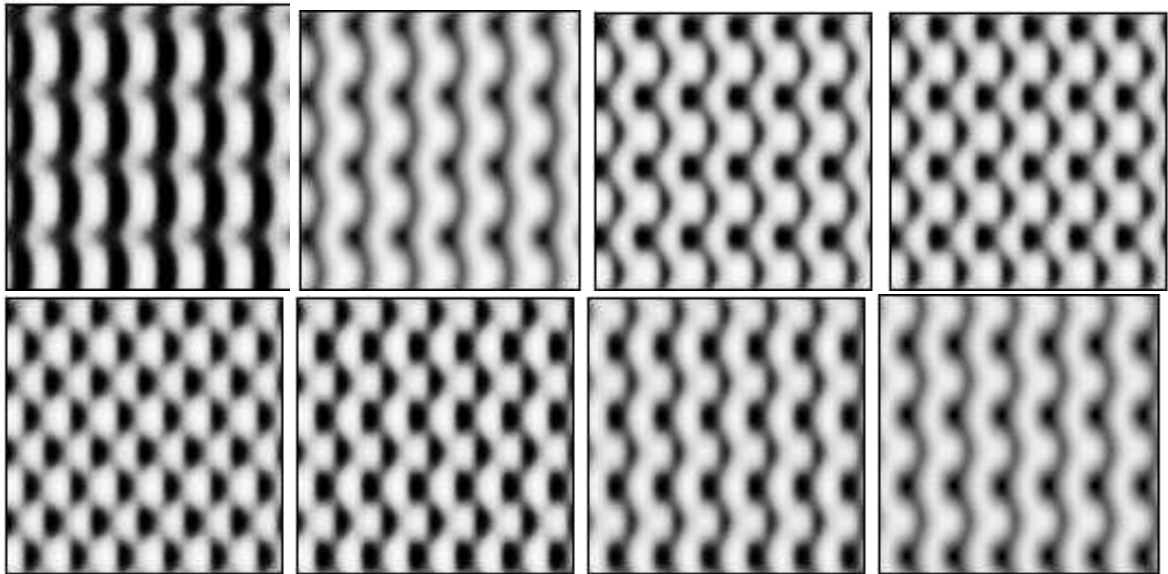


Figure 2.43: Knot instability at  $\varepsilon = 0.45$ ,  $\tau = 24$ ,  $Q = 14$ ,  $P = 10$ . Plots from left to right correspond to times  $t = 52.9, 53.1, 53.2, 53.26, 53.3, 53.4, 53.46$  and  $53.6$ . The aspect ratio is  $\Gamma = 12$ .

this regime a stationary knot pattern does practically not exist, since the amplitudes  $A, F$  are already very small (see Fig. 2.37c).

## 2.5 Direct Simulations

In this section, we present representative examples of simulations of the basic hydrodynamic Eqs. (2.5-2.9) of the rotating annulus for different parameters. For details of

the simulation codes, we refer to Sec. 1.5 and App. B. The simulations in this section have been started either from random initial condition or from a roll pattern with a superimposed noise. In the latter case, we are able to confirm the stability boundaries of convection rolls obtained from the Galerkin code since the noise contribution decays with time in the stable roll regime. In addition, we get insight into the basin of attraction of different competing locally stable states, when we start our simulations from random initial condition. First we focus on the large Prandtl number  $P = 10$  case, before the  $P = 0.1$  case will be discussed.

### 2.5.1 Simulations at large $P$

In this section, we analyze the patterns at large  $P$  obtained in various simulations at different parameter sets which have been indicated in Fig. 2.44. As already known from Fig. 2.14, stable zonal rolls exist in the entire  $\varepsilon_o, \tau$  regime left to the dashed line. This is confirmed by simulations started with random initial conditions. Indeed, as shown in Fig. 2.45, zonal roll structures perfectly aligned with the magnetic field are obtained after a relatively short time.

To confirm the existence of locally stable oblique rolls for small  $\tau$  (see also Fig. 2.16) value we disturbed a  $\chi = 45^\circ$  pattern obtained from a Galerkin solution. At first, we convince ourselves that superimposed noise in Fourier space would quickly die out. Alternatively, we applied a localized perturbation by reducing the convection in a small patch in the position space (see the second and third patterns in Fig. 2.46). In this case  $\chi = 45^\circ$  rolls changed their orientation into  $\chi = 63^\circ$  oblique roll which, according to Fig. 2.16, are stable.

In the case of moderate  $\tau$  values which are comparable to the value of  $Q$  oblique rolls, as predicted by linear analysis already at onset, are indeed found for low values of  $\varepsilon_o$ . A typical time evolution from random initial conditions to an oblique roll pattern is shown in Fig. 2.47. A more detailed analysis of the stable regions of oblique rolls has been presented in Sec. 2.3.2. The preferred angle  $\chi$  of oblique rolls increases as  $\varepsilon_o$  is increased. In particular we have found a large regime of stable zonal rolls ( $\chi = 90^\circ$ ) to the right of the dashed *SW* line in Fig. 2.44. Note that the range of stable zonal rolls in Fig. 2.17 overlaps to considerable extent with the region  $\tau > \tau_L$  where the stable critical oblique rolls are found. Accordingly we expect hysteresis phenomena. This tendency towards zonal rolls with increasing  $\varepsilon_o$  has also been observed experimentally [28] as well as theoretically [25] in the case  $Q = 0$ .

To the right of the dashed line of Fig. 2.14a at values of  $\varepsilon_o$  of order unity the formation of the stable zonal roll depends on the initial conditions. With superimposed noise, this property is demonstrated in Fig. 2.48 where oblique rolls evolve into a pattern of zonal rolls with two dislocations which are likely to disappear after much longer integration times. In contrast, when the time integration is started with random initial conditions a stationary pattern of zonal rolls has not been obtained asymptotically. Instead a spatio-temporally chaotic pattern persists in which zonal rolls dominate only locally as demonstrated in Fig. 2.49. Another example of this phenomenon is demonstrated in Figs. 2.50 and 2.51 for a much higher value of  $\tau$ . A slightly disturbed

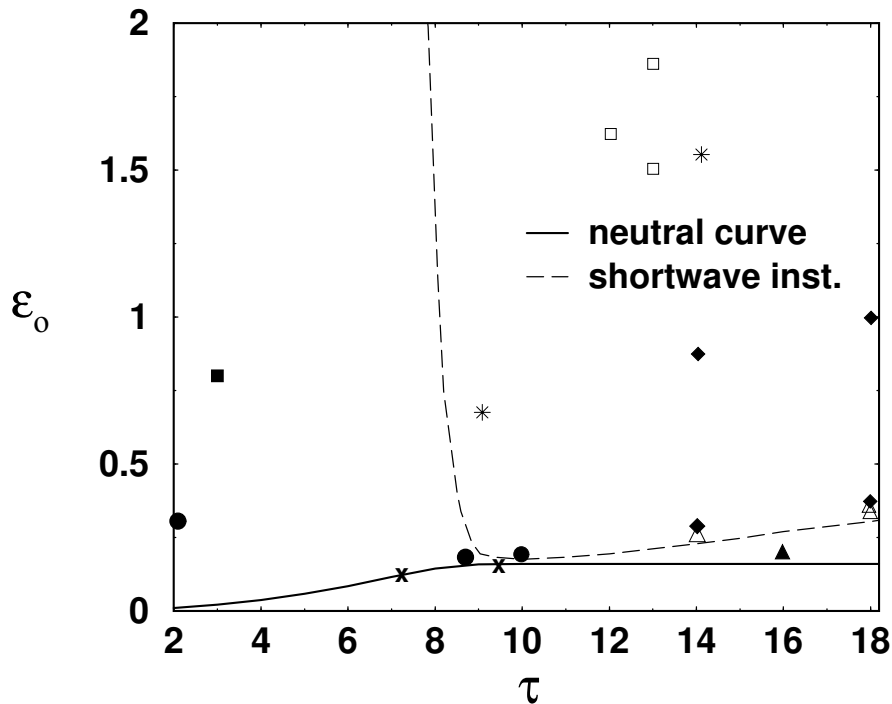


Figure 2.44: Stability diagram (see also Fig. 2.14) in the  $\tau - \epsilon_0$  plane for  $Q = 14$  and  $P = 10$ . Simulations discussed in the text correspond to the different symbols in the figure. Filled circles denote the oblique patterns, open squares indicate zig-zag patterns, open triangles correspond to knot patterns, filled diamonds indicate spatio-temporally chaotic convection and stars indicate the points where competition between different patterns has been observed.

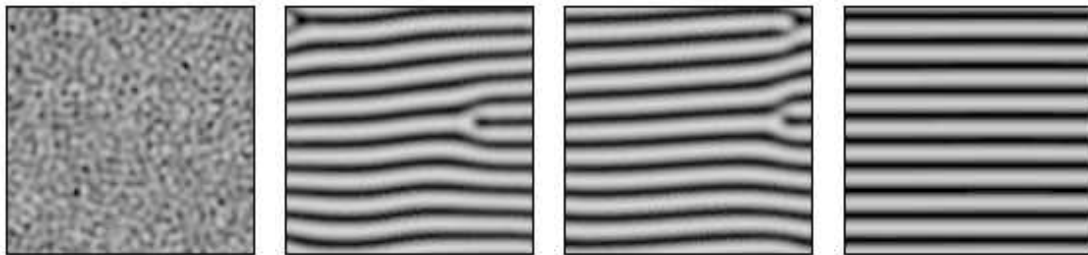


Figure 2.45: Zonal rolls for  $\tau = 3$ ,  $Q = 14$ ,  $\epsilon_0 = 0.8$ . The plots from left to right correspond to the times  $t = 0$ , 14.3, 28.57 and 114.3 in units of  $t_v$  (see the filled square in Fig. 2.44). The aspect ratio is  $\Gamma = 20$ . The  $x$ -coordinate increases towards the right and the  $y$ -coordinate is directed upwards.

zonal roll pattern recovers after some time (see Fig. 2.50), while starting from initial conditions we arrive at the “chaotic” attractor (Fig. 2.51).

The co-existence of time independent attractors and *spatio-temporally chaotic* ones is a well known phenomenon in problems of pattern formation. For an example we

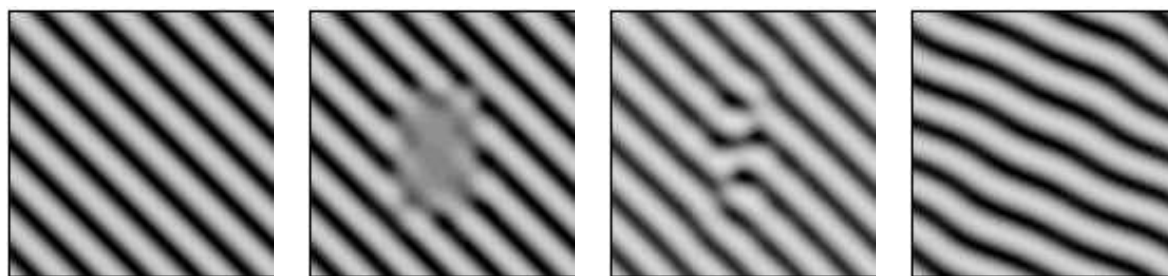


Figure 2.46: Stable oblique rolls ( $\chi = 45^\circ$ ) for  $\tau = 2$ ,  $Q = 14$ ,  $\varepsilon_o = 0.31$  (see also Fig. 2.16). The plots from left to right correspond to the times  $t = 0.5, 15.3, 19.8$  and  $31.3$  (see the filled circle in Fig. 2.44). The aspect ratio is  $\Gamma = 20$ . Here and in the following figures the temperature field in the plane  $z = 0.5$  is shown.

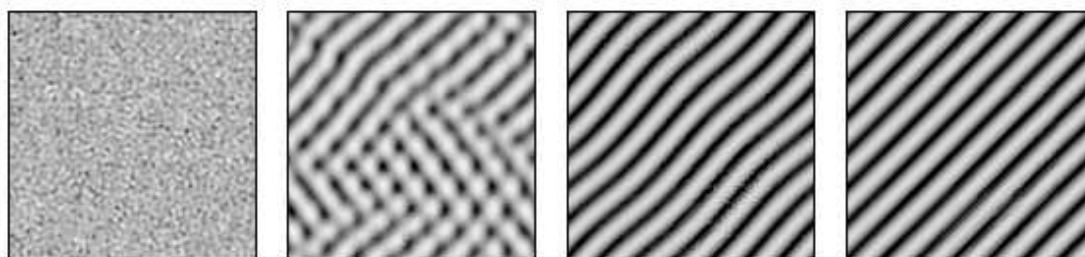


Figure 2.47: Oblique rolls for  $\tau = 8.7$ ,  $Q = 14$ ,  $\varepsilon_o = 0.18$  (see the filled circle in Fig. 2.44). The plots from left to right correspond to the times  $t = 0, 6.3, 12.6$  and  $50$ . The aspect ratio is  $\Gamma = 28$ .

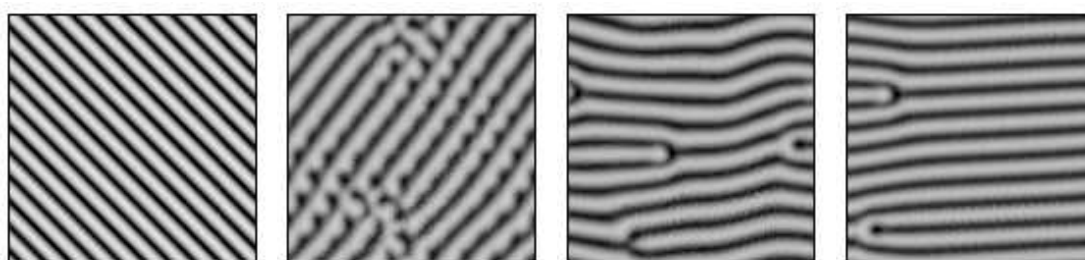


Figure 2.48: Time evolution for  $\tau = 9.1$ ,  $Q = 14$ ,  $\varepsilon_o = 0.65$  starting from initial conditions of oblique rolls with superimposed noise (see the star in Fig. 2.44). The plots from left to right correspond to the times  $t = 0.7, 3.3, 5.8$  and  $42.8$ . The aspect ratio is  $\Gamma = 22$ .

refer to the case of spiral defect chaos in *RB* convection [33, 34, 35].

For relatively higher values of  $\tau$  ( $> \tau_U$ ) the axial rolls become unstable against the subharmonic varicose (*SHV*) instability according to the Galerkin analysis. But *SHV* patterns are only stable for fairly small  $\varepsilon_o$  (see Sec. 2.4.2). Thus a stationary *SHV* pattern evolves to the oblique roll patterns at larger  $\varepsilon_o$ . An example is shown in Fig. 2.52. Note that *SHV* instability is well expressed in the transients; the angle of the

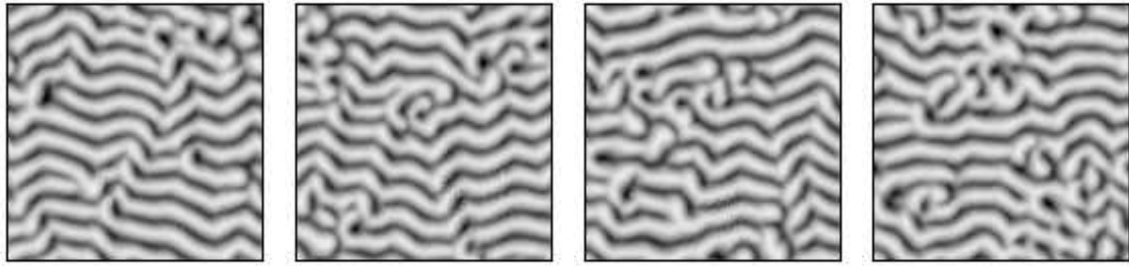


Figure 2.49: Time evolution for the same parameters as in Fig. 2.48 starting from random initial conditions (see the star in Fig. 2.44). The plots from left to right correspond to the times  $t = 4.83, 7.17, 11.3$  and  $46.7$ , respectively. Time is in units of  $t_v$ . The aspect ratio is  $\Gamma = 22$ .

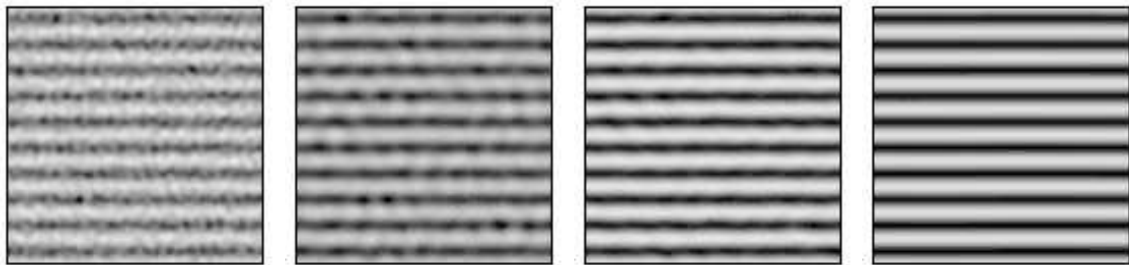


Figure 2.50: Stable zonal rolls for  $\tau = 14, Q = 14, \varepsilon_o = 1.54, q_{zonal} = 4$  (see the star in Fig. 2.44). The plots from left to right correspond to times  $t = 0, 0.125, 0.25$  and  $5$ . The aspect ratio is  $\Gamma = 20$ .

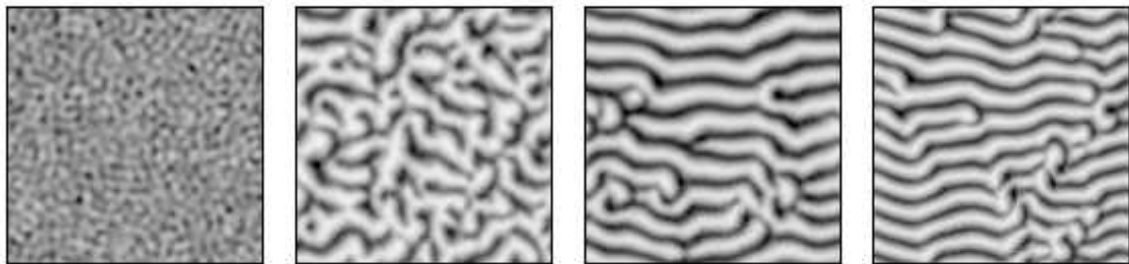


Figure 2.51: Time sequence for the random initial conditions for the same parameters as in Fig. 2.50 (see the star in Fig. 2.44). The plots from left to right correspond to times  $t = 0, 0.44, 1.32$  and  $22$ . The aspect ratio is  $\Gamma = 22$ .

oblique rolls is about  $\chi = 60^\circ$  characteristic for hexarolls which are a special case of *SHV* instability.

In contrast to Fig. 2.52 the system also exploits the knot instability which bifurcates nearby to arrive at the stable oblique rolls as shown in Fig. 2.53. The knots first become strong in zonal direction, then they lose their original orientation and become like oblique rolls. After some intermediate steps which include some phase shifts of

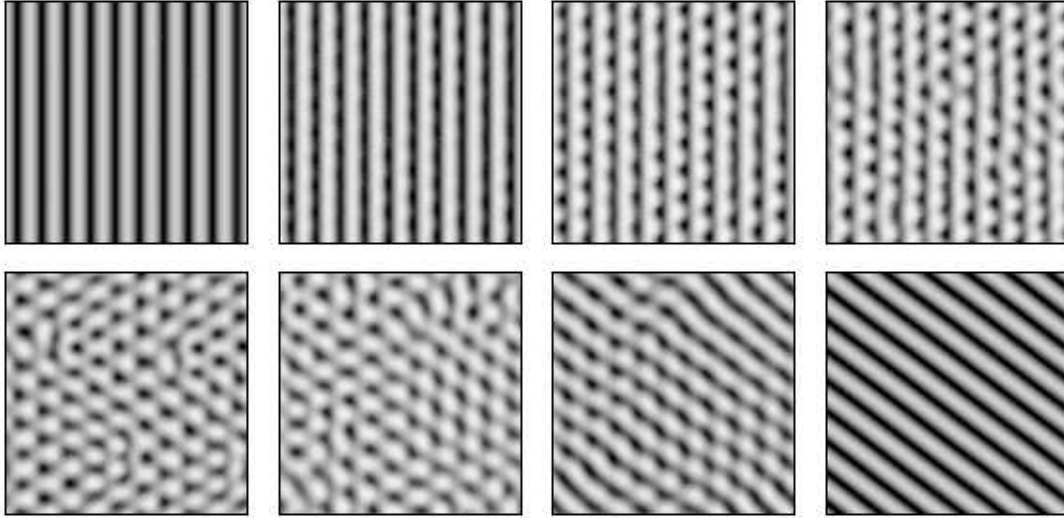


Figure 2.52: Stable oblique rolls just above the instability line for  $\tau = 10$ ,  $Q = 14$ ,  $\varepsilon_o = 0.19$  (see the filled circle in Fig. 2.44). The plots from left to right correspond to times  $t = 0, 1.1, 1.27, 1.81, 2, 2.9, 3.6$  and  $65.5$ . The aspect ratio is  $\Gamma = 20$ .

the rolls (see the patterns in middle line) the pattern evolves into an oblique structure. The transition interval of the shifting process can also be seen in the time variation of two leading modes (Fig. 2.54). Here,  $A$  and  $B$  amplitudes show strong fluctuations during the transition time.

At slightly higher value of  $\varepsilon_o$  a chaotic pattern is found which is dominated by a switching back and forth between the two equivalent oblique roll systems with angles of  $\psi = \pm 37^\circ$  as shown in Fig. 2.55. For even larger values of  $\varepsilon_o$  the oblique rolls are replaced by fully phase-turbulent convection in this regime. An example is shown in Fig. 2.56. We have included a graph of the power spectrum which corresponds to the last spatial pattern in Fig. 2.56. Note that the ring-like wave vector distribution is nearly isotropic with the approximate mean radius given by  $|\mathbf{q}_c|$ . This feature can be understood on the basis of the property that the stabilizing effects exerted by rotation and by the magnetic field in the two orthogonal directions are approximately equal.

In a region surrounding the open squares in Fig. 2.44 stationary zig-zag patterns have been found as attractors as shown, for example, in Fig. 2.57. Outside this region, however, spatio-temporally chaotic convection is usually found when the simulations are started with random initial conditions.

## 2.5.2 Simulations at low $P$

In Sec. 2.3.3, we have presented the stability diagram and the related results for  $P = 0.1$  obtained with the Galerkin procedure. In this part of the thesis, we discuss the simulations beyond the longwave and shortwave instability curves in Fig. 2.58. Comparing the present case with the high- $P$  one, additional instabilities such as *oscillatory oblique rolls*, *chaotic zonal* and *chaotic oblique rolls* are observable. First, we

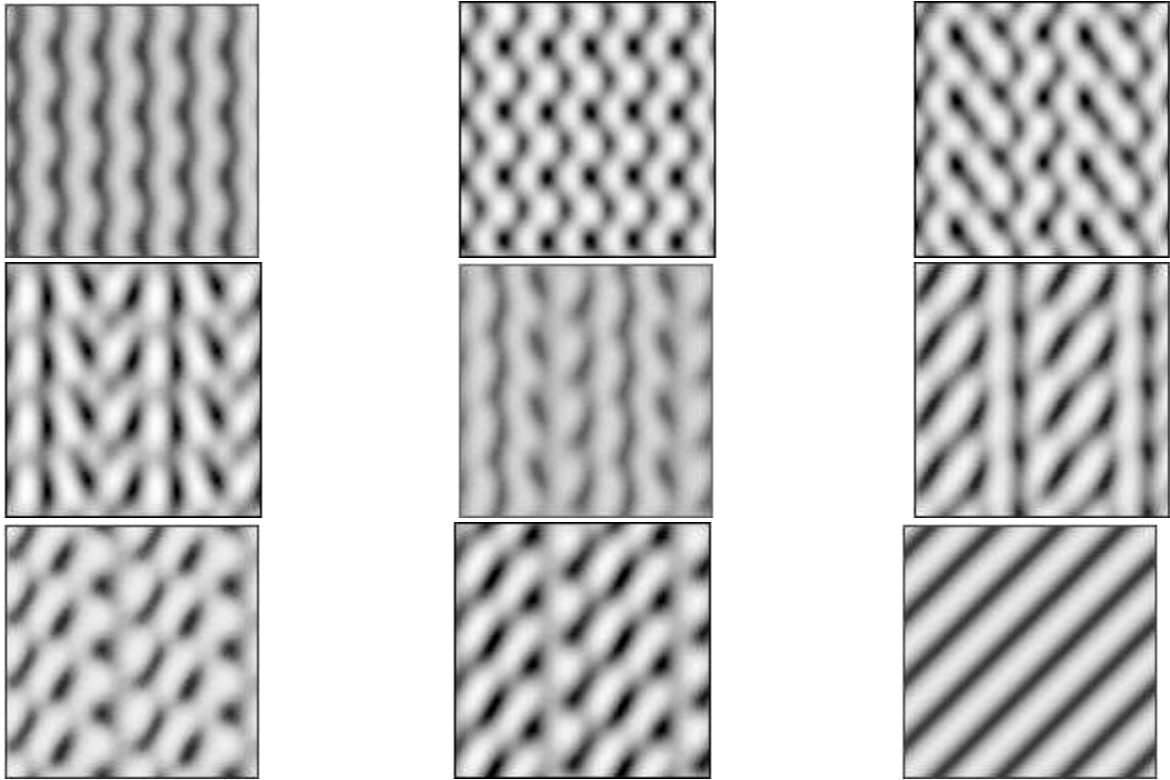


Figure 2.53: Transition from an axial roll to an oblique roll pattern via the knot instability for  $\varepsilon_o = 0.35$  at  $\tau = 14$ ,  $Q = 14$ ,  $P = 10$  (see the open triangle in Fig. 2.44). Plots from left to right correspond to times  $t = 18.7, 19, 26.3, 27.5, 27.7, 28.1, 28.4, 28.7$  and  $30.7$ . The aspect ratio is  $\Gamma = 12$ .

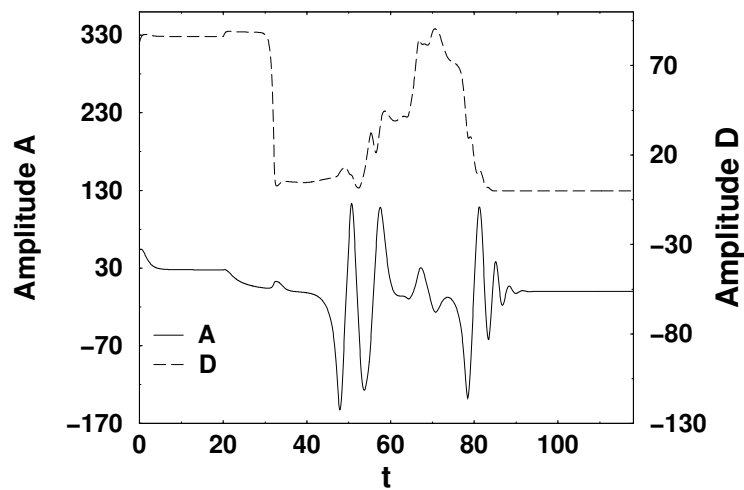


Figure 2.54: Amplitudes demonstrating the transition from an axial roll to an oblique roll pattern ( $A = 0$ ,  $D \neq 0$ ) via knot instability for the same parameters in Fig. 2.53.

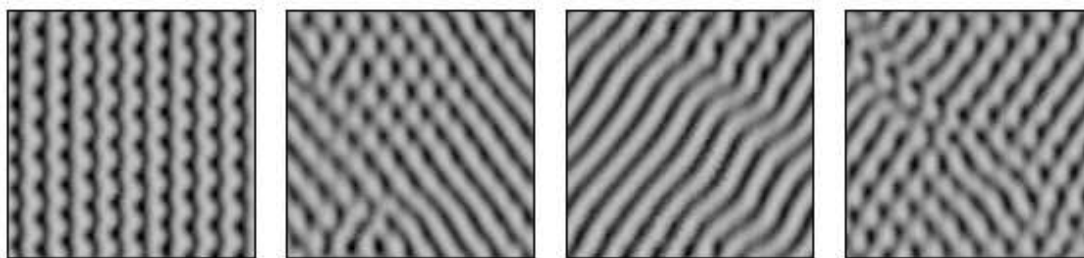


Figure 2.55: Time evolution of spatio-temporally chaotic oblique rolls for  $\tau = 14$ ,  $Q = 14$ ,  $\varepsilon_o = 0.37$  (see the filled diamond in Fig. 2.44). Corresponding times are  $t = 6.66$ ,  $10$ ,  $16.7$  and  $30$ , respectively. The aspect ratio is  $\Gamma = 20$ .

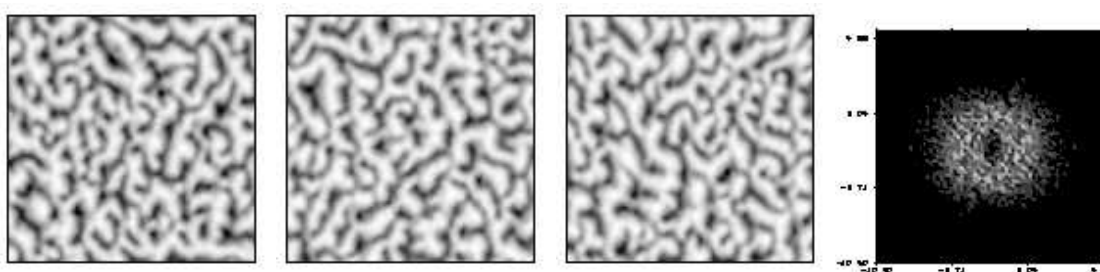


Figure 2.56: Spatio-temporal pattern for  $\tau = 18$ ,  $Q = 14$ ,  $\varepsilon_o = 1$  (see the filled diamond in Fig. 2.44). The last picture gives the power spectrum of the last pattern. The plots from left to right correspond to times  $t = 8.3$ ,  $16.7$  and  $25$ . The aspect ratio is  $\Gamma = 20$ .

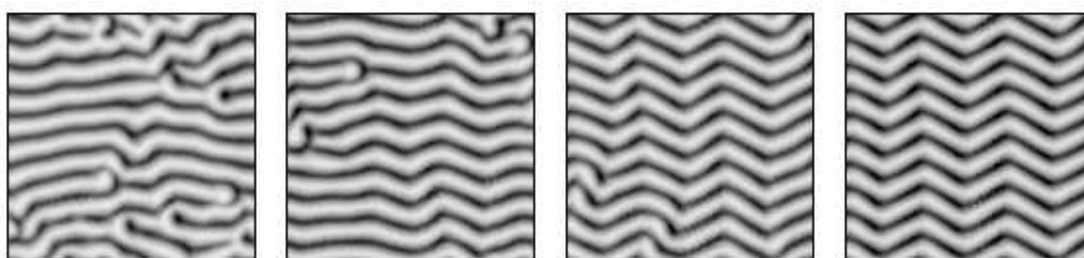


Figure 2.57: Zig zag pattern evolving from random initial condition for  $\tau = 13$ ,  $Q = 14$ ,  $\varepsilon_o = 1.51$ ,  $P = 10$  (see the open square in Fig. 2.44). The plots from left to right correspond to the times  $t = 0.49$ ,  $3.33$ ,  $6.66$  and  $10$ . The aspect ratio is  $\Gamma = 20$ .

present patterns of stable zonal rolls in the case  $\tau = 2$  and  $\varepsilon_o = 0.141$  in Fig. 2.59 which is just below the skewed-varicose ( $Sv$ ) instability line in Fig. 2.58. Note that for this small  $P$  value, the stability region becomes quite narrow for the zonal rolls (see also in Fig. 2.18). Noise of 1% (not visible) has been superimposed on the left pattern. It leads to a slight undulation of the rolls (center panel) before we end up with stable zonal rolls.

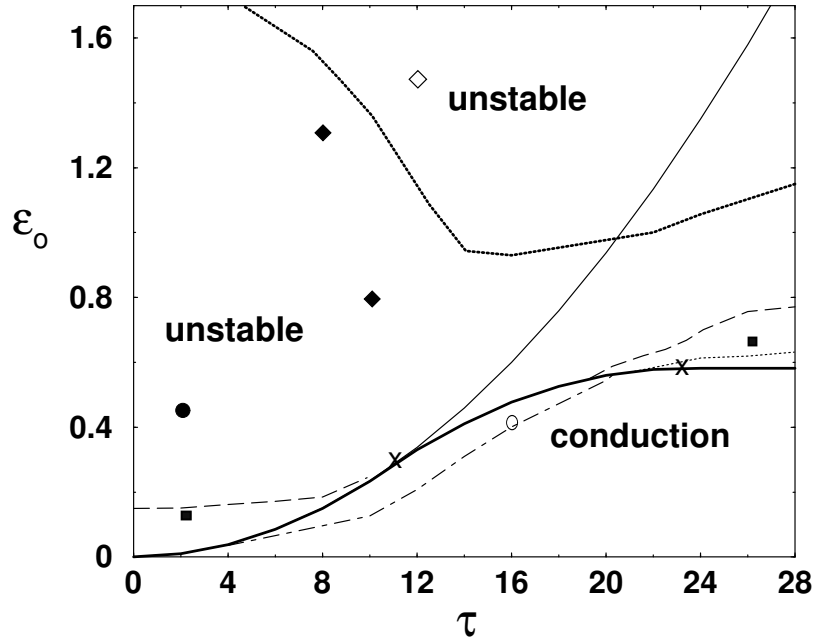


Figure 2.58: Stability diagram and convection patterns in the  $\tau - \epsilon_0$  plane in the case of  $Q = 54$  and  $P = 0.1$ . Simulations discussed in the text have been done at the indicated points. Squares correspond to zonal rolls, open (filled) diamonds indicate oscillatory (spatio-temporally chaotic) and open (filled) circles correspond to the subcritical (oblique) convection patterns. The threshold for the zonal rolls is indicated by the thin solid curve.

A longwave skewed-varicose  $Sv$  instability takes place for relatively high values of  $\epsilon$  as shown in Figs. 2.21, 2.18 in contrast to Fig. 2.59 at the same  $\tau$  ( $= 2$ ). A typical form of the  $Sv$  instability is presented in Fig. 2.60. Strong  $Sv$  undulations of the zonal roll pattern develop from the superimposed noise. Then the oblique rolls which has a roll angle  $\chi = -83^\circ$  is formed from a zonal roll. From the Galerkin analysis, we have found that the final oblique state is indeed stable above  $\epsilon_0 = 0.48$ . The destabilizing angle  $\psi$  of the Floquet vector  $\mathbf{s}$  is found as  $55^\circ$ .

In Fig. 2.61, the patterns of typical *spatio-temporal chaotic zonal roll* which occur especially for slightly larger values of  $\tau$  are started from random initial conditions. A Fourier spectrum of the last pattern shows that the main wave vector is along the  $y$  axis.  $Nu$  values also vary randomly with time as shown in Fig. 2.62. In Fig. 2.63, starting from the zonal rolls, spatio-temporal chaotic patterns have been generated at slightly larger  $\tau$ . These patterns are in principle similar to the ones which are presented in Fig. 2.61.

Since we have a subcritical bifurcation in a wide range of  $\tau$ , we have also carried out some simulations around the saddle-node point (see the dashed-dotted line in Fig. 2.58). Subcritical bifurcations are very common in rotating systems at low  $P$  (see [36, 37]). In Fig. 2.64, the convection patterns have finite amplitudes. Note that

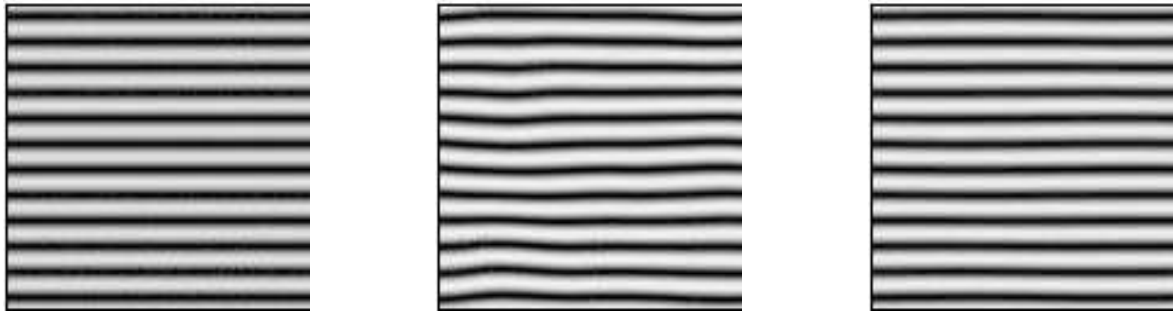


Figure 2.59: Stable zonal rolls just below the  $Sv$  instability line in the case  $\tau = 2$ ,  $Q = 54$ ,  $\varepsilon_o = 0.141$  and  $Pr = 0.1$  (see the filled square in Fig. 2.58). Plots from left to right correspond to times  $t = 0, 0.275$  and  $9$ . Aspect ratio is  $\Gamma = 24$ .

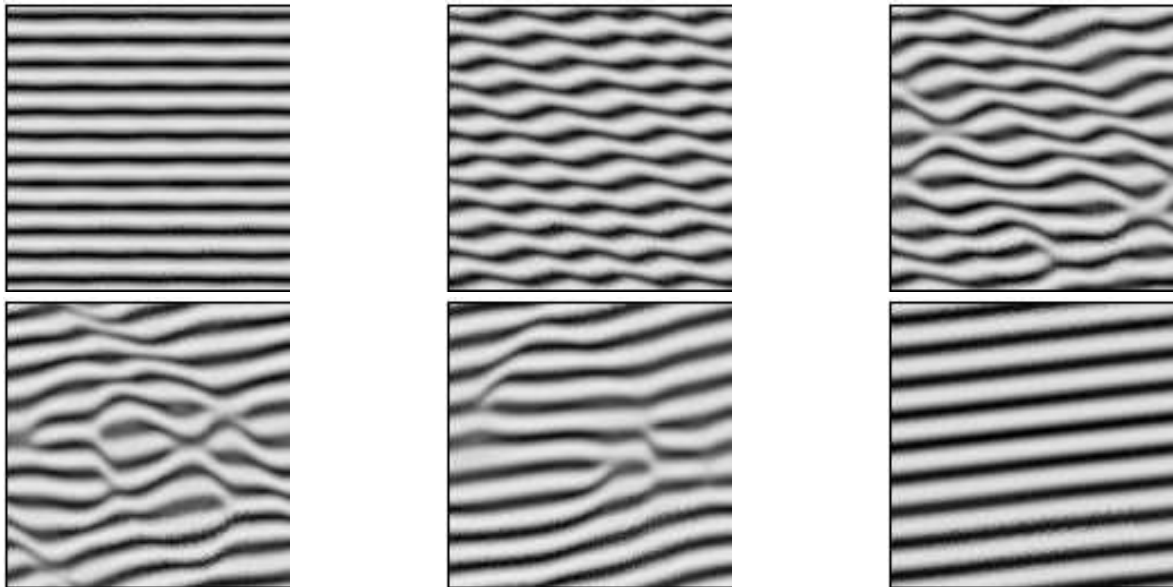


Figure 2.60: Transition from the zonal rolls to the oblique rolls via the  $Sv$  instability in the case  $\tau = 2$ ,  $Q = 54$ ,  $\varepsilon_o = 0.5$  and  $Pr = 0.1$  (see the filled circle in Fig. 2.58). Plots from left to right correspond to times  $t = 2, 4.5, 5.5, 6.7$  and  $9$ . Aspect ratio is  $\Gamma = 24$ .

the motion of rolls are similar to the case shown in Fig. 2.61. In the case of high  $\tau$  and  $\varepsilon$ , the system goes typically into a chaotic attractor for random initial conditions. In addition, there exists a certain region where oscillatory rolls are also formed (see Figs. 2.58, 2.18). A typical sample for *oscillatory oblique rolls* is given in Fig. 2.65. The oscillatory character is also reflected by the Nusselt number  $Nu$  as a function of time in the left plot of Fig. 2.66. The fluctuations mainly consist of two different frequencies. To determine the frequencies, we present the Fourier analysis of the  $Nu$  values in the right plot of Fig. 2.66. The high frequency is in good agreement with the

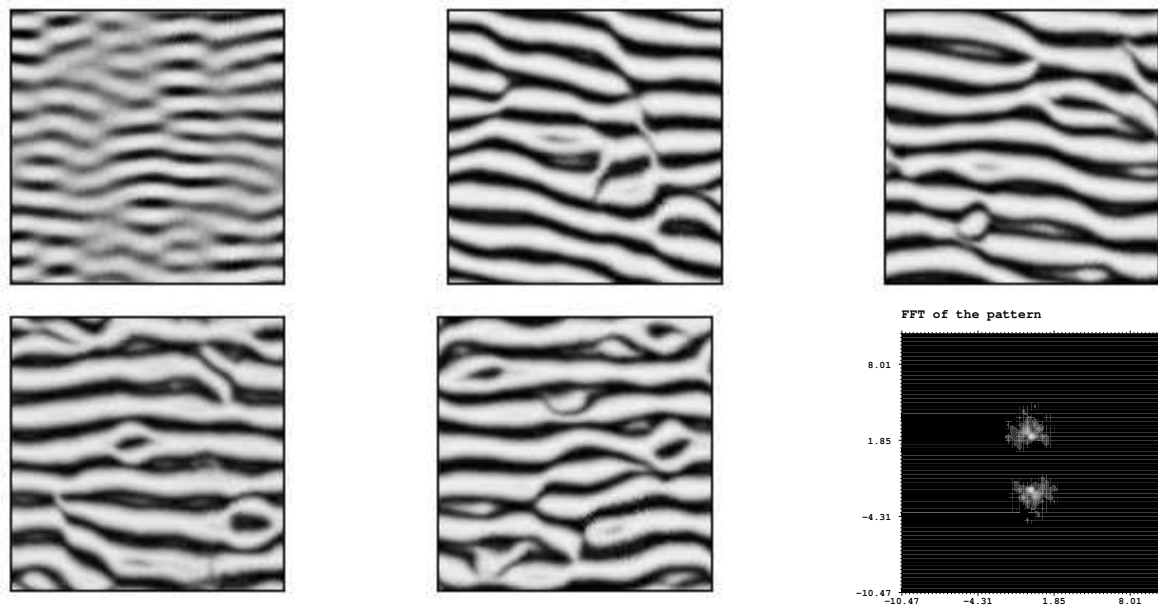


Figure 2.61: Patterns of chaotic zonal roll for  $\tau = 8$ ,  $Q = 54$ ,  $\varepsilon_o = 1.3$  and  $Pr = 0.1$  (see the filled diamond in Fig. 2.58). Random initial conditions were applied. The second picture of the third row give the Fourier spectrum shown to the right. Plots from left to right correspond to times  $t = 1.25, 2.5, 3.75, 5$  and  $6.25$ . Aspect ratio is  $\Gamma = 20$ .

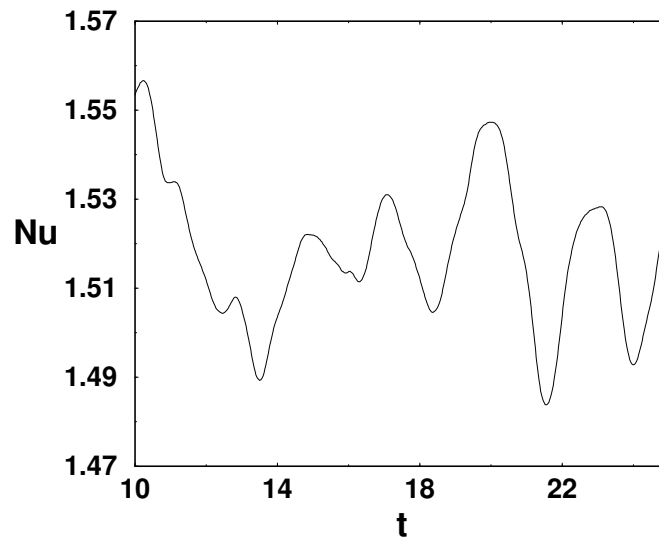


Figure 2.62: Oscillating  $Nu$  values as a function of time for the same parameters in Fig. 2.61.

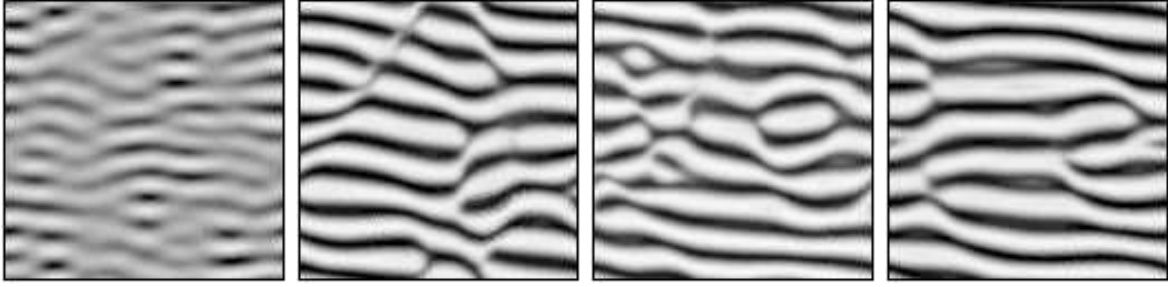


Figure 2.63: Evolution of chaotic zonal rolls starting from zonal rolls in the case  $\tau = 10$ ,  $Q = 54$ ,  $\varepsilon_o = 0.79$  and  $Pr = 0.1$  (see the filled diamond in Fig. 2.58). Plots from left to right correspond to times  $t = 0.75, 2, 8.5$  and  $9$ . Aspect ratio is  $\Gamma = 20$ .

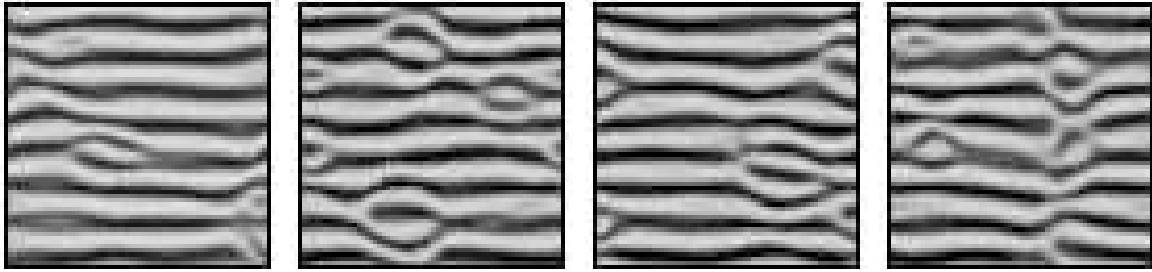


Figure 2.64: Evolution of a typical subcritical pattern for  $\tau = 16$ ,  $Q = 54$ ,  $\varepsilon_o = 0.417$  and  $Pr = 0.1$  (see the open circle in Fig. 2.58). Plots from left to right correspond to times  $t = 83.3, 91.7, 100$ , and  $108$ . Aspect ratio is  $\Gamma = 20$ .

Hopf frequency from Galerkin calculations ( $\omega = 15$ ).

For high  $\tau$  values, the shortwave knot instability dominates the patterns and this instability generates zonal patterns just above the neutral curve (see thin-dotted line in Fig. 2.18). A typical transition from an axial roll to a zonal one is represented in Fig. 2.67. The knot instability can be seen clearly in the transients.

To see the time evolution of the axial mode  $A$  and the mode  $D$  which is responsible for the knot instability (for details see Sec. A.2), we plotted these quantities in Fig. 2.68. First, the amplitude  $A$  increases up to a certain point to generate an axial roll. During this stage,  $D$  amplitude is exactly zero. When the knot instability takes place, there is a sudden drop in  $A$  which leads to the destruction of the axial mode. At that point, the fluctuations in  $D$  indicate the existence of instability. Finally, while  $A$  goes to zero with small fluctuations, the formation of the zonal roll has been completed with the help of the finite  $D$  mode. In addition,  $Nu$  values, which are constant around 1.06 for the axial rolls, first decrease slightly then increase rapidly during the instability up to 1.35 for zonal rolls.

According to the stability diagram in Fig. 2.14b, we do not expect a stable zonal roll state below the ( $P$  independent) zonal neutral curve at  $\varepsilon_o = 1.58$  for  $\tau = 26$ . Thus the generation of a stable zonal pattern at  $\varepsilon_o = 0.67$  looks surprising and we have explored the stability of the zonal rolls for this parameter set. We have found that the

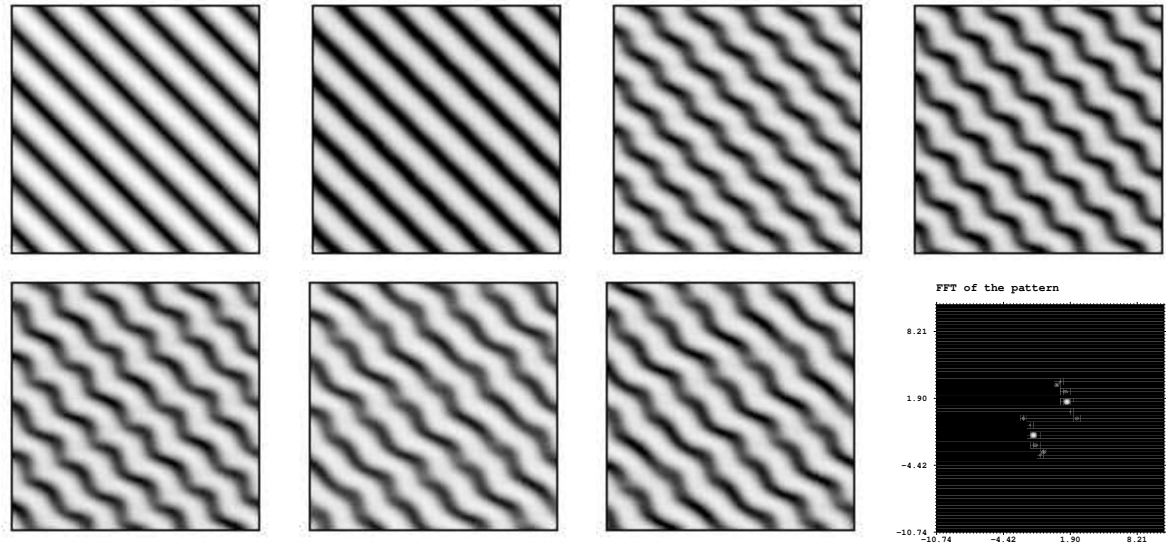


Figure 2.65: Oscillatory oblique patterns for  $\tau = 12$ ,  $Q = 54$ ,  $\varepsilon_o = 1.47$  and  $Pr = 0.1$  from the  $\psi = 45^\circ$ , oblique initial condition (see the open diamond in Fig. 2.58). The last plot gives the Fourier spectra of the previous pattern. Plots from left to right correspond to times  $t = 0, 6.6, 13.3, 20, 26.7, 33.3$  and  $40$ . The aspect ratio is  $\Gamma = 20$ .

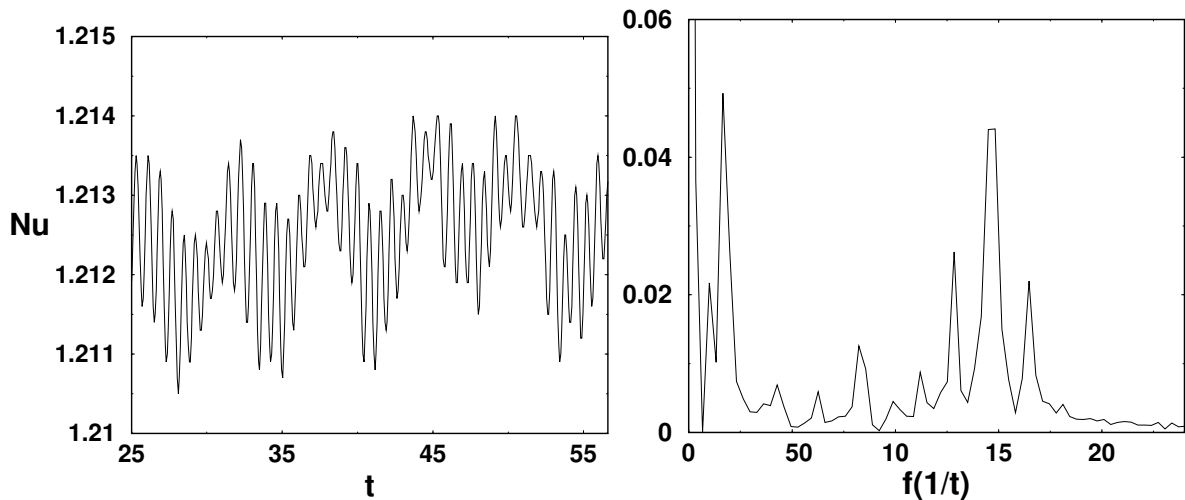


Figure 2.66: Oscillating  $Nu$  values as a function of time (left) and the  $FFT$  of the  $Nu$  oscillations for the same parameters in Fig. 2.65.

bifurcation of the zonal rolls was subcritical and thus enables the generation of stable zonal rolls in this region. We have plotted a representative graph of the subcritical bifurcation at  $\tau = 26$  in Fig. 2.69.

The saddle- node point has been found at  $\varepsilon = -0.46$  with respect to the neutral curve of zonal rolls and it corresponds to the value of  $\varepsilon_o = 0.395$  which is already below the neutral curve for the axial roll. Since the amplitude of the zonal roll is much larger

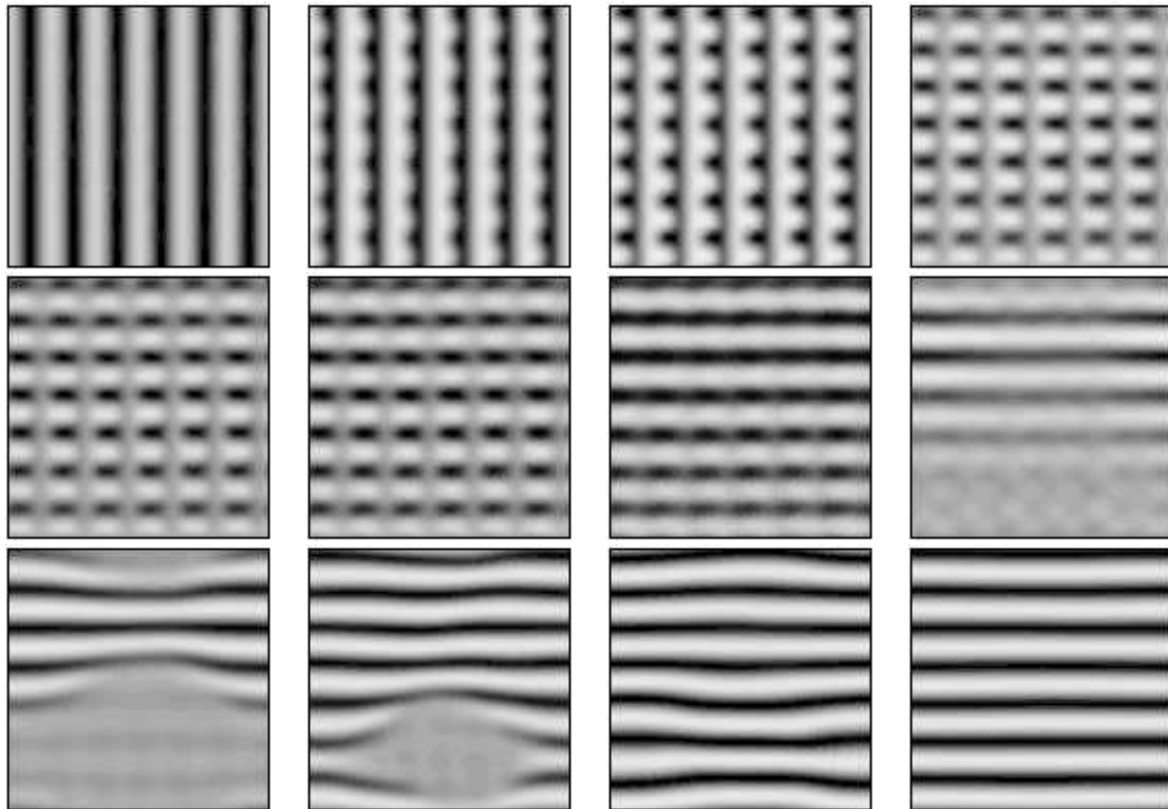


Figure 2.67: Generation of zonal rolls from the axial ones via knot instability for  $\tau = 26$ ,  $Q = 54$ ,  $\varepsilon_o = 0.67$  and  $Pr = 0.1$  (see the filled square in Fig. 2.58). Plots from left to right correspond to times  $t = 33, 39, 49, 59, 59.25, 59.5, 60, 61, 63.25, 65.25, 68.5$  and  $71.75$ . Aspect ratio is  $\Gamma = 12$ .

than the amplitude of the axial roll, the simulation typically produces zonal rolls for the random initial conditions. The filled square on the amplitude curve denotes the simulation point which is given in Fig. 2.67.

It is obvious that the bifurcation phenomena at small  $P$  are more intriguing than those for large  $P$ . In particular if experimental results are available to compare with, it would be worthwhile to construct more detailed stability diagrams as has been done for  $P = 10$  (Figs. 2.16, 2.17).

## 2.6 Concluding Remarks

Although only a small part of the parameter space of convection in a rotating cylindrical annulus has yet been investigated, the linear and nonlinear analyses have shown interesting results.

According to linear analysis which determines the onset of convection, mainly three different periodic roll structures have been found: zonal, axial and oblique rolls. An

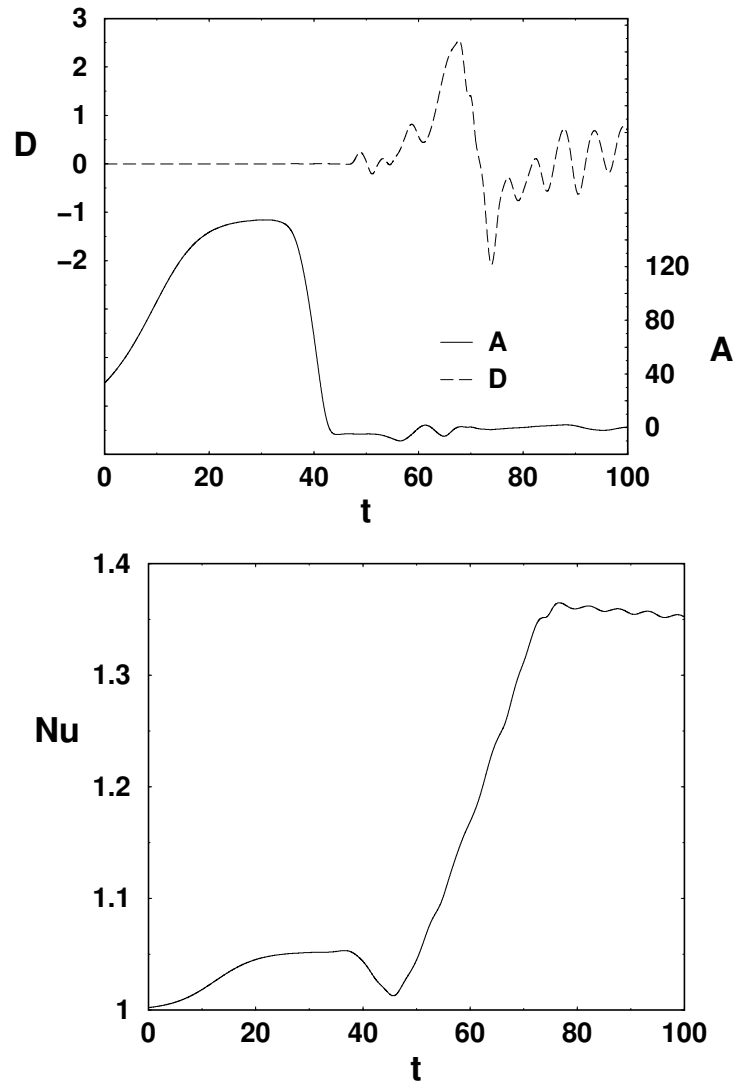


Figure 2.68: Amplitudes  $A$ ,  $D$  (above) and  $Nu$  (below) as a function of time for the same parameters in Fig. 2.67.

analytical model to estimate the onset of convection (i.e.  $R_c$ ,  $\mathbf{q}_c$ ) has been proposed for future works. The critical Rayleigh number  $R_c$  increases with increasing  $\tau$  and  $Q$ , whereas the critical wave number  $q_c$  decreases. The change in the inclination angle of the rolls from  $\chi = 90^\circ$  (zonal) to  $\chi = 0^\circ$  (axial) under increasing Coriolis number  $\tau$  was found to be a smooth function of  $\tau$ .

The secondary instability analysis showed that the Prandtl number  $P$  plays an important role for the various roll solutions. For high  $P$ , the general structure which was found in the linear analysis has not changed for small  $\varepsilon$  values. We have mainly observed generalized shortwave instabilities as well as knot and subharmonic skewed-varicose (*SHV*) instabilities. However, in the case of low  $P$ , we have found both longwave

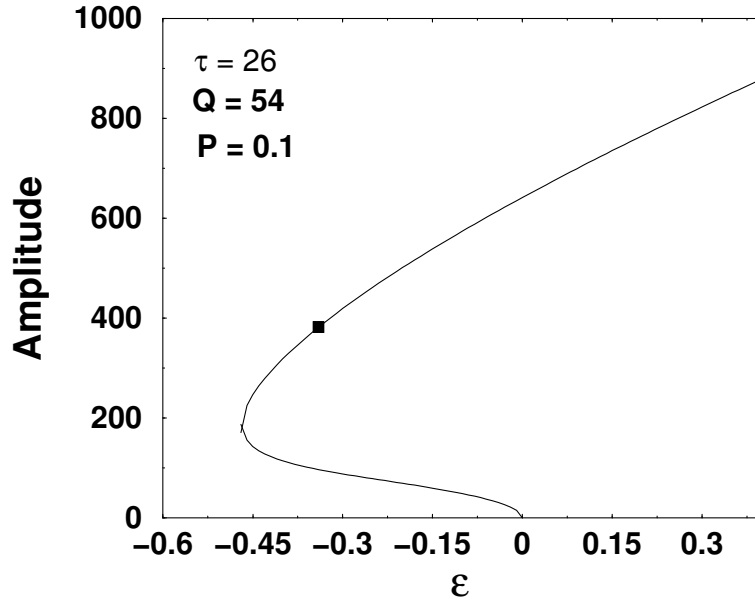


Figure 2.69: Amplitude of the zonal rolls as function of  $\varepsilon$  in the subcritical case for  $\tau = 26$ ,  $Q = 54$  and  $P = 0.1$ . Note that here we used the neutral curve of the zonal rolls to determine  $\varepsilon$ . The filled square denotes the simulation point in Fig. 2.67.

and shortwave instabilities. Among them, the skewed-varicose (*Sv*) instability is in fact responsible for the transition of zonal rolls into stable oblique rolls at small  $\tau$  whereas knot instability is seen for relatively high  $\tau$  and destabilizes the axial rolls. For intermediate  $\tau$  ( $4 \leq \tau \leq 21$ ), the primary bifurcation has been found to be subcritical. Similarly, the zonal rolls have also bifurcated subcritically for high  $\tau$  in the case  $Q = 54$  and well-defined zonal rolls just above the neutral curve have been observed.

From the simulations, a large variety of spatio-temporal patterns have been found. A comparison with experimental observations would be of interest. Unfortunately, there are not so many experiments in the literature, nevertheless we would like to underline some experimental studies motivated in the geophysical and astrophysical relevance of the problem. Brito and Cardin (private communication, 2003) have experimentally realized convection in an annular configuration with an azimuthal magnetic field in liquid sodium. Because of the low viscosity of this liquid metal they had to use high values of the Coriolis parameter  $\tau$  in order to achieve a centrifugal force exceeding gravity by a sufficiently large factor. The large value of  $\tau$  in their experiment prevented them to attain a value of  $Q$  comparable to that of  $\tau$  which appears to be necessary to obtain convection structures deviating from the axial roll structure. In another experiment, low values of  $\tau$  in centrifugally driven convection were realized when high Prandtl number fluids are used without magnetic field by Jaletzky and Busse [28]. Unfortunately high Prandtl number liquids usually do not offer typically high electrical conductivities which facilitate the attainment of sufficiently high values

of  $Q$ . However, high Prandtl number electrolytes could eventually solve this experimental problem. Finally an experiment on the  $RB$  convection in an electrolyte with a horizontal magnetic field without rotation has recently been performed by Andreev, et. al. [38]. In any case, our various codes are ready to analyze such experiments.

# Chapter 3

## Pattern Formation in Magnetic Ekman-Couette Layer

### Introduction

The notion of the Ekman layer goes back to a model introduced by V.W. Ekman to explain the drift of bodies on the surface of a viscous fluid in a rotating frame. His investigation was motivated by an observation of F. Nansen in 1893, that ice floating on the surface of the arctic ocean would move into a direction, which differs from that of the wind. The direction is determined by the balance of the Coriolis forces, the shear of the fluid, and the shear by the wind at the upper surface of the body. Without rotation an external stress at the surface of a fluid layer would lead to a Couette flow with a linear profile parallel to the stress. In the presence of rotation the stress profile rotates as well. Moreover the velocity field decays exponentially on a scale given by the Ekman depth  $D_E \sim 1/\sqrt{\Omega}$  where  $\Omega$  is the rotation frequency, i.e. the so-called Ekman layer develops. The Ekman-Couette layer problem is considered as a model for many phenomena in meteorology, geophysics and engineering sciences [39, 40]. For instance, engineers exploit Ekman boundary layer in rotating systems to enhance the effectivity of engines and turbines. One has to understand for instance rotating viscous flow near stationary or rotating disks. In this case, one observes two different solutions with respect to the boundary layers, an Ekman layer on the rotating disk and a Bödewadt layer on the stationary disk, which are separated by a geostrophic core. Typically with increasing rotation rate instabilities of the basic flow in the form of rolls appears. The bifurcations are stationary relative to appropriate rotating system for relatively low rotation rates and become oscillatory when the rotation increases further.

Earlier works on the Ekman problem have shown that mainly two different types of instabilities (type I and II) become important. The type I instability is associated with an inflection point in the profile of the velocity considered normal to the plates, whereas the type II instability, appearing at lower values of the critical Reynolds number  $Re_c$ , is related to the combined effects of the Coriolis force and viscous stresses [41]. The spatial structure of both instabilities consist of traveling vortices in the boundary layers. Their wavelength depends on the boundary layer thickness and the orientation of their

wavefronts (i.e.  $\phi_c$ ) with respect to the geostrophic flow ( $\phi_c$  is positive for type I and negative for type II instabilities). In addition, linear stability analyses of the flow between a rotating and a stationary disk have indicated that several solutions such as the Batchelor-type one with a separated boundary layer for high rotation rates are possible (see [42, 43, 44]). However, the critical values found by these authors did not withstand later analyses and the explanation of the instability mechanism was not satisfactory. For improved linear results and the clear description of the instabilities we refer to the study of Hoffman et al. [45]. In a later study on the same problem, an isolated solution was found describing a solitary vortex wave which does not seem to bifurcate from any other known solution [46]. From the point of experiments, there exist plenty of experimental studies on the stability of the Ekman-Couette layer in the literature [47, 48, 49, 50]. We refer to [51, 52, 53] for an extensive bibliography, especially for the investigation of the type I and II instabilities. The evolution of the fore-mentioned types of flow into the nonlinear regime and higher bifurcations have received relatively less attention in the literature. The experimental studies of Schouveiler et al. [54, 55, 56] present many different scenarios for a wide range of the geometrical restrictions and control parameters. For a basic state of Batchelor-type flow, the critical instability has the form of annular rolls or of spiral waves with positive angles developing for increasing rotation rate. It is possible that the two boundary layers merge at high rotation rate leading to spiral rolls with negative helicity. In addition, structures without spatial or temporal periodicity (such as solitary waves or spots) were observed far from the rotation axis during the transition to turbulence (see [42]).

In the present study, we concentrate on Ekman-Couette layer in the presence of an additional *magnetic field*. In the case of magnetic Ekman-Couette layer, the linear properties have been explored since the late 1960s. In an interesting variant of the Ekman layer, the so-called Hartmann layer is observed in electrically conducting viscous fluids under the influence of an additional magnetic field which participates in the balance between viscous, Coriolis and electromagnetic body forces [16, 57, 58, 59]. Benton and Loper [60, 61] have followed the establishment of the magnetic Ekman layer on the basis of analytical studies of an initial value problem. They describe a hydromagnetic “spin-up” mechanisms where the fluid moves radially outside at the upper boundary and sinks to the lower boundary. Loper also studied the analytical solution of a spherical boundary problem [62]. At sufficiently high Reynolds number  $Re$  the magnetic Ekman layer is unstable to  $2D$  rolls of a critical  $Re_c$  which increases with the magnetic energy ( $\cong Q$ ) [16]. One important direction of the research aims at characterization of the stable region in the parameter space. This is for instance, of relevance in the crystal growth processes. In a typical setting the crystals are grown out of a rotating melt; an additional magnetic field is helpful for stabilization [63, 64].

The magnetic activities between the mantle and the core of the earth and the other planets have been explored as well on the basis of magnetic Ekman layer models [65, 66, 67, 68]. Using realistic Ekman thickness Cupal formulated a model in 1998. He transformed the basic equations into a set of  $3D$  geodynamo equations with the use of mean field approximation [12]. Ponty and co-workers have investigated numer-

ically the basic dynamo processes relevant to field generation in the solar tachocline [13]. According to their horizontal plane layer geometry, the local representation of a differentially rotating spherical fluid shell was equivalent to an Ekman layer which is formed on the lower boundary with a strong localized spiraling shear flow. This basic state is easily destabilized either by a convective instability through uniform heating at the base of the layer, or by a purely hydrodynamic instability of the Ekman layer shear flow. The onset of instability is characterized by rolls with a horizontal wavevector inclined at some angle to the meanflow direction. In some studies the fluid flow was found to be stationary in an appropriately chosen moving frame, where it takes the form of a row of cats' eyes. In 1999, Desjardins et. al. have studied the nonlinear stability of Ekman-Hartmann type boundary layers in a rotating magnetohydrodynamics flow in a half-space and also between two confining planes [15]. They have proven rigorously that if the Reynolds number (defined with the Ekman depth as a characteristic length scale) was smaller than a certain critical value, the boundary layer was nonlinearly stable. It was also shown that increasing the normal component of the magnetic field leads to an increase of the critical Reynolds number. In a different model to study of the liquid Earth core, they have investigated the instability of mixed Ekman-Hartmann boundary layers [14]. The instabilities for high  $Re$  caused a critical band to exist with the center on the equator. Depending on the parameters, this band extended over some  $45^\circ$  away from the equator. In a most recent study, Pariev considered an Ekman boundary layer formed in a differentially rotating, conducting, incompressible fluid near the solid end plate limiting the axial extent of the flow in the presence of an axisymmetric magnetic field [69]. He was unable to find stationary solutions, when the shear exceeded a certain threshold and the magnetic field was sufficiently weak.

In this thesis, we investigate the linear and the nonlinear properties of the magnetic Ekman-Couette layer in a simple slab geometry. Although this case has no direct application to most of the examples mentioned before, it will certainly shed some light on the various mechanisms to be expected. In addition, it should be possible to compare directly with laboratory experiments. In fact, we recover the typical scenarios of shear instabilities. For instance at larger rotation rates, oscillatory bifurcations appear which can be classified as type I, type II. In Section 3.1, we give the set of basic equations with the description of the geometry. In Section 3.2, the results of linear analysis based on the Galerkin method and partially on the shooting method will be presented. Then, the results of nonlinear analysis will be discussed in Section 3.3.

## 3.1 Mathematical Formulation of the Problem and Numerical Methods

### 3.1.1 The Ekman spiral

As an appetizer we present in this section the Ekman spiral presumably the first example for a fluid flow in the presence of rotation and external stress. In 1905 V.W. Ekman found this exact solution for the shear profile of a rotating fluid layer in a special ge-

ometry [70]. He considered an infinitely deep fluid layer, where a spatially homogeneous stress is applied to the upper surface of the fluid in the  $x - y$  plane. In an idealization, the fluid layer is assumed to fill the lower half space ( $z < 0$ ) and Ekman concentrated on stationary solutions independent of the horizontal coordinates  $x, y$ . The velocity field  $\mathbf{u} = (U_x, U_y, 0)$  has to fulfill the Navier-Stokes equation:

$$0 = 2\Omega U_y + \nu \frac{\partial^2 U_x}{\partial z^2}, \quad 0 = -2\Omega U_x + \nu \frac{\partial^2 U_y}{\partial z^2}. \quad (3.1)$$

At the upper surface ( $z = 0$ ) an external stress  $\mathbf{S} = (S_x, 0)$  (for instance, produced by the wind at the surface of the ocean) is balanced by the viscous stress:

$$S_x = \rho\nu \frac{\partial U_x}{\partial z} \Big|_{z=0}, \quad 0 = \frac{\partial U_y}{\partial z} \text{ for } z = 0. \quad (3.2)$$

For  $z \rightarrow -\infty$ ,  $\mathbf{u}$  vanishes. The solution of (3.1) with boundary conditions (3.2) is easily obtained (e.g. for  $\Omega > 0$ ):

$$U_x = \frac{S_x D_E}{2\rho\nu} e^{z/D_E} \left( \sin \frac{z}{D_E} + \cos \frac{z}{D_E} \right), \quad (3.3a)$$

$$U_y = \frac{S_x D_E}{2\rho\nu} e^{z/D_E} \left( \sin \frac{z}{D_E} - \cos \frac{z}{D_E} \right), \quad (3.3b)$$

where  $D_E$ , the so-called Ekman depth, is given by  $D_E = \sqrt{\frac{\nu}{\Omega}}$ . It is more convenient to express the solution in terms of the modulus of the flow field  $U = \sqrt{U_x^2 + U_y^2}$  and its orientation  $\theta$  with respect to  $\mathbf{S}$ . Then the expression

$$U = |\mathbf{u}| = \frac{S_x D_E}{\sqrt{2}\rho\nu} e^{z/D_E}, \quad \tan \theta = \frac{\sin \frac{z}{D_E} - \cos \frac{z}{D_E}}{\sin \frac{z}{D_E} + \cos \frac{z}{D_E}}, \quad (3.4)$$

is obtained. Eq. (3.3) tells us that the velocity  $\mathbf{u}$  decreases exponentially with the depth of the fluid on the scale  $D_E$ . Furthermore  $\theta$  changes continuously: At  $z = 0, -\pi D_E/4, -\pi D_E/2$  we find the angles  $\theta = -45^\circ, -90^\circ, 45^\circ$ , respectively. Thus the flow direction subtends an angle of  $-45^\circ$  with  $\mathbf{S}$  at the surface and turns like a right handed spiral as function of depth  $z$ . For  $\Omega < 0$  the solution is analogous, except that we find a left handed spiral. Observing the Ekman spiral directly in nature is difficult, since turbulence comes into play. In addition, there exist several additional processes on the surface of a free fluid layer, such as inertial oscillations, eddies and geostrophic currents.

### 3.1.2 Basic equations and geometry

In this thesis, we consider fluid layers with finite depth  $d$  which are confined between two horizontal plates in the  $x - y$  plane. The fluid is considered to be incompressible, homogeneous, electrically conducting and the whole system is rotating about an axis perpendicular to the plates with angular velocity  $\Omega$ . The plates are assumed to move

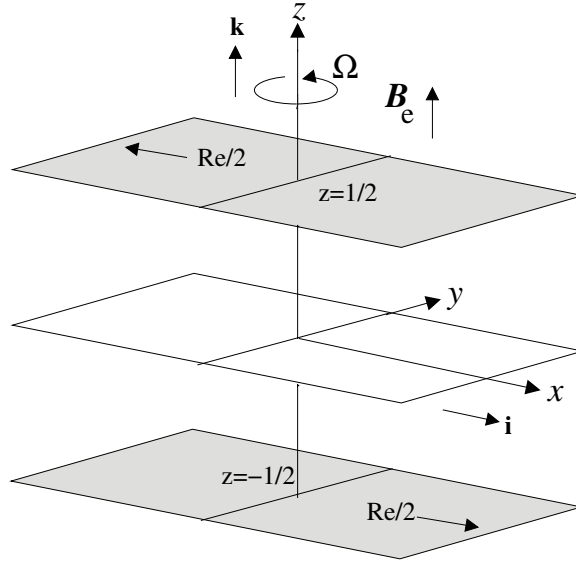


Figure 3.1: Schematic representation of the magnetic Ekman-Couette layer. The fluid layer fills the space  $-1/2 \leq z \leq 1/2$ .

with a constant velocity  $U_d$  parallel to the  $x$ -axis relative to each other (Fig. 3.1). Thus a velocity gradient across the fluid layer develops. In addition, a homogeneous external magnetic field  $\mathbf{B}_e$  is applied parallel to the rotation axis. As indicated in Fig. 3.1 we use a Cartesian coordinate system with the unit vectors  $\mathbf{i}$ ,  $\mathbf{j}$ ,  $\mathbf{k}$  in the direction of the  $x$ ,  $y$ ,  $z$ -axes. The gravity ( $\parallel -\mathbf{k}$ ) does not play a role in the system since the fluid is considered to be incompressible.

The hydrodynamic equations suitably nondimensionalized will depend on the Reynolds number  $Re$ , the Coriolis parameter  $\tau$  and the Chandrasekhar number  $Q$ , which are defined as:

$$Re = U_d d / \nu \quad , \quad \tau = \frac{\Omega d^2}{\nu} \quad , \quad Q = \frac{B_e^2 d^2}{\rho \mu \lambda \nu} \quad , \quad (3.5)$$

where  $\nu$ ,  $\mu$ ,  $\rho$  and  $\lambda$  denote the kinematic viscosity, the magnetic permeability, density and the magnetic diffusivity of the fluid, respectively. We use the thickness  $d$  of the layer as length scale, the vertical diffusion time,  $\frac{d^2}{\nu} = t_v$ , as time scale, and the imposed magnetic flux density  $B_e$  as scale of the magnetic field. The resulting equations are identical to Eqs. (2.3) except that here the temperature field  $\Theta$  is absent. Thus the basic equations of motion for the velocity field  $\mathbf{u}$  and for the magnetic induction  $\mathbf{b}$  in dimensionless form read as follows:

$$\frac{\partial}{\partial t} \mathbf{u} + \mathbf{u} \cdot \nabla \mathbf{u} + 2\tau \mathbf{k} \times \mathbf{u} = -\nabla \Pi + \nabla^2 \mathbf{u} + Q \mathbf{k} \cdot \nabla \mathbf{b}, \quad (3.6a)$$

$$\nabla \cdot \mathbf{u} = 0, \quad (3.6b)$$

$$\frac{\partial}{\partial t} \mathbf{b} + \mathbf{u} \cdot \nabla \mathbf{b} - \mathbf{b} \cdot \nabla \mathbf{u} = \frac{\lambda}{\nu} (\nabla^2 \mathbf{b} + \mathbf{k} \cdot \nabla \mathbf{u}), \quad (3.6c)$$

$$\nabla \cdot \mathbf{b} = 0, \quad (3.6d)$$

where all gradient terms in (3.6a) have been combined into the pressure term  $\nabla\Pi$ . The magnetic field in physical units has been represented in the form  $\mathbf{B} = B_e(\mathbf{k} + \frac{z}{\lambda}\mathbf{b})$  where  $\mathbf{k}$  is the unit vector in the  $z$ - direction.

Let us first determine the basic solutions  $\mathbf{U}_0, \mathbf{B}_0$  of Eqs. (3.6) which depend only on  $z$ . In this situation, Eqs. (3.6) reduce to

$$\frac{d^2}{dz^2}\mathbf{U}_0 - 2\tau\mathbf{k} \times \mathbf{U}_0 = -Q\frac{d}{dz}\mathbf{B}_0, \quad (3.7a)$$

$$\frac{d^2}{dz^2}\mathbf{B}_0 = -\frac{d}{dz}\mathbf{U}_0. \quad (3.7b)$$

We have no-slip boundary conditions for the velocity field.

$$\mathbf{u} = \mp \frac{1}{2}Re\mathbf{i}, \quad \text{at } z = \pm \frac{1}{2}. \quad (3.8)$$

The plates are assumed to be infinitely electrically conducting. We require  $\mathbf{B}_0 = 0$  at  $z = \pm \frac{1}{2}$  since the magnetic field can not penetrate into infinitely conducting plate.

The solutions of Eqs. (3.7) are now easily calculated as:

$$\mathbf{u} = \mathbf{U}_o = (U_{0x}(z), U_{0y}(z), 0), \quad (3.9a)$$

$$\mathbf{b} = \mathbf{B}_0 = (B_{0x}(z), B_{0y}(z), 0) \quad (3.9b)$$

with

$$U_{0x}(z) = -a \sin \Gamma z \cosh \beta z + b \cos \Gamma z \sinh \beta z \quad (3.10a)$$

$$U_{0y}(z) = a \cos \Gamma z \sinh \beta z + b \sin \Gamma z \cosh \beta z \quad (3.10b)$$

$$B_{0x}(z) = a'(\beta \cosh \beta z \sinh \beta z - \Gamma \cos \Gamma z \sin \Gamma z) + \\ b'(\beta \sinh \beta \frac{1}{2} \cosh \beta \frac{1}{2} + \Gamma \sin \Gamma \frac{1}{2} \cos \Gamma \frac{1}{2}) \quad (3.10c)$$

$$B_{0y}(z) = a'(-\beta \cos \Gamma z \sin \Gamma z - \Gamma \cosh \beta z \sinh \beta z) + \\ b'(\Gamma \sinh \beta \frac{1}{2} \cosh \beta \frac{1}{2} + \beta \sin \Gamma \frac{1}{2} \cos \Gamma \frac{1}{2}) \quad (3.10d)$$

The constants  $\beta$  and  $\Gamma$  are given as

$$\beta = \frac{1}{\sqrt{2}}\left(Q + (Q^2 + 4\tau^2)^{\frac{1}{2}}\right)^{\frac{1}{2}}, \quad \Gamma = \frac{1}{\sqrt{2}}\left(-Q + (Q^2 + 4\tau^2)^{\frac{1}{2}}\right)^{\frac{1}{2}}. \quad (3.11a)$$

Furthermore, the coefficients  $a, a', b, b'$  which depend linearly on  $Re$  are determined by

$$a\left\{\sin \frac{\Gamma}{2} \cosh \frac{\beta}{2}\right\}^{-1} = -b\left\{\cos \frac{\Gamma}{2} \sinh \frac{\beta}{2}\right\}^{-1} \\ = \frac{Re}{2}\left\{\sin^2 \frac{\Gamma}{2} \cosh^2 \frac{\beta}{2} + \cos^2 \frac{\Gamma}{2} \sinh^2 \frac{\beta}{2}\right\}^{-1} \quad (3.12a)$$

$$a' = \frac{Re}{2}\left((\sinh \beta z \cos \Gamma z)^2 + (\cosh \beta z \sin \Gamma z)^2\right)^{-1} \quad (3.12b)$$

$$b' = \frac{Re}{2}\left((\sinh \beta \frac{1}{2} \cos \Gamma \frac{1}{2})^2 + (\cosh \beta \frac{1}{2} \sin \Gamma \frac{1}{2})^2\right)^{-1}. \quad (3.12c)$$

It is certainly helpful to visualize the meanflow  $\mathbf{U}_o$  and  $\mathbf{B}_o$ . In Fig. 3.2, we present the profiles of  $\mathbf{U}_o$  and  $\mathbf{B}_o$  between the upper and lower plates for various parameter sets  $\tau, Q$ . It is evident that the velocity components  $U_x, U_y$  are increasingly concentrated at the boundaries with increasing  $\tau$  for constant  $Q$  values. Note also that  $U_x$  and  $U_y$  are antisymmetric with respect to reflections at the midplane  $z = 0$ , while the magnetic field components  $B_x$  and  $B_y$ , which vanish at the boundaries, are even in  $z$ . With increasing  $\tau$ , the functional form of  $B_x, B_y$  does not change too much in the central part ( $-0.25 < z < 0.25$ ). However their values at the boundaries change dramatically (see the plots Fig. 3.2c,f). In Fig. 3.3, we present an example of the derivatives of  $\mathbf{U}_o(z)$  and of  $\mathbf{B}_o(z)$  in the case of  $\tau = 10, Q = 40$ . It is obvious that  $\frac{d}{dz}B_{0x}, \frac{d}{dz}B_{0y}$  in Fig. 3.3 are proportional to  $-U_{0x} - U_{0y}$  in Fig. 3.2 which is consistent with the Eqs. (3.7).

In the following we concentrate on two scalar quantities to characterize  $\mathbf{U}_o$ . At first, we consider the magnitude of the shear  $Sh$  (in units of  $Re$ ) exerted by the flow at the upper boundary which is given as:

$$Sh = \frac{1}{Re} \sqrt{\left(\frac{\partial}{\partial z}U_{0x}\left(\frac{1}{2}\right)\right)^2 + \left(\frac{\partial}{\partial z}U_{0y}\left(\frac{1}{2}\right)\right)^2}. \quad (3.13)$$

$Sh$  is plotted as a function of the rotation rate  $\tau$  and magnetic energy  $Q$  in Fig. 3.4.  $Sh$  increases rapidly from its limit  $Sh = 1$  at  $\tau = Q = 0$  both with increasing  $\tau$  and  $Q$ . Note that the curve reflects the characteristic structure of Ekman layer since  $Sh \sim \sqrt{\tau}$  in the  $Q \rightarrow 0$  limit. With increasing magnetic field  $\sqrt{Q}$ , the shear increases as well like  $Sh \sim \sqrt{Q}$  for low  $\tau$ . However,  $Sh$  remains almost constant as function of  $Q$  in the case of high  $\tau$ . In the case of strong magnetic field  $Q$ ,  $Sh$  increases almost linearly with  $\tau$  (see e.g.  $Q = 100$ ).

Secondly, we consider the angle  $\gamma$  between the direction of the shear at the upper boundary and the  $x$ - axis which reads:

$$\gamma = \arctan\left(\frac{\frac{\partial U_y}{\partial z}\big|_{\frac{1}{2}}}{\frac{\partial U_x}{\partial z}\big|_{\frac{1}{2}}}\right). \quad (3.14)$$

The angle  $\gamma$  is plotted as function of  $\tau$  and  $Q$  in Fig. 3.5. It is remarkable how rapidly  $\gamma$  attains the asymptotic Ekman value of  $45^\circ$  with increasing  $\tau$  in the case of Eq. (3.14) for low values of magnetic energy  $Q$ . However, this asymptotic behavior is not seen for high magnetic field. In fact, the angles decrease continuously with  $Q$ . For instance,  $\gamma \sim 35^\circ$  for  $(\tau, Q) = (100, 100)$ . It is also obvious that  $\gamma$  decreases linearly as function of  $Q$  at large rotation rates.

Our main topic in the following section is the investigation of instabilities of the basic solutions  $\mathbf{U}_o, \mathbf{B}_o$  (Eq. (3.9)) which lead to flow fields which depend on  $x, y, t$  as well. As usual we introduce the standard poloidal-toroidal decompositions for the solenoidal vector fields  $\mathbf{u}$  and  $\mathbf{b}$ , (see Eqs. (3.6b) and (3.6d)):

$$\mathbf{u} = \mathbf{U}_o + \bar{\mathbf{u}} + \nabla \times (\nabla \times \mathbf{k}v) + \nabla \times \mathbf{k}w =: \mathbf{U}_o + \bar{\mathbf{u}} + \delta v + \varepsilon w, \quad (3.15a)$$

$$\mathbf{b} = \mathbf{B}_o + \bar{\mathbf{b}} + \nabla \times (\nabla \times \mathbf{k}h) + \nabla \times \mathbf{k}g =: \mathbf{B}_o + \bar{\mathbf{b}} + \delta h + \varepsilon g, \quad (3.15b)$$

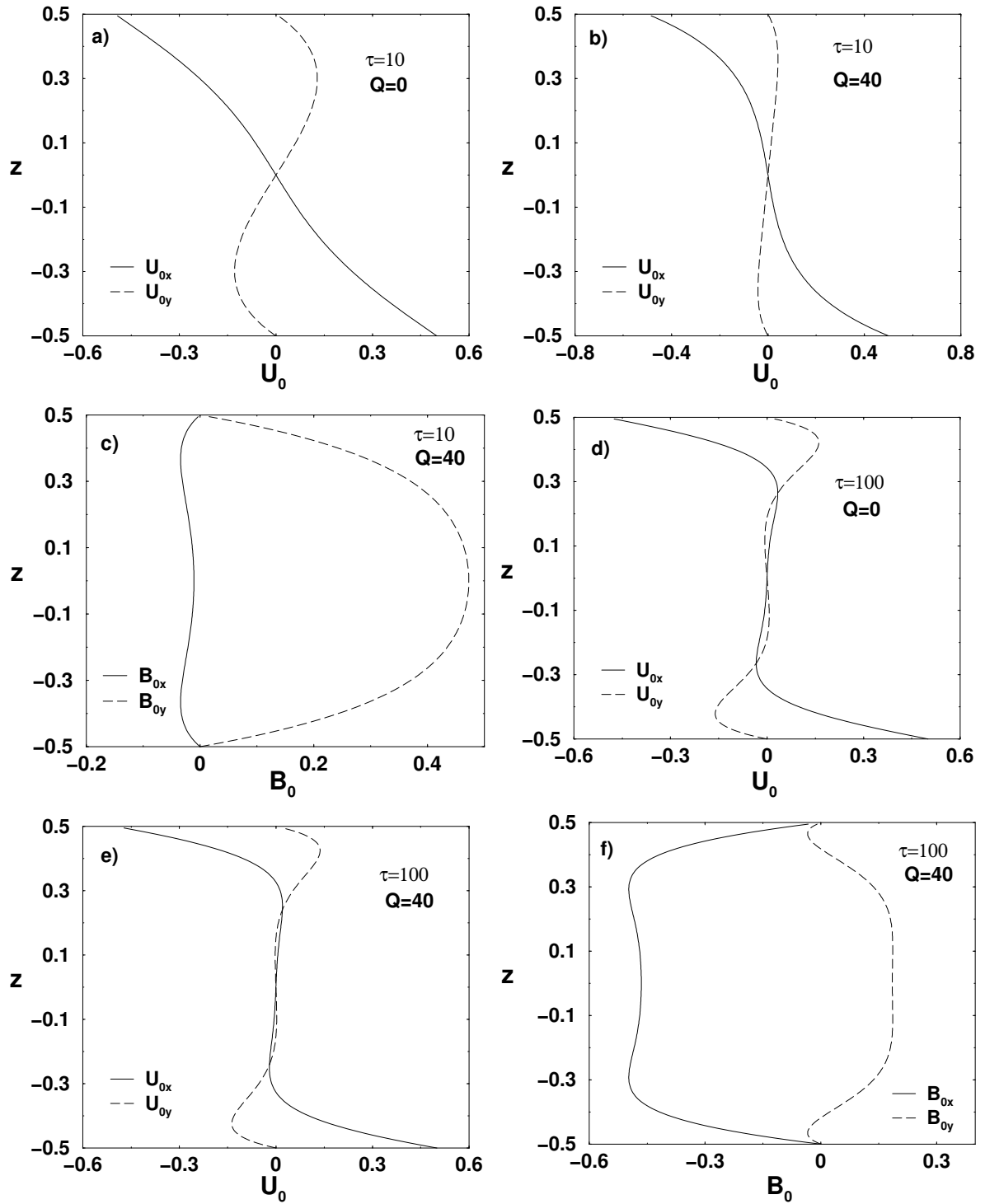


Figure 3.2: Profiles of  $U_0$  and  $B_0$  as function of  $z$  for several parameter sets.

where the overbars in  $\bar{\mathbf{u}}$  and  $\bar{\mathbf{b}}$  denote the average of  $\mathbf{u} - \mathbf{U}_0$  and  $\mathbf{b} - \mathbf{B}_0$  over the  $x, y$ - plane. The functions  $v, h$  and  $w, g$  which describe the poloidal and toroidal

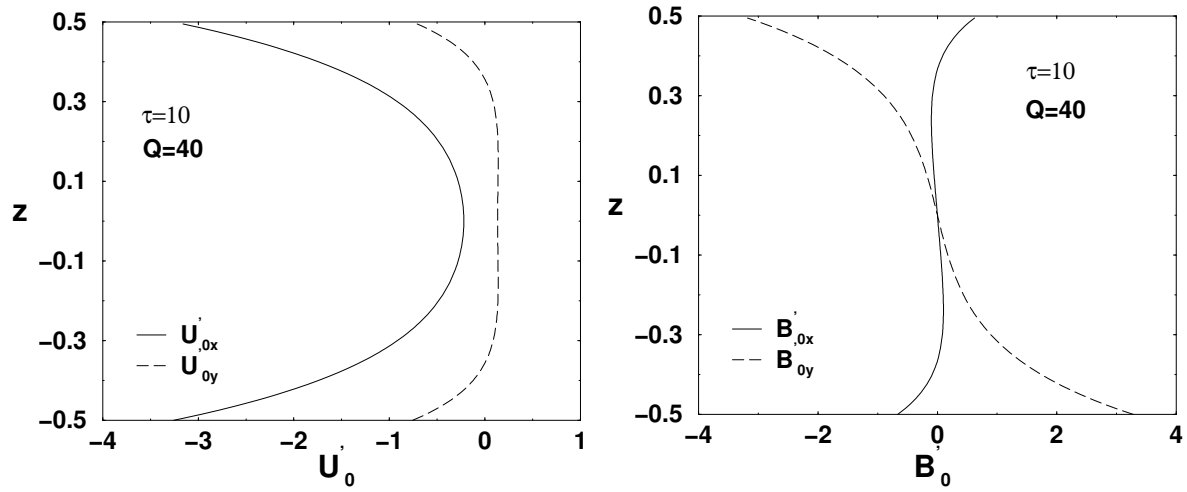


Figure 3.3: The stresses  $\frac{dU_0}{dz}$  and  $\frac{dB_0}{dz}$  with respect to  $z$  in the case of  $\tau = 10$ ,  $Q = 40$ .

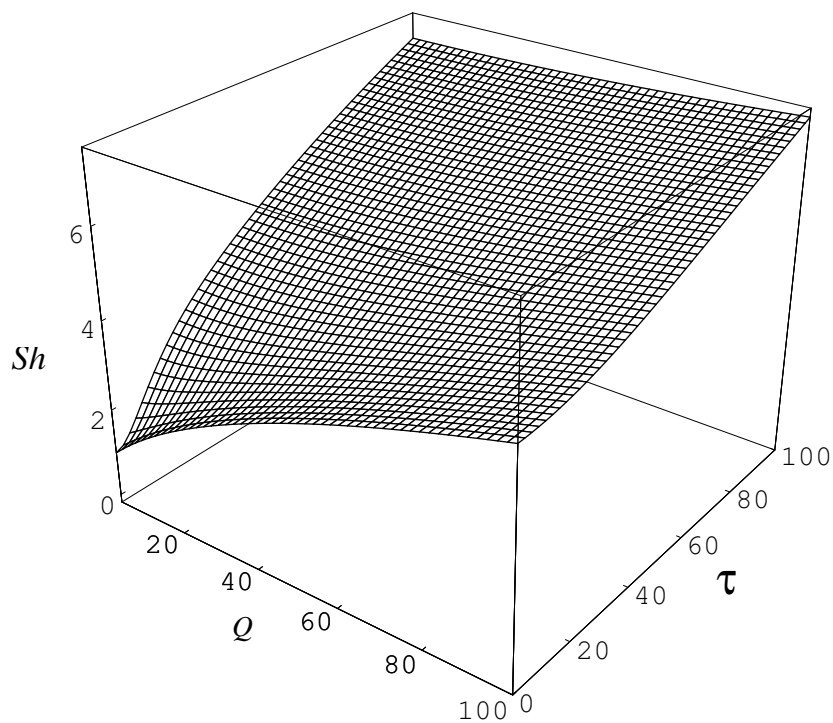


Figure 3.4: The modulus of the shear (Eq. (3.13)) as function of  $\tau$  and  $Q$ .

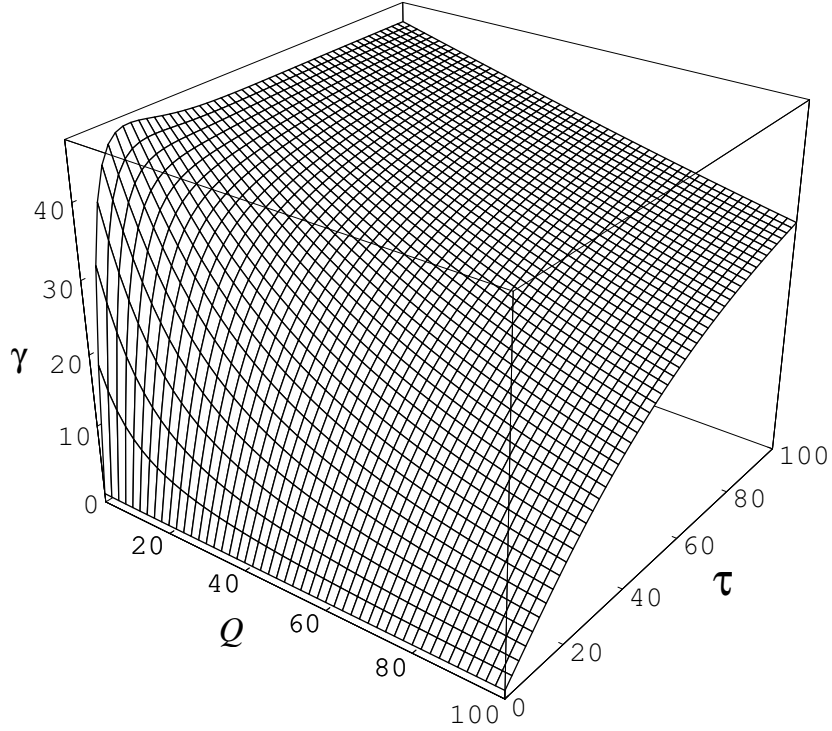


Figure 3.5: The variation of the stress angle  $\gamma$  in degrees (see Eq. (3.14)) at the upper boundary in the  $\tau, Q$  parameter space.

potentials of the velocity and the magnetic field, respectively, are uniquely defined if the conditions  $\bar{v} = \bar{h} = \bar{w} = \bar{g} = 0$  are imposed. In the following we will also use  $\mathbf{U}(z) := \mathbf{U}_0(z) + \bar{\mathbf{U}}(z)$  for the  $x - y$  independent parts of velocity fields.

To simplify the analysis in the following, we shall focus our attention on the case of liquid metals where the ratio  $\frac{\lambda}{\nu}$  is of the order  $10^4$  to  $10^6$ . In this limit we can drop all terms on the left hand side of (3.6c). After applying  $\delta$  and  $\varepsilon$  on (3.6c) in this limit, we obtain for the potentials  $h, g$  the following equations:

$$\nabla^2 \Delta_2 h = -\mathbf{k} \cdot \nabla \Delta_2 v, \quad (3.16a)$$

$$\nabla^2 \Delta_2 g = -\mathbf{k} \cdot \nabla \Delta_2 w. \quad (3.16b)$$

It appears that Eq. (3.16a) for  $h$  with the corresponding boundary condition has not to be solved explicitly, since  $h$  can be eliminated from the problem by replacing  $\nabla^2 \Delta_2 h$  in (3.6a) with  $-\mathbf{k} \cdot \nabla \Delta_2 v$  in accordance with (3.16a) since  $\delta(Q\mathbf{k} \cdot \nabla \mathbf{b}) \sim -Q \frac{\partial^2}{\partial z^2} \Delta_2 v$ .

After the application of the differential operators  $\delta$  and  $\varepsilon$  on the velocity equation (3.6a) we arrive in the limit  $\lambda \gg \nu$  at the following equations for velocity potentials

$v$ ,  $w$  and the magnetic potential  $g$  which are almost identical to Eqs. (2.6):

$$\begin{aligned} \frac{\partial}{\partial t} \nabla^2 \Delta_2 v + \boldsymbol{\delta} \cdot (\mathbf{u} \cdot \nabla \mathbf{u}) &= \nabla^4 \Delta_2 v - 2\tau \frac{\partial}{\partial z} \Delta_2 w - \mathbf{U} \cdot \nabla \nabla^2 \Delta_2 v \\ &+ \frac{\partial^2}{\partial z^2} \mathbf{U} \cdot \nabla \Delta_2 v - Q \frac{\partial^2}{\partial z^2} \Delta_2 v, \end{aligned} \quad (3.17a)$$

$$\begin{aligned} \frac{\partial}{\partial t} \Delta_2 w + \boldsymbol{\varepsilon} \cdot (\mathbf{u} \cdot \nabla \mathbf{u}) &= \nabla^2 \Delta_2 w + 2\tau \frac{\partial}{\partial z} \Delta_2 v - \mathbf{U} \cdot \nabla \Delta_2 w \\ &+ \frac{\partial}{\partial z} \mathbf{U} \cdot \boldsymbol{\varepsilon} \Delta_2 v + Q \frac{\partial}{\partial z} \Delta_2 g, \end{aligned} \quad (3.17b)$$

$$\nabla^2 g = -\frac{\partial}{\partial z} w. \quad (3.17c)$$

In addition, the equations for the mean flow  $\bar{\mathbf{u}}$  and the mean magnetic induction are obtained by averaging the velocity (3.6a) and magnetic induction equations (3.6c) over the  $x - y$  plane.

$$\frac{\partial}{\partial t} \bar{\mathbf{u}} + 2\tau \mathbf{k} \times \bar{\mathbf{u}} - \frac{\partial}{\partial z} \overline{\Delta_2 v \left( \nabla_2 \frac{\partial}{\partial z} v + \boldsymbol{\varepsilon} w \right)} = \frac{\partial^2}{\partial z^2} \bar{\mathbf{u}} + Q \frac{\partial}{\partial z} \bar{\mathbf{b}}, \quad (3.18a)$$

$$\frac{\partial^2}{\partial z^2} \bar{\mathbf{b}} + \frac{\partial}{\partial z} \bar{\mathbf{u}} = 0. \quad (3.18b)$$

In writing down Eqs. (3.17, 3.18a) we have introduced the horizontal gradient,  $\nabla_2 \equiv \nabla - \mathbf{k}(\mathbf{k} \cdot \nabla)$ , and the horizontal Laplacian,  $\Delta_2 \equiv \nabla_2 \cdot \nabla_2$ . In line with Eqs. (3.8, 3.15) the basic Eqs. (3.17, 3.18) must be solved subject to the boundary conditions

$$v = \frac{\partial}{\partial z} v = w = \frac{\partial}{\partial z} g = 0 \quad \text{at} \quad z = \pm \frac{1}{2}. \quad (3.19)$$

The boundary conditions for  $v, w$  result from the no-slip boundary conditions for the velocity field  $\mathbf{u}$ . The condition for  $g$  results from the following consideration: The infinitely conducting boundary plates shield perfectly the magnetic field which thus vanishes outside the fluid layer. Consequently, there exist a fluctuating surface current density  $\mathbf{j}(x, y, t)$  on the plates which fulfills the following expressions over the plate.

$$\nabla \times (\mathbf{B}_{ext} - \mathbf{B}_i) = \mu_0 \mathbf{j}, \quad (3.20)$$

Here  $\mathbf{B}_{ext}$  denotes the (vanishing) external magnetic field and  $B_i$  the inner field. In other words, the electric current  $\mathbf{j}_{el} = \sigma(\mathbf{E} + \mathbf{u} \times \mathbf{B})$  occurs in the limit  $z \rightarrow \pm 1/2$  where  $\mathbf{u}$  vanishes considering  $\Delta_2 g \neq 0$ . In addition, using  $\mathbf{k} \times \nabla \times$  and  $\nabla$  of  $\mathbf{B}$  in terms of the magnetic potentials  $h, g$  at the boundaries, we arrive at

$$\mathbf{k} \times \nabla \times \mathbf{B} = -\nabla^2 \nabla_2 h + \mathbf{k} \times \nabla \nabla \cdot \mathbf{k} g = 0, \quad (3.21)$$

$$\nabla \cdot \mathbf{B} = 0. \quad (3.22)$$

Thus, we end up with the condition  $\frac{\partial}{\partial z} g = 0$  at  $z = \pm \frac{1}{2}$  in Eq. (3.19).

Following Eq. (1.1), the magnetohydrodynamic equations (3.17, 3.18a) are written in a condensed notation as:

$$\mathcal{D} \frac{d}{dt} \mathbf{V}(\mathbf{x}, t) = \mathcal{L} \mathbf{V}(\mathbf{x}, t) + \mathbf{N}(\mathbf{V}(\mathbf{x}, t), \mathbf{V}(\mathbf{x}, t)), \quad \mathcal{L} = \mathcal{A} + Re \mathcal{B}, \quad (3.23)$$

where the symbolic vector  $\mathbf{V}(\mathbf{x}, t) = (v, w, g, \bar{\mathbf{u}})$  represents all fields in Eqs. (3.17, 3.18a).  $\mathbf{V}(\mathbf{x}, t) \equiv 0$  corresponds to the basic state. In line with the investigations [24, 25] we assume the idealization of an infinitely extended fluid layer in the horizontal plane. Thus we use periodic boundary conditions (i.e the  $x, y$ -dependence is captured by a 2D Fourier series). The vertical boundary conditions are satisfied by a Galerkin ansatz in analogy to Eq. (2.12). The representations of  $v$  and  $w$  are identical but the potential  $g$  requires a slightly modified form. Since we have to fulfill  $\frac{\partial}{\partial z} g(z = \pm 1/2) = 0$  (see Eq. (3.19)) the following ansatz is used:

$$g(x, y, z, t) = \sum_{n=1}^N \sum_{l, m=-M}^M g_{lmn}(t) \exp[i(lq_x x + mq_y y)] \frac{d}{dz} S_n(z). \quad (3.24)$$

Due to the strong variation of the velocity fields at boundaries  $z = \pm \frac{1}{2}$  for large  $\tau$ , we have to keep in general more Galerkin modes than in the *RBC* problem in Chap. 2, typically we took  $N = 14$  as a satisfactory cutoff in our calculations.

In addition to Galerkin methods, we have also used the standard shooting method to solve the linear stability problem. However the shooting method is not well suited for systematic scans of the  $\tau, Q$  parameter space. It becomes in fact very tedious since the resulting determinants are not robust against variation of the parameters. However in test of consistency the two methods gave practically the same result when they were compared.

## 3.2 Linear Analysis

In principle, we follow closely the methods already explained in detail in Chap. 2. The onset of instability is stationary when  $\tau$  is small, but oscillatory for the high  $\tau$  (i.e  $\tau > 25$ ) as has also been found in earlier studies of the  $Q = 0$  case [41, 45]. In contrast to the *RBC* problem however the chirality is always broken since the critical rolls are oblique.

To give a first impression of the  $\tau$  dependence of the critical Reynolds number  $Re_c$  we have plotted a representative example of  $Re_c$  as function of  $\tau$  in Fig. 3.6. One observes three different types of destabilization. At low  $\tau$  the bifurcation is stationary and the threshold curve looks almost parabolic. Above  $\tau = 25$  the bifurcation becomes oscillatory. At first, we have the type I instability until fairly high  $\tau$  ( $\sim 52$ ), where a crossover to the type II bifurcation takes place, which differs by the orientation of the rolls.

In the following subsections, we will discuss the different branches of  $Re_c$  in Fig. 3.6. As in Chap. 2, we calculate the critical Reynolds number  $Re_c$  as the minimum

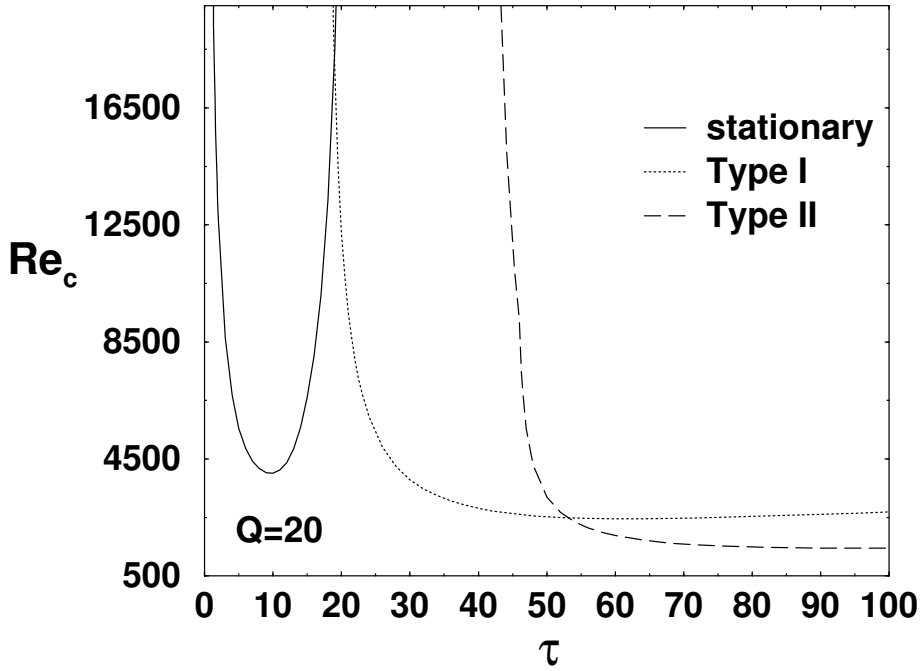


Figure 3.6: Critical Reynolds numbers  $Re_c$  for the onset of disturbances of the stationary modes (solid) and modes for type I (dotted) and type II (dashed) as a function of  $\tau$  in the case of  $Q = 20$ .

of the neutral curve  $R_0(\mathbf{q})$  at the critical wavevector  $\mathbf{q}_c$ . In the previous chapter (Chap. 1) the wavevectors  $\mathbf{q}$  have been represented as  $\mathbf{q} = |\mathbf{q}|(\cos(\chi), \sin(\chi))$  where  $\chi$  denotes the angle of  $\mathbf{q}$  with the positive  $x$ -axis. Because of the equivalence of  $\mathbf{q}$  and  $-\mathbf{q}$  we can restrict  $\chi$  to the interval  $(0 \leq \chi \leq \pi)$  without loss of generality. For historical reasons, we will use in this chapter sometimes Cartesian coordinates  $(\xi, \eta)$  in the  $(x, y)$  plane where the  $\eta$  axis is aligned with  $\mathbf{q}$ , i.e. the  $(\xi, \eta)$  coordinate system is rotated by an angle  $-\phi$  ( $-\pi/2 \leq \phi \leq \pi/2$ ) with respect to the  $(x, y)$  system where  $\phi = \chi - \pi/2$ . From now on we call  $\phi$  the *obliqueness* or *orientation* angle. Thus we have  $\mathbf{q} = q(\cos(\phi + \pi/2), \sin(\phi + \pi/2)) = q(-\sin(\phi), \cos(\phi))$ . In the Ekman layer problem,  $|\phi|$  is typically small ( $\lesssim 23^\circ$ ), i.e.  $\mathbf{q}$  is always approximately parallel to the  $y$ -axis and the roll axis is almost parallel to the shear direction.

### 3.2.1 Stationary bifurcation at small $\tau$

This section is devoted to the stationary destabilizations of the basic solutions Eqs. (3.9, 3.10) (see Fig. 3.2) at low  $\tau$ . In Fig. 3.7a we present the critical Reynolds number  $Re_c$ . The threshold diverges in the limit  $\tau = 0$  and around  $\tau = 30$ , where the type I oscillatory instability prevails (see below). As function of  $\tau$ , we have an almost parabolic shape for intermediate  $\tau$  as already visible in Fig. 3.6. The threshold increases with the magnetic energy ( $Q$ ) which thus stabilizes the basic state. The curvature of the parabola increases with increasing  $Q$ . For large  $\tau$  (see e.g.  $Q = 20$

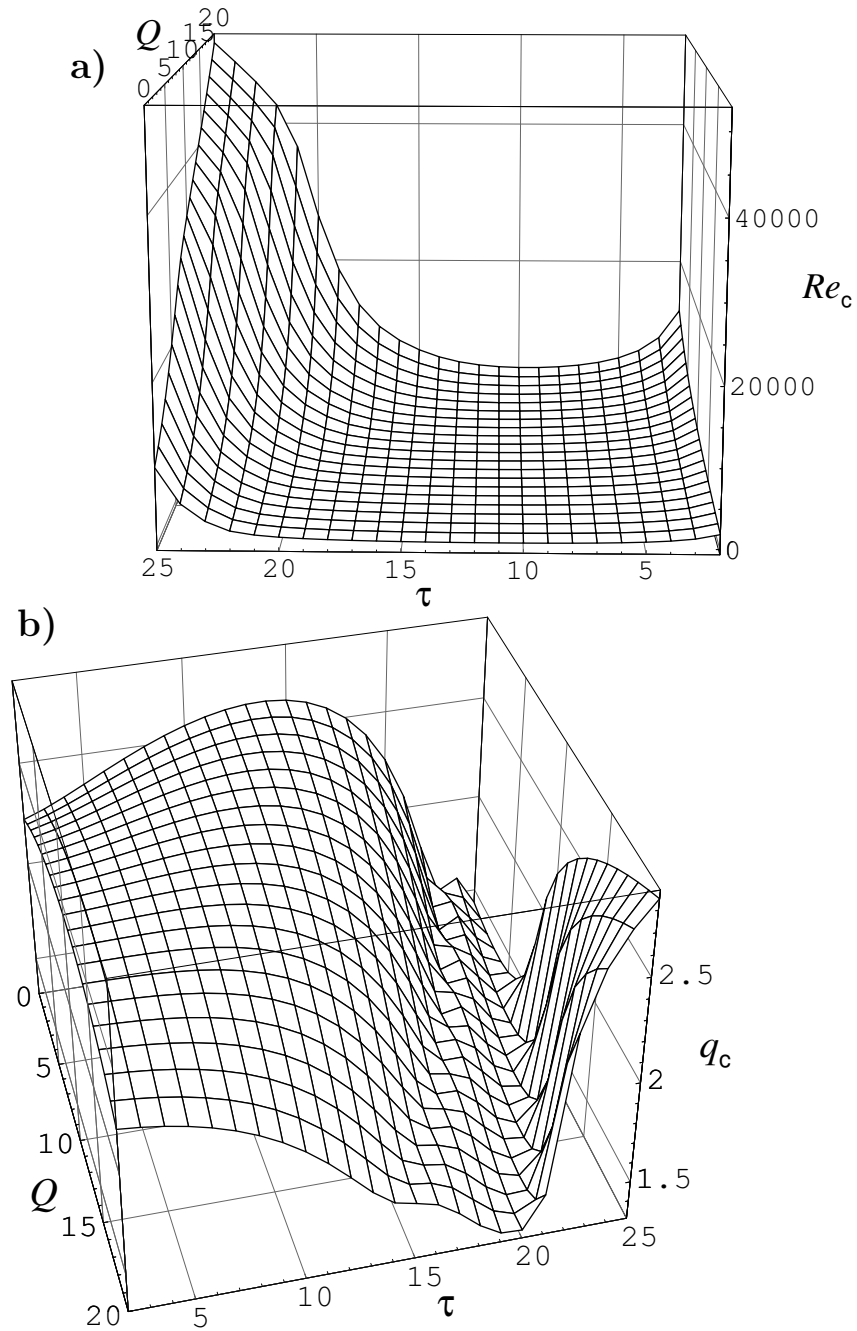


Figure 3.7: (a) The critical Reynolds number  $Re_c$  and (b) the modulus  $q_c$  of the critical wavevector  $\mathbf{q}_c$  as functions of  $\tau$  and  $Q$  for the stationary case.

and  $20 < \tau < 25$ ) a linear increase of  $Re_c(\tau)$  takes over.

The modulus  $q_c$  of  $\mathbf{q}_c$  is plotted in Fig. 3.7b. The most interesting point is a kind of valley which appears for high  $Q$  values and which moves towards relatively smaller values of  $\tau$ . The critical wave number  $q_c$  increases along the valley with increasing  $Q$ . Starting at small  $\tau$ ,  $Q$  the critical wave number  $q_c$  first passes a local maximum before

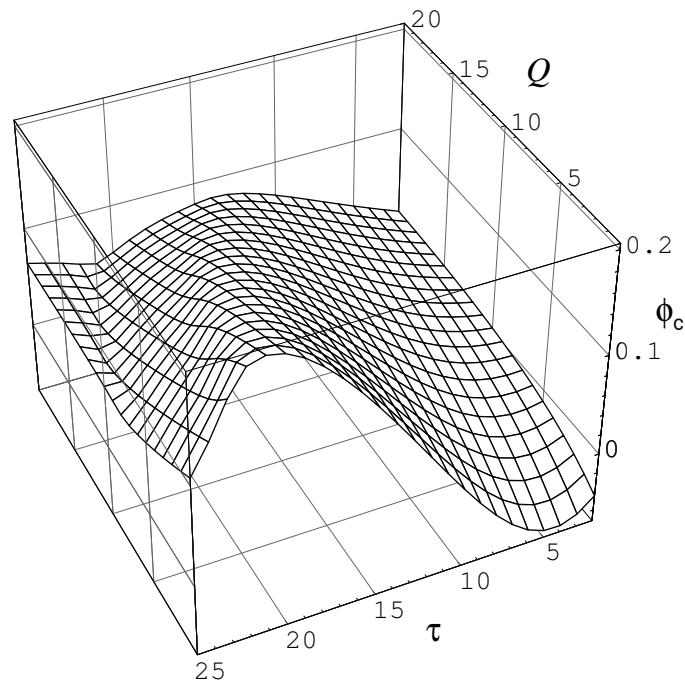


Figure 3.8: The critical obliqueness angle  $\phi_c$  (i.e.  $\phi_c = (90^\circ - \chi_c)$ ) in radian as functions of  $\tau$  and  $Q$  for the stationary case.

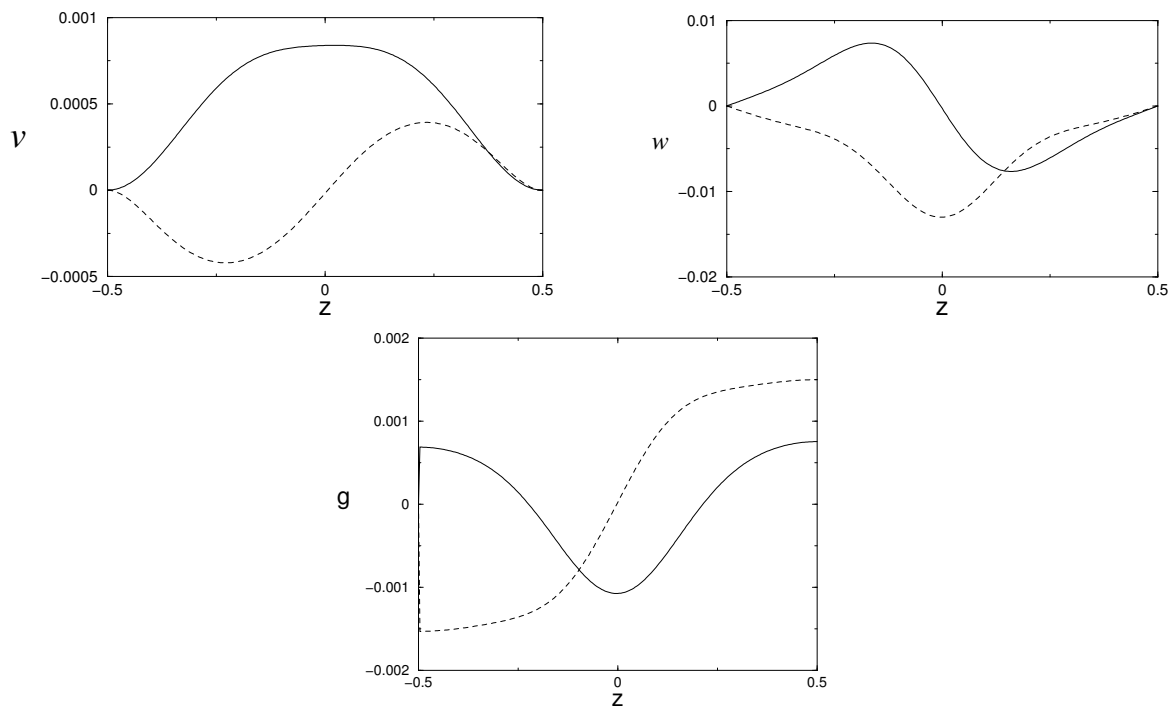


Figure 3.9: The typical evolution of scalar functions as function of  $z$  at  $Re = 940$ ,  $\tau = 10$ ,  $Q = 5$ ,  $q = 2.5$  and  $2.41^\circ$ .

entering the valley regime while the local maximum vanishes at large  $Q$ .

In Fig. 3.8, we show the critical obliqueness angle  $\phi_c$ . With decreasing  $\tau$ ,  $\phi_c$  slightly decreases, passes a local maximum and decays to small values (either positive or negative) near  $\phi_c = 0$ . For large  $Q$ , this decay is almost linear while for  $Q = 0$  a shallow local minimum is shown. For instance, for  $\tau = 2$  and  $Q = 0$  we have  $\phi = -2.52^\circ$ . Some selected numerical values for the critical data with respect to  $\tau$  and  $Q$  have been collected in Table 3.1.

	$Q = 0$			$Q = 5$			$Q = 10$		
	$Re_c$	$q_c$	$\phi_c$ (deg.)	$Re_c$	$q_c$	$\phi_c$ (deg.)	$Re_c$	$q_c$	$\phi_c$ (deg.)
$\tau = 5$	853.09	2.35	-3.66	1350.64	2.44	-0.676	2105.61	2.46	0.802
$\tau = 10$	624.19	2.56	0.516	931.4	2.54	2.349	1415.67	2.46	3.438
$\tau = 15$	697.38	2.62	6.818	1021.74	2.48	6.99	1593.75	2.25	6.76
$\tau = 20$	1128.73	2.26	11.17	1903.29	1.87	9.568	4212.76	1.57	7.047
	$Q = 15$			$Q = 20$			$Q = 25$		
	$Re_c$	$q_c$	$\phi_c$ (deg.)	$Re_c$	$q_c$	$\phi_c$ (deg.)	$Re_c$	$q_c$	$\phi_c$ (deg.)
$\tau = 5$	3323.91	2.38	1.547	5553.04	2.17	1.776	10796.95	1.80	1.662
$\tau = 10$	2254.02	2.27	3.896	4015.36	1.95	3.724	9129.49	1.61	2.922
$\tau = 15$	2846.19	1.87	6.073	6598.56	1.59	4.526	17087.88	1.40	2.979
$\tau = 20$	9933.69	1.45	4.756	26479.19	1.35	2.979	50342.24	2.33	2.464

Table 3.1: Some critical parameters of magnetic Ekman-Couette layer problem for the stationary roll solution.

In the following we will present some more detailed information about the linear analysis of the stationary modes. First, we have plotted in Fig. 3.9 the scalar potentials  $v$ ,  $w$ ,  $g$  which determine according to Eqs. (3.15, 3.16) the velocity and the magnetic field.  $v$  and  $w$  vanish at the boundaries  $z = \pm \frac{1}{2}$ . However,  $g$  is finite at the boundaries consistent with the boundary conditions Eq. (3.19). To give an impression of the periodic roll structures, the  $z$ - profiles of stream function  $\partial_\eta v$ , longitudinal velocity  $\partial_\eta w$  and magnetic field strength  $\partial_\eta g$  are presented in Fig. 3.10 in a plane perpendicular to the roll axis. The stationary rolls seem to cover the entire fluid layer. Besides, the contour lines of magnetic field strength  $\partial_\eta g$  are seen to be finite at the boundaries (Fig. 3.10c). In addition, an asymmetry along  $z = 0$  plane (i.e. middle of the layer) can be clearly identified.

In Fig. 3.11, we show a representative example ( $\tau = 17$ ,  $Q = 10$ ) of the eigenvalue spectra slightly above  $Re_c$  in the  $q_x - q_y$  plane. As seen in the left plot where the growth rates  $\sigma$  are drawn, there exist a few local maxima. Among these maxima, the highest one corresponds to the critical Reynolds number  $Re_c$ .

Note also a local maxima near  $(q_x, q_y) = (0, 0)$  which does not affect the entire dynamics. The angle between roll axis and  $y$ - axis,  $\phi = \arctan(q_x/q_y)$ , is easily extracted from the location of the absolute maxima. In the right panel of Fig. 3.11, the corresponding imaginary parts  $\omega$  of the leading eigenvalues  $\lambda$  are plotted. The regime of vanishing  $\omega$  is mainly associated with positive  $\phi$  except for the narrow cone

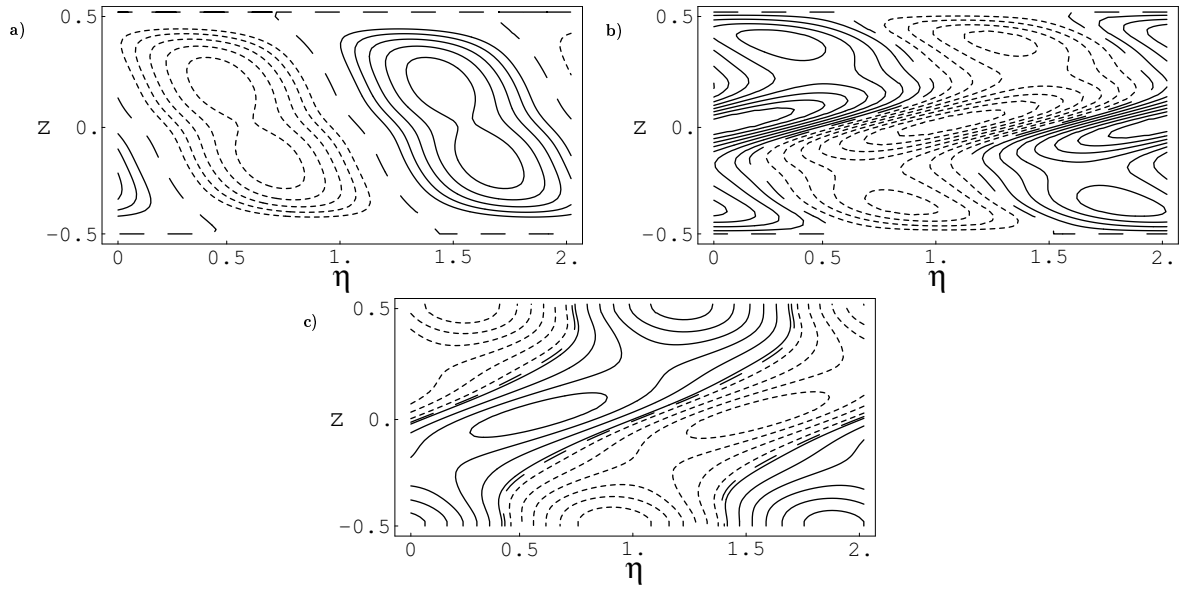


Figure 3.10: Contour plot representation of (a) the stream function  $(\partial_\eta v)$ , (b) lines of constant velocity  $(\partial_\eta w)$  and (c) the magnetic field in direction of  $\xi$ , (i.e.  $\eta = (x \sin \phi + y \cos \phi)$ ) for  $Re = 11691.5$ ,  $\tau = 10$ ,  $Q = 25$ ,  $\phi = 1.89^\circ$  and  $q = |\mathbf{q}| = 2.1$ .

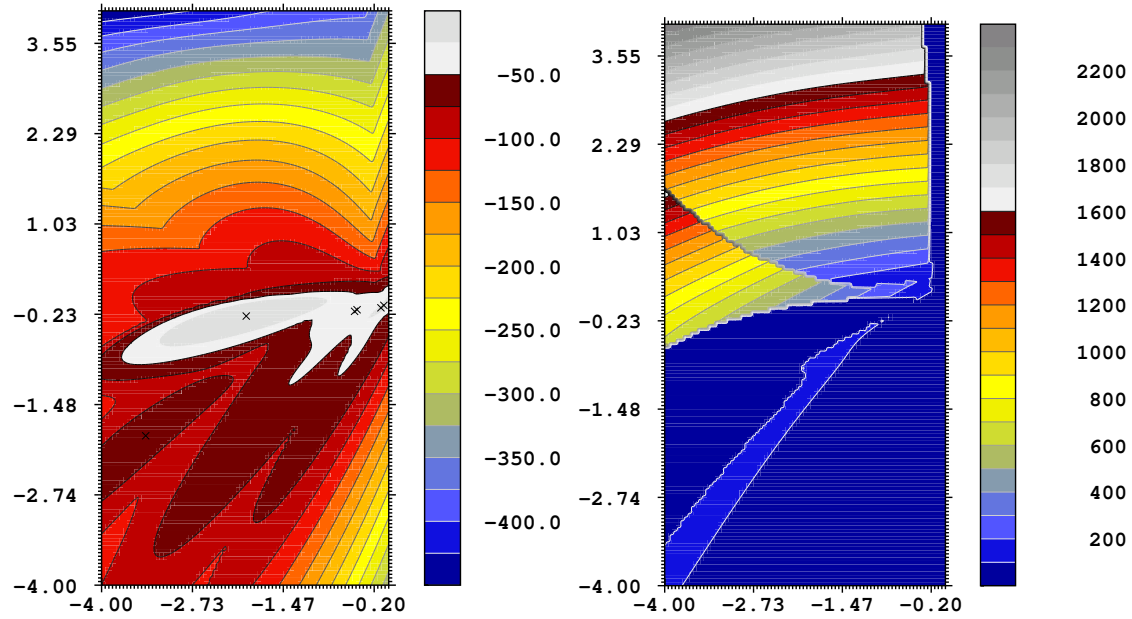


Figure 3.11: Real (left panel) and imaginary (right panel) parts of the leading eigenvalues as function of  $q$  at  $Re_c = 1968$  for  $\tau = 17$ ,  $Q = 10$ . Note that the local maximas are denoted by crosses.  $q_y$  and  $q_x$  vary along the horizontal and the vertical directions, respectively. The absolute maximum is at  $q_c = 2.013$ . The critical roll angle is given as  $\phi_c = \arctan (q_x/q_y) = 7.68^\circ$ .

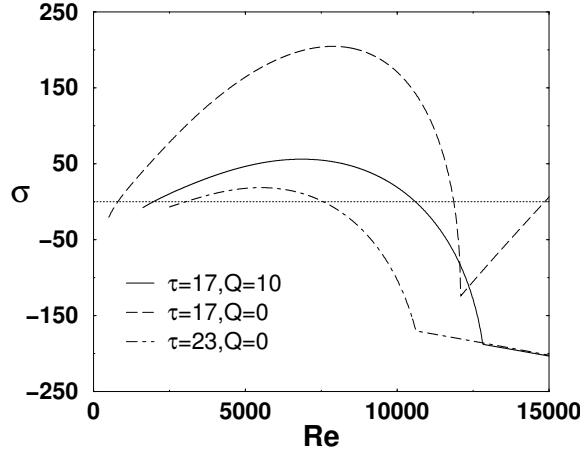


Figure 3.12: The maximal growthrate  $\sigma$  at  $\mathbf{q} = \mathbf{q}_c$  as function of  $Re$  in the case of  $\tau = 17$ ,  $Q = 0$  (dashed line),  $\tau = 17$ ,  $Q = 10$  (solid) and  $\tau = 23$ ,  $Q = 0$  (dash-dotted). Critical values of parameters  $Re_c = 796.3$ ,  $q_c = 2.55$  and  $\phi_c = 9^\circ$  (dashed);  $Re_c = 1968$ ,  $q_c = 2.01$  and  $\phi_c = 7.68^\circ$  (solid);  $Re_c = 3125.1$ ,  $q_c = 1.44$  and  $\phi_c = 9.51^\circ$  (dash-dotted).

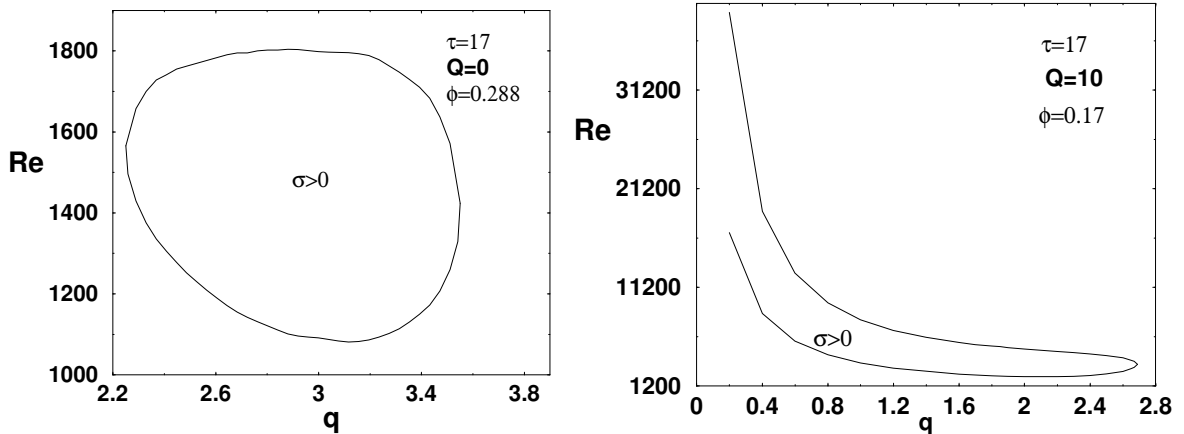


Figure 3.13: Threshold of instabilities in the case of  $\phi \neq \phi_c$  at  $\phi = 0.288$ ,  $\tau = 17$ ,  $Q = 0$  (left panel) and  $\phi = 0.17$ ,  $\tau = 17$ ,  $Q = 10$  (right panel). Note that  $\phi_c = 0.157$  for left panel and  $\phi_c = 0.134$  for right panel.

with finite  $\omega$ .

The topology of the  $\sigma(\mathbf{q})$  surface changes with  $Re$ . For instance, in Fig. 3.12 we present the variation of maximal growthrate  $\sigma$  for different parameters. Starting at small  $Re$ ,  $\sigma$  becomes positive at  $Re = Re_c$ . Then  $\sigma$  increases passes a maximum and becomes again negative at a larger value  $Re$ , above which the basic state restabilizes. Note that  $\mathbf{q}_c$  (i.e.  $q_c$ ,  $\phi_c$ ) varies considerably as function of  $Re$ . In addition, the stabilizing effect of the external magnetic field is seen clearly when the two curves for  $\tau = 17$  are compared. Moreover for relatively high  $\tau$  ( $\sim 23$ ) the unstable region shrinks as demonstrated in Fig 3.12.

Moving away from  $\mathbf{q} = \mathbf{q}_c$  the  $Re$  intervals of positive  $\sigma$  in Fig. 3.13 vary. In Fig. 3.13, we plotted two typical examples of this kind. For instance, the unions of the intervals where  $\sigma > 0$  for varying  $|\mathbf{q}|$  at fixed  $\phi$  can produce a closed region in the  $Re, q$  plane. For the special case  $Q = 0$  our results are in perfect agreement with earlier findings [45].

### 3.2.2 The oscillatory instabilities for high Coriolis number

In this section, we present the oscillatory shear flow instabilities for larger values of  $\tau$ . In this case, the flow is rather confined to boundary layers near the plates. We will dis-

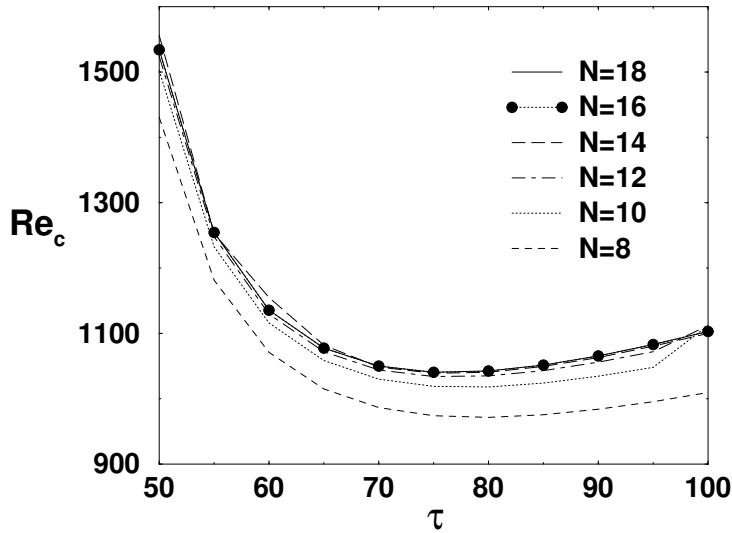


Figure 3.14: The effect of number of  $z$  modes (i.e. truncation parameter  $N$ ) at  $Re_c = 1084.7$ ,  $\tau = 74$ ,  $Q = 2$ ,  $q_c = 2.93$  and  $\phi = 18.9^\circ$  in the case of type II instability.

tinguish between two different bifurcations which we call type I and type II. They differ with respect to sign of the obliqueness angle  $\phi_c$  and the modulus of  $\mathbf{q}_c$ . The oscillatory instability corresponds to a Hopf bifurcation. Thus we have two equivalent solutions with imaginary parts  $\pm\omega_c$  which correspond  $\sim \exp[i\mathbf{q}_c\mathbf{x} \pm \lambda_c t] \sim \exp[i(\mathbf{q}_c\mathbf{x} \pm \omega_c t)]$  (for details see Chap. 1).  $\omega_c > 0$  corresponds to waves which will be shown to move almost parallel to  $-\mathbf{q}_c$  at the lower plate on which we will focus without loss of generality.

With respect to the numerics, we had to use more Galerkin modes for the calculation of both oscillatory instabilities (type I&II) to resolve the boundary layers. To exemplify this dependence on  $N$  we present in Fig. 3.14 the critical Reynolds number  $Re_c$  for type II instability. According to this graph,  $N = 14$  is seen to be sufficient for a reliable calculation of the neutral curve.

In the following paragraphs, we present separately the linear analysis of the type I/II instabilities.

### The type I instability

In this section the type I oscillatory instability which prevails at medium  $\tau$  will be discussed. In Fig. 3.15a, we present the critical Reynolds number  $Re_c$ . This quantity first decreases with increasing  $\tau$  up to a certain  $\tau$  ( $\sim 50$  for small  $Q$ ), where the slope changes sign, before  $Re_c$  starts slightly increasing.  $Re_c$  increases monotonously as function of  $Q$ .

In the presence of a finite magnetic field ( $Q \neq 0$ ) the shear flow is stabilized and  $Re_c$  becomes larger. The critical wave number  $q_c = |\mathbf{q}_c|$  is shown in Fig. 3.15b. With decreasing  $\tau$ , this quantity decreases from  $q_c = 5.47$  (at  $\tau = 100$ ) to  $q_c = 2.43$  (at  $Q = 40$ ). There is only a weak  $Q$ -dependence. The critical obliqueness angle  $\phi_c$  (between  $\mathbf{q}$  and  $y$ -axis) is shown in Fig. 3.16. It is seen that  $\phi_c$  is independent of  $Q$  for high  $\tau$  ( $\phi_c = -7.4^\circ$  at  $\tau = 100$ ). However in particular for small  $Q$ ,  $\phi_c$  increases slightly. For high  $Q$ , the increase in  $\phi_c$  is almost linear with increasing  $\tau$  (see  $Q = 40$  in Fig. 3.16a). Finally the Hopf frequency  $\omega_c$  is shown in Fig. 3.16b.  $\omega_c$  decreases at first with decreasing  $\tau$ , then passes a minimum for  $\tau \simeq 55$  and increases again. This behavior is qualitatively the same for all  $Q$  but quantitatively  $\omega_c$  increases with increasing  $Q$ .

In addition to these plots, we would like to add more detailed information on the type I instability. In Table 3.2 we have compared some selected numerical data of our investigation with earlier studies in the literature. We have found excellent agreement, which shows that our numerical Galerkin methods are trustworthy. In Fig. 3.17, we

	$Re_c$	$q_c$	$\phi_c$ (deg.)	$\omega_c$
present work	2246.52	5.52	-6.932	1352.92
Hoffmann et al.	2244.6	5.5	-6.88	1346.5
Lilly	2240	5.5	-6.8	—

Table 3.2: Onset of the type I instability at  $\tau = 100$  and a comparison with the results of Hoffmann et al. [45] and Lilly [41] in our units for a single Ekman layer in the limit  $Q = 0$ .

show the profiles of the scalar potentials  $v$ ,  $w$ ,  $g$  as function of  $z$  for a particular  $q$  in the case of  $\omega_c > 0$  in analogy to Fig. 3.9 in the stationary case. The graphs are not very illuminating in detail, but show clearly that the instabilities are rather concentrated near the lower plate as to be expected.

As a complement, again in analogy to Fig. 3.10 in the stationary case, we show the scalar potentials in the  $\eta-z$  plane for  $\omega_c > 0$  in Fig. 3.18. One observes roll structures, which are concentrated near the lower plate. (Note that the structure do not depend on  $\xi$ ; i.e. the coordinate perpendicular to the paper plane.)

It is obvious that, the streamlines  $\partial_\eta v$ , the lines of velocity  $\partial_\eta w$  and magnetic field strength  $\partial_\eta g$  do not have a clear  $z$ -symmetry in contrast to the stationary solution (Fig. 3.18). The mirror symmetric solution ( $z \rightarrow -z$ ) is provided here by the  $-\omega_c$  solution. Note that the streamlines bend to the right hand-side at the lower part of the layer; this feature does not change with increasing  $Q$ .

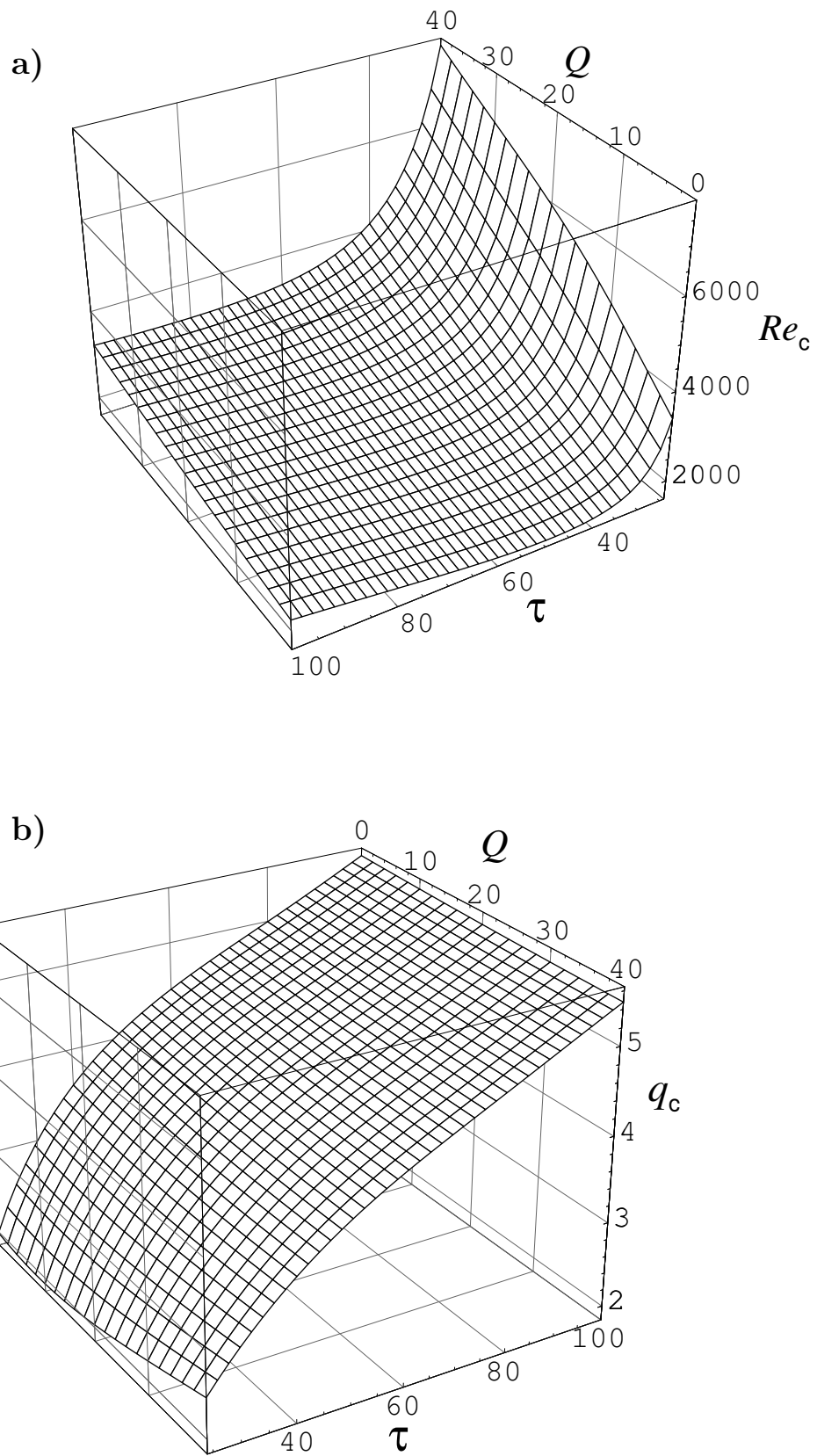


Figure 3.15: (a) The critical Reynolds number  $Re_c$  and (b) the modulus  $q_c$  of critical wavevector, as functions of  $\tau$  and  $Q$  in the case of the type I instability.

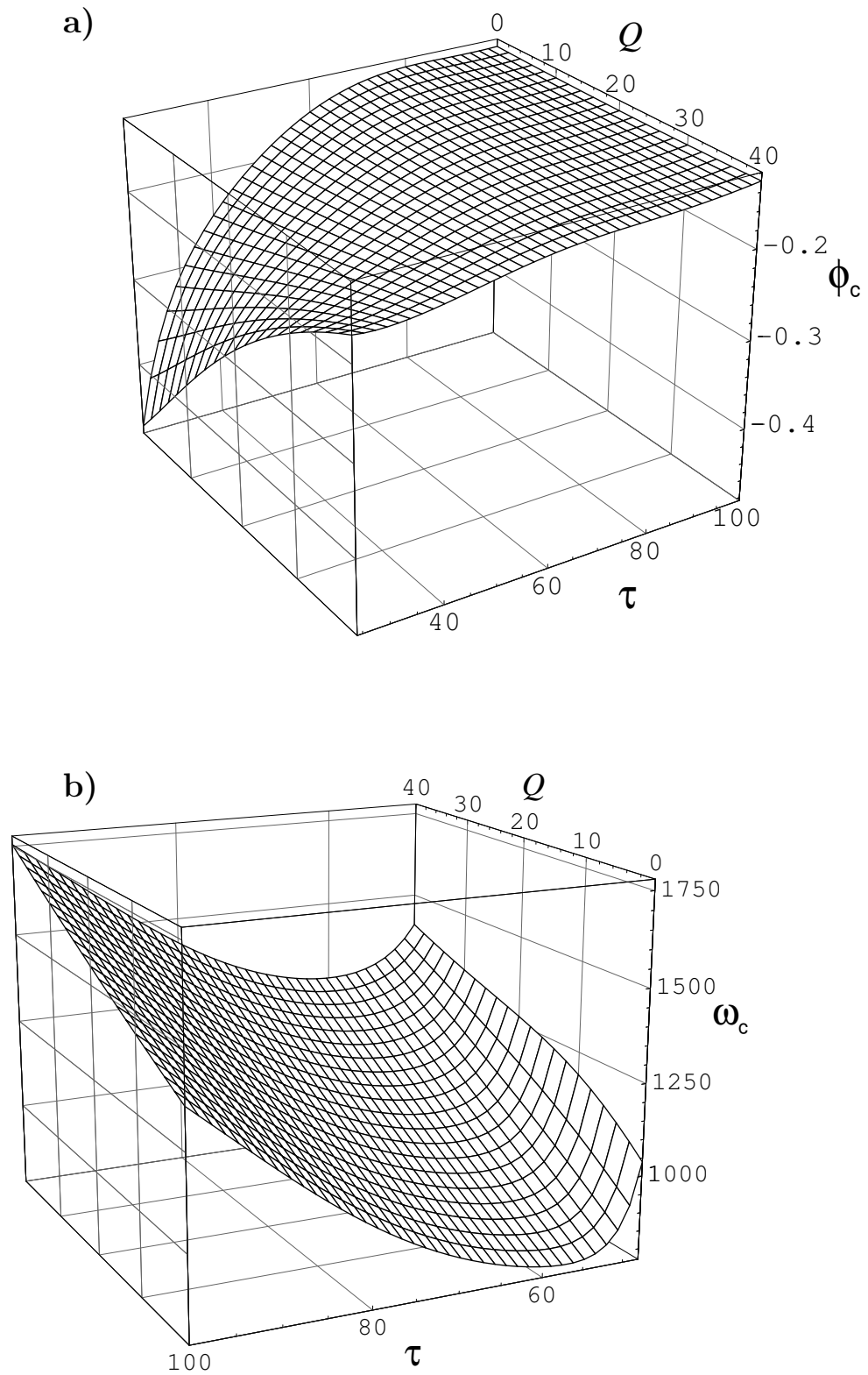


Figure 3.16: (a) The critical orientation angle  $\phi_c$  in radians and (b) the Hopf frequency  $\omega_c$  as functions of  $\tau$  and  $Q$  in the case of type I instability.

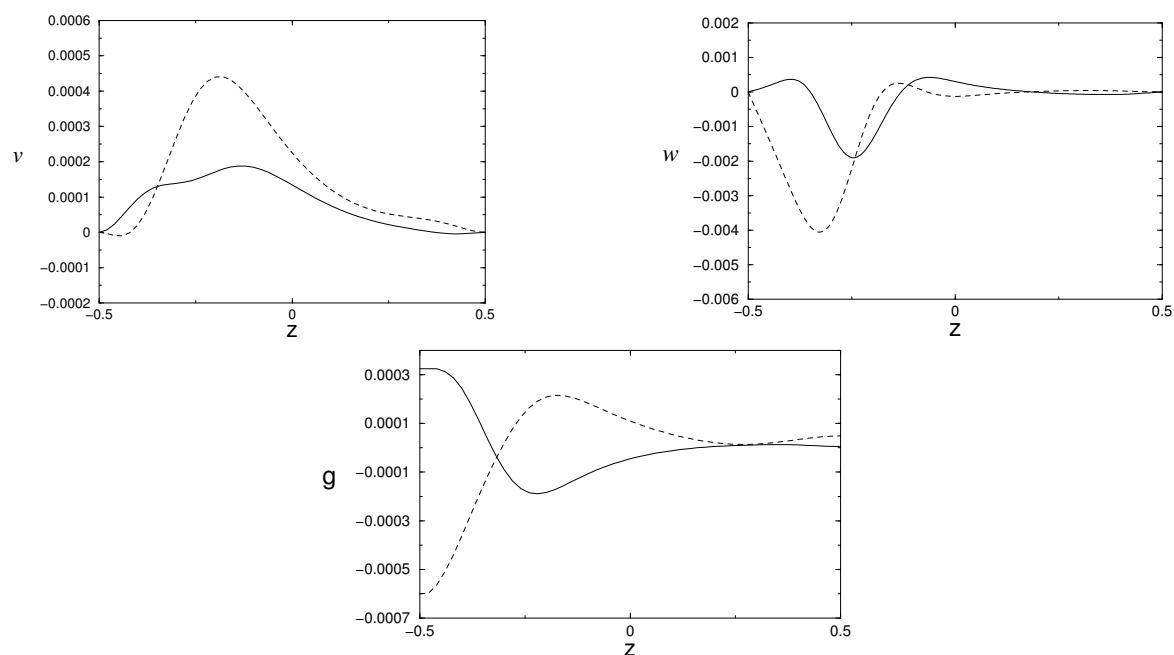


Figure 3.17: A typical profile of scalar potentials  $v$ ,  $w$ ,  $g$  as function of  $z$  for  $Re = 2251$ ,  $q = 4.95$ ,  $\phi = -7.62^\circ$  at  $\tau = 80$  and  $Q = 10$ .

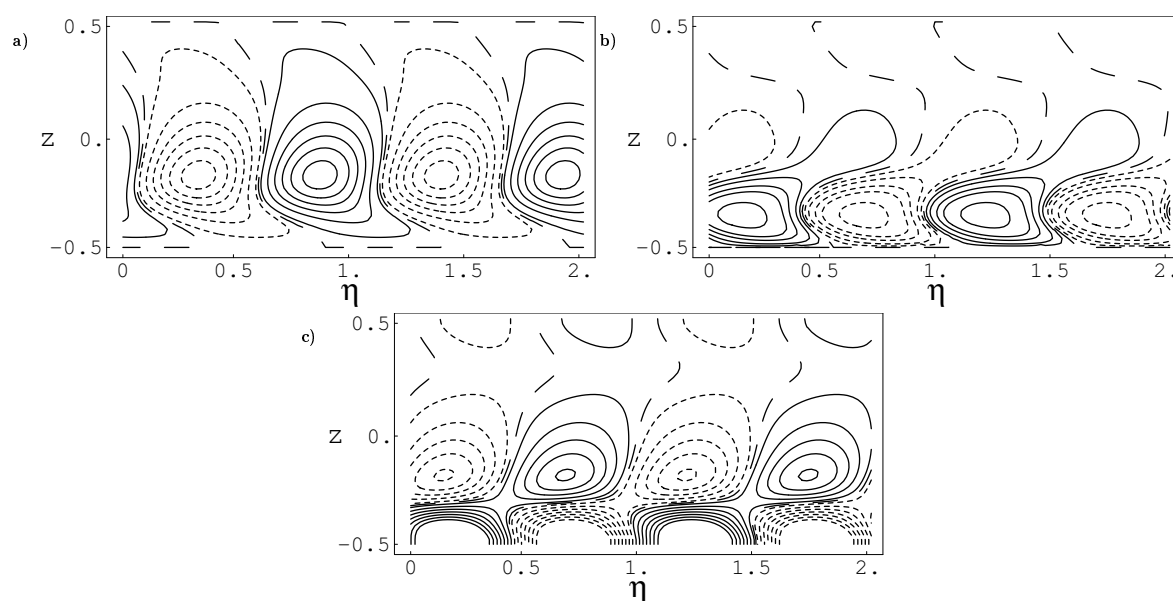


Figure 3.18: A typical contour plot of the (a) stream function  $\partial_\eta v$ , (b) the longitudinal velocity component  $\partial_\eta w$  and (c) magnetic field along  $\xi$ -direction, (i.e.  $\eta = (x \sin \phi + y \cos \phi)$ ) for  $\tau = 90$ ,  $Q = 25$ ,  $\phi = -18.3^\circ$  and  $q = 3.3$ . (Type I,  $\omega = \omega_c > 0$ .)

### The type II instability

In this subsection, we present some details on the type II oscillatory instability.

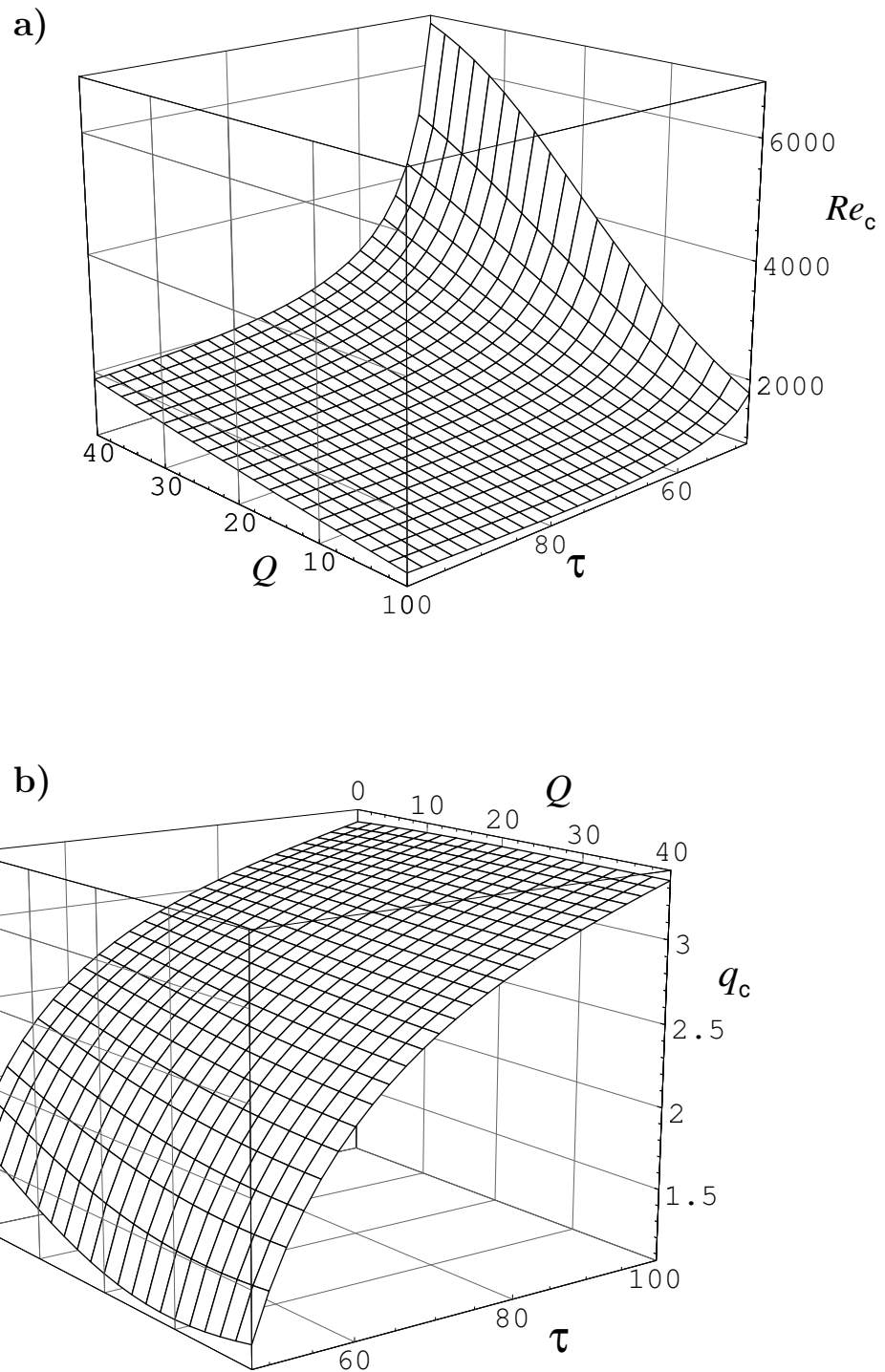
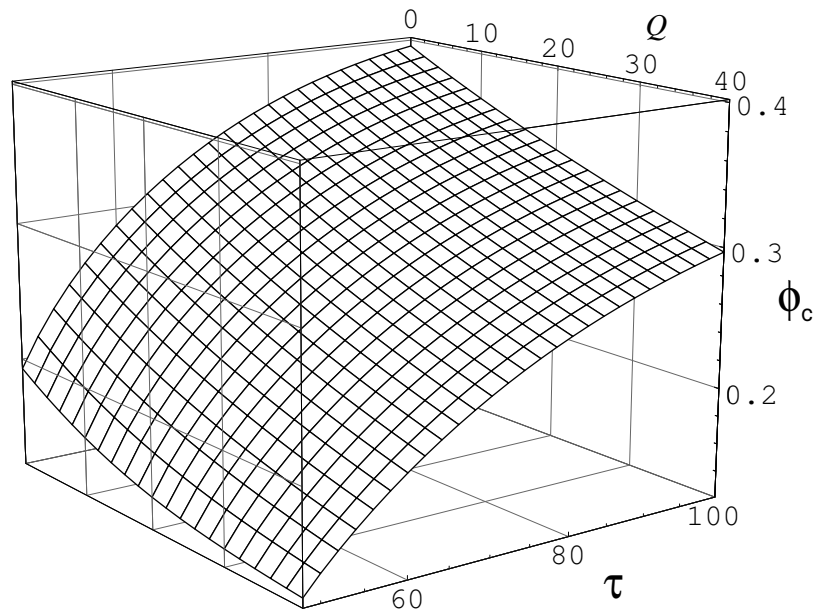


Figure 3.19: (a) The critical Reynolds number  $Re_c$  and (b) the critical wave number  $q_c$ , as functions of  $\tau$  and  $Q$  in the case of the type II instability.

a)



b)

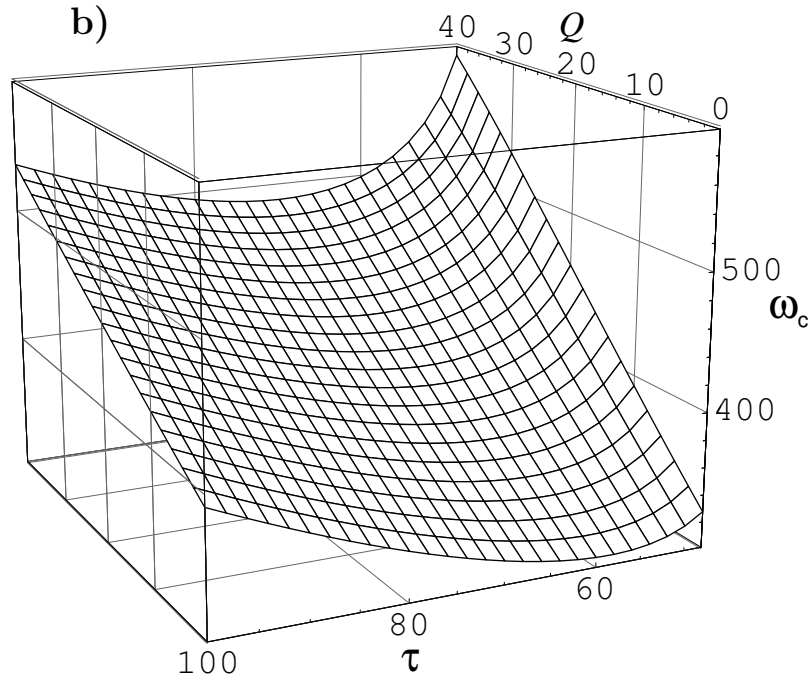


Figure 3.20: (a) The critical orientation angle  $\phi_c$  and (b) the critical Hopf frequency  $\omega_c$  as functions of  $\tau$  and  $Q$  in the case of the type II instability.

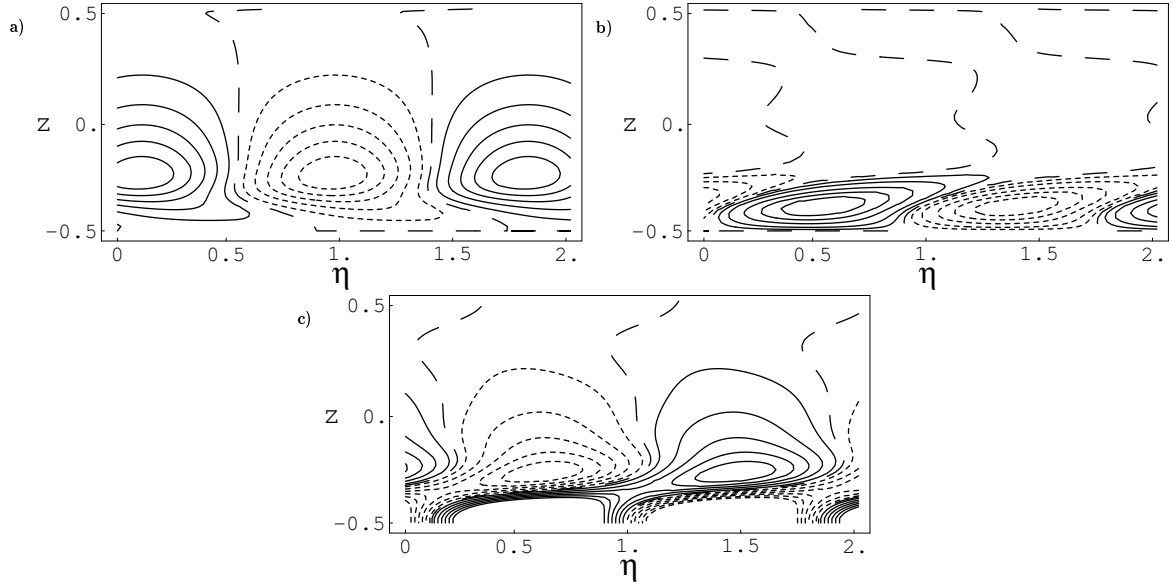


Figure 3.21: A typical contour plot representation of (a) the stream function  $\partial_\eta v$ , (b) the longitudinal velocity component  $\partial_\eta w$  and (c) the magnetic field strength  $\partial_\eta g$  along a coordinate axis  $\eta$  parallel to the wavevector  $\mathbf{q}$ , (i.e.  $\eta = (x \sin\phi + y \cos\phi)$ ) for  $Re = 3287.7$ ,  $\tau = 95$ ,  $Q = 25$ ,  $\phi = 11.46^\circ$  and  $q = 2.08$ . The solution for  $\omega = +\omega_c$  is mainly concentrated at the lower boundary  $z = -1/2$ , where the external stress excites a traveling wave to the left.

In Fig. 3.19a the critical Reynolds number  $Re_c$  is plotted as function of  $\tau$ ,  $Q$ .  $Re_c$  decreases with increasing  $\tau$  as shown in Fig. 3.6. In particular we draw the attention to the strong increase of  $Re_c$  with  $Q$  (the stabilizing magnetic field). The critical wave number  $q_c$  which is shown in Fig. 3.19b also increases as function of  $\tau$  in the case of constant  $Q$  similar to type I instability. It is interesting that the wave numbers do not change too much with respect to  $Q$ . In general,  $q_c$  is smaller than the one in the type I case. The main differences between two oscillatory instabilities are found in the critical values of the angle  $\phi_c$  ( $\angle(\mathbf{q}_c, y)$ ) in Fig. 3.20a. The angle  $\phi_c$  is opposite in sign to the type I angle. The magnetic energy  $Q$  has an important impact for moderate and high  $\tau$  values. The  $\phi_c$  values decrease linearly with respect to  $Q$  for high  $\tau$ , whereas  $\phi_c$  values are always constant in the case of type I instability (see in Fig. 3.16a).  $\phi_c$  values decrease from  $21.77^\circ$  (at  $Q = 0$ ) to  $16.62^\circ$  (at  $Q = 40$ ) as function of  $Q$  for  $\tau = 100$ . Another difference between two instabilities can be seen for the moderate  $\tau$ . While  $\phi_c$  values increase in the positive direction in the case of type I, they decrease almost linearly in the case of type II instability. The Hopf frequency  $\omega_c$  is drawn in Fig. 3.20b as functions of  $\tau$  and  $Q$ . In general, the graph looks very similar to the corresponding one for the type I instability (Fig. 3.16b). Here, the values also increase linearly with the magnetic energy  $Q$ .

In Table 3.3, we compare some selected critical data for  $Q = 0$  with earlier studies. According to this table (Table 3.3) our results for the onset of type II instabilities agree also well with the earlier results as already demonstrated in the type I case.

	$Re_c$	$q_c$	$\phi_c$ (deg.)	$\omega_c$
present work	1105.14	3.31	22.66	391.58
Hoffmann et al.	1105.3	3.3	22.9	391.2
Lilly	1100	3.3	22.6	—

Table 3.3: Onset of the type II instability at  $\tau = 100$  in a comparison with the results of Hoffmann et al. [45] and Lilly [41] in our units for a single Ekman layer.

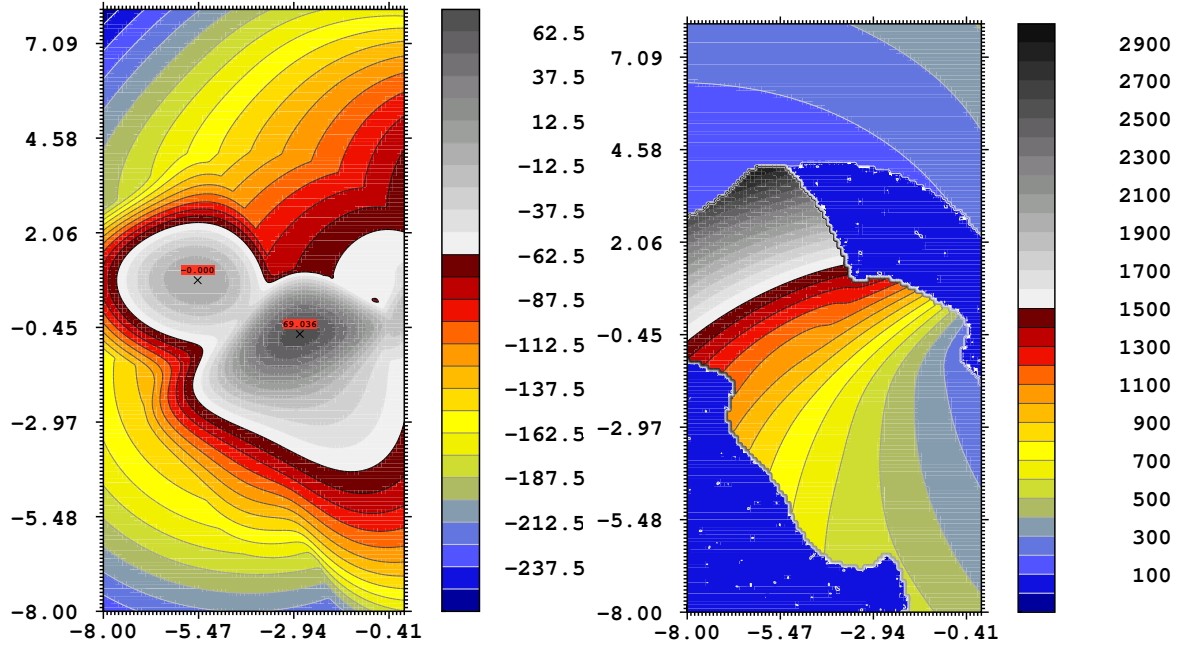


Figure 3.22: Real (left panel) and imaginary (right panel) parts of the leading eigenvalues as function of  $\mathbf{q} = (q_x, q_y)$  at  $Re = 2144.7$  for  $\tau = 100$  and  $Q = 10$ . The two maxima in the left plot correspond to the type I ( $q_x = 0.714$ ,  $q_y = -5.48$ ) and II ( $q_x = -1.196$ ,  $q_y = -3.12$ ) instabilities.  $q_y$  and  $q_x$  vary along the horizontal and the vertical axes, respectively.

The scalar potentials in  $\eta - z$  plane for  $\omega > 0$  are shown in Fig. 3.21. Note the asymmetry of the contour lines which are concentrated near the lower boundary in analogy to the type I instability (Fig. 3.21). The scalar function  $g$  is finite at the boundaries (Fig. 3.21c) since  $\frac{\partial g}{\partial z}(z = \pm \frac{1}{2}) = 0$ .

In analogy to the stationary case (Fig. 3.11) we would like to add a small discussion on the maximal eigenvalues of oscillatory instabilities type I&II, since they affect the nonlinear features as well. We have considered the case ( $\tau = 100$ ,  $Q = 10$ ) where  $Re_c = 2449.7$  for type I and  $Re_c = 1271.5$  for type II. According to Fig. 3.22, the leading eigenvalues as function of  $\mathbf{q}$  display a complicated structure which reflects the presence of both instability types. The real part (left panel) has two local maxima which correspond to type I and II instabilities. It is obvious that the type I instability is related to the upper local maxima which has a negative  $\phi$  and the maximal real part

of type I instability ( $\sigma_I$ ) is close to zero. Whereas the type II instability is related to the lower local maxima with a relatively large real part  $\sim 63$  ( $\sigma_{II}$ ). Note also that type II instability has a positive  $\phi$ . In addition, the wavenumber of the type I instability is relatively larger than that of the type II instability. For example, at  $\tau = 100$ , when  $\sigma_I$  approaches to zero, type II growthrate is already above the neutral curve (i.e.  $\sigma_{II} > 0$ ). In the right panel of Fig. 3.22, the imaginary parts  $\omega$  of the leading eigenvalues are drawn. We find some local maxima which are associated with finite  $\omega$  on the left panel. Note also that  $\omega$  values which correspond to the type I instability are higher than the ones of the type II instability (also see Fig. 3.16b and 3.20b). The regions of finite  $\omega$  values do not have a regular shape.

### 3.3 Nonlinear Analysis of Roll Solutions

In this section we present the results for the nonlinear properties of rolls on the basis of the weakly nonlinear analysis and the Galerkin calculations. For this goal, we concentrate mainly on the region near onset with small  $\varepsilon$  ( $= (Re - Re_c)/Re_c$ ). Even there the analysis is far from complete in view of the large parameter space of  $\tau$  and  $Q$  that has to be scanned. In general, we have focused on the stationary instabilities which occurs at relatively low  $\tau$  values. In the case of oscillatory instabilities (i.e. type I&II), we present only some weakly nonlinear results.

First, we present Sec. 3.3.1 covering some calculations on the Nusselt numbers  $Nu$  which are, the indicators of the horizontal average of momentum transport through the boundaries in the case of both stationary and oscillatory instabilities. The stability diagrams and some features of the secondary bifurcations for the stationary rolls will be discussed in Sec. 3.3.2. In Sec. 3.3.3, the weakly nonlinear analysis near the codimension-2 point will be described for high rotation rates  $\tau$ .

#### 3.3.1 Nusselt number

A global characterization of the nonlinear properties is provided by the Nusselt number  $Nu_x, Nu_y$  as the horizontally averaged directional shear components at the boundaries due to the velocity fields  $U_x, U_y$ . In analogy to the thermal Nusselt number it is useful to single out the contribution of the basic flow. Without loss of generality we can restrict ourselves to the lower boundary and define:

$$Nu_x = 1 + \frac{\partial \bar{u}_x}{\partial z} \Big|_{z=-1/2}, \quad Nu_y = 1 + \frac{\partial \bar{u}_y}{\partial z} \Big|_{z=-1/2}. \quad (3.25)$$

Here,  $\bar{\mathbf{u}}$ , which describes the nonlinear contributions to  $\mathbf{U}_0$  is given in Eq. (3.18a);  $\mathbf{U}_0$  is given in Eq. (3.10). For our purpose, it is convenient to use the directional shear components  $Nu_\xi, Nu_\eta$  in the rotated coordinate system  $(\xi, \eta)$ , where the  $\eta$  axis is aligned with the wavevector  $\mathbf{q}$  of the rolls. We arrive at the following definitions:

$$Nu_\xi = 1 + \frac{\partial \bar{u}_\xi}{\partial z} \Big|_{z=-1/2}, \quad Nu_\eta = 1 + \frac{\partial \bar{u}_\eta}{\partial z} \Big|_{z=-1/2}. \quad (3.26)$$

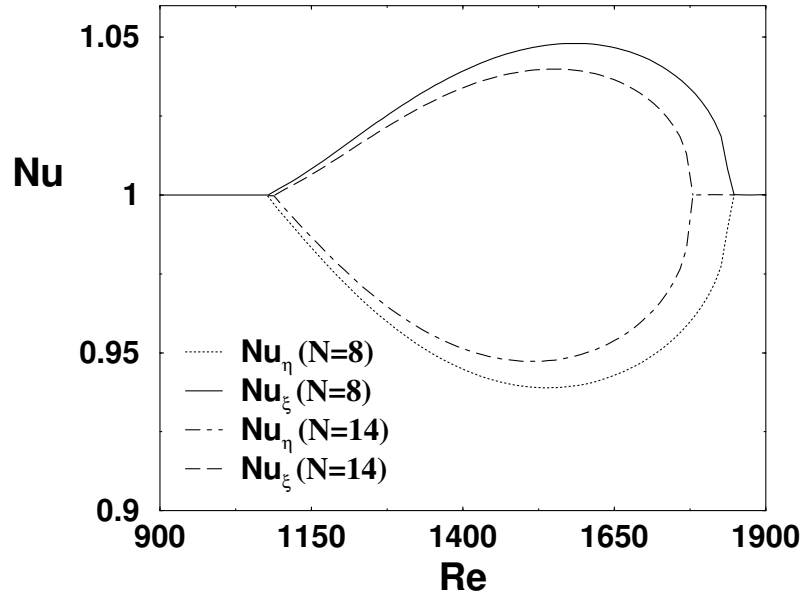


Figure 3.23: The Nusselt numbers for  $\tau = 17$ ,  $Q = 0$ ,  $q = 3.1$  and  $\phi = 16.5$  as functions of  $Re$  for two different values of truncation parameter  $N$ .

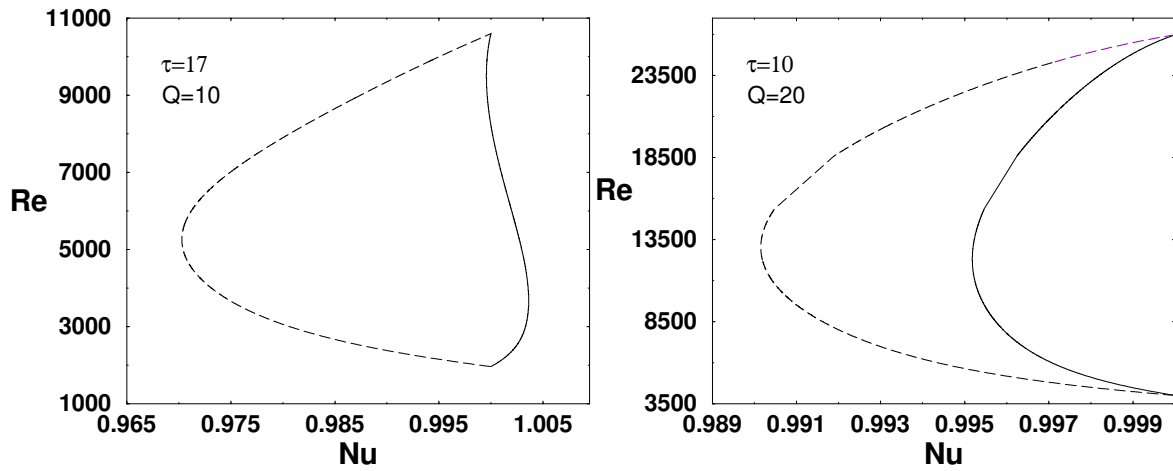


Figure 3.24: Nusselt numbers  $Nu$  for increasing Reynolds number  $Re$  in the case of stationary instability. Solid (dashed) lines denote  $Nu_\xi$  ( $Nu_\eta$ ) values at  $\tau = 17$ ,  $Q = 10$ ,  $q_c = 2.01$ ,  $\phi_c = 7.67^\circ$  (left panel) and  $\tau = 10$ ,  $Q = 20$ ,  $q_c = 1.94$ ,  $\phi_c = 3.72^\circ$  (right panel).

At first, we focus on the stationary case where the nonlinear solutions are calculated with the help of a full Galerkin analysis. In Fig. (3.23) we study the dependence on the truncation parameter  $N$  for  $\tau = 17$  and  $Q = 0$ . Apparently, we see only quantitative changes with increasing  $N$ . Note the restabilization of the basic flow ( $Nu = 1$ ) at  $Re = 1761$  which was already mentioned in Fig. 3.13.

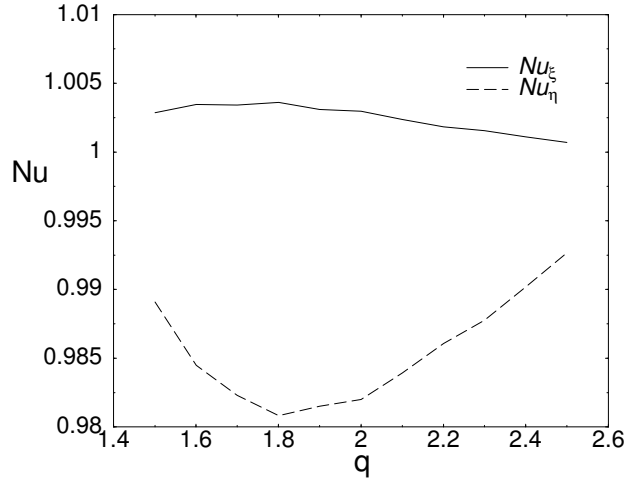


Figure 3.25: Nusselt numbers  $Nu_\xi$  (solid line) and  $Nu_\eta$  (dashed line) as function of the wave number  $q$  at  $\tau = 17$ ,  $Q = 12$ ,  $Re = 2550.1$  ( $\varepsilon = 0.001$ ),  $\phi_c = 7.16^\circ$  (stationary bifurcation).

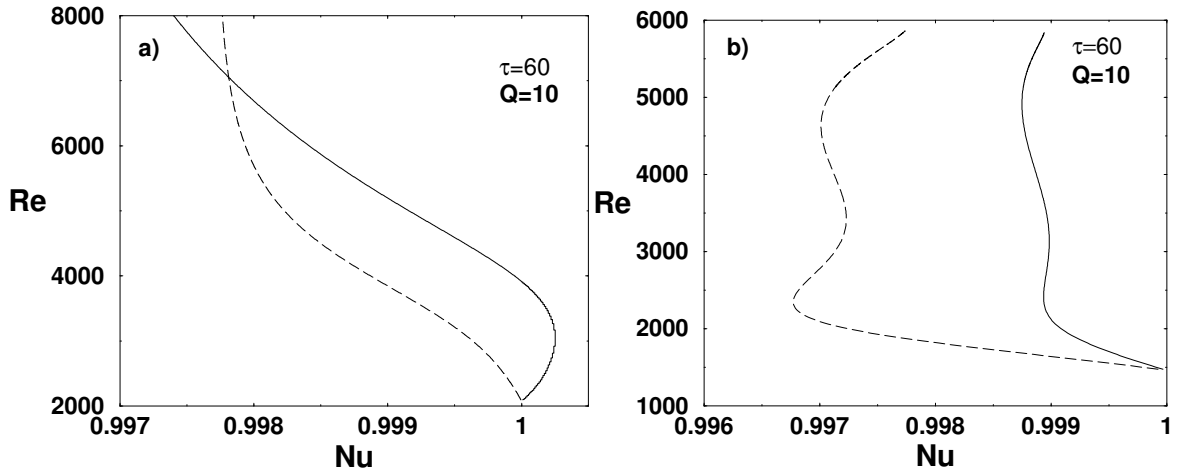


Figure 3.26: Nusselt numbers  $Nu$  for increasing Reynolds number  $Re$  in the case of oscillatory instabilities. Solid (dashed) lines denote  $Nu_\xi$  ( $Nu_\eta$ ) values in the case of (a) type I at  $\tau = 60$ ,  $Q = 10$ ,  $q_c = 4.38$ ,  $\phi_c = -8.94^\circ$  and (b) type II (right panel) at  $\tau = 60$ ,  $Q = 10$ ,  $q_c = 2.43$ ,  $\phi_c = 14.3^\circ$ .

Fig. 3.24 shows the directional Nusselt numbers  $Nu$  for increasing  $Re$  in the case of two other representative parameter sets ( $\tau = 17, Q = 10$ ) and ( $\tau = 10, Q = 20$ ). It is obvious that the curves are globally similar. In Figs. 3.24, 3.26,  $Nu_\eta < 1$ , thus the meanflow contribution due to the rolls reduces the basic stress. In contrast,  $Nu_\xi$  can have both signs. The Nusselt numbers depend on the wavevector  $\mathbf{q}$  of the roll solutions. In Fig. 3.25 we show a representative example with varying wavenumber  $\mathbf{q}$  at fixed  $\phi = \phi_c$ . It is clear that for a certain  $\mathbf{q}$ ,  $Nu_\eta$  and  $Nu_\xi$  have extrema which correspond roughly speaking to maxima of the amplitudes.

In the following we present some examples of the Nusselt numbers for the oscillatory instabilities of type I and II. The results are obtained from a weakly nonlinear analysis strictly valid near onset. In Fig. 3.26, we show two representative samples. The global characteristics of the  $Nu$  curves differ qualitatively for increasing  $Re$  from the ones in the stationary case (Fig. 3.24). For instance, in the  $\xi$ - direction (i.e. along the roll axis), the shear first increases just beyond the onset of instability, then it decreases with increasing  $Re$  (Fig. 3.26a).

### 3.3.2 Stability diagrams of stationary rolls at low $\tau$

In this section, we discuss the stationary roll solutions and their instability not too far from onset on the basis of weakly nonlinear and Galerkin solutions. As a foreword, we found that the primary bifurcation is always supercritical according to the analyses.

In Fig. 3.27, we start with the stability diagram of rolls in the  $q - \varepsilon$  plane. Note that we use  $\varepsilon$  as  $\varepsilon := (Re - Re_c)/Re_c$  with respect to  $Re_c = Re_0(\tau, Q, \mathbf{q}_c)$  to describe the distance from onset. Instabilities exist above the neutral curve  $Re_0(\tau, Q, \mathbf{q})$ . As discussed in the previous section we have found oblique rolls with the roll axis are nearly parallel to  $x$ - axis. The critical obliqueness angle  $\phi_c$  varies as function of  $\tau$  changes from  $\phi_c = -3.72^\circ$  to  $\phi_c = 11.45^\circ$ . The threshold  $Re_c$  decreases at first then increases beyond a certain  $\tau$  as function of  $\tau$ , parabolically. The stability diagrams in Fig. 3.27 for two different magnetic energies ( $Q = 10, 20$ ) are qualitatively similar.

Before the details on the stability diagrams, we would like to compare the linear solution with the nonlinear one for a small  $\varepsilon$ . In Fig. 3.28, we show a typical contour plot of the stream function and the lines of constant velocity along the roll axis which holds for  $\varepsilon = 0.02$ ,  $\tau = 12$ ,  $Q = 14$  in both linear (upper panel) and nonlinear (lower panel) cases. The plots do not differ so much since  $\varepsilon$  is relatively small. An antisymmetric feature with respect to the midplane ( $z = 0$ ) which has already mentioned in the linear regime (see, for instance, Fig. 3.10) is observable also in the nonlinear case. Besides, in the lower panel of Fig. 3.28, the effect of nonlinear disturbance to the typical roll solution is seen clearly. The stream function and the lines of constant velocity change mostly at the middle of the planes ( $z = 0$ ) due to the nonlinear disturbance of the basic state. There exist a strong gradient at the middle of the layer and this gradient destroys the linear properties. Note also that the stream function  $\partial_\eta v$  and the lines of constant velocity  $\partial_\eta w$  preserve their asymmetric feature with respect to  $z = 0$  plane near the onset.

For the stability diagrams, we have also considered the case of varying  $|\mathbf{q}_c|$  at fixed critical angle  $\phi_c$ . At first we concentrate on the case of  $Q = 10$ . As shown in Fig. 3.27a, we have observed both longwave and shortwave instabilities on the  $q - Re$  plane. Longwave instabilities were mainly found for small  $\varepsilon$ . For  $q < q_c$ , a zig-zag instability occurs. The standard Eckhaus instability curve is very close to the zig-zag instability for small  $q$ . The stable region is restricted from above for all  $q$  by a skewed-varicose instability which occurs around  $\varepsilon = 0.25$  for  $q = q_c$ . For fairly high  $\varepsilon$ , shortwave instabilities take place. For increasing  $\varepsilon$  one first hits the curve of a cross-roll instability. Then, an oscillatory instability occurs for  $q > q_c$ .

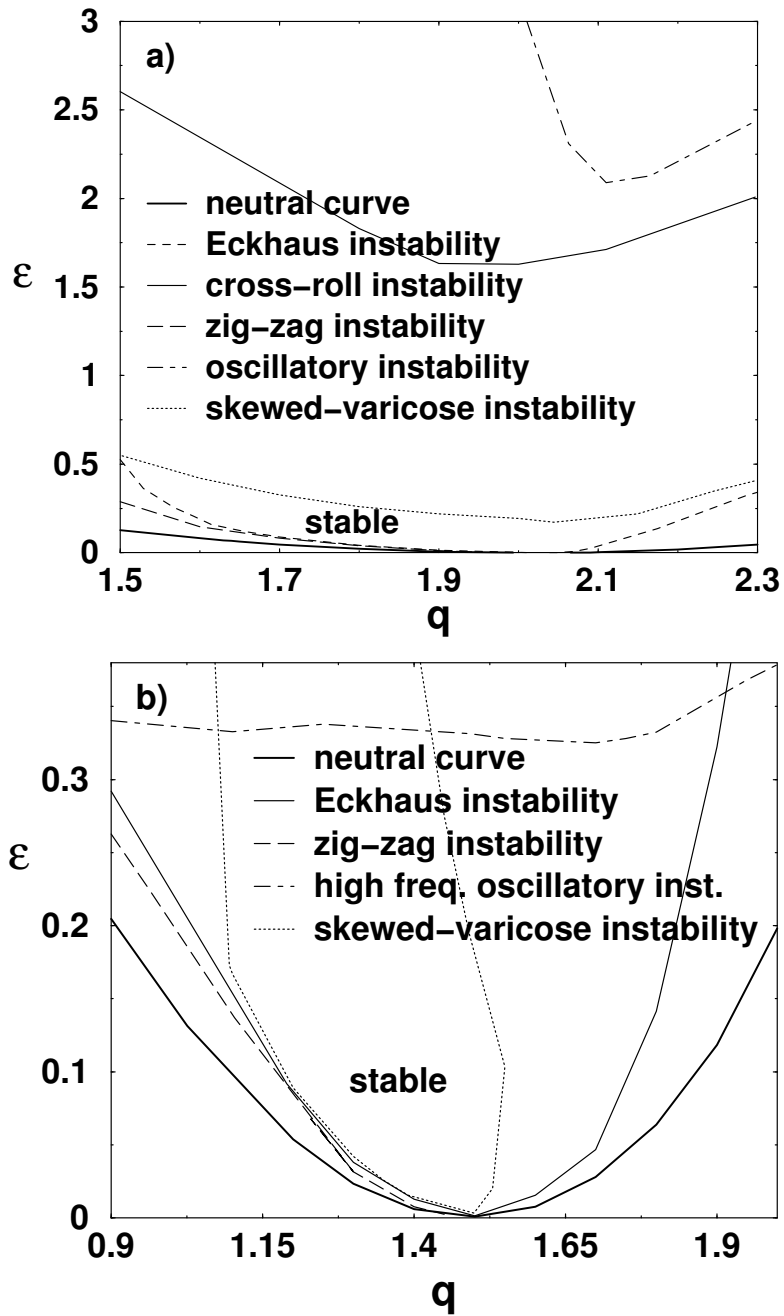


Figure 3.27: Stability diagram in the stationary case for (a)  $\tau = 17$ ,  $Q = 10$ ,  $\phi = \phi_c = 7.73^\circ$ , (b)  $\tau = 17$ ,  $Q = 20$ ,  $\phi = \phi_c = 4.06^\circ$ .

Fig. 3.27b shows the stability diagram for a relatively strong magnetic energy,  $Q = 20$  where the critical angle is given as  $\phi_c = 4.06^\circ$ . According to Fig. 3.27b, both longwave and shortwave instabilities destabilize the stationary rolls. Similar to Fig. 3.27a, the longwave instabilities are located near the neutral curve, whereas the stability balloon is bounded from above by a shortwave instability at relatively high  $\varepsilon$ .

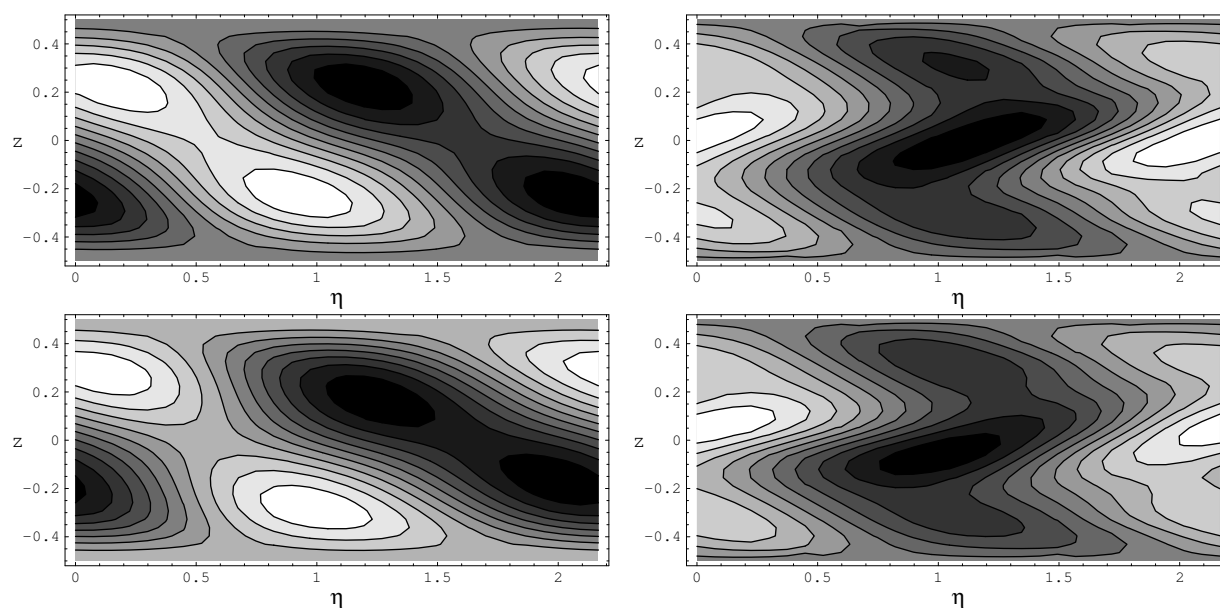


Figure 3.28: Contour plot of the stream function  $\partial_\eta v$  (left panel) and the longitudinal velocity component  $\partial_\eta w$  (right panel) along the roll axis for the linear modes at onset (upper panel) and for the nonlinear solution (lower panel) at small  $\varepsilon = 0.02$  ( $Re = 2100$ ) for  $\tau = 12$ ,  $Q = 14$ ,  $\phi = 4.93^\circ$  and  $q = 2.23$

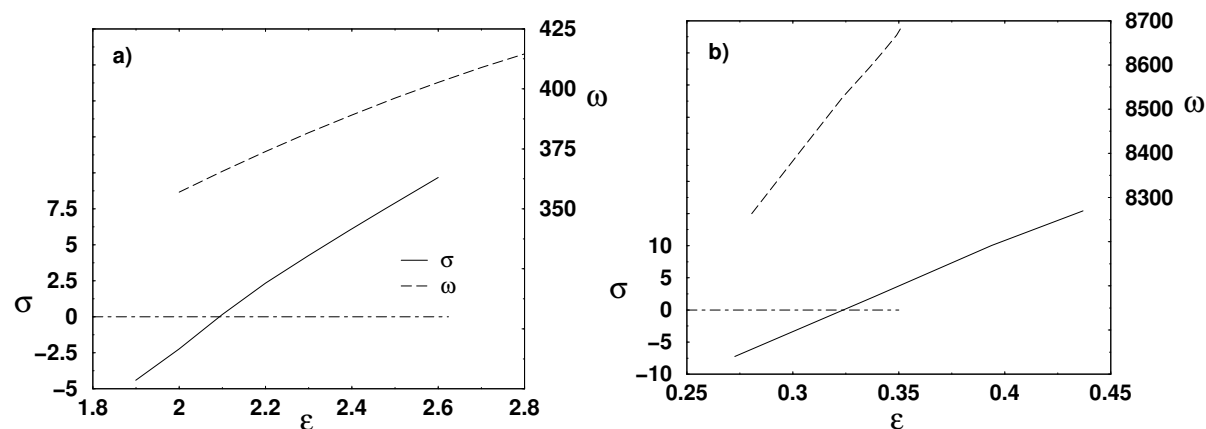


Figure 3.29: The real part  $\sigma$  and the imaginary part  $\omega$  of the leading eigenvalue as function of  $\varepsilon = \frac{Re - Re_c}{Re_c}$  ( $Re_c = 1968$ ) at (a)  $\tau = 17$ ,  $Q = 10$ ,  $q = 2.1$ ,  $\phi = \phi_c = 7.73^\circ$  and (b)  $\tau = 17$ ,  $Q = 20$ ,  $q = 1.55$  and  $\phi = 4^\circ$ . Dash-dotted lines correspond to  $\sigma = 0$

The stable region is mainly limited from below by a skewed-varicose instability. Zig-zag and Eckhaus instabilities show their typical features as also seen in Fig. 3.27a.

A high frequency oscillatory instability around  $\varepsilon = 0.34$  closes the stability balloon from above, which we will discuss in more detail. First, we address the  $Q = 10$  case

as in Fig. 3.27a. The real and imaginary parts of linear eigenvalue for the fastest growing mode as function of  $Re$  have been plotted in Fig. 3.29a. The growth rate  $\sigma$  becomes positive around  $\varepsilon = 2.09$ ; the Hopf frequency is found as  $\omega = 375$ . Addressing the oscillatory instability in Fig. 3.27b ( $Q = 20$ ), the onset has been determined as  $Re = 13080$  for  $q = 1.55$  (Fig. 3.29b). The Hopf frequency in this case has a value of about  $\omega = 8500$ .

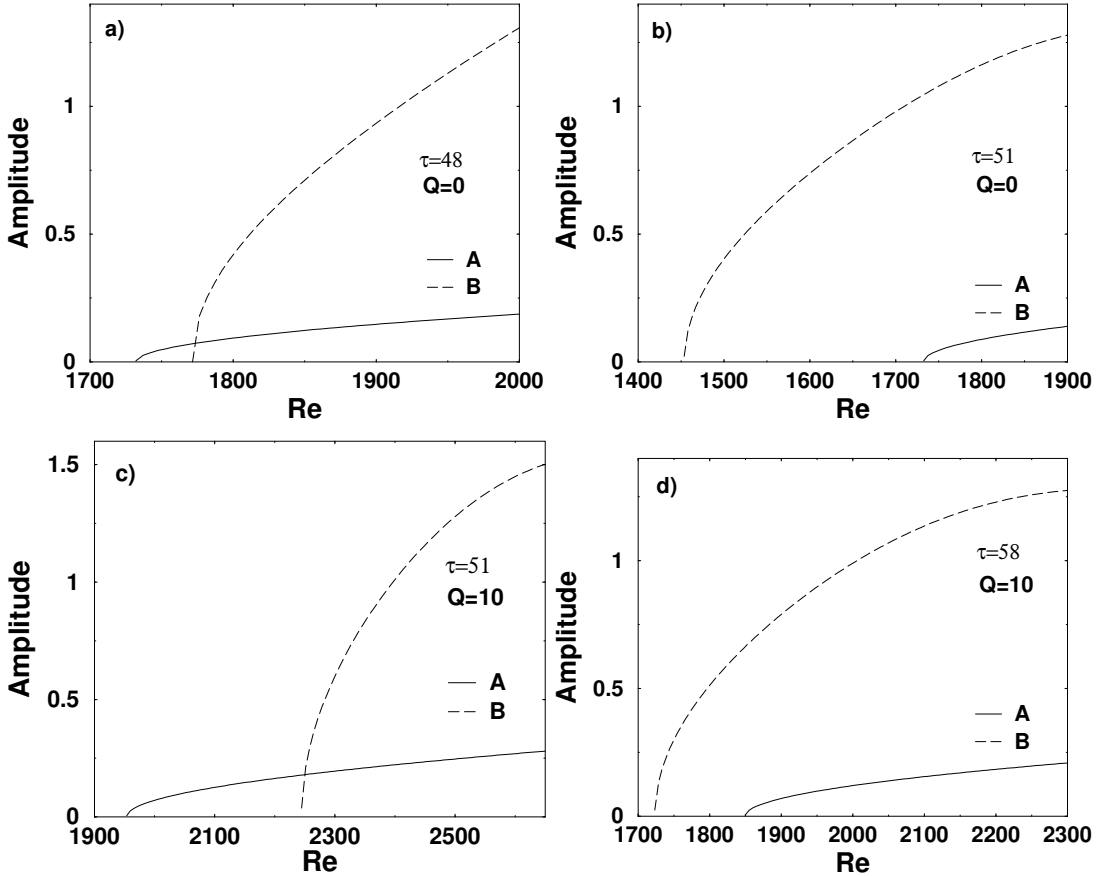


Figure 3.30: Amplitudes  $A$  (type I) and  $B$  (type II) for (a)  $\tau = 48$ , (b)  $\tau = 51$  at  $Q = 0$  and for (c)  $\tau = 51$ , (d)  $\tau = 58$  at  $Q = 10$ .

### 3.3.3 Weakly nonlinear analysis near the codimension-2 point

As already mentioned before, in relatively high rotation rates ( $\tau \gtrsim 25$ ), there exist oscillatory instabilities which are classified as types I and II. We have only performed weakly nonlinear analysis near onset. At moderate  $\tau$  ( $\sim 50$ ) a codimension-2 point between two oscillatory instabilities exists (see also Fig. 3.6), for the codimension-2 point the type I and II solutions coexist at the same  $Re_c$  value in the  $\tau - Q$  plane. For our calculational method in terms of the weakly nonlinear analysis around the codimension-2 point, we refer to Sec. 1.3.3. According to our calculations, the primary

bifurcations are always supercritical. In Fig. 3.30, the amplitudes of type I ( $A$ ) and II ( $B$ ) instabilities are plotted as function of  $Re$ . In Fig. 3.30a, the type I instability precedes the type II instability with increasing  $Re$ , whereas for larger  $\tau$  we have found the opposite case (see Fig. 3.30b). For finite  $Q$  we have a similar scenario, however the codimension-2 point is shifted to larger  $\tau$ . For example, the codimension-2 point is around  $\tau = 56$  for  $Q = 10$ . For  $(\tau, Q) = (49, 0)$ , there exist the prediction of a mixed state of type I/II modes (both  $A$  and  $B$  finite) in Fig. 3.30b [45]. We have determined the coefficients of the coupled amplitude equations and have been unable to confirm this prediction. In parallel we have made simulations in this case and found no mixed states either.

## 3.4 Numerical Simulation of the Ekman-Couette Patterns

In this part, we will present some representative patterns from our simulations and discuss their features for different parameter sets in the case of stationary and oscillatory instabilities. According to the linear analysis, we always have oblique rolls which have a relatively small orientation angle  $\phi$  ( $6^\circ$ ) to the direction of the meanflow. To resolve this angle we have performed most simulations on a  $256 \times 256$  grid in the  $x - y$  plane. The computational effect is fairly large, since at least 12 Galerkin modes are necessary in the  $z$ - direction to resolve the Ekman layers.

In the patterns presented below, the vertical component of the velocity field (i.e.  $v(x, y, z, t)$ ) at different vertical positions  $z$  is shown. The  $x$ - coordinate increases towards the right and the  $y$ - coordinate is directed upwards. First, we focus on the small rotation rates  $2 < \tau < 25$ ; the  $\tau > 25$  case (i.e. oscillatory instabilities) will be discussed later.

### 3.4.1 Simulations at low $\tau$

At small rotation rates  $\tau$ , we have found stationary roll structures from the Galerkin analysis in Sec. 3.3.2 (see Fig. 3.27a). This is confirmed in Fig. 3.31, where we arrive at a stationary pattern as well, starting from random initial conditions at low  $\varepsilon$ . In Fig. 3.32, it is shown that the directional shear components  $Nu_\xi$ ,  $Nu_\eta$  at  $z = 0.4$  become time independent.

In the following, we show some further simulations to confirm the stability diagram in Fig. 3.27.

In Fig. 3.33, we demonstrate for  $\varepsilon = 1.74$ ,  $q = 1.8$  the transverse instability which takes place for the relatively high  $\varepsilon$  values according to Fig. 3.27a. In pattern, we see some modulations aligned in the same direction with the roll axis. In the region where the stationary rolls are oscillatorily unstable against transverse modulations, we have found stable traveling wave with an orientation as in the type I case. An example is shown in Fig. 3.34.

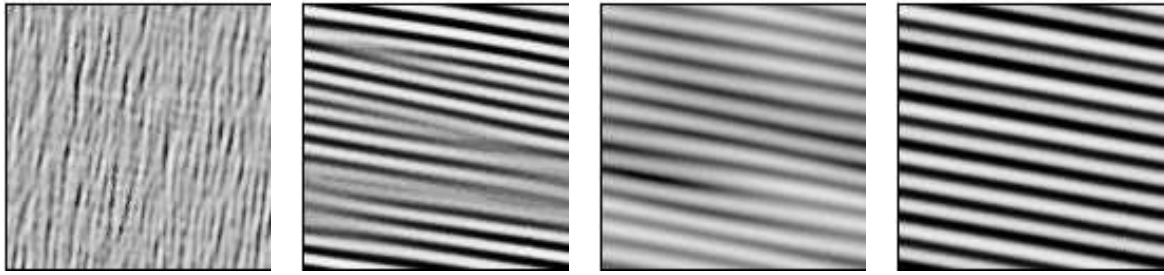


Figure 3.31: Typical stationary oblique roll patterns from random initial condition for  $\tau = 17$ ,  $Q = 10$ ,  $\varepsilon = 0.01$ , ( $Re_c = 1968$ ),  $q = q_c = 2.01$  and  $\phi = 7.7^\circ$  at  $z = 0.4$  (see Fig. 3.27a). The plots from left to right correspond to the times  $t = 0, 0.03, 0.23$  and  $0.6$ . The aspect ratio is  $\Gamma = 26$ .

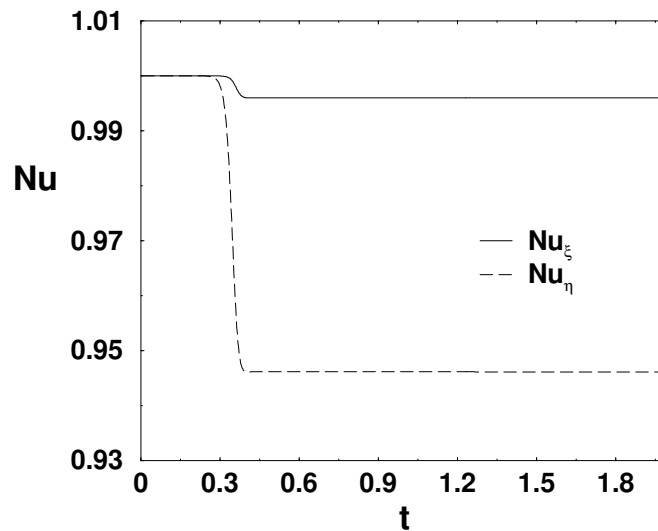


Figure 3.32: Time evolution of the Nusselt numbers  $Nu$  for the same parameters as in Fig. 3.31 in units of  $t_v$ .

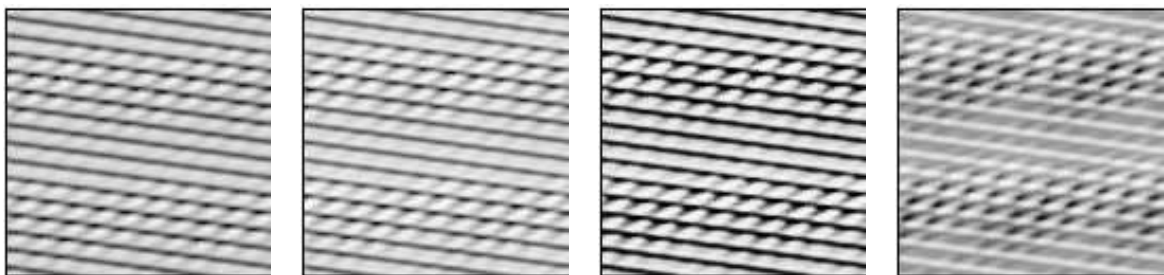


Figure 3.33: Transverse instability for  $\tau = 17$ ,  $Q = 10$ ,  $\varepsilon = 1.74$  ( $Re_c = 1968$ ),  $q = 1.8$  and  $\phi = 3.43^\circ$  (see Fig. 3.27a). The plots from left to right correspond to the times  $t = 0.0112, 0.0113, 0.0114$  and  $0.0116$ . The aspect ratio is  $\Gamma = 34$ .

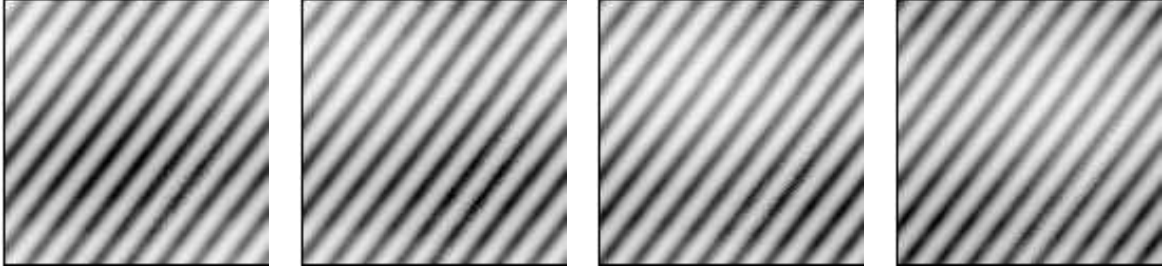


Figure 3.34: Oscillatory instability for  $\tau = 17$ ,  $Q = 10$ ,  $\varepsilon = 2.55$ ,  $q = 2.2$  and  $\phi = -36.8^\circ$  (see Fig. 3.27a). The plots from left to right correspond to the times  $t = 0.193, 0.195, 0.197$  and  $0.199$ . The aspect ratio is  $\Gamma = 28$ .

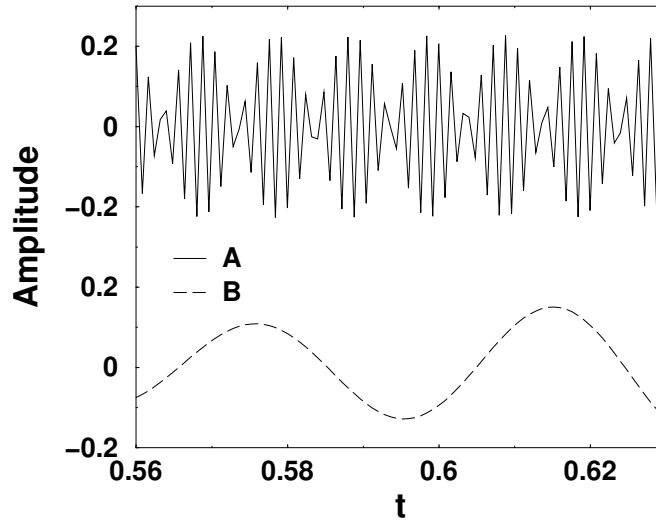


Figure 3.35: Leading two amplitudes in the case of oscillatory instabilities. Parameters are as in Fig. 3.34.

In Fig. 3.35 we show the leading amplitude  $A$  for the corresponding wave number  $\mathbf{q} = 3.22 (-0.8, 0.6)$ . The frequency  $\omega_A$  of the wave is very near to the Hopf frequency of the oscillating rolls. Superimposed to the traveling wave we have also observed a periodic motion in  $y$ -direction. The corresponding amplitude  $B$  of this mode is shown in Fig. 3.35. Note that the frequency of  $B$  is fairly small and corresponds to a very small wave number ( $q = 0.31$ ).

### 3.4.2 Simulations in the traveling wave regime

The most interesting simulations have been found for the oscillatory states which bifurcate at moderate and high rotation rates  $\tau$ . In this section, the simulations of the type I/II instabilities will be presented for various parameter sets. We would like to emphasize that we show the patterns for  $\omega > 0$ , which are concentrated near the lower plate. The traveling waves are described as  $\cos(q_x x + q_y y + \omega t)$  in our simulation code

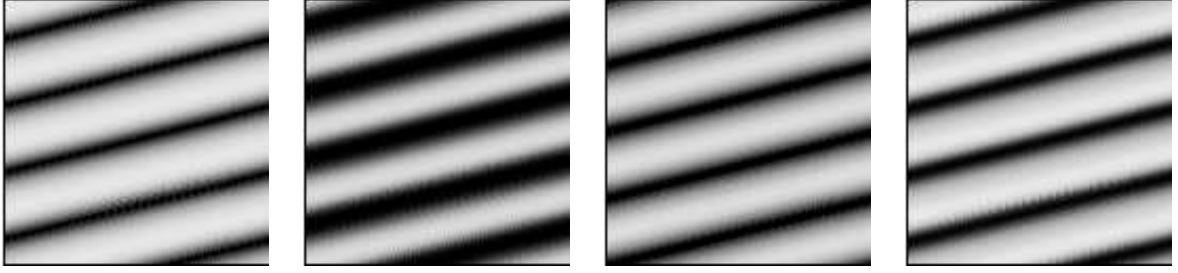


Figure 3.36: Rolls of type I travels in positive  $y$ - direction from random initial condition for  $\tau = 80$ ,  $Q = 40$ ,  $\varepsilon = 0.02$ , ( $Re_c = 3187.8$ ),  $q_c = 4.89$ ,  $\phi_c = -8^\circ$  and  $\omega_c = 1526$  at the plane  $z = -0.4$ . The plots from left to right correspond to the times  $t = 1.480$ , 1.484, 1.488 and 1.492. The aspect ratio is  $\Gamma = 10$ .

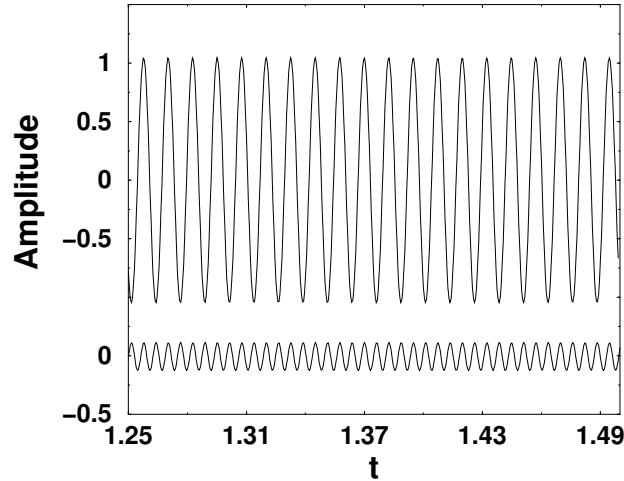


Figure 3.37: The amplitudes of the leading modes (at  $q_c$  and  $2q_c$ ) as function of time for the same parameters in Fig. 3.36.

with  $q_x > 0$  and  $|q_y| \gg |q_x|$ . In this case, the instability types of the traveling rolls are identified by the help of  $q_y$ . The waves correspond to type I instability have  $q_y < 0$  and practically move in positive  $y$ - direction, but in the case of type II instability,  $q_y > 0$  and the waves move in negative  $y$ - direction. First we start with the type I instability patterns which have a negative orientation angle  $\phi$  with

$\mathbf{q} = -|\mathbf{q}|(\sin(\phi), \cos(\phi)) = (q_x, q_y)$ . In Fig. 3.36, a typical traveling wave resulting from a type I instability is shown for relatively high  $Q$ . The pattern is recorded near the lower boundary plate, and the rolls move in positive  $y$ - direction. As function of time, the optical contrast of the patterns also change, as shown in the second plot. The leading amplitudes have been plotted in Fig. 3.37. It is obvious that the amplitudes for the leading two modes are time periodic. The second mode is the higher harmonic since the frequency has doubled.

In the case of type II instability, a typical time evolution with a positive orientation

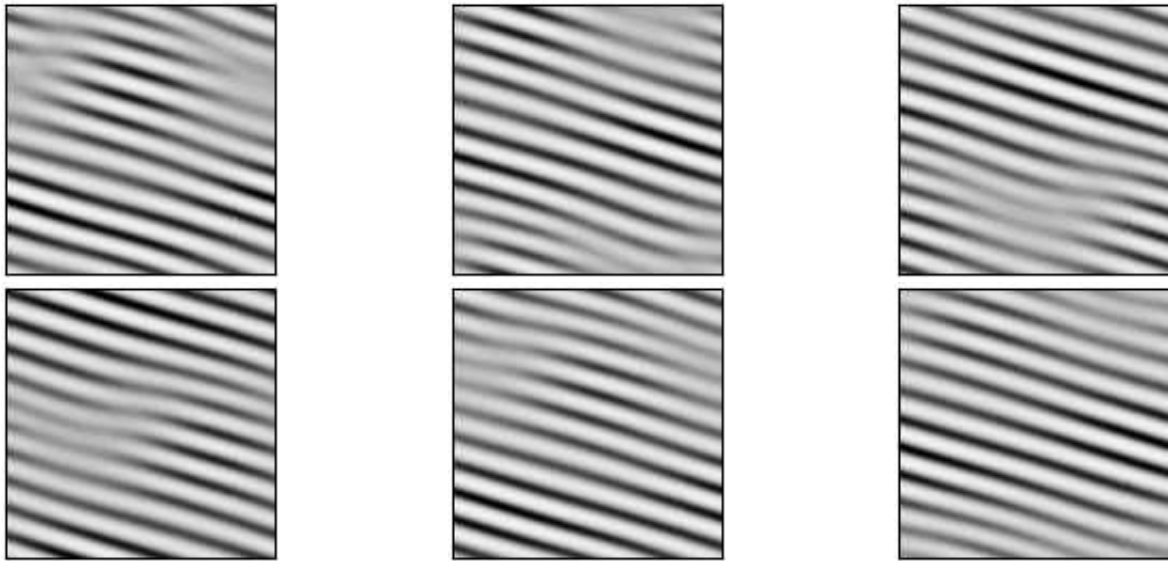


Figure 3.38: Type II instability rolls traveling in negative  $y$ - direction. Random initial condition for  $\tau = 60$ ,  $Q = 0$ ,  $\varepsilon = 0.01$ ,  $\varepsilon = 0.01$ , ( $Re_c = 1135.3$ ),  $q_c = 2.52$ ,  $\phi_c = 16.4^\circ$  and  $\omega_c = 308.3$  at the plane  $z = 0$ . The plots from left to right correspond to the times  $t = 0.122, 0.124, 0.126, 0.128, 0.13$  and  $0.132$ . The aspect ratio is  $\Gamma = 24$ .

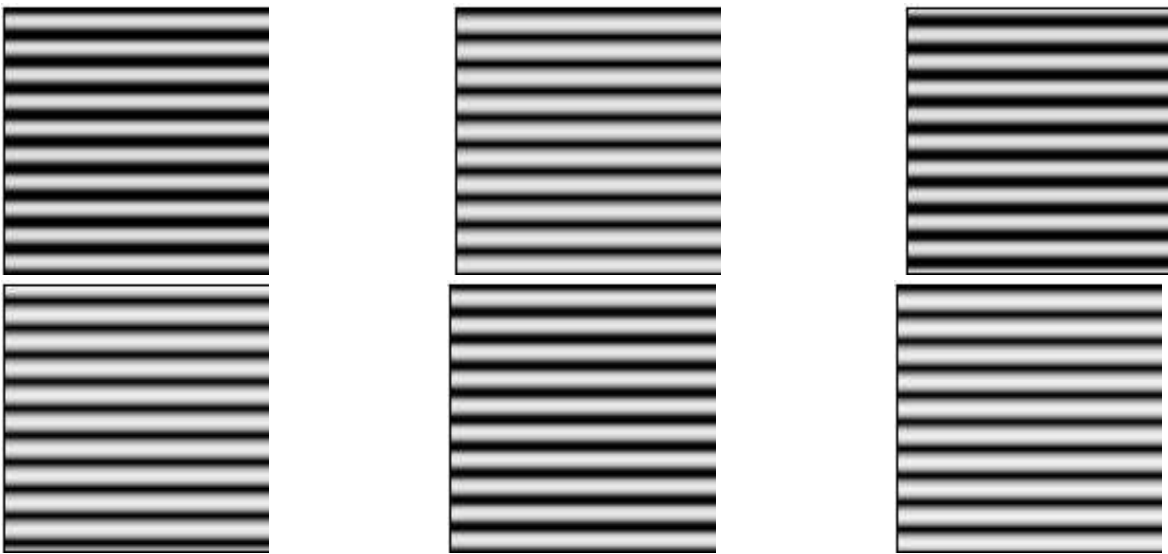


Figure 3.39: Rolls arising from the type II instability in a rotated coordinate system aligned with  $\mathbf{q}_c$  which travel in negative  $y$ - direction for  $\tau = 60$ ,  $Q = 10$ ,  $\varepsilon = 0.01$ , ( $Re_c = 1473.9$ ),  $q_c = 2.43$ ,  $\phi_c = 14.67^\circ$  and  $\omega_c = 353$  at the plane  $z = 0.4$  (see Sec. 3.2). The plots from left to right correspond to the times  $t = 0.167, 0.171, 0.176, 0.18, 0.184$  and  $0.189$ . The aspect ratio is  $\Gamma = 20$ .

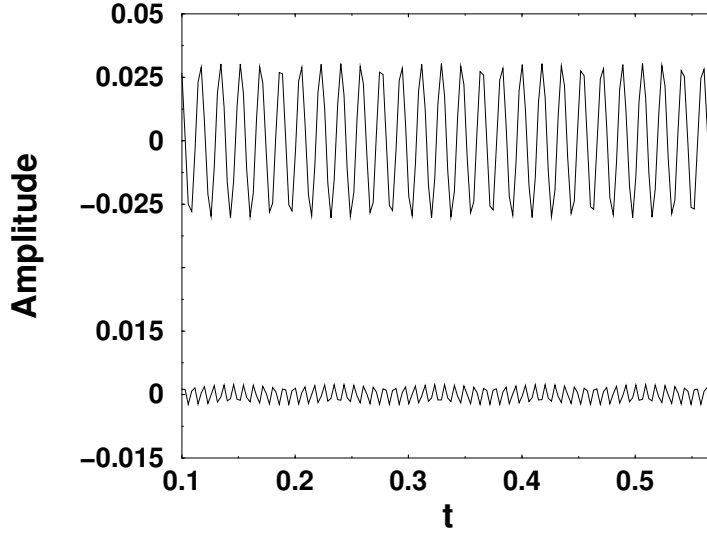


Figure 3.40: The amplitudes of the leading modes (at  $q_c$  and  $2q_c$ ) as function of time for the same parameters in Fig. 3.38. Time is in the units of  $t_v$

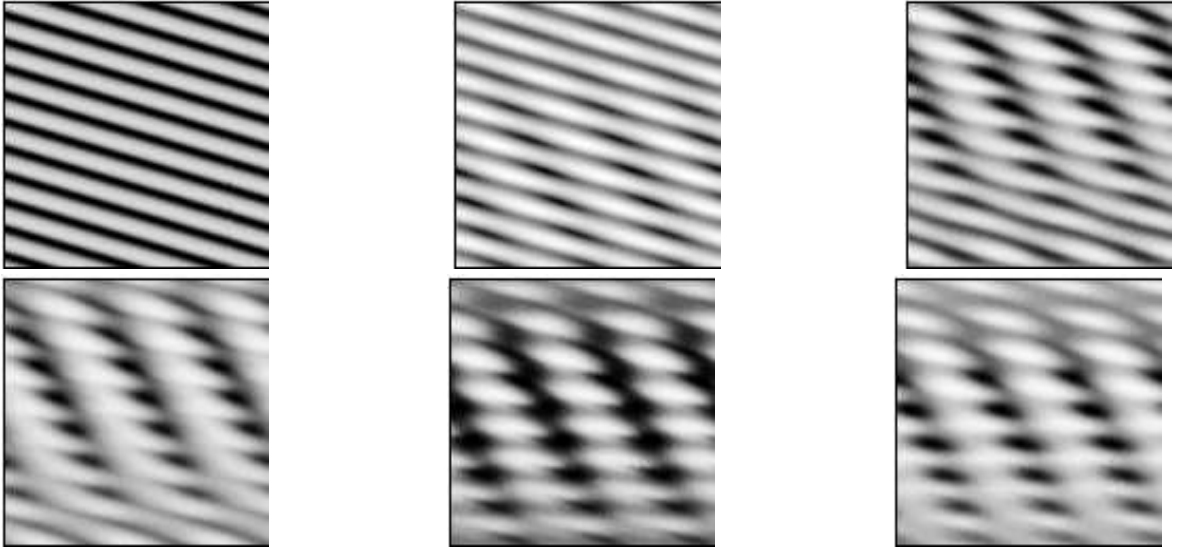


Figure 3.41: Transverse instability of the type II rolls for  $\tau = 80$ ,  $Q = 20$ ,  $\varepsilon = 0.7$  ( $R_c = 1486.7$ ) at  $z = 0.4$  plane. Note that the type II rolls move in negative  $y$ -direction. The plots from left to right correspond to the times  $t = 0.04$ ,  $0.124$ ,  $0.142$ ,  $0.148$ ,  $0.154$  and  $0.158$ . The aspect ratio is  $\Gamma = 26$ .

angle is shown in Fig. 3.38. Here, the rolls travel in negative  $y$ - direction. Since we start with a random initial condition, there exist some dislocations at the beginning.

We have also performed some simulations in the case of type II instability using the rotated coordinate system  $(\xi, \eta)$  aligned with  $\mathbf{q}_c$ . One has only to adapt the direction of the meanflow in our codes, since the hydrodynamic equations are rotationally invariant.

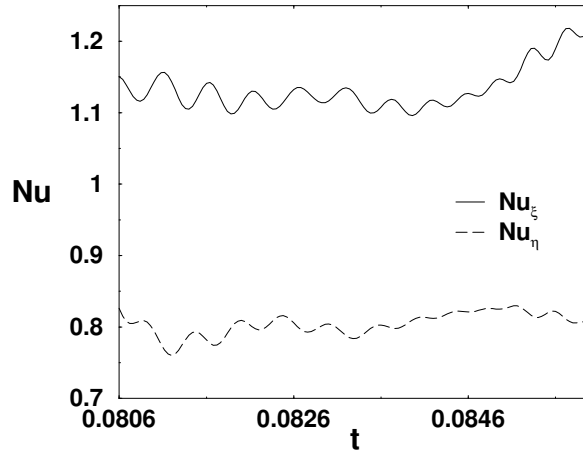


Figure 3.42:  $Nu$  values as function of time for the same parameters during the instability in Fig. 3.41.

According to Fig. 3.39, the patterns move downward to the left for  $\tau = 60$  and  $Q = 10$ . In Fig. 3.40 we have plotted the two leading modes. The second mode ( $B$ ) is a higher harmonic and thus also much weaker in amplitude than the leading mode near  $Re_c$ .

In Fig. 3.41, a transverse instability of the type II state has been presented for  $\varepsilon = 0.7$ . The simulation starts with ideal type II rolls with the orientation angle  $\phi = \phi_c = 17^\circ$ , after some time a destabilization of the state is seen. The destabilizing angle of the instability has been found as  $\phi = 57^\circ$ . The wave number decreases considerably to  $q = 1.1$  after the instability. According to Fig. 3.42, the directional  $Nu$  components are not constant with time because of the secondary instabilities. For relatively low  $Re$ , we have observed that the Nusselt numbers are constant for pure type II rolls.

## 3.5 Solitary Vortex Solutions

Beside the periodic solutions, which follow the bifurcation sequence from the initial state, we have also found stationary solitary vortex solutions. We devote this section to some features of this solution.

The solitary vortex solutions exist in a parameter region different from the spatially periodic patterns. The phenomenon of the solitary wave forms has already been observed in experimental studies for last two decades. We suggest the reader two of the latest studies by Schouveiler et al [71] and Serre et al. [72]. In their studies, the spots and other solitary forms were observed in a stator-rotator disc geometry at sufficiently large  $Re$ . These solutions are not associated with a destabilization of the basic state. Theoretically they have been found for the present geometry by Busse and his co-worker [46].

To investigate this type of solution, we have in principle used a stationary standard Galerkin scheme. We have neglected all coefficients and corresponding equations satisfying the truncation condition  $N + M > N_t$  (see Eq. (2.12d)), where  $N_t$  is a nat-

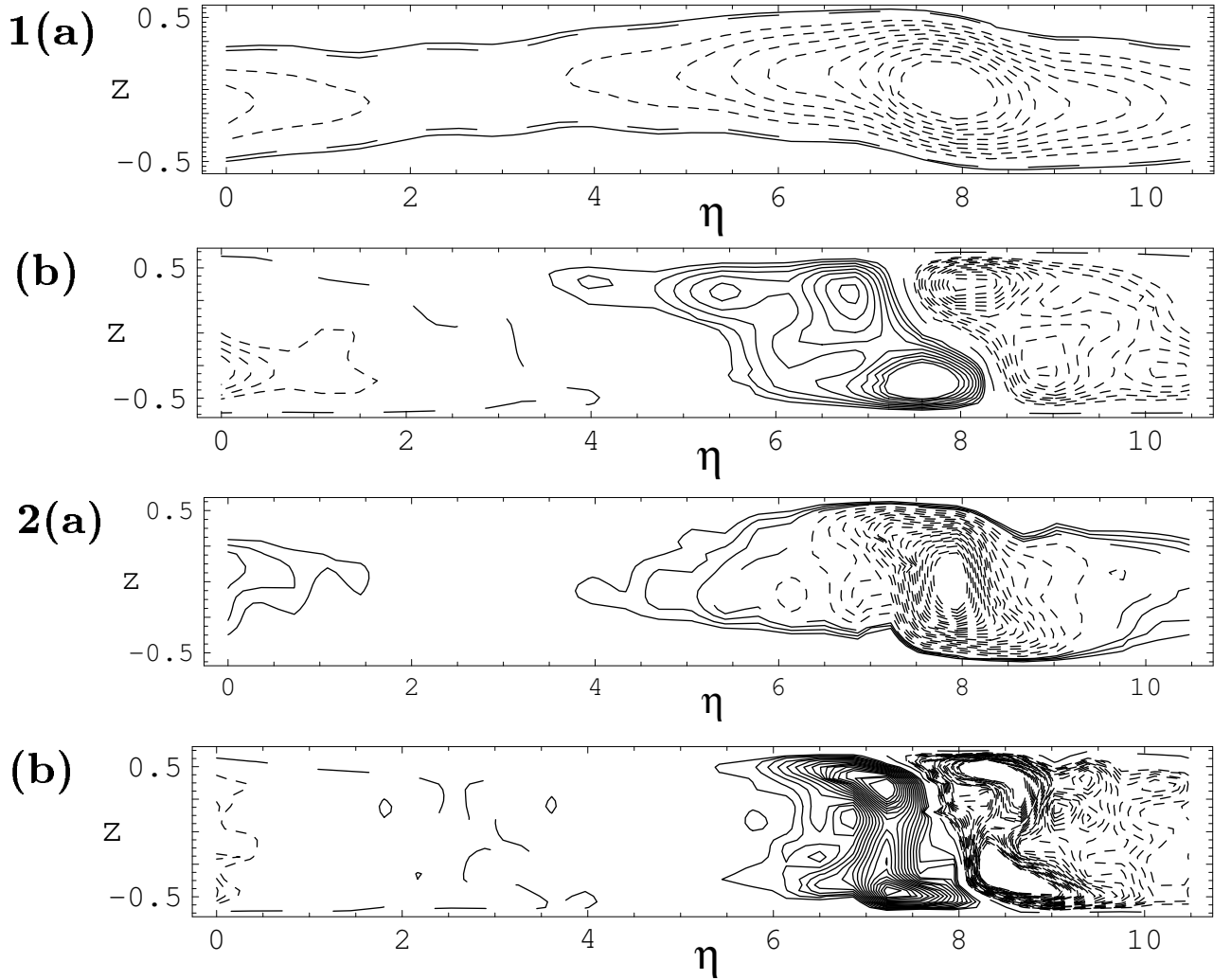


Figure 3.43: The solitary vortex solution in the  $\eta-z$ -plane for (1)  $Re = 2610$ ,  $\tau = 10$ ,  $Q = 9$ ,  $\phi = 0.57^\circ$ , (2)  $Re = 1980$ ,  $\tau = 70$ ,  $Q = 1$ ,  $\phi = 30.3^\circ$ . (a) The lines of  $\frac{\partial v}{\partial \eta}$  and (b) constant  $\xi$ -component of the velocity.

ural number which has been set equal to 10 or higher in the computations. Whenever significant changes with respect to the results obtained for  $N_t + 2$  have been noticed, higher values of  $N_t$  up to  $N_t = 16$  have been used in the calculations.

To provide an overview for the reader, some typical contour plot representations of the solitary waves are shown in the  $\eta-z$  plane for various parameter sets in Fig. 3.43. We have used periodic boundary condition in the  $\eta$  direction. The *integral interval*  $L_\eta$  is parameterized by a wave number  $q$  according to  $L_\eta = 2\pi/q$ . Note that there exist only one vortex in the entire  $\eta$  direction in each plot. The solitary solutions are in fact independent from the integration interval  $L_\eta$ . According to Fig. 3.43, the streamlines exhibit less smooth behavior for relatively higher magnetic energy  $Q$  for small Reynolds numbers  $Re$ . Comparing Figs. 3.43(1,2) it is obvious that the solitary

vortices are much more localized at high  $\tau$ . To show the effect of horizontal spacing ( $L_\eta$ ), we plotted Fig. 3.44. When the horizontal distance  $L_\eta$  has been increased, the solitary characteristic of the vortices becomes more obvious.

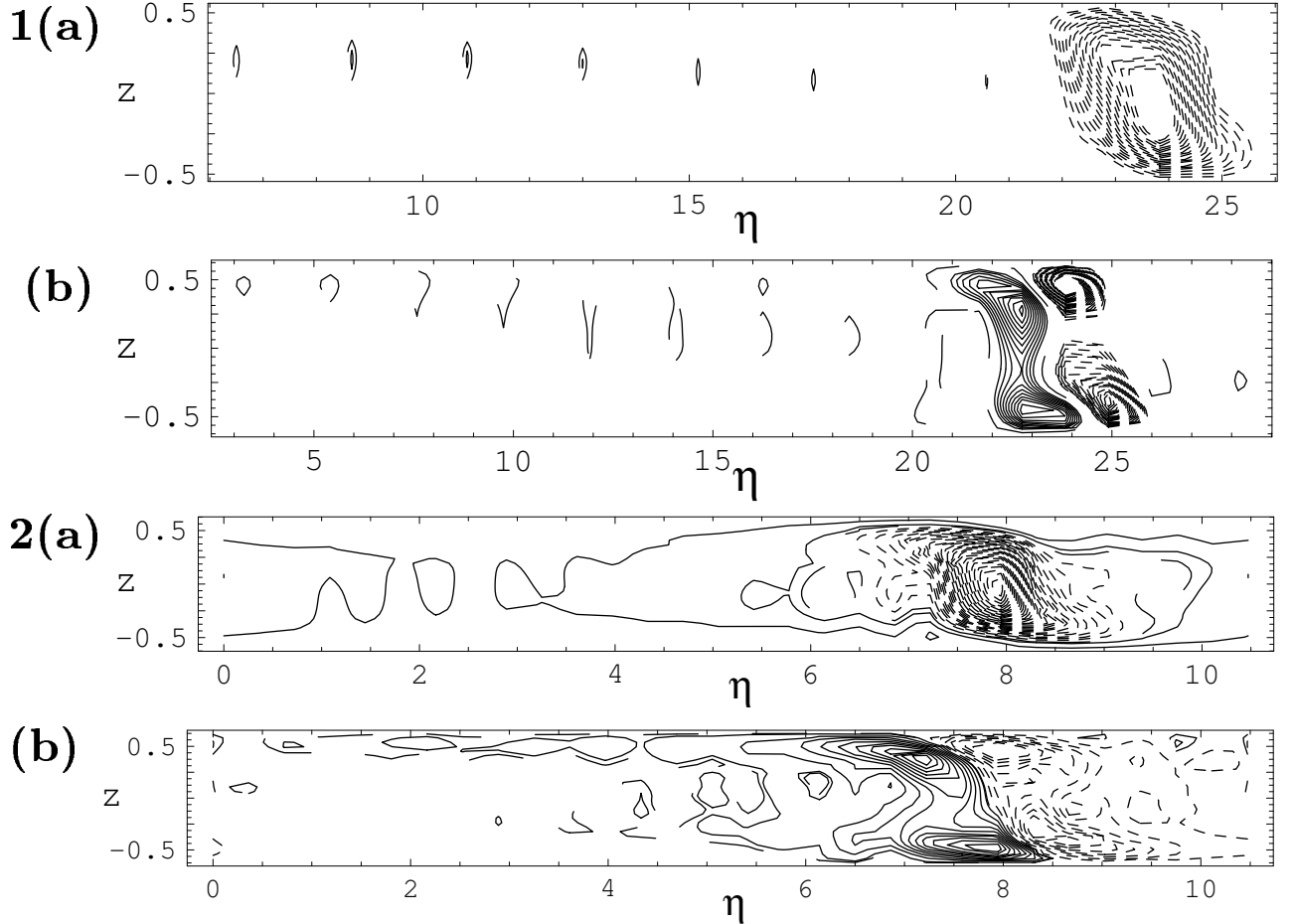


Figure 3.44: The effect of the modification of the integral interval  $L_\eta$  to the generation of solitary vortex solutions. Streamlines of the solitary vortex solution in the  $\eta - z$ -plane for (1)  $Re = 2020$ ,  $\tau = 70$ ,  $Q = 25$ ,  $q \sim 1/L_\eta = 0.2$ ,  $\phi = 30.3^\circ$ , (2) the same parameters except  $q \sim 1/L_\eta = 0.6$ . (a) The lines of  $\frac{\partial v}{\partial \eta}$  and (b) constant  $\xi$ -component of the velocity.

In the following, we will first address the shear components for different parameter sets. Secondly, some other characteristics of the solitary vortex will be pointed out. In the last part, a short section on stability analysis will be presented.

### 3.5.1 The directional Nusselt numbers

In this part, we will present some features of the shear from the solitary vortex structures. For the mathematical details of the directional shear, we refer to the Sec. 3.3.1.

At first we would like to start with a representative graph which shows the effect of the truncation parameter  $N_t$  (Fig. 3.45). In this graph, we have calculated the components

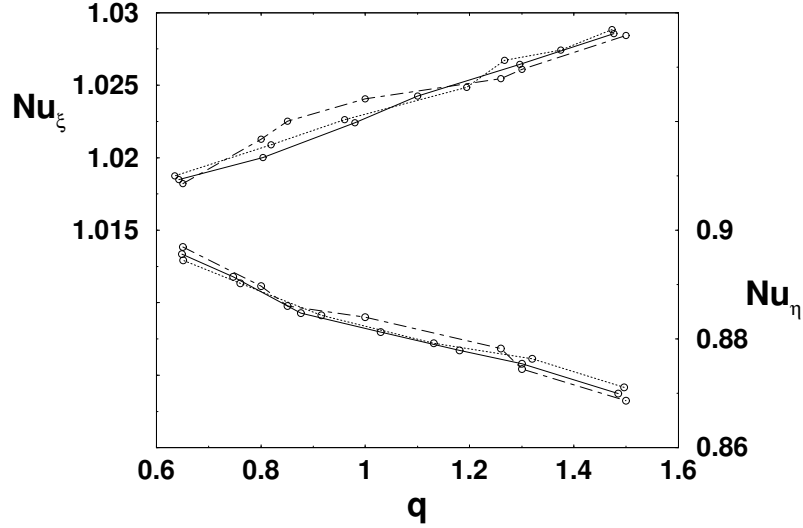


Figure 3.45: The components of the Nusselt numbers  $Nu_\xi$  (upper lines) and  $Nu_\eta$  (lower lines) for  $\tau = 10$ ,  $Q = 9$ ,  $\phi = -5.72^\circ$  and  $Re = 2000$ . The solid, dotted and dash-dotted lines show the results for the truncation parameters  $N_t = 14$ ,  $N_t = 10$  and  $N_t = 8$ , respectively.

of  $Nu$  as function of  $q \sim \frac{1}{L_\eta}$ . We denoted the  $1D$ - spacing along the  $\eta$  direction with  $L_\eta$  which determines the horizontal distance of the cell in which the solitary wave forms were observed. It is clear that, for sufficiently large  $q$  values, an isolated wave form shows a linear dependence on  $q$  since the fraction of space occupied by the solitary vortices increase linearly by  $q$ . This behavior can not be seen for the other roll solutions such as standard stationary Ekman rolls and oscillatory rolls (see also Fig. 3.25). In Fig. 3.45, the linear dependence of the Nusselt numbers on the wave number  $q$  changes slightly by the truncation parameter  $N_t$ . Note also that  $N_t = 14$  is in principle sufficient for the investigation of the solitary vortex motions.

In Fig. 3.46, we have plotted the components of  $Nu$  for increasing  $Re$  in the case  $\tau = 17$  and  $Q = 0$ . The behavior of the  $Nu$  curves are entirely different then the case of both stationary and oscillatory instabilities. The solitary vortices always give two different values for each  $Nu$  components at a certain  $Re$ . However stationary Ekman solutions give well defined curves and they always have only one value for each of the  $Nu$  components for certain  $Re$  values. With decreasing  $Re$ , the shear increases up to a certain point in both directions, then it decreases until meeting a turning point. They never come to  $Nu_\xi = Nu_\eta = 1$  point for low  $Re$  in contrast to the stationary and oscillatory solutions.

In Fig. 3.47, the directional  $Nu$  values as function of  $Re$  are drawn for a finite  $Q$  ( $= 9$ ). Here we have also plotted the  $Nu$  components for standard stationary Ekman

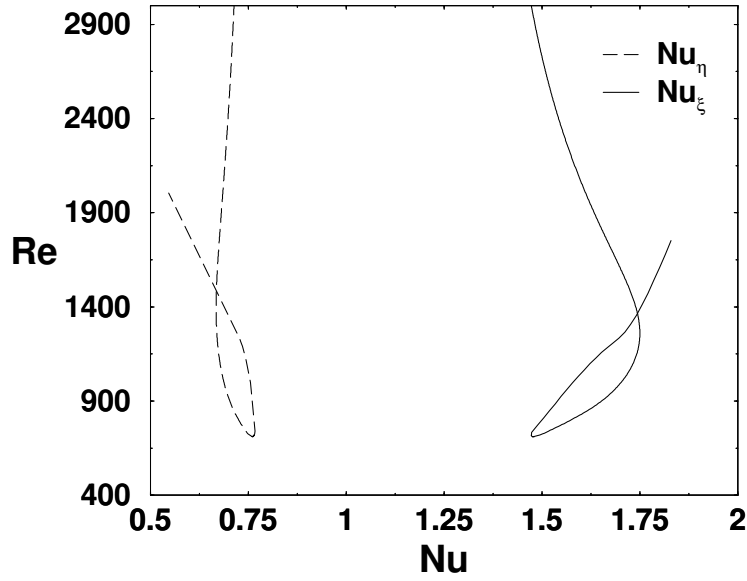


Figure 3.46: The Nusselt numbers  $Nu_\xi$  (dashed) and  $Nu_\eta$  (solid) as function of  $Re$  for  $\tau = 17$ ,  $Q = 0$ ,  $\phi = 16.5^\circ$  and  $q = 3.1$ .

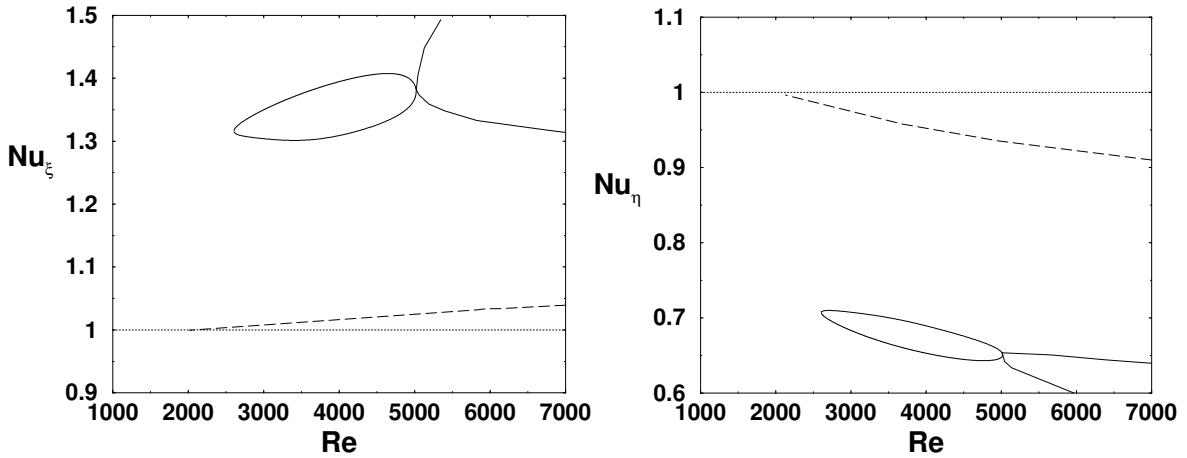


Figure 3.47: The directional Nusselt numbers  $Nu_\xi$  and  $Nu_\eta$  for stationary Ekman rolls (dashed lines) and for the solitary vortex solutions (solid lines) in the case  $\tau = 10$ ,  $Q = 9$ ,  $q = 0.6$ ,  $\phi = 9.74^\circ$ .

rolls (dashed lines). In principle, the magnetic field does not change the global features of the shear at the boundaries since the curves are very similar to the ones in Fig. 3.46. Besides, the directional components of the shear are much higher ( $Nu_\xi \approx 1.35$ ,  $Nu_\eta \approx 0.75$ ) than the ones in the stationary case ( $Nu_\xi \approx 1.05$ ,  $Nu_\eta \approx 0.9$ ).

In Fig. 3.48 the directional Nusselt numbers  $Nu_\xi$  and  $Nu_\eta$  are shown as function of the orientation angle  $\phi$ , for which the localized solutions were found, in the case  $\tau = 25$  and  $Q = 6.3$ . It is seen that the exerted shears on the plates give an elliptical

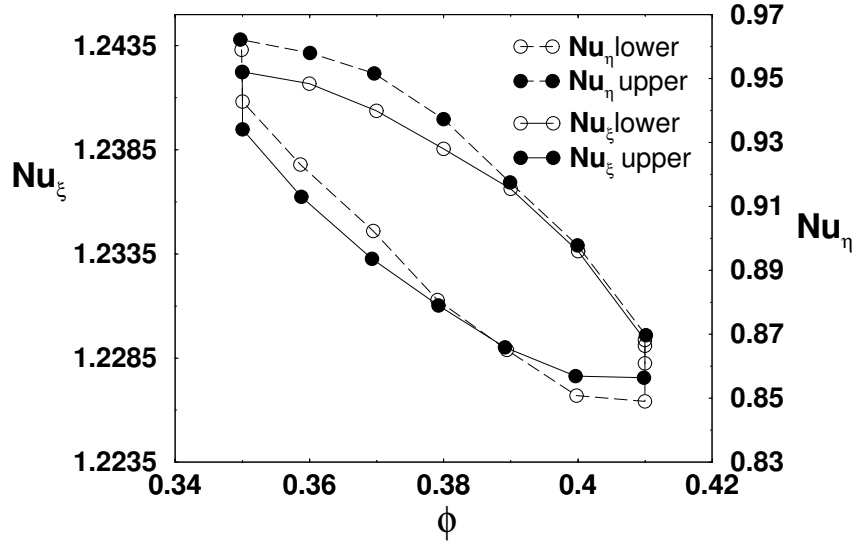


Figure 3.48: The directional  $Nu$  components as function of the orientation angle  $\phi$  in the case  $Re = 1820$ ,  $Q = 6.3$ ,  $\tau = 25$ ,  $q = 0.9$ . Filled (open) circles correspond to solutions of the upper (lower) branch.

curve as function of  $\phi$ . The point is that there is always only one solitary vortex in the interval  $0 \leq \eta \leq \frac{2\pi}{q}$  over which the shear has been averaged.

### 3.5.2 The onset of the solitary vortex solutions

In this section, we will mainly discuss the onset of the solitary vortex solutions in the case of finite magnetic energy  $Q$ . Initially, we would like to emphasize that the same terminology which was used in the linear stability analysis for the determination of  $Re_c$  is considered, here. We have scanned  $Re$  values for certain  $\tau$  and whenever we have found a localized structure for a  $Re$  value, we have reconstructed our solution for lower  $Re$ . A representative  $\tau - Re$  plot is shown to determine the onset of the solitary vortex solution in the case  $Q = 6.25$  (Fig. 3.49a). For small  $\tau$ ,  $Re_c$  curve decreases up to a certain  $\tau$  ( $\sim 25$ ), then the onset increases and occurs at higher  $Re$  for high  $\tau$ . Comparing our findings with the literature, this global feature was also found by Hoffmann and Busse [46] in the case of  $Q = 0$ , but, for instance, our onset for  $(\tau, Q) = (100, 6.25)$  is slightly higher than their results for  $(\tau, Q) = (100, 0)$ . Thus, we conclude that the onset of solitary vortex solution increases by  $Q$ .

In Fig. 3.49b, the orientation angles  $\phi_c$  which correspond to the critical values in Fig. 3.49a are shown as function of  $\tau$ . For low  $\tau$ ,  $\phi_c$  first increases almost linearly, then it produces a local minima around  $\tau = 50$ . For high rotations, it continues to increase, again.

For three different  $Q$  value, we have calculated the critical Reynolds numbers  $Re$  as functions of the orientation angle  $\phi$  in Fig. 3.50a. It is clear from the graph that the  $\phi$  values are very important for the generation of the solitary structures, in fact, one

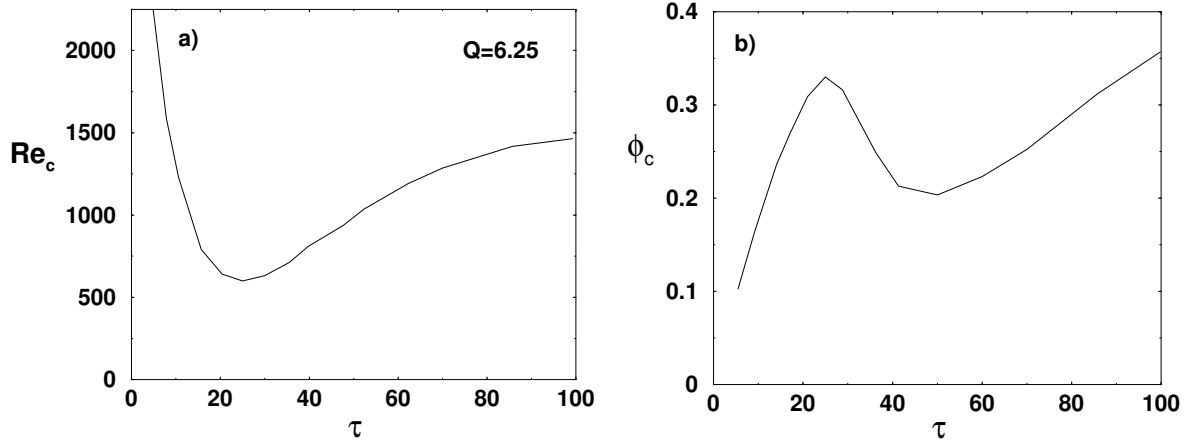


Figure 3.49: (a) Critical Reynolds numbers  $Re_c$  for the existence of solitary vortex solutions and (b) the corresponding orientation angle  $\phi_c$  in the case of  $Q = 6.25$ .

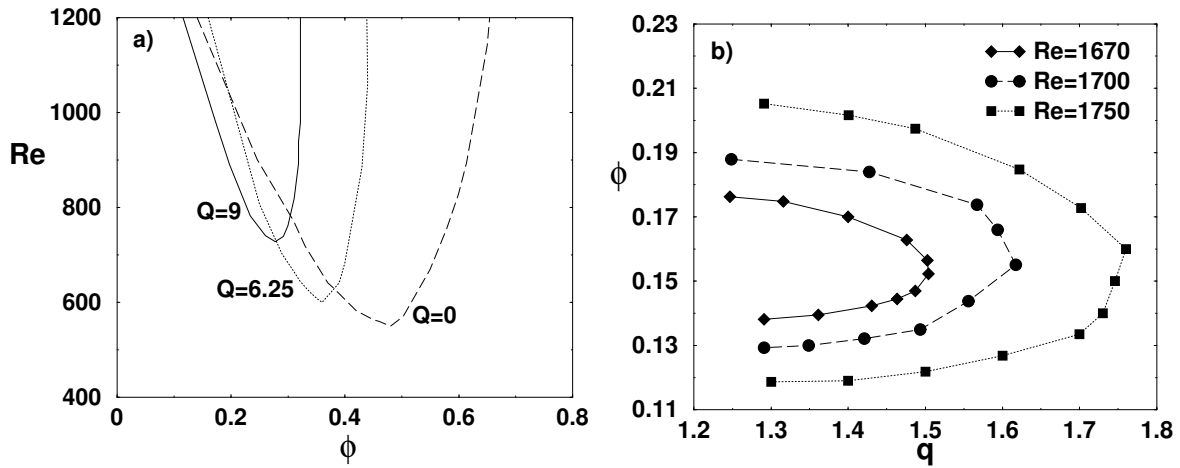


Figure 3.50: (a) Reynolds numbers  $Re$  as function of the critical orientation angle  $\phi$  for several  $Q$  values in the case of  $\tau = 25$ . (b) The range of angles  $\phi$  for which solitary vortex solutions exist as function of  $q$  in the case  $\tau = 25$  and  $Q = 6.25$ .

can not find solitary rolls for an arbitrary angle. In addition,  $Re$  values as function of  $\phi$  indicate parabola-like curves, but the widths of the curves shrink with increasing  $Q$ . Note also that the critical orientation angles  $\phi_c$  (i.e. the minimal points of parabolas) skip to lower angles and the onset Reynolds number increases with increasing  $Q$ .

In Fig. 3.50b, the relation between  $\phi$  and  $q$  is drawn. There exist a finite range of  $\phi$  which increases as the parameter  $q$  decreases.

### 3.5.3 Stability analysis of the solitary vortex solutions

In this section, we will present the stability analysis of the solitary vortex solutions with the help of Galerkin method. As already discussed in the previous parts of the

thesis (see in Chap. 1), the growthrates  $\sigma$  can be obtained from the solution of an eigenvalue problem which includes the infinitesimal disturbances for a given stationary solitary vortex solution.

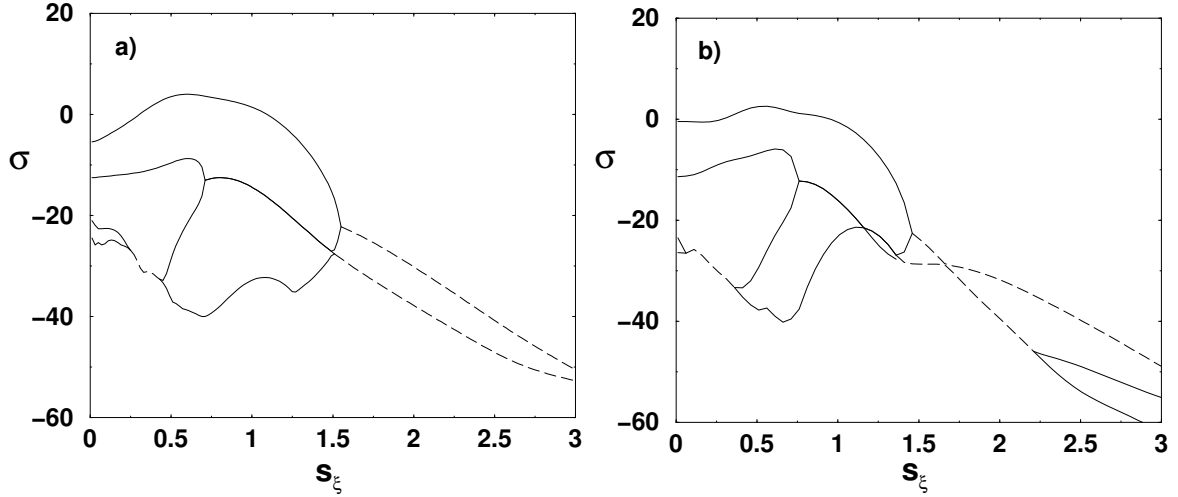


Figure 3.51: Growthrates  $\sigma$  as function of  $s_\xi$  in the case  $Re = 730$ ,  $\tau = 25$ ,  $Q = 9$ ,  $q = 0.6$  and  $\phi = 14.3^\circ$ . the upper (lower) solutions. Growthrates with vanishing (finite) imaginary parts are denoted by solid (dashed) lines for the (a) upper and (b) lower solution branches.

It is found that as a consequence of the solitary nature, the solitary vortex solutions are not sensitive to changes in the wavenumber  $q$ . Thus, the dependence on the Floquet parameter  $s_\xi$  (disturbance component parallel to the roll axis) is much more interesting.

Typical examples of the growthrate  $\sigma$  as function of  $s_\xi$  from the stability analysis are shown in Fig. 3.51 in the case  $\tau = 25$ ,  $Q = 9$ . The largest  $\sigma$  are characterized by vanishing imaginary parts  $\omega$  and exhibit two maxima at  $s_\xi = 0$  and at a finite value of  $s_\xi$  which increases with  $Re$ . This behavior is mainly found for the upper branch of the solution characterized by a higher value of  $Nu_\xi$  than the lower branch. The maximum of  $\sigma$  at the finite value of  $s_\xi$  exceeds the ones at  $s_\xi = 0$  for lower values of  $Re$  and  $\tau$  while the opposite property is found for the larger values of  $Re$  and  $\tau$ . For the lower branch, on the other hand, the growthrate  $\sigma$  appears to reach its highest value always at a finite value of  $s_\xi$  which is higher than zero, but it increases with decreasing  $Re$ . As  $Re$  reaches the minimum value of about 726.2 the growthrate spectra of the upper and lower branch approach each other as must be expected for reasons of continuity. While the upper solution exhibits a higher amplitude than the lower solution, it still appears to be always unstable even though the growthrates are usually much smaller than for the lower solution.

## 3.6 Concluding Remarks

In this chapter of the thesis, we have investigated for the first time linear and non-linear properties of the Ekman-Couette layer in the presence of an external magnetic field perpendicular to the layer. For increasing Coriolis number  $\tau$ , a stationary steady instability first occurs, then two different types of oscillatory instabilities which are characterized as type I/II take place for  $\tau > 25$ . The critical parameters have been determined as functions of  $\tau$  and the magnetic field energy  $Q$  with the help of Galerkin methods. Critical values of the Reynolds number  $Re_c$ , wave number  $q_c$  and the orientation angle  $\phi_c$  are in good agreement with the earlier results in the case of the conventional Ekman-Couette layer problem for  $Q = 0$  [41, 45]. We have observed that the onset of instabilities increases with increasing  $Q$ . This stabilizing effect of the magnetic field has also been observed in many other comparable systems such as magnetic Rayleigh-Bénard convection and magnetohydrodynamic convection [27, 8, 73, 38].

According to stability analysis of the stationary roll solutions, there exist long-wave and shortwave instabilities. Modulational instabilities have been observed slightly above the neutral curve, while the shortwave transverse and the oscillatory instabilities take place for relatively higher  $\varepsilon$ . In the case of oscillatory instabilities, we have explored the vicinity of codimension-2 point where the type I and II instabilities compete. The codimension-2 point occurs at higher  $\tau$  for increasing  $Q$ . We could not find any mixed state where two instabilities interact with each other as predicted for  $Q = 0$  [45].

Complementary to the Galerkin analysis for the first time direct numerical simulations have been carried out for the stationary and oscillatory instabilities with the use of different parameter sets which are in good agreement with the Galerkin analysis for this problem.

From a Galerkin analysis, a solitary localized vortex solutions have been found even below the onset of stationary and type II instabilities. Unfortunately, neither for  $Q = 0$  nor for finite  $Q$  we have been able to find stable solutions for the solitary vortices.



# Chapter 4

## General Conclusion

Our goal was to investigate the pattern formation phenomena in two different rotating fluid systems under the influence of the magnetic field. Initially, we focused on the mathematical tools and methods, which were intensely used in the exploration of two pattern forming systems, detailed in Chapter 1. The periodic roll solutions and their stability analysis were described. In addition, we mentioned the order parameter equations as well as the considerations and the solutions of the complex amplitude equations. The analytical background on the resonant- modes interactions which govern the subharmonic varicose and knot instabilities in rotating annulus problem was then explained. In addition, the basic concepts of the direct numerical simulation were presented.

We devoted Chapter 2 to the convection problem in the rotating cylindrical annulus under the influence of azimuthal magnetic field. As a first step, a one-mode approximation was considered to obtain the critical Rayleigh number  $R_c$  and critical wave vector  $\mathbf{q}_c$  as function of the Coriolis number  $\tau$  and magnetic energy  $Q$ . The results were in good agreement with the exact values of critical parameters obtained from Galerkin analysis. In a further step, nonlinear roll solutions were constructed and their stabilities beyond the neutral curve  $\varepsilon = \frac{R-R_c}{R_c} > 0$  were examined for selected sets of  $\tau$ ,  $Q$ . Both longwave and shortwave instabilities for  $\mathbf{q} \neq \mathbf{q}_c$  were found. In the case of high Prandtl numbers  $P$ , the stable regions of rolls with different roll angles  $\chi$  were identified in  $\tau - \varepsilon$  plane. A multi-stability of the patterns were proven, i.e. various roll patterns were in a competition. Beside the spatially- periodic patterns, a complicated space-time dynamism in a large parameter region was found. Among the instabilities, we focused on the subharmonic skewed-varicose (*SHV*) and knot instabilities since both instabilities were not explored for the finite values of Coriolis number  $\tau$  and magnetic energy  $Q$  in the literature, yet. Both the stability diagrams and the amplitudes of the instabilities were confirmed by a number of patterns produced by the direct numerical simulations.

In Chapter 3, the magnetic Ekman-Couette layer was investigated, theoretically. Using similar analytical methods as in the previous chapter, the basic equations were solved as an eigenvalue problem under the appropriate boundary conditions. For low and high values of Coriolis number  $\tau$ , we found stationary and oscillatory instabilities,

respectively. The critical Reynolds numbers  $Re_c$ , wave numbers  $q_c$  and the orientation angles of rolls  $\phi_c$  were obtained from the linear analysis for different  $\tau$ ,  $Q$  sets. The onset of instabilities increased with the magnetic energy  $Q$ . Our results were in a good agreement with the earlier results for  $Q = 0$  [41, 45]. According to the nonlinear analyses on the stationary Ekman roll solutions, we found both longwave and shortwave instabilities for finite  $Q$ . Longwave instabilities such as Eckhaus, zig-zag ( $ZZ$ ) and skewed-varicose ( $Sv$ ) dominated for small  $\varepsilon$ . In addition, an oscillatory shortwave instability was observed for relatively high  $\varepsilon$ . In the case of oscillatory instabilities at high  $\tau$ , we carried out a weakly nonlinear analysis at the vicinity of codimension-2 point. The codimension-2 point increased to higher  $\tau$  values for increasing  $Q$ . We could not find a mixed state of two oscillatory instabilities (i.e. type I/II). The direct simulations for both steady and oscillatory instabilities produced interesting patterns for the first time in this problem. For relatively higher  $\varepsilon$ , subharmonic modes were also observed from simulations. In addition, some localized and unstable solitary vortex structures which did not bifurcate from the standard Ekman roll solutions were found and some of their features were determined for finite  $Q$ .

Since the lack of experimental studies on both of the problems, we could not compare our results directly with experiments at the moment. A number of codes are available for future researches to compare the results of theory with the results of experiments whenever experiments are planned.

# Appendix A

## Coupled Amplitude Equations for the *SHV* and Knot instabilities

In this appendix we will discuss in detail the subharmonic varicose (*SHV*) and the knot instability of axial rolls, which have been already mentioned in Sec. 1.4 (see also Fig. 1.3). The presentation follows closely standard routes (see e.g. [24, 25, 32])

### A.1 Subharmonic varicose instability

The subharmonic varicose (*SHV*) patterns, which result from the *SHV* instability of axial rolls ( $\mathbf{q}_1 = (q, 0)$ ), correspond to the special choice  $s_x = (q/2)$  with  $\mathbf{s} = (s_x, s_y)$  in Eq. (1.31). If in particular  $s_y = \frac{\sqrt{3}}{2}q$  is chosen the vectors  $\mathbf{q}_j, j = 1, 2, 3$  span a hexagon and in this case the notion “hexaroll” pattern has been introduced. Since  $\mathbf{q}_6 = -\mathbf{q}_3$  and  $\mathbf{q}_7 = -\mathbf{q}_2$  one can identify:  $F \rightarrow C^*, G \rightarrow B^*$  in the general resonance conditions (1.33). Thus we restrict ourselves in general to the modes  $A, B, C, D, E$  in this subsection (see Fig. 1.3, left panel) .

The main features of the *SHV* instability appear already when considering only the modes  $A, B, C$ , which leads to the following coupled amplitude equations ([24]):

$$\partial_t A = \sigma_A A - \eta_1 B^* C^* - A \left[ a_{11} |A|^2 + a_{12} |B|^2 + a_{13} |C|^2 \right], \quad (\text{A.1a})$$

$$\partial_t B = \sigma_B B - \eta_2 A^* C^* - B \left[ a_{21} |A|^2 + a_{22} |B|^2 + a_{23} |C|^2 \right], \quad (\text{A.1b})$$

$$\partial_t C = \sigma_C C - \eta_3 A^* B^* - C \left[ a_{31} |A|^2 + a_{32} |B|^2 + a_{33} |C|^2 \right]. \quad (\text{A.1c})$$

The additional resonance couplings  $\propto \eta$  between the modes in quadratic order (in comparison with the non-resonant coupled amplitude equations (1.29)) are characterized by purely imaginary coefficients  $\eta_j, j = 1, 2, 3$  in the case of the rotating annulus, whereas the  $a_{ij}$  are real. The calculation is simplified, since certain coefficients have the same values, due to the axial symmetry in our system:

$$\sigma_C = \sigma_B, \quad \eta_2 = \eta_3, \quad a_{21} = a_{31}, \quad a_{12} = a_{13}, \quad a_{22} = a_{33}, \quad a_{23} = a_{32}. \quad (\text{A.2})$$

The calculation of the coefficients  $\eta_i$  is straightforward. According to our general scheme we obtain, for instance, for  $\eta_1$ :

$$\eta_1 = \langle \mathbf{U}(\mathbf{q}_1) | \hat{\mathbf{N}}(\mathbf{U}(-\mathbf{q}_2), \mathbf{U}(-\mathbf{q}_3)) \rangle \quad (\text{A.3})$$

where we use the notation  $\mathbf{U}(\mathbf{q}_i) := \mathbf{U}_1(\mathbf{q}_i)$ . The calculation of most of the cubic coefficients is straightforward as well. For instance  $a_{11}$  is found in Eq. (1.30). The coefficient  $a_{12}$  contains one contribution  $a_{12}^I$ , whose calculation is not problematic:

$$a_{12}^I = \langle \mathbf{U}(\mathbf{q}_1) | \left[ \hat{\mathbf{N}}(\mathbf{U}(\mathbf{q}_2), \mathbf{V}_\perp(\mathbf{q}_1, -\mathbf{q}_2)) + \hat{\mathbf{N}}(\mathbf{U}(\mathbf{q}_1), \mathbf{V}_\perp(\mathbf{q}_2, -\mathbf{q}_2)) \right] \rangle. \quad (\text{A.4})$$

The remaining contribution  $a_{12}^{II}$  is given as:

$$a_{12}^{II} = \langle \mathbf{U}(\mathbf{q}_1) | \hat{\mathbf{N}}(\mathbf{U}(-\mathbf{q}_2), \mathbf{V}_\perp(\mathbf{q}_1, \mathbf{q}_2)) \rangle. \quad (\text{A.5})$$

Because of  $\mathbf{q}_1 + \mathbf{q}_2 = -\mathbf{q}_3$  we have to restrict the second-order solution  $\mathbf{V}_\perp(\mathbf{q}_1, \mathbf{q}_2)$  to the subspace orthogonal to  $\mathbf{U}(-\mathbf{q}_3)$  by a suitable projection, as explained in Sec. 1.3.1. It is obvious that otherwise  $a_{12}$  would contain a contribution, that is already considered explicitly in the term  $\propto \eta_1$ .

The axial symmetry of our system allows symmetric solutions  $|B| = |C|$  which govern the *SHV* patterns, also according to our numerical results. As already mentioned, due to translational invariance two phases of the amplitudes can be arbitrarily chosen and we take  $A, B$  to be real and positive. It will turn out that  $C$  is purely imaginary. To determine the *SHV* instability from Eq. (A.1) only the terms linear in the  $B, C$  have to be kept:

$$\partial_t B = \sigma_B B - \eta_2 C^* A_0 - a_{21} B A_0^2, \quad (\text{A.6a})$$

$$\partial_t C^* = \sigma_C C^* + \eta_2 A_0 B - a_{31} C^* A_0^2. \quad (\text{A.6b})$$

It is obvious that perturbations of  $A$  do not contribute in linear order in  $B, C$ . The amplitude  $A$  is thus given as  $A_0 = \sqrt{\sigma_A/a_{11}}$  (see Eq. (A.1a)). Eqs. (A.6) are solved with the ansatz:  $B = X_2 \exp(\sigma t)$  and  $C = X_3 \exp(\sigma t)$ . In a compact vector-matrix notation the resulting eigenvalue problem reads as:

$$\sigma \begin{pmatrix} X_2 \\ X_3^* \end{pmatrix} = \begin{pmatrix} \sigma_B - a_{21}|A_0|^2 & -\eta_2 A_0 \\ \eta_2 A_0 & \sigma_B - a_{21}|A_0|^2 \end{pmatrix} \begin{pmatrix} X_2 \\ X_3^* \end{pmatrix} =: \mathcal{M} \begin{pmatrix} X_2 \\ X_3^* \end{pmatrix}. \quad (\text{A.7})$$

We define the new variables,

$$k := \sigma_B - a_{21}|A_0|^2, \quad d := |\eta_2|A_0, \quad (\text{A.8})$$

and arrive at the secular equation  $(k - \sigma)^2 - d^2 = 0$  of Eq. (A.7), which yields two real roots  $\sigma_\pm = \pm|d| + k$  and thus:

$$\sigma_{SH} = |\eta_2|A_0 + \sigma_B - a_{21}A_0^2. \quad (\text{A.9})$$

The condition,  $\sigma_{SH} > 0$  describes the *SHV* instability regime of rolls and the *SHV* threshold at  $R = R_{SH}$  where  $\sigma_{SH}(R)$  passes zero. The non-normalized eigenvector

$\mathbf{X}$  of Eq. (A.7) for the largest eigenvalue,  $\sigma = \sigma_{SH}$  and the corresponding orthogonal adjoint  $\mathbf{X}_{ad}$  are given as:

$$\mathbf{X} = \begin{pmatrix} X_2 \\ X_3^* \end{pmatrix} = \begin{pmatrix} 1 \\ i \end{pmatrix} \quad ; \quad \mathbf{X}_{ad} = \begin{pmatrix} X_2 \\ X_3^* \end{pmatrix}^\dagger = (1, -i) \quad (\text{A.10})$$

with  $\mathbf{X}_{ad} \cdot \mathbf{X} = 2$  (hermitian scalar product).

Eqs. (A.1) can be solved without difficulty in the nonlinear *SHV* regime ( $B, C$  finite). Here we sketch only the weakly nonlinear analysis which starts with the following ansatz:

$$\begin{pmatrix} B \\ C^* \end{pmatrix} = A_{SH} \begin{pmatrix} 1 \\ i \end{pmatrix}. \quad (\text{A.11})$$

At first, the correction of the roll amplitude  $A_0$  in the *SHV*-state is obtained by linearizing Eq. (A.1a) about  $A_0$  ( $A \rightarrow A_0 + \delta A$ ) up to the order  $\mathcal{O}(|B|^2, |C|^2)$ :

$$0 = \sigma_A \delta A - 3a_{11} A_0^2 \delta A - a_{12} A_0 |B|^2 - a_{13} A_0 |C|^2 - \eta_1 B^* C^* \quad (\text{A.12})$$

A simple calculation leads to ( $C^* = iB$ ):

$$\delta A = |A_{SH}|^2 \left[ \frac{2a_{12} A_0 + i\eta_1}{-2\sigma_A} \right] =: |A_{SH}|^2 c_A. \quad (\text{A.13})$$

We found  $i\eta_1$  always to be positive. Thus  $c_A < 0$  as it should be. Up to order  $\mathcal{O}(A_{SH}^3)$ , Eqs. (A.6) can be written as

$$\mathcal{M} \begin{pmatrix} B \\ C^* \end{pmatrix} - \bar{\mathbf{N}} = 0. \quad (\text{A.14})$$

Here, the vector  $\bar{\mathbf{N}}$ , which includes all cubic terms, reads:

$$\bar{\mathbf{N}} = \begin{pmatrix} 2a_{21} A_0 B \delta A + a_{22} |B|^2 B + a_{23} |C|^2 B + \eta_2 C^* \delta A \\ 2a_{31} A_0 C^* \delta A + a_{32} |B|^2 C^* + a_{33} |C|^2 C^* - \eta_2 B \delta A \end{pmatrix}. \quad (\text{A.15})$$

Replacing  $C^*$  by  $iB = iA_{SH}$  the amplitude is determined from the solvability condition:

$$0 = \mathbf{X}_{ad} \cdot (\mathcal{M} A_{SH} \mathbf{X}) - \mathbf{X}_{ad} \cdot \bar{\mathbf{N}}. \quad (\text{A.16})$$

Using the symmetries (A.2) and inserting  $\delta A$  (A.13) one obtains easily for the amplitude  $A_{SH}$ :

$$A_{SH}^2 = \frac{\sigma_{SH}}{c_A(2a_{21}A_0 + i\eta_2) + a_{22} + a_{23}} \equiv \frac{\sigma_{SH}}{N_{SH}} \quad (\text{A.17})$$

Here we have exploited the relation  $\mathbf{X}_{ad} \cdot (\mathcal{M} \mathbf{X}) = 2\sigma_{SH}$ . From the necessary condition,  $A_{SH}^2 > 0$  the bifurcation to hexarolls at  $R = R_{SH}$  is supercritical if  $N_{SH} > 0$  ( $\sigma_{SH} > 0$  for  $R > R_{SH}$ ), while it would be subcritical for  $N_{SH} < 0$ . We found in most cases  $N_{SH} > 0$  since  $-c_A \eta_{12} > 0$  prevailed in  $N_{SH}$ . Due to  $\sigma_{SH} \sim R - R_{SH}$ ,  $A_{SH}^2$  starts linearly in  $R - R_{SH}$  as well.

The analysis presented above is sufficient to capture the basic *SHV* mechanism and becomes exact in the limit  $\tau \rightarrow 0$ . However, it is less satisfactory from a quantitative point of view in our system, since for finite magnetic field the *SHV* instability appears at finite  $\tau$ : The *SHV* onset was shifted in some cases by 15% and more compared to exact value. A closer look has revealed that additional resonant couplings to the vectors  $\mathbf{q}_4, \mathbf{q}_5$  shown in Fig. 1.2 are important. We arrive at a generalization of the previous three coupled amplitude equations (A.1), which contain additional, in particular cubic resonant coupling terms.

$$\begin{aligned} \partial_t A &= \sigma_A A - A [a_{11}|A|^2 + a_{12}|B|^2 + a_{13}|C|^2 + a_{14}|D|^2 + a_{15}|E|^2] \\ &\quad - \eta_{11} B^* C^* - \eta_{12} B E - \eta_{13} C D - \rho_{11} A^* B^* D - \rho_{12} A^* C^* E, \end{aligned} \quad (\text{A.18a})$$

$$\begin{aligned} \partial_t B &= \sigma_B B - B [a_{21}|A|^2 + a_{22}|B|^2 + a_{23}|C|^2 + a_{24}|D|^2 + a_{25}|E|^2] \\ &\quad - \eta_{21} A^* C^* - \eta_{22} A E^* - \rho_{21} A^* A^* D - \rho_{22} C D E^*, \end{aligned} \quad (\text{A.18b})$$

$$\begin{aligned} \partial_t C &= \sigma_C C - C [a_{31}|A|^2 + a_{32}|B|^2 + a_{33}|C|^2 + a_{34}|D|^2 + a_{35}|E|^2] \\ &\quad - \eta_{31} A^* B^* - \eta_{32} A D^* - \rho_{31} A^* A^* E - \rho_{32} B D^* E, \end{aligned} \quad (\text{A.18c})$$

$$\begin{aligned} \partial_t D &= \sigma_D D - D [a_{41}|A|^2 + a_{42}|B|^2 + a_{43}|C|^2 + a_{44}|D|^2 + a_{45}|E|^2] \\ &\quad - \eta_{41} A C^* - \rho_{41} A A B - \rho_{42} B C^* E, \end{aligned} \quad (\text{A.18d})$$

$$\begin{aligned} \partial_t E &= \sigma_E E - E [a_{51}|A|^2 + a_{52}|B|^2 + a_{53}|C|^2 + a_{54}|D|^2 + a_{55}|E|^2] \\ &\quad - \eta_{51} A B^* - \rho_{51} A A C - \rho_{52} B^* C D. \end{aligned} \quad (\text{A.18e})$$

We focus on the solutions of Eq. (A.18) which develop from the secondary *SHV* instability of axial rolls. Then solutions with  $|B| = |C|$  and  $|D| = |E|$  prevail, the phases are fixed by the resonance terms  $\propto \eta_i, \rho_i$ . The optimal choice for the *SHV* instability turns out to be:

$$C^* = i B, \quad E^* = i D; \quad \text{with real } B > 0, \quad D < 0. \quad (\text{A.19})$$

The coefficients are calculated as before, typically projections in the second order solutions have to be performed. For instance when calculating  $\rho_2$  the contribution:

$$\rho_2 = \langle \mathbf{U}(\mathbf{q}_2) | \hat{\mathbf{N}}(\mathbf{U}_1(-\mathbf{q}_1), \mathbf{V}_\perp(-\mathbf{q}_1, \mathbf{q}_4)) \rangle. \quad (\text{A.20})$$

is problematic. Because of  $-\mathbf{q}_1 + \mathbf{q}_4 = -\mathbf{q}_3$  we have to discard in  $\mathbf{V}_\perp(\mathbf{q}_1, -\mathbf{q}_4)$  the component parallel to  $\mathbf{V}(-\mathbf{q}_3)$  to avoid double counting.

To calculate the *SHV* growth rate  $\sigma_{SH}$  on the basis of Eq. (1.35) only the linear terms in  $B, C, D, E$  have to be kept. Eliminating  $C, E$  with  $C^* = i B, E^* = i D$  (A.19) we end up with:

$$\sigma_{SH} B = \sigma_B B - i \eta_{21} A_0 B - i \eta_{22} A_0 D - a_{21} B A_0^2 - \rho_{21} D A_0^2, \quad (\text{A.21a})$$

$$\sigma_{SH} D = \sigma_D D - i \eta_{41} A_0 B - a_{41} D A_0^2 - \rho_{41} A_0^2 B, \quad (\text{A.21b})$$

where  $A_0^2 = \sigma_A / c_{11}$  as before. The quadratic equation for  $\sigma_{SH}$  resulting from Eq. (A.21) is easily solved. With the help of the abbreviations:

$$m_{11} = \sigma_B - a_{12} A_0^2 - i \eta_{21}, \quad m_{12} = -i \eta_{22} A_0 - \rho_{21} A_0^2, \quad (\text{A.22})$$

$$m_{22} = \sigma_D - a_{41} A_0^2, \quad m_{21} = -i \eta_{41} A_0 - \rho_{41} A_0^2, \quad (\text{A.23})$$

we arrive at

$$\sigma_{SH} = \frac{m_{11} + m_{22}}{2} + \sqrt{\left(\frac{m_{11} + m_{22}}{2}\right)^2 - m_{11} m_{22} + m_{12} m_{21}} \quad (\text{A.24})$$

Note that the  $m_{ij}$  are real in our case since the  $\eta$ 's are purely imaginary.

Since  $\sigma_D < \sigma_B$  in our case a satisfactory approximation for  $\sigma_{SH}$  is obtained by adiabatically neglecting the time derivative of  $D$  in Eqs. (A.21):

$$D = \frac{i \eta_{41} A_0 + \rho_{41} A_0^2}{\sigma_D - a_{41} A_0^2} B =: c_D B, \quad (\text{A.25})$$

which leads immediately to the following expression of  $\sigma_{SH}$ :

$$\sigma_{SH} = \sigma_B - a_{21} A_0^2 - i A_0 (\eta_{21} + \eta_{22} c_D) - \rho_2 c_D A_0^2. \quad (\text{A.26})$$

Even if two first terms in Eq. (A.26) are negative the remaining ones, which make use of different resonance mechanism, give positive contributions, which prevail above  $R = R_{SH}$ . In particular the term  $\propto \rho_2$  leads to a considerable improvement of the previous expression  $\sigma_{SH}$  (A.9), where the terms  $\propto \rho_2, \eta_{22}$  were missing.

The weakly nonlinear analysis of the stationary solutions of Eqs. (A.18) follows closely the previous detailed analysis for the simpler model (A.1). The quadratic correction  $\delta A \propto B^2$  to  $A_0$  is obtained from Eq. (1.35a) as:

$$\delta A = \frac{A_0 [2a_{12} + 2a_{14}|c_D|^2 + c_D[\rho_{11} + \rho_{12}] - c_D[i\eta_{12} - i\eta_{13}] + i\eta_{11}] B^2}{-2\sigma_A} =: c_A B^2 \quad (\text{A.27})$$

Furthermore the following correction  $\delta D \propto B^3$  to  $D$  derives from Eq. (1.35b):

$$\begin{aligned} \delta D &= \frac{c_D [2a_{41}c_A A_0 + a_{42} + a_{43} + |c_D|^2(a_{44} + a_{45}) + \rho_{42}] + 2\rho_{41}c_A A_0 + i\eta_4 c_A}{\sigma_D - a_{41} A_0^2} B^3 \\ &=: c_D^{(3)} B^3. \end{aligned} \quad (\text{A.28})$$

Finally, the expansion of  $B$ - equation Eq. (A.18b) to cubic order in  $B$  leads to the Landau equation:

$$0 = \sigma_{SH} B - a_{SH} B^3 \Rightarrow B = \frac{\sigma_{SH}}{a_{SH}} \quad (\text{A.29})$$

with the cubic coefficient

$$\begin{aligned} a_{SH} &= 2a_{21} A_0 c_A + a_{22} + a_{23} + (a_{24} + a_{25}) |c_D|^2 + \rho_2 A_0^2 c_D^{(3)} \\ &+ i\eta_{21} c_A + i\eta_{22} c_A c_D + i\eta_{22} A_0 c_D^{(3)} + 2\rho_{21} A_0 c_A c_D + \rho_{22} c_D^2. \end{aligned} \quad (\text{A.30})$$

The  $SHV$  bifurcation is forward if  $a_{SH} > 0$ .

In general, we found the weakly nonlinear analysis of the  $SHV$  instability very helpful for the construction of fully nonlinear “ $SHV$ ” solutions via Galerkin methods (see Chap. 2).

## A.2 Coupled amplitude equations for knots

The knot patterns correspond to the special choice of  $\mathbf{s} = (s_x, s_y)$  with  $s_x = 0$  in Eq. (1.31). In this case the general mode couplings presented in Fig. 1.2 simplify considerably as demonstrated in Fig. 1.3b. Since  $\mathbf{q}_2 = -\mathbf{q}_7, \mathbf{q}_3 = -\mathbf{q}_6$  we can identify  $C, B$  with  $F^*, G^*$  and in addition  $G$  with  $F^*$  ( $\mathbf{q}_7 = -\mathbf{q}_6$ !). Thus we can restrict ourselves to the amplitudes  $A, D, E, F$  in Fig. 1.2 and arrive at the coupled amplitude equations:

$$\begin{aligned} \partial_t A &= \sigma_A A - A [a_{11}|A|^2 + a_{14}|D|^2 + a_{15}|E|^2 + a_{16}|F|^2] \\ &\quad - \eta_{11}EF - \eta_{12}F^*D - \rho_1 A^*DE, \end{aligned} \quad (\text{A.31a})$$

$$\begin{aligned} \partial_t D &= \sigma_D D - D [a_{41}|A|^2 + a_{44}|D|^2 + a_{45}|E|^2 + a_{46}|F|^2] \\ &\quad - \eta_{41}AF - \rho_{41}AAE^* - \rho_{42}FFE, \end{aligned} \quad (\text{A.31b})$$

$$\begin{aligned} \partial_t E &= \sigma_E E - E [a_{51}|A|^2 + a_{54}|D|^2 + a_{55}|E|^2 + a_{56}|F|^2] \\ &\quad - \eta_{51}AF^* - \rho_{51}AAD^* - \rho_{52}F^*F^*D, \end{aligned} \quad (\text{A.31c})$$

$$\begin{aligned} \partial_t F &= \sigma_F F - F [a_{61}|A|^2 + a_{64}|D|^2 + a_{65}|E|^2 + a_{66}|F|^2] \\ &\quad - \eta_{61}A^*D - \eta_{62}AE^* - \rho_{61}F^*DE^*. \end{aligned} \quad (\text{A.31d})$$

As already observed in the refined analysis of the the *SHV* instability (cf. Eqs. (1.35)) we find resonant couplings between the modes in quadratic order  $\sim \eta$  and in cubic order  $\sim \rho$ . The calculation of the coefficients in Eq. (A.31) follows the general scheme discussed before. In particular double-counting of modes has to be avoided by suitable projections on the space perpendicular to the modes  $A, C, D, F$ , when calculating the quadratic terms.

We will confine ourselves at first to the calculation of the onset of the knot instability, i.e. we keep only the terms linear in the  $D, E, F$ .

$$\sigma_{KN} D = \sigma_D D - a_{41}DA_0^2 - \eta_{41}FA_0 - \rho_{21}E^*A_0^2, \quad (\text{A.32a})$$

$$\sigma_{KN} E = \sigma_E E - a_{51}EA_0^2 - \eta_{51}A_0F^* - \rho_{51}A_0^2D^*, \quad (\text{A.32b})$$

$$\sigma_{KN} F = \sigma_F F - a_{61}FA_0^2 - \eta_{61}A_0D - \eta_{62}A_0E^*. \quad (\text{A.32c})$$

The amplitude  $A$  in Eqs. (A.32) has been replaced by  $A_0 = \sqrt{\sigma_A/a_{11}}$ , since perturbations of  $A$  in Eq. (A.31) do not contribute in linear order. Eqs. (A.32) can be studied with increasing degree of complexity. In a previous study of the knot instability [24] the special case  $E = D = 0$  (“cross-roll instability”) was considered. The linear growthrate of knot solutions is then given as  $\sigma_{KN} = \sigma_F - a_{61}A_0^2$ . In our case this approximation has no merits, since we observe the knot bifurcation at values of  $R$  where  $\sigma_F$  is strongly negative. In an alternative approach we might restrict ourselves to coupled equations for  $D$  and  $E$ . This corresponds to the wavy approximation discussed first in the context of the inclined layer [74], where the resonance terms  $\propto \rho_{ij}$  are exploited. However, the general case is simple as well. It turns out that  $D = -E$  holds ( $D$  real) and we have to solve the eigenvalue problem:

$$\sigma_{KN} D = \sigma_D D - a_{41}DA_0^2 - \eta_{41}FA_0 + \rho_{41}DA_0^2, \quad (\text{A.33a})$$

$$\sigma_{KN} F = \sigma_F F - a_{61}FA_0^2 - \eta_{61}DA_0 + \eta_{62}DA_0. \quad (\text{A.33b})$$

The fact that both  $D$  and  $F$  modes become important for higher  $\tau$  as already been mentioned in [25]. The linear eigenvalue problem (A.33) is easily solved with the help of following abbreviations:

$$m_{11} = \sigma_D - a_{41}A_0^2 + \rho_{41}A_0^2, \quad m_{12} = -\eta_{41}A_0 \quad (\text{A.34})$$

$$m_{22} = \sigma_F - a_{61}A_0^2, \quad m_{21} = -\eta_{61}A_0 + \eta_{62}A_0; \quad (\text{A.35})$$

$\sigma_{KN}$  is given by the right hand side of Eq. (A.24).

Since  $\sigma_F \ll \sigma_D$  an excellent approximation to  $\sigma_{KN}$  can be obtained by adiabatically eliminating the amplitude  $F$  using Eq. (A.33b):

$$F = \frac{(\eta_{61} - \eta_{62})A_0}{\sigma_F - a_{61}A_0^2} D =: c_F D. \quad (\text{A.36})$$

$\sigma_{KN}$  is now immediately obtained from Eq. (A.33a) as follows:

$$\sigma_{KN} = \sigma_D - \eta_{41}c_F A_0 + (\rho_{41} - a_{41}) A_0^2. \quad (\text{A.37})$$

The coefficients  $\eta_{41}, c_F$  are imaginary and their real product is negative in our case. Consequently the inclusion of the resonance terms  $\propto \eta_{41}, \rho_{41}$  reduces in our case substantially the threshold of the knot instability in comparison to the pure wavy roll ansatz ( $\sigma_{KN} = \sigma_D + \rho_{41} A_0^2$ ). In fact we will typically meet situations where  $\sigma_{KN} > 0$  despite  $\sigma_D < 0$ .

The weakly nonlinear analysis follows closely the *SHV* case in the previous section. The quadratic correction  $\delta A \propto D^2$  to  $A_0$  is obtained (see A.31a) as:

$$\delta A = \frac{A_0 [2a_{14} + a_{16}|c_F|^2 - \rho_1] - c_F(\eta_{11} + \eta_{12})}{-2\sigma_A} D^2 =: c_A D^2 \quad (\text{A.38})$$

Furthermore the following correction  $\delta F \propto D^3$  to  $F$  derives from Eq. (A.31d):

$$\delta F = \frac{c_F(2a_{61}c_A A_0 + a_{64} + a_{65} + a_{66}|c_F|^2 + \rho_{61}c_F) + c_A(\eta_{61} - \eta_{62})}{\sigma_F - a_{61}A_0^2} D^3 =: c_F^{(3)} D^3. \quad (\text{A.39})$$

Finally, the expansion of  $B$ - equation (A.31b) to cubic order in  $B$  leads to the Landau equation:

$$0 = \sigma_{KN}D - a_{KN} D^3 \Rightarrow D^2 = \frac{\sigma_{KN}}{a_{KN}} \quad (\text{A.40})$$

with

$$a_{KN} = 2a_{41}A_0c_A + a_{44} + a_{45} + a_{46}|c_F|^2 + \eta_{41}c_Ac_F + \eta_{41}A_0c_F^{(3)} - 2\rho_{41}A_0c_A - \rho_{42}c_F^2. \quad (\text{A.41})$$

The knot bifurcation is forward if  $a_{KN} > 0$ .



# Appendix B

## Numerical Details of the Simulation Process

The basic concepts and numerical elements of our simulation code have been designed in Bayreuth over the last decade. The code has been successfully applied to various convection systems (see e.g. [75, 32, 5]). For our purpose, we had to include the magnetic field effects for the rotating annulus. Major modifications were required in the Ekman-Couette problem. The new codes were tested in detail by comparison to Galerkin calculation.

### B.1 The Galerkin modes

In this thesis, we consider spatially extended systems in two horizontal directions ( $x$ ,  $y$ ), which are bounded by plates in the vertical direction ( $z$ ). Certain boundary conditions have to be fulfilled at the plates which are guaranteed by Galerkin expansions with respect to the appropriate test functions. For most fields we used trigonometric functions  $S_n(z) = \sin[n\pi(z + \frac{1}{2})]$ , which vanish at the plates (i.e. at  $z = \pm 1/2$  in reduced units). For the poloidal velocity potentials which vanish together with their derivatives at  $z = \pm 1/2$  we use the Chandrasekhar functions  $C_n(z)$ , which are defined as follows:

$$C_n(z) = \frac{\cosh \beta_n z}{\cosh \frac{1}{2}\beta_n} - \frac{\cos \beta_n z}{\cos \frac{1}{2}\beta_n}, \quad (n = 1, 3, 5, \dots), \quad (\text{B.1})$$

$$C_n(z) = \frac{\sinh \beta_n z}{\sinh \frac{1}{2}\beta_n} - \frac{\sin \beta_n z}{\sin \frac{1}{2}\beta_n}, \quad (n = 2, 4, 6, \dots). \quad (\text{B.2})$$

Here  $\beta_n$  are determined as the roots of the equations,

$$\tanh \beta/2 + \tan \beta/2 = 0 \text{ for odd } n, \quad \coth \beta/2 - \cot \beta/2 = 0 \text{ for even } n.$$

In the horizontal  $x$ ,  $y$  direction we use a pseudo-spectral method which involves *FFT*'s (Fast Fourier Transforms).

## B.2 The Adams-Bashforth time integration scheme

According to Eq. (1.13) the hydrodynamic equations can be written as

$$\partial_t A_i = \lambda_i A_i - \langle U_i | N_2(t) \rangle. \quad (\text{B.3})$$

Here,  $N_2(t)$  is an abbreviation for  $N_2(U_i, U_i)$ . Using the ansatz,

$$A_i(t) = \exp[\lambda_i t] \hat{A}_i(t) \quad (\text{B.4})$$

and eliminating the linear term in Eq. (B.3) the following equation is found after time integration:

$$\hat{A}_i(t + dt) - \hat{A}_i(t) = - \int_t^{t+dt} \exp[-\lambda_i t'] \langle U_i | N_2(t') \rangle dt'. \quad (\text{B.5})$$

In a next step the term  $\langle U_i | N_2(t') \rangle$  is approximated by the leading terms of a Taylor expansion around  $t$ ; the derivation is discretized. Thus we arrive at

$$\begin{aligned} \hat{A}_i(t + dt) - \hat{A}_i(t) = & - \int_t^{t+dt} \exp[-\lambda_i t'] \\ & \left\{ \langle V_i | N_2(t) \rangle + (t' - t) \frac{\langle V_i | N_2(t) \rangle - \langle V_i | N_2(t - dt) \rangle}{dt} \right\} dt'. \end{aligned} \quad (\text{B.6})$$

After performing the time integration (Eq. B.6) reads as

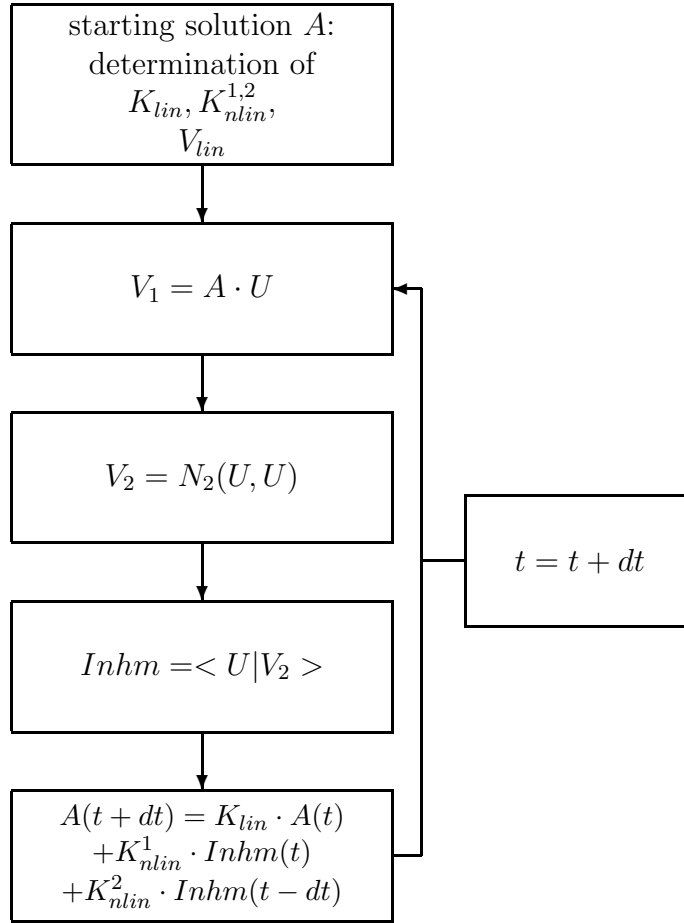
$$\begin{aligned} A_i(t + dt) = & \exp[\lambda_i dt] A_i(t) - \\ & \left\{ \frac{\exp[\lambda_i dt]}{\lambda_i} \left( 1 + \frac{1}{\lambda_i dt} \right) - \frac{1}{\lambda_i} \left( 2 + \frac{1}{\lambda_i dt} \right) \right\} \langle V_i | N_2(t) \rangle - \\ & \left\{ \frac{1}{\lambda_i} \left( 1 + \frac{1}{\lambda_i dt} \right) - \frac{1}{(\lambda_i)^2 dt} \exp(\lambda_i dt) \right\} \langle V_i | N_2(t - dt) \rangle. \end{aligned} \quad (\text{B.7})$$

Eq. (B.7) is written as

$$A_i(t + dt) = A_i(t) K_{lin} - K_{nlin}^1 \langle V_i | N_2(t) \rangle - K_{nlin}^2 \langle V_i | N_2(t - dt) \rangle$$

where the coefficients  $K_{lin} = \exp[\lambda_i dt]$  and the nonlinear evolution coefficients  $K_{nlin}^i$ , ( $i = 1, 2$ ) in the curly brackets have been introduced. These coefficients are calculated once at the start of the simulation. Note that we have suppressed the  $\mathbf{q}$ -dependence in all terms in this reduction.

We can summarize the time integration process by the help of a flow chart:



### B.3 Construction of the fields

In the simulation code, the complex expansion coefficients  $A_i(\mathbf{q}, t)$  with the corresponding linear eigenvectors  $U_{lin}(\mathbf{q})$  include the whole information. For instance the Fourier coefficients of the temperature field  $\Theta(\mathbf{x}, z, t)$  read

$$\Theta(\mathbf{q}, z, t) = \sum_j A_j(\mathbf{q}, z, t) U_j(\mathbf{q}, z). \quad (\text{B.8})$$

Here  $j$  runs over the  $3N$  eigenvectors. From the temperature, Fourier coefficients  $\Theta(\mathbf{x}, z, t)$  are constructed in real space:

$$\Theta(\mathbf{x}, z, t) = \Re \left( \sum_{\mathbf{q}} \Theta(\mathbf{q}, z, t) \exp(i\mathbf{q}\mathbf{x}) \right). \quad (\text{B.9})$$

An analogous expansion holds for the other fields, too. Near onset the fields are mostly determined by the dominant eigenvectors, (i.e for  $j = 1$ ) in Eq. (B.8).

Typically we use grey-scale plots for the fields at constant vertical coordinate  $z$  as function of  $x, y$ . In some cases, we show also contour plots in the  $x - z$  plane.



# Bibliography

- [1] A. C. Newell, T. Passot, and J. Lega. Order parameter equations for patterns. *Ann. Rev. Fluid Mech.*, 25:399–453, 1993.
- [2] M. C. Cross and P. C. Hohenberg. Pattern formation outside of equilibrium. *Rev. Mod. Phys.*, 65(3):851–1112, 1993.
- [3] F.H. Busse. Nonlinear properties of thermal convection. *Rep. Prog. Phys.*, 41:1929–1967, 1978.
- [4] F.H. Busse. Fundamentals of thermal convection. In *Mantle Convection: Plate Tectonics and Global Dynamics*, editors, W.R. Peltier. Gordon and Breach, Montreux, 1989.
- [5] E. Bodenschatz, W. Pesch, and G. Ahlers. Recent developments in Rayleigh-Bénard convection. *Annu. Rev. Fluid Mech.*, 32:709–778, 2000.
- [6] P. Manneville. *Dissipative structures and weak turbulence*. Academic Press, San Diego, 1990.
- [7] G. Dangelmayr and L. Kramer. Mathematical tools for pattern formation. In *Evolution of Spontaneous Structures in Dissipative Continuous Systems*, editor, F.H. Busse and S.C. Müller, pages 1–85. Springer, Berlin, 1998.
- [8] I.A. Eltayeb. Hydromagnetic convection in a rapidly rotating fluid layer. *Proc. R. Soc. Lond. A*, 326:229–254, 1972.
- [9] I.A. Eltayeb. Overstable hydromagnetic convection in a rapidly rotating fluid layer. *J. Fluid Mech.*, 71(1):161–179, 1975.
- [10] F.H. Busse and F. Finocchi. The onset of thermal convection in a rotating cylindrical annulus in the presence of a magnetic field. *Phys. Earth Plan. Int.*, 80:13–23, 1993.
- [11] M. Petry, F.H. Busse, and F. Finocchi. Convection in a rotating cylindrical annulus in the presence of a magnetic field. *Eur. J. Mech. B/Fluids*, 16(6):817–833, 1997.
- [12] I. Cupal. Ekman layer in 3D-model of the geodynamo. *Studia Geoph. et Geod.*, 42:261–271, 1998.

- 
- [13] Y. Ponty, A.D. Gilbert, and A.M. Soward. Kinematic dynamo action in large magnetic Reynolds number flows driven by shear and convection. *J. Fluid Mech.*, 435:261–287, 2001.
- [14] B. Desjardins, E. Dormy, and E. Grenier. Instability of Ekman-Hartmann boundary layers, with application to the fluid flow near the core mantle boundary. *Phys. Earth Planet. Interiors*, 123:15–26, 2001.
- [15] B. Desjardins, E. Dormy, and E. Grenier. Stability of mixed Ekman-Hartmann boundary layers. *Nonlinearity*, 12:181–199, 1999.
- [16] P.A. Gilman. Instabilities of the Ekman-Hartmann boundary layer. *Phys. Fluids*, 14(1):7–12, 1971.
- [17] W. Pesch and L. Kramer. General mathematical description of pattern-forming instabilities. In *Pattern Formation in Liquid Crystals*, editor, A. Buka and L. Kramer, pages 69–90. Springer, New York, 1996.
- [18] W. Pesch. Complex spatiotemporal convection patterns. *Chaos*, 6(3):348–357, 1996.
- [19] We used refined bisection methods taken from *Numerical Recipes* (the routines “zbrac” and “zbrent”).
- [20] For a search in a fixed direction in the  $\mathbf{q}$ -plane (e.g. for longitudinal or transverse rolls) we use a golden section search (“golden”) and for a two dimensional search (oblique rolls) a downhill simplex method (“amoeba”); again from *Numerical Recipes*.
- [21] F.H. Busse. Stability of finite amplitude cellular convection and its relation to an extremum principle. *J. Fluid Mech.*, 30:625, 1967.
- [22] E. Plaut and W. Pesch. Extended weakly nonlinear theory of planar nematic convection. *Phys. Rev. E*, 59:1747–1769, 1998.
- [23] L.D. Landau. On the theory of phase transitions. In *Collected Papers of L.D. Landau Part I&II*, editor, D. ter Haar. Gordon and Breach Science, New-York, 1967.
- [24] M. Auer, F.H. Busse, and R.M. Clever. Three-dimensional convection driven by centrifugal buoyancy. *J. Fluid Mech.*, 301:371–382, 1995.
- [25] F.H. Busse, M.A. Zaks, and O. Brausch. Centrifugally driven thermal convection at high Prandtl numbers. *Physica D*, 184:3–20, 2003.
- [26] D. A. Egolf. The dynamical dimension of defects in spatiotemporal chaos. *Phys. Rev. Lett.*, 81:4120–4123, 1997.

- 
- [27] S. Chandrasekhar. *Hydrodynamics and Hydromagnetic Stability*. Oxford Uni. Press, London, 1961.
- [28] M. Jaletzky and F.H. Busse. New patterns in centrifugally driven thermal convection. *Proc. Nat. Acad. Sci.*, 97:5060–5064, 2000.
- [29] E. Kurt, F.H. Busse, and W. Pesch. Hydromagnetic convection in a rotating annulus with an azimuthal magnetic field. *Theor. Comput. Fluid Dyn.*, to be published, 2004.
- [30] R. Lifshitz. The symmetry of quasiperiodic crystals. *Physica A*, 232(3-4):633–647, 1996.
- [31] R. Lifshitz. Theory of color symmetry for periodic and quasiperiodic crystals. *Rev. Mod. Phys.*, 69(4):1181–1218, 1997.
- [32] O. Brausch. *Rayleigh-Bénard Konvektion in verschiedenen isotropen und anisotropen Systemen*. PhD thesis, Universität Bayreuth, 2001.
- [33] R.V Cakmur, D.A. Egolf, B.B. Plapp, and E. Bodenschatz. Bistability and competition of spatiotemporal chaotic and fixed point attractors in Rayleigh-Bénard convection. *Phys. Rev. Lett.*, 79:1853–1856, 1997.
- [34] W. Decker, W. Pesch, and A. Weber. Spiral defect chaos in Rayleigh-Bénard convection. *Phys. Rev. Lett.*, 73:648–651, 1994.
- [35] D.A. Egolf, IV. Melnikov, W. Pesch, and R.E. Ecke. Mechanisms of extensive spatiotemporal chaos in Rayleigh-Bénard convection. *Nature*, 404 (6779):733–736, 2000.
- [36] K.M.S Bajaj, G. Ahlers, and W. Pesch. Rayleigh-Bénard convection with rotation at small Prandtl numbers. *Phys. Rev. E*, 65:1–13, 2002.
- [37] D.R. Fearn, C.J. Lamb, D.R. McLean, and R.R. Ogden. The influence of differential rotation on magnetic instability, and nonlinear magnetic instability in the magnetostrophic limit. *Geophys. Astrophys. Fluid Dyn.*, 86(3-4):173–200, 1997.
- [38] O. Andreev, C. Haberstroh, and A. Thess. Visualisation of magnetoconvection. *Phys. Fluids*, 15:3886–3889, 2003.
- [39] B.W. Atkinson and J.W. Zhang. Mesoscale shallow convection in the atmosphere. *Rev. Geophys.*, 34:403–431, 1996.
- [40] D. Etling and R.A. Brown. Roll vortices in the planetary boundary-layer - a review. *Boundary-Layer Meteo.*, 65(3):215–248, 1993.
- [41] D.K. Lilly. On the instability of Ekman boundary flow. *J. Atmos. Sci.*, 23:481–496, 1966.

- 
- [42] P.L. Sankov and E.M. Smirnov. Bifurcation and transition to turbulence in the gap between rotating and stationary parallel disks. *Fluid Dyn.*, 19:695–702, 1985.
- [43] P.L. Sankov and E.M. Smirnov. Stability of viscous flow between rotating and stationary disks. *Fluid Dyn.*, 26(6):857–864, 1991.
- [44] M. Itoh. On the stability of flow between coaxial rotating disks. *ASME*, 114:83–89, 1991.
- [45] N.P. Hoffmann, F.H. Busse, and W.-L. Chen. Transitions to the complex flows in the Ekman-Couette layer. *J. Fluid Mech.*, 366:311–331, 1998.
- [46] N.P. Hoffmann and F.H. Busse. Isolated solitary vortex solutions for the Ekman-Couette layer. *Eur. J. Mech. B - Fluids*, 19:391–402, 2000.
- [47] A.J. Faller. An experimental study of the instability of the laminar Ekman boundary layer. *J. Fluid Mech.*, 15:560–576, 1963.
- [48] A.J. Faller and R.E. Kaylor. Investigations of stability and transition in rotating boundary layers. In *Dynamics of Fluids and Plasmas*, editors, S.I. Pai. Academic Press, New-York, 1996.
- [49] A.J. Faller. Instability and transition of the disturbed flow over a rotating disk. *J. Fluid Mech.*, 230:245–269, 1991.
- [50] D.R. Caldwell and C.W. Van Atta. Characteristics of Ekman boundary layer instabilities. *J. Fluid Mech.*, 44:79–95, 1970.
- [51] E. Crespo del Arco, P. Maubert, A. Randriamampianina, and P. Bontoux. Spatio temporal behaviour in a rotating annulus with a source-sink flow. *J. Fluid Mech.*, 32:1–27, 1996.
- [52] E. Serre, S. Hugues, E. Crespo del Arco, A. Randriamampianina, and P. Bontoux. Spiral and circular instability patterns in an Ekman boundary layer flow. *Int. J. Heat Fluid Flows*, 22(1):82–93, 2000.
- [53] E. Serre and J.P. Pulicani. A 3D pseudospectral method for convection in a rotating cylinder. *Computers and Fluids*, 30(4):491–519, 2001.
- [54] L. Schouveiler, P. Le Gal, M.P. Chauve, and Y. Takeda. Experimental study of the stability of the flow between a rotating and a stationary disk. In *Advances in Turbulence VI*, editor, S. Gavrilakis. Kluwer Academic Publishers, Dordrecht, 1996.
- [55] L. Schouveiler, P. Le Gal, and M.P. Chauve. Stability of a travelling roll system in a rotating disk flow. *Phys. Fluids*, 10:2695–2697, 1998.

- [56] L. Schouveiler, P. Le Gal, M.P. Chauve, and Y. Takeda. Spiral and circular waves in the flow between a rotating and a stationary disk. *Experiments in Fluids*, 26:179–187, 1999.
- [57] P.A. Gilman and E.R. Benton. Influence of an axial magnetic field on steady linear Ekman boundary layer. *Phys. Fluids*, 11:2397–2401, 1968.
- [58] R. Hide. Dynamics of atmospheres of major planets with an appendix on viscous boundary layer at rigid bounding surface of an electrically-conducting rotating fluid in presence of a magnetic field. *J. Atmos. Sci.*, 26:841, 1969.
- [59] D.B. Ingham. Magneto-hydrodynamic flow in a container. *Phys. Fluids*, 12:389, 1969.
- [60] E.R. Benton and E. Loper. On spin-up of an electrically conducting fluid: 1. Unsteady hydromagnetic Ekman-Hartmann boundary-layer problem. *J. Fluid Mech.*, 39:561, 1969.
- [61] E. Loper. Steady hydromagnetic boundary layer near a rotating, electrically conducting plate. *Phys. Fluids*, 13(12):2999–3002, 1970.
- [62] E. Loper. General solution for the linearized Ekman-Hartmann layer on a spherical boundary. *Phys. Fluids*, 13(12):2995–2998, 1970.
- [63] L.M. Witkowski and J.S. Walker. Numerical solutions for the liquid-metal flow in a rotating cylinder with a weak transverse magnetic field. *Fluid Dyn. Res.*, 30:127–137, 2002.
- [64] S. Kaddeche, D. Henry, T. Putelat, and H. Ben Hadid. Instabilities in liquid metals controlled by constant magnetic field-Part I: vertical magnetic field. *J. Crystal Growth*, 242:491–500, 2002.
- [65] B. Carter, D. Langlois, and D.M. Sedrakian. Centrifugal buoyancy as a mechanism for neutron star glitches. *Astron. Astrophys.*, 361:795–802, 2000.
- [66] D. Mackay and K. Galsgaard. Evolution of a density enhancement in a stratified atmosphere with uniform vertical magnetic field. *Solar Physics*, 198:289–312, 2001.
- [67] K. Zhang and C.A. Jones. The influence of Ekman boundary layers on rotating convection. *Geophys. and Astrophys. Fluid Dyn.*, 71:145–162, 1993.
- [68] K. Zhang and P. Roberts. On stabilising/destabilising effects of Ekman boundary layers in rotating convection. *Geophys. and Astrophys. Fluid Dyn.*, 88:215–223, 1998.
- [69] V.I. Pariev. Laminar MHD Ekman layer in differentially rotating fluid: Linear theory. *Magnetohydrodynamics*, 39(2):123–146, 2003.

- 
- [70] V.W. Ekman. On the influence of the Earth's rotation on ocean currents. *Arkiv. Mat. Astr. Fys. Bd.*, 2:53, 1905.
- [71] L. Schouveiler, P. Le Gal, and M.P. Chauve. Instabilities of the flow between a rotating and a stationary disk. *J. Fluid Mech.*, 443:329–350, 2001.
- [72] E. Serre, E. Crespo del Arco, and P. Bontoux. Annular and spiral patterns in flows between rotating and stationary discs. *J. Fluid Mech.*, 434:65–100, 2001.
- [73] T. Tagawa, A. Ujihara, and H. Ozoe. Numerical computation for Rayleigh-Bénard convection of water in a magnetic field. *Int. J. Heat and Mass Transfer*, 46(21):4097–4104, 2003.
- [74] F.H. Busse and R.M. Clever. Three- dimensional convection in an inclined layer heated from below. *J. Engineering Math.*, 26:1–19, 1992.
- [75] W. Decker. *Mathematische Methoden zur Beschreibung strukturbildender Systeme - eine kritische Analyse*. PhD thesis, Universität Bayreuth, 1995.





## Acknowledgments

Initially, I would like to express my deepest sense of gratitude to my scientific advisors Prof. Dr. W. Pesch and Prof. Dr. F.H. Busse for their patient guidance, encouragement, and their invaluable help that I received around three years in “*Festspielstadt Bayreuth*”. I learned so much from them. I would like to emphasize Prof. Dr. W. Pesch’s helps especially about the mathematical, numerical tricks which he has taught me to solve the basic equations and basic concepts about the nonlinear paradigm. I can not forget his support to improve my scientific English as well as “Deutsch”. In the case of the identification of instabilities, the special courses of Prof. Dr. F.H. Busse which I have attended in three-year-time helped me. Thank you very much!

Secondly, I was always able to get advices and helps from my colleagues in Bayreuth University. Their names read as Dr. Norbert P. Hoffmann, Dr. Michael Westerbürg, Alejandro Luque, Dr. Radostin Simitev, Dr. Juan P. Zagorodny. Thanks a lot!

I feel like saying “Thanks, Dr. Pavel Akimov!” for his precious help and talks at the coffee breaks. By the way, what is the latest state in the Russian football league, Pavel?

I wish to thank my friends Adem Mermer, Aykut Karakuzu, Dincer Haslak, Dr. Halil Düzgün, Yakup Keskin, Peter S. Frank and Fatih Cetinel for their nice friendship and moral support during my study. Special thanks to Görkem Uludüz and Clara Winkler for their helps.

My deepest thanks are for my wife, Hilal. She has always been with me by heart beyond the green mountains of Bavaria as my spiritual guide. Finally, I can never thank my mother and father enough for all their love and support.